Functional imaging of pathophysiological neural circuit activity using electrical impedance tomography

Karolina Kozeniauskaite

A thesis submitted for the degree of

Doctor of Philosophy

of

University College London

Department of Medical Physics and Biomedical Engineering

University College London

January 2025

Declaration

I, Karolina Kozeniauskaite, confirm that the work presented in this thesis is my own. Where information has been derived from other sources, I confirm that this has been indicated in the thesis.

Signed:

Abstract

Electrical impedance tomography (EIT) is a novel neuroimaging method which relies on a principle of bioimpedance and its changes with neuronal activity for imaging brain circuits. In recent years, EIT has demonstrated the capability of tracing physiological and pathological neural circuit activity in the rat cerebral cortex with a resolution of milliseconds and micrometres. Thus, EIT represents a unique tool for investigating neural circuit dynamics in rodent models of normal and epileptiform brain activity to improve the diagnostics and therapeutics for pharmacoresistant epilepsy patients. The aim of this thesis was to further develop EIT for a high-resolution real-time imaging of pathophysiological activity throughout the rat brain using intracranial or scalp electrodes. The main purpose of the work was to assess the feasibility of detecting epileptogenic activity anywhere in the rat brain with intracranial depth EIT and assessing its utility in presurgical epilepsy monitoring. Experimental work performed to address the aim and the purpose is presented in Chapters 2 – 6 preceded by a detailed review of the literature and the technical background in Chapter 1. Overall, the results show that, with the present EIT technology, functional imaging of neural circuits in rodent brain cannot be achieved with sufficient resolution using non-penetrating electrodes placed on the scalp (Chapter 2) or on the cerebral cortex (Chapter 3). On the other hand, intracranial EIT with penetrating depth electrodes can track both fast and slow changes during pathological neural activity, such as epileptic seizures, with a mesoscopic resolution of 0.2 – 0.3 mm and $\leq$20 ms (Chapters 5 and 6). This requires implementation of a novel stereo-electrode array and experimental setup, the development of which is detailed in Chapter 4. Collectively, the finding of this thesis suggest that EIT can produce functional images of brain circuit activity with unmatched spatiotemporal and depth resolution if combined with intracranial depth electrodes. These results support continued development of EIT for research and clinical use with promising prospects in the field of epilepsy.

Impact Statement

Understanding neural circuit dynamics in healthy and diseased brain is an all-time endeavour of neuroscientific research. However, the progress is limited by the availability of the appropriate techniques. Despite the expansion in micro- and macroscopic neuroimaging modalities, the tools for investigating brain function at a level of neural networks are sparse. This gap is critical when considering such disorders as epilepsy which is characterised by aberrant neural network activity with associated neurological, motor and psychiatric symptoms. Whilst pharmacotherapy is generally effective, approximately one third of the patients are resistant to the standard drug treatment. In cases of severe and debilitating refractory epilepsy, patients may be considered for surgical intervention with the hope of improved quality of life upon the removal of putative epileptogenic tissue. Nonetheless, up to 80 % of surgeries lead to seizure relapse due to inaccurate localisation of the epileptogenic zone (EZ) owing to the limitations in the spatiotemporal resolution of the existing diagnostic neuroimaging techniques. Whilst a sub-millimetre and millisecond accuracy is necessary for delineating the precise recruitment of epileptogenic circuits, most commonly-used neuroimaging modalities cannot achieve such granularity in both their spatial and temporal characteristics. Therefore, the functional images of neural circuit dynamics typically lack the granular detail necessary to accurately depict epileptic activity. Electrical impedance tomography carries the potential to circumvent these issues. EIT is a medical imaging technique which reconstructs images of internal conductivity changes of an object using peripherally placed electrodes. Since impedance of brain tissue can change due to both electrical activity ('fast' changes) and concomitant neurometabolic phenomena ('slow' changes), intracerebral impedance changes can act as direct markers of regional brain activation by physiological and pathological stimuli. Previous EIT studies using intracranial epicortical electrodes in rats achieved a maximal spatiotemporal resolution of 200 µm and 2 ms, both of which align with the requirements for epilepsy neuroimaging. These findings suggested that EIT could potentially overcome the issues with EZ localisation in surgical epilepsy patients and, therefore, resolve a significant problem in epilepsy standard-of-care. However, the depth sensitivity of EIT was shown to be restricted to the cerebral cortex and the hippocampus, located ~2.5 – 3 mm below the surface of the rat brain. Since imaging of both superficial and deep epileptogenic sources at a mesoscopic spatiotemporal resolution is desirable, previous findings suggested that further development was necessary in order to successfully translate EIT into the current clinical practice.

The aim of the work presented in this thesis was to extend the detection limits of brain EIT beyond the top 3 mm of the brain whilst maintaining high spatiotemporal resolution achieved previously (~200 µm, ~2 ms). The broader goal was to develop a viable neuroimaging method for rat studies and a prototype for clinical use. To achieve this goal, the research was focused on improving the depth sensitivity of brain EIT hindering its large-scale implementation in neuroscientific research and medical neuroimaging.

The first part of this thesis focused on the feasibility of real-time EIT of slow neural activity in rats with non-penetrating electrodes on the scalp or on the brain surface. This was intended to assess the potential for replacing functional magnetic resonance neuroimaging (fMRI) with slow neural EIT for imaging cerebral haemodynamic changes associated with regional brain activation in rodent research and beyond. To date, such objective has not been explored in great depth in EIT research and was mainly discussed in theory with limited but promising experimental evidence. Successful accomplishment of this goal was considered to carry significant impact on the current neuroimaging landscape. In Chapter 2, substitution between fMRI and EIT was proposed based on an initial theoretical assessment and comparison of the key fMRI and EIT attributes, including the spatiotemporal resolution, cost, versatility, availability and the types of neurophysiological processes which can be imaged with these techniques. Ultimately, research presented in this thesis showed that, despite high temporal resolution, portability, reduced complexity and cost of use of EIT in comparison to fMRI, the spatial and depth resolution of scalp and epicortical slow neural EIT were at present inferior to fMRI. Therefore, it was concluded that the technical capabilities of scalp and epicortical slow neural EIT were insufficient for routine use in animal research as well as imaging and mapping of epileptogenic networks in humans.

Having established that the current spatiotemporal limits of scalp and epicortical slow neural EIT did not fit the needs for accurate mapping of neural circuit dynamics, the second half of this thesis concentrated on implementation of a novel penetrating intracranial array for fast and slow EIT in the murine brain. Collectively, the results of this part of the thesis demonstrated that the coverage and the depth resolution of brain EIT could be improved substantially by using penetrating intracranial electrodes. An optimised electrode configuration was shown to enable real-time EIT of fast electrical activity during seizures in anaesthetised rats with a millisecond and micrometre accuracy which was unachievable with planar boundary electrodes. These preliminary findings encourage continued development of intracranial EIT with depth arrays and suggest its future implementation as an adjunct imaging modality in epilepsy patients with pre-implanted probe electrodes. Pilot data indicate that a combination of fast and slow depth neural EIT recordings could provide unique information about neural circuit dynamics during seizures and enable reconstruction of a personalised epileptogenic network at an enhanced spatiotemporal resolution.

Acknowledgements

This thesis would have not come to light without the support of the following people. First and foremost, I would like to thank my primary supervisor, Professor David Holder, for seeing potential in me and offering to join his group, for appreciating my passion for science and, most importantly, for teaching me “to see the wood for the trees”.

I would also like to thank sincerely my secondary supervisor Dr Kirill Aristovich – for introducing me into an unfamiliar world of mathematics and engineering, for debating me on neuroscientific dilemmas and for his never-ending support during experiments and beyond.

A special thank you to Professor Sebastian Brandner and his team for assisting me with histological analysis. Similarly, thank you to Dr Nicole Thompson for sharing her insight and expertise on interpreting the histology results.

I feel privileged to have learnt the animal work from Dr Svetlana Mastitskaya and Dr Sana Hannan – thank you for teaching me all the animal preparation and surgical techniques.

Thank you to Adam Fitchett, Kai Mason, and Yuval Gal-Shohet for helping with the data analysis, modelling and engineering challenges.

Lastly but not least, I would like to express my deepest gratitude to my parents, Nijole and Remigijus, my sister Gabriele, and my partner Chris. Their unwavering support, love and encouragement pushed me forward even during the most challenging of times.

Table of Contents

List of figures

List of abbreviations

2D – two-dimensional

3D – three-dimensional

AC – alternating current

aCSF – artificial cerebrospinal fluid

AD – afterdischarge

Ag-AgCl – silver-silver chloride

AMPA – α-amino-3-hydroxy-5-methyl-4-isoxazol epropionic acid

AP – anteroposterior

ASL – arterial-spin labelling

ATP – adenosine triphosphate

BBB – blood-brain barrier

BOLD – blood-oxygenation-level dependent

Ca^{2+} – calcium ion

CBF – Cerebral Blood Flow

CBV – Cerebral Blood Volume

cc – corpus callosum

CeM – central amygdaloid nucleus

Cg – cingulum

Cl^- – chloride ion

CMRGlu – cerebral metabolic rate of glucose

$CMRO_2$ – cerebral metabolic rate of oxygen

CNS – central nervous system

CPu – caudate putamen

CR3 – complement receptor 3

CSF – cerebrospinal fluid

CT – computed tomography

D3V – dorsal third ventricle

DBS – deep brain stimulation

DC – direct current

dfMRI – diffusion functional magnetic resonance imaging

DG – dentate gyrus
DOI – diffuse optical imaging
DV – dorsoventral
dV – voltage change
dZ – impedance change
ECG - electrocardiogram
ECoG – electrocorticography
EEG – electroencephalography
EIS – electrical impedance spectroscopy
EIT – Electrical Impedance Tomography
EPSP – excitatory post-synaptic potential
ESI – EEG source imaging
ESM – electrical stimulation mapping
EZ – epileptogenic zone
f – fornix
F18-FDG – fluorine-18-fluorodeoxyglucose
FEM – finite element model
FLE – frontal lobe epilepsy
fMRI – Functional Magnetic Resonance Imaging
fnEIT – fast neural electrical impedance tomography
fNIRS – functional near-infrared spectroscopy
FWHM – full width at half maximum
GABA – gamma-aminobutyric acid
GFAP – glial fibrillary acidic protein
Hb – haemoglobin
H&E – haematoxylin and eosin
IB$_4$ – B4 isolectin
IBP – intra-arterial blood pressure
ic – internal capsule
IP – intraperitoneal
IPSP – inhibitory post-synaptic potential
IV – intravenous
J – normalised current density

K$^+$ – potassium ion

Kir2.1 – inward-rectifier potassium channel

LDDM – laterodorsal thalamic nucleus, dorsomedial part

LDVL – laterodorsal thalamic nucleus, ventrolateral part

LFP – local field potential

LGP – lateral globus pallidus

LH – lateral hypothalamus

LSCI – laser speckle contrast imaging

LSS – lateral stripe of the striatum

LV – lateral ventricle

M1 – primary motor cortex

M2 – secondary motor cortex

MD-EIT – magnetic-detection electrical impedance tomography

MEG – magnetoencephalography

ML – mediolateral

MR – magnetic resonance

MRI – magnetic resonance imaging

MSI – MEG source imaging

µSWD – averaged spike-and-wave discharge

MTLE – mesial temporal lobe epilepsy

Na$^+$ – sodium ion

NIRS – near-infrared spectroscopy

NMDA – N-methyl-D-aspartate

OCT – optical coherence tomography

OI – optical imaging

OISI – optical intrinsic signal imaging

OPM – optically-pumped magnetometers

PEDOT:PSS – poly(3,4-ethylenedioxythiophene) polystyrene sulfonate

PET – Positron Emission Tomography

PLA – polylactic acid

PO – posterior thalamic nuclear group

PS – parastrial nucleus

PSP – post-synaptic potential

PSWD – polyspike-and-wave discharge

PT – paratenial thalamic nucleus

R – resistance

RF – radiofrequency

ROI – region of interest

RT – reticular nucleus of the thalamus

S1 – primary somatosensory cortex

S1BF – facial primary somatosensory cortex (whisker barrel field)

S1DZ – primary somatosensory cortex, dysgranular zone

S1FL – forelimb primary somatosensory cortex

S1HL – hindlimb primary somatosensory cortex

S1Tr – trunk primary somatosensory cortex

S2 – the secondary somatosensory cortex

SEEG – stereotactic electroencephalography

SEP – somatosensory evoked potential

SESI – SEEG source imaging

SI – substantia innominata

SIB – substantia innominata, basal part

SMC – smooth muscle cells

snEIT – slow neural electrical impedance tomography

SNR – signal-to-noise ratio

SOZ – seizure onset zone

SPECT – single-photon emission computed tomography

SQUID – superconducting quantum interference device

SWD – spike-and-wave discharge

TC – thalamocortical

VASO – vascular space occupancy

VL – ventrolateral thalamic nucleus

VLH – ventrolateral hypothalamic nucleus

VM – ventromedial thalamic nucleus

VP – ventral pallidum

VPL – ventral posterolateral thalamic nucleus

VPM – ventral posteromedial thalamic nucleus

X – reactance

Z – impedance

$Z_{\delta\sigma}$ − Z-score of reconstructed conductivity change

$\delta\sigma$ − conductivity change

Chapter 1

Introduction and Literature Review

Electrical impedance tomography (EIT) is a medical imaging tool which reconstructs images of functional conductivity changes inside the body of interest using boundary electrical impedance measurements. EIT has been investigated for functional imaging of pulmonary, cardiac, peripheral and central nervous system (CNS) activity, the latter of which forms the core of this thesis. This chapter constitutes a literature review which contains an overview of the most prominent functional brain imaging techniques, the general principles of EIT and the review of the previous studies imaging functional brain circuit activity under normal and pathological conditions using ‘slow’ or ‘fast’ EIT. The chapter is concluded by an outline of the purpose and the rationale behind this PhD project and the studies undertaken to address the stated objectives.

1.1 Functional neuroimaging

For the last several decades, functional brain imaging has been under continued innovation allowing us to greatly expand our knowledge about the brain physiology from a microscopic to a macroscopic resolution. This has largely improved our understanding of neural networks and pathways underlying various cognitive processes and neurological disorders thereof. To understand where EIT stands amongst a myriad of other neuroimaging tools, it is necessary to discuss the types of functional changes in the brain that are typically imaged and what techniques are currently used to image those changes. Hence, the following section will outline the nature and the mechanisms behind the brain activity changes occurring in response to pathophysiological stimuli. This will be followed by a comprehensive overview of the existing functional neuroimaging tools and their benefits and drawbacks in relation to imaging brain activity.

1.1.1 ‘Fast’ and ‘slow’ activity changes in the brain

Functional brain activity can be parametrically described by two broad categories of changes occurring in the brain. ‘Fast’ neural changes refer to the electrical activity of neurons which develop over milliseconds in response to exogenous or endogenous stimuli. Consequently, the metabolic demand of actively firing neurons is greatly augmented leading to a relatively slow alteration in cerebral haemodynamics which lasts for seconds and therefore corresponds to ‘slow’ activity-related changes in the brain. Albeit describing distinct signalling pathways, fast and slow neural changes interact in a complex manner and, therefore, have both been utilised in functional neuroimaging as direct and indirect markers of pathophysiological brain activity.

1.1.1.1 ‘Fast’ neural changes

In neurons, electrical activity is propagated by the movement of ions across plasma membrane. Transient changes in intracellular and extracellular concentrations of ions, predominantly sodium (Na^+), potassium (K^+), and calcium (Ca^{2+}) cations, create electric potential differences which can be measured *in vivo* at a single-cell or circuit level using extracranial or intracranial electrodes. These neural activity changes occur at a millisecond timescale and, therefore, are considered ‘fast’ and reflect functional changes in brain activity directly.

Fast neural activity is typically classified into two types, spiking and synaptic activity. Spikes, or action potentials, are brief events (1 – 2 ms in duration) representing the neuronal output signal. Action potentials are triggered when the resting membrane potential exceeds a threshold potential causing the coordinated opening of voltage-gated ion channels and thereby allowing the influx and efflux of Na^+ and K^+, respectively (Hodgkin & Huxley, 1952). The local change in the resting membrane potential is propagated along the axon to its terminal and results in the release of neurotransmitters into the synaptic cleft. Neurotransmitters then bind to the receptors on the post-synaptic cell membrane and trigger a post-synaptic potential (PSP), a second type of detectable fast neural activity (Byrne, 2014).

Depending on neurotransmitter released and the receptor it activates, PSPs can be excitatory or inhibitory (EPSP and IPSP, respectively) and, thus, increase or decrease the spiking in the post-synaptic neuron, respectively (Byrne, 2014). Compared to spikes, PSPs are much slower and last tens to hundreds of milliseconds (Benardo, 1994; Byrne, 2014; Hartzell, 1981). Overall, excitatory neurotransmission predominates over the inhibitory one and is considered the primary means of neural communication in the brain. The main excitatory neurotransmitter glutamate triggers an EPSP by binding to its ionotropic postsynaptic N-methyl-D-aspartate (NMDA) and α-amino-3-hydroxy-5-methyl-4-isoxazol epropionic acid (AMPA) receptors which lead to an influx of Ca^{2+} or K^+ and Na^+, respectively (Mayer, 2005). This raises the resting potential of the post-synaptic neuron above the threshold and triggers an action potential. On the contrary, IPSPs cause a decrease in the resting potential of the post-synaptic cell. That can be achieved by an influx of negatively charged ions as it is in the case of gamma-aminobutyric acid (GABA) receptor which permits the inward movement of chloride (Cl^-) ions upon its activation by GABA neurotransmitter (Wu & Sun, 2015). Generally, inhibitory neurotransmission plays more of a modulatory role fine-tuning the neural circuit activity to achieve the necessary level of net excitation or net inhibition (Gu et al., 2019; Sears & Hewett, 2021).

1.1.1.2 'Slow' neural changes

Brain is one of the most metabolically active organs in the body. Under physiological conditions, it normally consumes around 10 times more oxygen and 12 times more glucose than the rest of the body (Weber, 2015). Considering the lack of energy storage capacity in the brain, a sudden spike in energy consumption by an active brain region needs to be offset within an adequate spatiotemporal precision. This inherently means an enhanced delivery of blood to the cerebral tissue. A timely metabolic support to neurons is achieved through the mechanisms of neurovascular coupling which links localised increase in neuronal activity to the haemodynamic changes in the surrounding brain tissue.

The earliest accounts on the relationship between changes in brain activity and cerebral haemodynamics date back to the late 19th century. Empirical observations of coordinated increase in brain volume and systemic blood pressure upon the presentation of sensory or chemical stimuli to animals led to the first hypotheses about the neurovascular coupling (Roy and Sherrington, 1890). Nevertheless, it was not until the advent of the autoradiographic techniques and later development of positron emission tomography (PET) and functional magnetic resonance imaging (fMRI) that a clear link between neuronal activity and cerebral blood supply was established (Fox et al., 1985; Lassen et al., 1978; Ogawa et al., 1992). Since then, the mechanistic pathways linking neuronal and vascular networks in the brain have been investigated with increasing precision enabled by the development of neuroimaging techniques.

The principles of neurovascular coupling are closely tied to the brain's vascular anatomy and, therefore, should be considered in its context. The primary locus of functional hyperaemia is the capillary bed which receives arterial blood from the penetrating cerebral arterioles branching off the pial arteries and arterioles on the surface of the cortex (Weber, 2015). High-resolution optical imaging and fMRI studies show that the immediate response is generated in the microvasculature and then propagated retrogradely to the larger vessels (Chen et al., 2011; Hillman et al., 2007; Yu et al., 2012).

The anatomy of capillaries enables a rapid haemodynamic response through an efficient exchange of gas and metabolites. The capillary wall comprises a single-cell endothelial layer which is held together by tight junctions constituting the blood-brain barrier (BBB) (Oldendorf, 1977). The monolayer is covered by the basal lamina with contractile mural cells, called pericytes, and then encapsulated by astrocytic end-feet. Gas exchange occurs via passive diffusion whereas glucose requires an active transport. The energy substrate is delivered to neurons directly or via astrocytes where glucose is converted into intermediary substrates, lactate or pyruvate, and then shuttled to neurons for oxidative metabolism (Herrero-Mendez et al., 2009; Weber, 2015).

The neurovascular response in the capillary bed is driven by the basic fluid dynamics and by the vasoactive by-products of synaptic activity. The former mechanism relates the change in the oxygen content in the capillary blood to the change in the cerebral blood flow (CBF). De-oxygenation of red blood cells increases their deformability which is inversely related to the blood viscosity (Wei et al., 2016). Hence, the capillary flow increases in the vicinity of the metabolically active neurons. The second mechanism regulating capillary response involves synaptic transmission of glutamate. The activation of ionotropic and metabotropic glutamate receptors on the post-synaptic neurons and astrocytes, respectively, have been shown to result in Ca^{2+}-dependent production and release of potent vasodilators, such as nitric oxide and prostaglandins (Hall et al., 2014; Lacroix et al., 2015; Mapelli et al., 2017). Additionally, a neural activity-related increase in extracellular K^+ itself can stimulate local CBF changes. One of the suggested mechanisms involves highly-debated contraction of capillaries due to an ATP-dependent efflux of K^+ from pericytes (Grubb et al., 2020; Sancho et al., 2022). A less controversial explanation involves the activation of inward-rectifier K^+ (Kir2.1) channels on endothelial cells initiating a retrograde hyperpolarising signal which causes vasodilation in upstream arterioles and increases perfusion towards the site of signal initiation (Longden et al., 2017).

Endowed with smooth muscle cells (SMCs), arterioles and arteries have long been appreciated in the regulation of CBF. SMCs are not only receptive to vasoactive substances released by neurons and astrocytes but also respond to changes in intravascular pressure via the myogenic mechanism (Faraci et al., 1993; Harder et al., 2011; Ko et al., 1990; Li & Iadecola, 1994). The regulation of vascular smooth muscle tone relies on the interplay between K^+ and Ca^{2+} and their respective channels (Dogan et al., 2019; Nelson et al., 1995; Osol et al., 2002). Increased intracellular Ca^{2+} depolarises the SMC membrane and leads to vasoconstriction whereas hyperpolarisation due to K^+ efflux causes vasodilation. This has been suggested as the basis for cerebrovascular autoregulation and activity-induced neurovascular response (Harder et al., 2011). The hyperpolarising signal is retrogradely conducted from the capillary endothelium to the SMCs where it triggers the orchestrated movement of Ca^{2+} and K^+ which fine-tunes the spatiotemporal topology of the CBF response (Longden et al., 2017; Moshkforoush et al., 2020).

1.1.2 Imaging of fast neural activity

The first category of functional imaging techniques probes neural activity changes directly. This is mainly achieved using electrophysiology techniques which operate with a temporal resolution of milliseconds. Two examples are electroencephalography (EEG) and magnetoencephalography (MEG), both of which are abundantly applied in research and clinical practice to measure spontaneous and evoked fast neural activity. A detailed discussion of these techniques is provided in the sub-sections below followed by a summary of the main benefits and drawbacks at the end of the review.

1.1.2.1 Electroencephalography

EEG records differential scalp measurements of electric field potentials generated by the synchronised activity of large populations of neurons at rest or in response to pathophysiological stimuli (Brienza & Mecarelli, 2019). In principle, the EEG signal is the result of spatiotemporally summated PSPs of cortical neurons with degrading depth sensitivity due to volume conduction phenomenon (Brienza & Mecarelli, 2019; Olejniczak, 2006). Therefore, the main drawback of EEG is poor spatial resolution and specificity as pinpointing the subcortical sources from the scalp EEG is practically impossible due to an ill-posed inverse problem (Kaiboriboon et al., 2012; Wendel et al., 2009). In the last few decades, this issue has been addressed through the development of mathematical and computational models and algorithms which have enabled three-dimensional (3D) EEG source imaging (ESI). However, the result of ESI as well as its accuracy is highly dependent on the density of electrodes and the choice of a priori mathematical models, therefore, the solution is not straightforward and is often error-prone (Beniczky & Sharma, 2019; Kaiboriboon et al., 2012).

1.1.2.2 Magnetoencephalography

MEG operates in a similar fashion to EEG, except it registers changes in magnetic, rather than electric, fields created by coordinated electrical activity of neurons (Cohen, 1968). Instead of scalp electrodes, MEG is typically performed using superconducting quantum interference devices (SQUIDs) as magnetometers which require cryogenic cooling to operate and, therefore, are housed in a liquid helium dewar a few centimetres above the head surface (Cohen, 1972). This is one of the main limitations of MEG as it impacts not just the practicality of MEG recordings but also the signal strength which decreases with the square of the distance between the sensor and the measurement source. Moreover, the neuromagnetic fields are extremely weak (around 10^{-15} T) and are easily obscured by the Earth’s magnetic field necessitating a magnetically shielded environment for performing MEG (Singh, 2014). Luckily, recent developments in room-temperature optically-pumped magnetometers (OPMs) have been able to mitigate the signal reduction with decreased scalp-sensor separation distance and allow neural recordings in freely moving subjects (Boto et al., 2018; Iivanainen et al., 2017; Iivanainen et al., 2019). Nevertheless, magnetic shielding remains a challenge as OPMs pose even more stringent requirements for interference reduction (Hill et al., 2022).

Despite the above downsides, the relative transparency of head tissues to the magnetic fields gives MEG an advantage over EEG which suffers from signal distortion by the skull, the scalp and the cerebrospinal fluid (CSF) (Barth et al., 1986; Okada et al., 1999). Consequently, MEG source imaging (MSI) has been shown to exhibit enhanced spatial fidelity in comparison to ESI (Hedrich et al., 2017; Leijten et al., 2003). However, due to magnetic field orientation, MEG is blind to perfectly radial sources of neural activity and is most sensitive to tangential sources which are normally more superficial (Barkley & Baumgartner, 2003; Beniczky & Sharma, 2019). On the other hand, in comparison to MSI, ESI exhibits slightly increased sensitivity to deeper sources oriented radially (Haueisen et al., 2012; Piastra et al., 2021). Therefore, the depth sensitivity and specificity of MEG is limited and combining EEG and MEG yields the most accurate source localization as these techniques offer complementary information (Aydin et al., 2015; Ding & Yuan, 2013; Sharon et al., 2007). Nonethelss, both MSI and ESI can still suffer from cancellation of signals of the opposite polarity obscuring certain sources when activity is widespread (Ahlfors et al., 2010).

1.1.2.3 Summarised benefits and limitations of EEG/MEG

In summary, the main advantages of EEG and MEG are their non-invasive imaging set-up and high temporal resolution which enables direct tracing of fast neural activity. However, these techniques offer severely limited spatial and depth resolution with additional disadvantage of increased sensitivity to motion artefacts. These drawbacks therefore severely limit the accuracy and the extent to which neural activity can be imaged using these techniques.

1.1.3 Imaging of slow neural activity

Functional brain activity can also be inferred from the regional metabolic and haemodynamic changes in the brain. These epiphenomena are utilized in various brain imaging techniques as the surrogate markers for functional brain activity. The below section details the most popular techniques which fall into this category. The concluding section summarises the respective benefits and drawbacks of each technique in the context of high-resolution functional neuroimaging,

1.1.3.1 Functional Magnetic Resonance Imaging

One of the most popular techniques is functional magnetic resonance imaging. The principles of fMRI rely on the magnetic properties of hydrogen nuclei, the most abundant atoms in biological tissues (Logothetis, 2008). When a strong external magnetic field is applied to the body, hydrogen nuclei align creating a magnetization vector which is then perturbed by the application of a radiofrequency (RF) field (Buxton, 2013; Logothetis, 2008; Uludag & Ugurbil, 2015). The resulting change in the orientation of the magnetization vector is short-lived and decays exponentially as nuclei return to a more energetically favourable alignment. This process is called relaxation and is described by various time constants, such as T1, T2 and T2* (effective T2), which are generally tissue-specific (Logothetis, 2008). The RF energy emitted during the relaxation from each location in the image plane is measured and translated into corresponding intensity levels of an MR image.

MR image contrast and its spatial specificity are achieved through a combination of acquisition parameters which utilise differential tissue susceptibility to relaxation process and to small magnetic field gradients superimposed on a homogenous external magnetic field. It necessitates a carefully designed sequence of RF and gradient pulses tailored to a desired MR image. The most common sequences are gradient-echo and spin-echo pulse sequences which use gradient reversal and RF pulses, respectively, to acquire an MR image (Buxton, 2013; Logothetis, 2008). When the image is T2 or T2*-weighted, the contrast arises from the magnetic field inhomogeneities which, in the case of functional brain imaging, are the result of time-dependent changes in tissue perfusion and variation in its physicochemical characteristics (Ogawa et al., 1992; Ogawa et al., 1990b).

Functional MRI maps the propagation of brain activity from regional changes in blood flow, volume or oxygenation. These imaging modalities are reflected in the relaxation-rate changes due to spin motion, diffusion, or field non-uniformity (Logothetis, 2008). At present, several different fMRI sub-types exist, each of which utilise a specific endogenous or exogenous contrast agent to visualise a distinct property of cerebral haemodynamics. Some of the most popular types of contrast include arterial-spin labelling (ASL) used for measuring CBF, vascular space occupancy (VASO) used for measuring cerebral blood volume (CBV) and blood-oxygenation-level dependent (BOLD) contrast, with the latter being at the forefront of functional brain imaging.

BOLD contrast arises from differences in magnetic susceptibility of oxygenated and deoxygenated haemoglobin (Ogawa et al., 1990; Ogawa et al., 1990b). In comparison to oxy-haemoglobin which has weak effects on external magnetic field, deoxy-haemoglobin is strongly paramagnetic. When increased neural activity prompts functional hyperaemia, blood supply overshoots the oxygen consumption rate. This results in local increase in oxygenated blood which appears bright in MR image due to reduction in T2* signal (Ogawa et al., 1992). Because of the nature of BOLD contrast, it is inherently biased towards large venules and veins at the cortical surface compromising its spatial specificity (Ogawa et al., 1990b; Olman et al., 2007). Fortunately, the contribution of large vessels can be minimized by increasing magnetic field strength or using spin-echo sequence over the traditionally employed gradient-echo sequence. Therefore, the spatial resolution of fMRI can be improved from ≥ 1 mm to submillimetre resolution at high (1.0 – 3.0 T) to ultra-high (≥ 7.0 T) fields, respectively (Han et al., 2019; Hulvershorn et al., 2005; Parkes et al., 2005).

Despite excellent spatial precision of BOLD-fMRI, its temporal resolution is limited. The main limiting factors entail inherently slow dynamics of BOLD response, which is dependent on the distribution of cerebral vascular network, and the temporal profile of the image acquisition sequence employed to cover a sufficient field of view (Silva et al., 2007; Yoo et al., 2018). High resolution studies in rats and humans resolve the onset of BOLD signal change with a temporal accuracy of a tens (c. 50 ms) to hundreds of milliseconds (250 – 500 ms) (Jung et al., 2021; Pfeuffer et al., 2002; Silva & Koretsky, 2002). However, the peak signal change is universally reported to take seconds to develop due to physiological constraints of neurovascular coupling (De Zwart et al., 2005; Silva et al., 2007). The temporal mismatch between the BOLD signal and the timing of neural activity is further complicated by the non-linearity of BOLD response and hinders the accurate interpretation of fMRI data (Birn & Bandettini, 2005; de Zwart et al., 2009; Liu et al., 2010; Pfeuffer et al., 2003). Therefore, simultaneous EEG and fMRI measurements are often undertaken to establish the electrophysiological correlates of BOLD signal and map it to the specific EEG phenomena, for example, ictal and interictal activity or stimulus-evoked responses (Chaudhary et al., 2012; Eichele et al., 2005; LeVan et al., 2010).

1.1.3.2 Positron Emission Tomography

Another well-established functional brain imaging technique is positron emission tomography. PET utilises peripherally injected radioactive tracers to estimate the cerebral metabolic rate of oxygen (CMRO$_2$) or cerebral glucose consumption rate (CMRGlu) as well as CBF (Heiss et al., 1984; Kudomi et al., 2013; Poulsen et al., 1997). The measurements are based on the detection of radiation emitted by the radioisotope incorporated into a biologically active molecule (Bolomey, 1985; Ter-Pogossian et al., 1975). In functional PET imaging, the most widely used radiopharmaceutical is glucose analogue fluorodeoxyglucose (FDG) tagged with a radionucleotide fluorine-18 (F18-FDG) (Shukla & Kumar, 2006). Upon intravenous (IV) injection of F18-FDG, it is allowed to accumulate in the brain where, once phosphorylated by hexokinase, it becomes trapped in neurons (Chiaravalloti et al., 2019). Following the distribution of the radiotracer into the brain, the radioisotope undergoes a positron emission decay when it emits a positively charged electron (Raichle, 1983; Shukla & Kumar, 2006). The emitted positron interacts with free electrons in the tissue resulting in the release of energy in the form of two photons which are coincidently captured by the detectors arranged in a ring around the body and allows the precise localisation of emitted radioactivity.

Traditionally, PET images are acquired at regular intervals after 15 – 40 min following an IV bolus of radioactively labelled deoxy-glucose (Heiss et al., 1984; Sokoloff et al., 1977; Theodore et al., 1983; Vlassenko et al., 2006). This provides snapshots of glucose consumption throughout the brain at discrete time points. Changes in brain activity are then evaluated qualitatively by comparing baseline and task-based images which are usually taken in two separate imaging sessions (Haier et al., 1992; Swartz et al., 1994; Vlassenko et al., 2006). The logistics of PET image acquisition not only complicates the interpretation of data but also limits the temporal resolution of the acquired images to several minutes. An alternative method, recently proposed by Villien et al. (2014), supports dynamic functional PET imaging by employing constant tracer infusion throughout a single scanning session and increases the temporal resolution to 1 min (Jamadar et al., 2019; Villien et al., 2014).

As far as the spatial accuracy of FDG-PET is concerned, it is mostly circumscribed by the technical specifications of the scanners and by the positron range (Shukla & Kumar, 2008). The latter is considered an ultimate limitation of PET as it denotes the maximal distance that the emitted positron travels in the tissue before interacting with an electron. Positron range is radionuclide-dependent and sits around 2 – 3 mm for fluorine-18 (Shukla & Kumar, 2006). Therefore, the spatial resolution of a typical human FDG-PET scan is limited to several millimetres with slightly higher resolution of 1 – 1.5 mm in rodents (Alf et al., 2013; Amend et al., 2019; Jamadar et al., 2019). Although interest in solitary use of FDG-PET for imaging brain activity is slowly fading, the integration of FDG-PET with higher resolution functional imaging tools is gaining more popularity. Multimodal imaging studies combining FDG-PET with fMRI or EEG/MEG are performed to correlate the neurometabolic changes to the haemodynamic changes or electromagnetic brain activity providing an insight into their spatiotemporal overlap during physiological and pathological brain activity (Guo et al., 2022; Jamadar et al., 2021; Rajkumar et al., 2021; Wang et al., 2015; Widjaja et al., 2013).

1.1.3.3 Optical Imaging

Arguably, the largest group of functional imaging techniques can be ascribed to optical imaging (OI). OI encompasses all neuroimaging methods which rely on the differing biophysical properties of various brain tissues when exposed to visible, infrared, or ultraviolet light. The vast range of OI techniques span from micrometre resolution two-photon microscopy to spectroscopic and tomographic techniques, such as near-infrared spectroscopy (NIRS) or optical coherence tomography (OCT), with a coarser resolution of millimetres (Devor et al., 2012). In either case, functional OI techniques are mostly based on intrinsic differences in light absorption or scattering by the blood and the surrounding brain tissue allowing them to probe activity-dependent cerebral haemodynamic changes. For example, as with fMRI, cerebral blood oxygenation changes can be detected using optical intrinsic signal imaging (OISI) or diffuse optical imaging (DOI) (Frostig & Chen-Bee, 2012). Both techniques rely on light-absorbing properties of haemoglobin, particularly spectral differences of its oxygenated and deoxygenated forms. In comparison to BOLD-fMRI, OISI offers a superior spatiotemporal resolution (≤ 100 µm and ≤ 100 ms, respectively), albeit at a cost of invasiveness as it requires craniotomy and durotomy for sufficient light penetration (Devor et al., 2012). In contrast, DOI is non-invasive and enables deeper tissue penetration capable of generating not only topographic but also tomographic images of functional haemodynamic changes in the brain (Eggebrecht et al., 2014; Gratton et al., 1995; Siegel et al., 2003). DOI is regarded as a multichannel extension of functional NIRS (fNIRS) which utilises the translucency of the skull and other head tissues to near-infrared light but its strong absorption by haemoglobin at different oxygenation states (Jobsis-vander Vliet, 1999; Watanabe et al., 2000). In fNIRS, a region of interest is illuminated at carefully selected wavelengths of light to enable the detection of the relative changes in either oxygenated versus deoxygenated haemoglobin, or total haemoglobin which corresponds to a change in CBV (Lee et al., 2017). Although advantageous in its ability to simultaneously measure several haemodynamic modalities, DOI suffers from severely reduced spatial resolution which is physically restricted by the spacing of optodes and ranges from several centimetres to a maximal resolution of tens of millimetres achieved to date (Ferradal et al., 2016; Wolf et al., 2007).

Another indirect measure of neural activity which can be detected with OI is CBF. Flow measurements are typically inferred from the dynamic changes in the light back-scattered by moving red blood cells. A few examples of such techniques are OCT and laser speckle contrast imaging (LSCI). Combining the principles of low-coherence light interferometry with Doppler effect, OCT can acquire 3D images of functional CBF changes with a spatial resolution of 1 – 15 µm and temporal resolution of < 100 ms (Popescu et al., 2011; Srinivasan et al., 2010; Wang et al., 2011). On the other hand, LSCI quantifies time-varying blurring of light diffraction, or speckle, pattern which is expressed as speckle contrast, inversely proportional to blood flow (Senarathna et al., 2013). Therefore, LSCI yields two-dimensional (2D) images of tissue perfusion with reduced depth penetration. Nonetheless, the spatiotemporal resolution of LSCI is comparable and, in some instances, superior to that of OCT (Devor et al., 2012; Durduran et al., 2004; Senarathna et al., 2013; Wang et al., 2011).

1.1.3.4 Summarised benefits and limitations of fMRI/PET/OI

In conclusion, the overarching advantage of fMRI/PET/OI is their sub-millimetre spatial resolution and the ability to provide whole-brain coverage with high accuracy and precision. Both fMRI and PET as well as some of the OI modalities, such as DOI, are also strictly non-invasive which broadens their application and enables combination with other techniques, such as EEG/MEG. However, fMRI/PET/OI are designed to detect secondary neural changes which occur as a result of increased neuronal firing but does not represent fast neural changes directly. Consequently, the temporal resolution of these neuroimaging modalities is severely limited and can be considered their main drawback.

1.2 Electrical Impedance Tomography

Despite the abundance of functional neuroimaging tools, a single non-invasive technique capable of generating tomographic images of brain activity with both, mesoscopic spatial resolution and temporal accuracy of milliseconds, is yet to be developed. EIT carries the potential to meet these criteria due to its unique principles based on the electrical bioimpedances of brain tissues and their physiological and pathological changes over time. In this section, the reader is introduced into the key concepts of EIT, its hardware and image reconstruction process. The basics of EIT are followed by a thorough review of the previous functional brain imaging studies performed with EIT and its early prototypes. The historical overview of brain EIT aims to illustrate not only its progress but also to highlight the promising results as avenues for further development towards a universal high-resolution 3D brain imaging technique.

1.2.1 Bioimpedance

The interaction of biological tissues with externally applied electric current is described by bioimpedance, a governing principle of EIT. Biophysically, impedance is a composite measure of two parameters, resistance, R, and reactance, X (Holder, 2021b). Resistance defines the opposition of the system and its elements to the flow of charged particles, that is, electrons or ions, with the latter being the predominant charge transfer in the intracellular and extracellular space. The flow of electric current through a biological tissue can be related to its resistance via Ohm’s law which is relevant to both direct (DC) and alternating (AC) externally applied electric current (Holder, 2021b). On the other hand, reactance refers to the capacitive and inductive properties of biological tissues which create the opposition to AC flow by accumulating and releasing charge with each AC cycle. Reactance is attributed to the presence of an insulating lipid bilayer which constitutes the plasma membrane of cells and segregates highly conductive intracellular and extracellular compartments (Cooper, 2000). Therefore, biological tissue can be modelled as an electric circuit composed of parallel extracellular and intracellular resistances with a series capacitor representing the outer cell membrane (Fig. 1.1A; Holder, 2021b). Quantitatively, the total impedance of such circuit can be expressed as a complex number with resistance and reactance representing its real and imaginary parts, respectively.

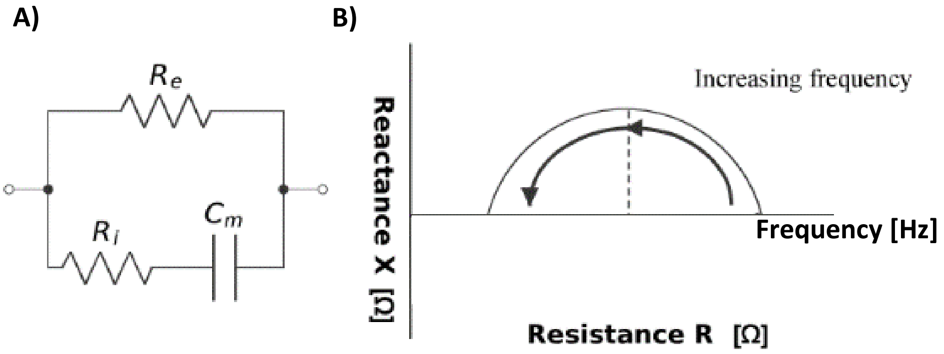

Figure 1.1. Principles of bioimpedance represented in a bioelectrical model (A) and in a mathematical (B) model. (A) Cell represented as an electric circuit composed of intracellular (Ri) and extracellular (Re) resistances and membrane capacitance (Cm). (B) Cole-Cole plot showing how the capacitive (X) and resistive (R) components of bioimpedance change with the frequency of applied current. Figure adapted from Holder (2021b).

Bioimpedance is dependent on the tissue type, its architecture, and the frequency of the applied current (Gabriel et al., 2009; Gabriel et al., 1996). At low frequencies, the current flow is confined to the extracellular space as it is highly conductive due to the abundance of Na$^+$, K$^+$, and Cl$^-$ (Goldman, 1943). The cell membrane acts as a capacitor which is fully charged and prevents the current passage into cells (Fig. 1.1A). Thus, the total impedance of the tissue in this case is almost purely resistive. However, as the frequency increases, more current can cross the capacitive phospholipid bilayer and if the frequency of AC exceeds the membrane time constant, the capacitance becomes negligible, and the current is diverted through the intracellular space (Holder, 2021b). Therefore, at high frequencies, the entire impedance of the model circuit is again resistive. Such frequency-dependence of capacitive and resistive components of impedance can be illustrate by a Cole-Cole plot (Fig. 1.1B).

1.2.2 Principles of bioimpedance in neural tissue

The bioimpedance of neural tissue presents a special case due to its internal electromotive properties and, therefore, is presented separately here. During the action potential, the opening of voltage-gated Na^+, Ca^{2+} and K^+ channels permits the redistribution of cations between intra- and extracellular spaces (Bezanilla, 2007; Hodgkin & Huxley, 1952). This transient change in conductivities of the respective ions yields a measurable change in impedance of neural tissue which coincides with the neurotransmission event causing it (Cole & Curtis, 1939). Because the capacitive reactance of cellular membrane is inversely proportional to the applied frequency, the impedance change related to neuronal depolarisation is largest at low frequencies. However, regardless of the frequency of the applied current, the recorded change in impedance is effectively resistive as the capacitance of cell membrane varies minimally between the resting state and when voltage-gated ion channels open (Cole & Curtis, 1939; Goldman, 1943). Therefore, the local reduction in impedance of nervous tissue can be detected with EIT by measuring the real resistive component of impedance. It is often expressed with reference to the general tissue parameter termed resistivity, ρ, or its inverse, conductivity, δ, which respectively describe the difficulty or the ease with which the current passes through a specific material or tissue type (Holder, 2021b).

1.2.3 Principles of EIT

EIT is an imaging technique which utilises the differing bioelectric properties of living tissues for generating their tomographic images from boundary impedance measurements. To achieve that, electrodes are placed on the surface of the body and imperceptible electric currents are applied while simultaneously recording the resulting voltage (Holder, 2021b). Traditionally, a four-electrode method is used where a constant current is injected, and voltage is measured through successive pairs of electrodes obviating the impedances of the electrodes from the collected measurements. When electric current is applied to a subject, it diffuses internally according to the resistivity of the composite tissues with the most current flowing through the least resistive path. This therefore produces a distinct pattern of transfer impedances calculated using Ohm’s law from the recorded boundary voltages.

A collection of single-channel impedance measurements forms the basis for an imaging dataset which is used to reconstruct a three-dimensional distribution of impedances within a volume of a body (Holder, 2021b). Unfortunately, estimating the internal tissue characteristics from the surface measurements is an ill-posed and ill-conditioned mathematical problem, leaving absolute EIT extremely challenging (Lionheart & Adler, 2021). Therefore, most applications, including brain EIT, employ time-difference or frequency-difference EIT for imaging impedance changes related to functional activity. Differential measurements significantly improve the accuracy of EIT reconstruction as the geometric discrepancies between the model used for image reconstruction and the real-life data are minimized. The instrumentation, data collection principles and image reconstruction pertaining to functional brain EIT will be discussed in further detail in the following sections.

1.2.3.1 EIT systems and instrumentation

A typical EIT system currently in place for functional neuroimaging is composed of an electrode array, a single or multiple current sources which can deliver a constant AC at a wide range of frequencies (typically up to 50 kHz) and amplitudes, a voltage recorder which amplifies and digitises the recorded signal, a multiplexer which switches between the injection pairs, and a custom controller, termed ScouseTom, which interconnects each component in the circuit and interfaces them with the software on a computer (Fig. 1.2; Avery et al., 2017). The recorded signal is processed off-line by demodulation and application of digital filters which extract the impedance signal of the relevant frequency.

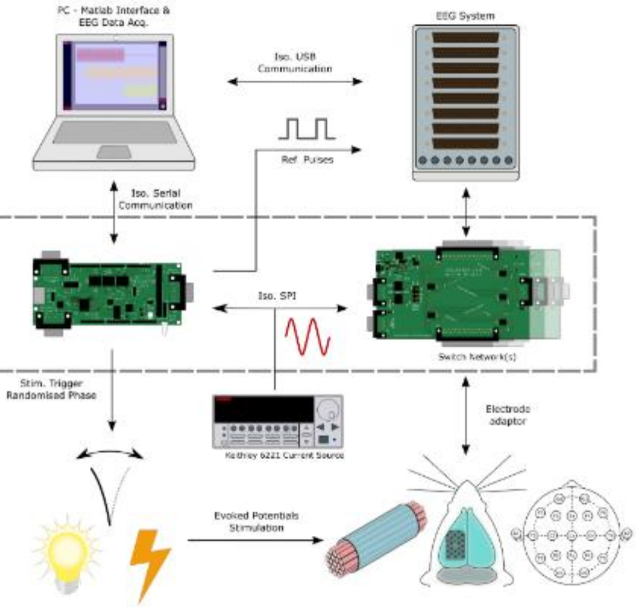

Figure 1.2. An overview of the ScouseTom EIT system. Arduino controller (highlighted by the punctate line) integrates all the parts together by controlling the current source and multiplexing the injection pairs as well as randomising the external stimulation triggers which ensure that stimulus-locked neural activity is evoked at random phases of the injected current. The resulting voltage is sampled by an EEG amplifier which is connected to the computer for storing the collected data. Figure taken from Avery et al. (2017).

Of particular importance in any EIT system is the geometry of the electrodes used for current injection and voltage measurement. Most EIT applications, including imaging of lung ventilation and perfusion, utilise arrays of 16 electrodes (Holder, 2021b). However, neural EIT has employed arrays containing between 16 to 128 electrodes for extracranial and intracranial recordings (Faulkner, 2019; Holder, 1992b). When selecting electrodes for EIT, the main concern is the contact impedance between the electrode and the body surface (Boone &

Holder, 1996; Cardu et al., 2012). In the case of current injection, unstable contact impedance can introduce additional noise while poor contact impedance at the recording electrodes can result in large measurement errors and distort the results (Adler, 2004). Non-invasive brain EIT performed to date have mostly taken advantage of the existing scalp silver-silver chloride (Ag-AgCl) EEG cup electrodes which provide reasonable contact when used in combination with skin abrasion and a conductive gel (Tidswell et al., 2001). Other studies utilised custom-made epicortical electrode arrays with contacts coated in poly(3,4-ethylenedioxythiophene) polystyrene sulfonate (PEDOT:PSS) or platinum to minimize the contact impedance (Faulkner, 2019).

1.2.3.2 EIT data acquisition

EIT data acquisition is based on multiple single-channel impedance measurements which can be collected serially or in parallel. The injection electrode addressing order as well as the subset of the voltage measurements required to reconstruct an image are defined by an EIT protocol (Adler, 2021b). The EIT protocol is normally optimised such that it maximises the sensitivity of the measurements to the localised change in conductivity (Faulkner et al., 2017). One complete round of EIT protocol produces a set of linearly independent transfer impedance measurements which form a single EIT image frame (Holder, 2021a). Image acquisition rate can therefore be defined by the frame rate, that is, the number of images acquired per unit time.

Serial data acquisition is often implemented where activity being imaged is short-lived or where the use of parallel system is impractical due to a high frequency of the recorded impedance changes. A single carrier frequency is injected through sequential pairs of electrodes and recorded by the remaining electrodes. Differential impedance measurements are obtained by comparing the data frames from two timepoints, current and baseline, and is termed time-division multiplexing (Holder, 2021a). The number of all possible independent current injection pairs in an array containing N number of contacts is $N - 1$. Since the boundary voltage measurements from the injecting electrodes are typically not used, the total number of unique impedance measurements that can be taken is $N\,x\,(N - 3)\,/\,2$ (Adler, 2021a). However, adjacent stimulation and measurement pair pattern has an impaired depth sensitivity due to limited current penetration. Therefore, the spacing between injection electrodes is often increased and defined by the ‘skip’ parameter. In brain EIT, where arrays with large number of electrodes are used, the protocol can be further optimised to include only a subset of unique injection pairs which yield the highest sensitivity in the perturbed region without the loss of information necessary for image reconstruction (Faulkner et al., 2017). Due to a resistive skull barrier, the best signal is obtained when the current injection electrodes are diametrically opposed.

In contrast to serial acquisition, parallel EIT entails simultaneous injection of multiple frequencies and is often referred to as frequency-division multiplexing (Avery et al., 2017; McEwan et al., 2006). Current is injected and voltage is recorded by the same electrodes; therefore, parallel data acquisition demands impeccable contact impedances across the electrode array. On the other hand, the advantage of parallel data acquisition is that imaging time is significantly shortened by overlapping the current drive pairs. Nevertheless, due to hardware constraints, parallel EIT has mainly been used in research and is continued to be developed with prospects of using it for real-time functional brain imaging of slow impedance changes during epileptic activity (Witkowska-Wrobel, 2020).

The frequency of the applied current varies with the physiological application. Original EIT systems developed for imaging pulmonary function used 50 kHz because of minimal skin-electrode impedance at this carrier frequency (Yang et al., 2017). Therefore, 50 kHz was also used in early brain EIT studies. Unfortunately, the recorded signal suffered from low amplitude and signal-to-noise ratio (SNR) (Tidswell et al., 2001). This was attributed to the frequency-dependent reduction in bioimpedance of nervous tissue which in turn resulted in a small difference between impedance of the resting and active brain tissue. In support of that, biophysical modelling showed that the functional impedance change due to fast neural activity diminished beyond 100 Hz and was maximal at DC (Liston et al., 2012). However, later studies demonstrated that the prevalence of spontaneous brain EEG in this bandwidth significantly contaminated the signal and reduced the SNR, and therefore was unsuitable for recording fast impedance changes in the brain (Oh et al., 2011). The concomitant studies in rats characterized the frequency response of functional fast impedance changes in the brain at 100 Hz – 10 kHz and confirmed the existence of a frequency "sweet-spot" at around 1.5 kHz where the noise and the signal amplitude balanced to yield the maximal possible SNR (Faulkner et al., 2018a; Hannan et al., 2018a).

The amplitude of EIT injection current is subsequently determined by the injection frequency. As the frequency of the applied current rises, higher current level can be accepted due to decreased ability to accumulate charge which can otherwise cause excitotoxicity in the neural tissue (McCreery et al., 1990). Non-invasive EIT employs current amplitudes which are insensible and safe as defined by the safety standards for medical devices (IEC 60601). Similarly, invasive EIT uses current levels which do not cause visible tissue damage (Hannan et al., 2019). In addition to that, particularly in intracranial brain EIT of fast impedance changes, the current density at the injection electrodes must be limited below the threshold for neural excitation to avoid unsolicited neuromodulatory effects which can affect the recorded signal (Gilad et al., 2007; Hannan et al., 2019; Rattay, 1999; Rattay, 1998).

1.2.3.3 Image reconstruction

Historically, the first EIT images of lung ventilation were generated by a back-projection method borrowed from the most popular 3D imaging techniques such as X-ray computed tomography (CT) (Schofield et al., 2020; Wei et al., 2005). A series of overlapping transfer impedance measurements were back projected on to a 2D computer simulation of an imaged object and produced a blurred image which was sharpened by the application of various filters (Barber et al., 1992; Barber & Brown, 1983). However, using 2D models for the head proved to be insufficient as they introduced significant errors into the reconstructed images (Holder, 2021a).

Currently, EIT images of brain activity are reconstructed using anatomically realistic 3D head models in combination with a sensitivity matrix, or Jacobian matrix, an array of numerical values relating the resistivity changes in each element of the head model with the recorded boundary voltages at each electrode (Aristovich et al., 2014). This approach requires the solution of a ‘forward’ and an ‘inverse’ mathematical problem. Firstly, the Finite Element Model (FEM) mesh is created by segmenting the MRI or CT images of the head into distinct conductivity layers (Adler, 2021b). FEM is then used to calculate the forward solution which predicts the distribution of the boundary voltages when the injection current and the conductivity of each voxel is pre-specified. This produces a ‘sensitivity matrix’ which is inverted to resolve the internal conductivity distribution from the known boundary voltages (Lionheart & Adler, 2021). This is termed an ‘inverse’ problem which is solved by the iterative adjustment of the model via the comparison of the measured and the predicted boundary voltages. Unfortunately, there are several caveats to the solution due to an ill-posed and ill-conditioned nature of the inverse problem. The solution is contingent on the changes in the obtained dataset, therefore, small errors in the boundary voltage measurements can cause large deviations in the internal conductivity distribution.

1.2.4 Brain EIT

Brain EIT is based on the anatomical and physiological properties of the head and brain tissues as well as the temporal characteristics of functional brain activity changes. Brain can be coarsely divided into three main compartments which include blood, CSF and nervous tissue composed of the grey matter and the white matter. These four types of tissue have distinct dielectric properties which vary with frequency (Yang et al., 2017). Blood and CSF both are uniformly conductive aqueous solutions with a roughly constant conductivity across a frequency range relevant to EIT (Baumann et al., 1997; Gabriel et al., 2009). In contrast, the conductivity of grey and white matter significantly decreases with frequency (Gabriel et al., 1996; Logothetis et al., 2007). Furthermore, brain is encapsulated by three meninges, then covered by the skull and the scalp, all of which are relatively resistive layers compared to the tissues comprising the brain (Jiang et al., 2020; Weise et al., 2022).

The resistivity distribution of the head and brain tissues is important when considering functional impedance changes in the brain which accompany fast and slow pathophysiological brain activity. Due to its high temporal resolution, EIT is capable of imaging both fast and slow functional brain impedance changes occurring over milliseconds or seconds, respectively. As the spatial resolution of EIT does not currently permit acquisition of detailed static anatomical images of the brain, brain EIT has been confined to dynamic brain imaging of fast and slow brain circuit activity during evoked responses and epilepsy as well as slow metabolic shifts during stroke and spreading depression.

1.2.4.1 EIT of normal brain activity

EIT can image fast and slow brain impedance changes which accompany neuronal depolarisation and associated epiphenomena during physiological brain stimulation. Whereas fast neural impedance changes can be easily explained by the underlying changes in membrane permeability to ions, the cause of slow changes is not clearly defined.

Slow neural EIT of physiological brain activity

The earliest studies demonstrating notable cerebral impedance changes following physiological stimulation were performed in animals with chronically implanted electrodes. For instance, Adey and colleagues recorded impedance decreases in response to physiologically arousing stimuli in the pyramidal cell layer in cat hippocampus (Adey et al., 1962). This impedance decrease was attributed to the redistribution of ions between the extracellular and intracellular compartments preceding the excitation of hippocampal neurons by various sensory stimuli. The observed changes were long-lasting, therefore, the authors proposed CBF and CBV fluctuations as the potential underlying causes. Similarly, Birzis and Tachibana demonstrated consistent impedance decreases in the cerebral cortex and hippocampus of unrestrained cats in response to alerting auditory stimuli (Birzis & Tachibana, 1964). This pattern of impedance changes was linked to CBF changes as the impedance drop correlated with the tachycardic response following the startle stimulus.

The first study which used EIT to record slow impedance changes during physiological brain activity was performed in rabbits using a ring of intracranial Ag/AgCl electrodes (Holder et al., 1996). Reproducible impedance decreases of -2.7 % and -4.5 % and adjacent increases of 2.9 % and 1.7 % were reported during visual and somatosensory stimulation, respectively. Reduction in impedance was linked to the regional changes in CBV whereas the concurrent impedance rise in the surrounding brain areas was hypothesised to result from cell swelling and CSF fluctuations, or to be artefactual. Collectively, the results of the early studies suggested that impedance changes associated with neurovascular response to exogenous stimuli could be utilised as a marker for functional brain activity. Unfortunately, the recording techniques were very invasive and could not be directly translated into clinical research, therefore, carried little potential to be used as a routine functional imaging modality.

Non-invasive slow impedance measurements in humans were first successfully attempted in our group by Tidswell et al. (2001). Impedance changes were measured during somatosensory, visual and motor stimulation. Congruent to the findings from the epicortical recordings in rabbits, both increases and decreases in cerebral impedance were recorded in human subjects during somatosensory, visual and motor stimulation (Tidswell et al., 2001). The amplitudes of the positive changes were 0.62 %, 0.63 % and 0.19 % and those of the negative changes were -0.46 %, -0.44 % and -0.22 % for somatosensory, visual and motor stimulation, respectively. These figures were approximately 10 times smaller than those recorded directly from the cortex, likely owing to the resistivity of the skull. In a more recent study, using an updated EIT recording system, Witkowska-Wrobel (2020) demonstrated a similar pattern and magnitude of single-channel slow impedance changes in human subjects during visual stimulation. However, the author concluded that the observed changes were driven largely by artifacts as the recording electrodes which detected significant changes were not located over the occipital brain area expected to be activated by the visual stimuli (Witkowska-Wrobel, 2020). Moreover, clear and accurate images of slow activity could not be reconstructed from this data reinforcing the likely artefactual nature of the observed slow impedance changes.

Overall, the comprehensive evidence from the studies of slow cerebral impedance changes during functional brain activity supported strong physiological basis for the observed pattern of responses. Data collected to date points to local haemodynamic changes as a primary driver for slow neural activity during physiologically evoked responses in the brain. Nevertheless, the lack of the direct evidence for the source of the bipolarity of slow impedance changes observed in more recent slow neural EIT studies warrants further investigation. The biphasic responses detected with an open-skull preparation in rabbits can be explained by the intracranial hypertension and subsequent cerebral oedema. However, somewhat conflicting outcomes from the extracranial slow impedance recordings in humans suggest that different physiological and non-physiological factors might be at play. Therefore, more research into the nature and the physiological underpinnings of the pattern of slow functional impedance responses in the brain is needed.

Fast neural EIT of physiological brain activity

The first reports of impedance changes directly associated with neuronal firing were made in the 1930s (Cole & Curtis, 1939). Impedance drops recorded across the neuronal membrane were concurrent with the time scale of the action potentials, therefore, were attributed to changes in Na^+ and K^+ conductivities due to the opening of voltage-gated ion channels (Hodgkin & Huxley, 1952).

The use of impedance measurements as a direct and unique marker for imaging neural activity was proposed by David Holder (Holder, 1987). Preliminary measurements of fast impedance changes during visual and somatosensory evoked activity in humans were undertaken with an early prototype of EIT, called Applied Potential Tomography, and showed that changes were insufficiently large (0.002 – 0.02 %) to be used for image reconstruction (Holder, 1989). An early indication was that non-invasive fast neural EIT might not be possible due to marked signal attenuation by the skull. Therefore, further studies were mainly performed in animal models where a cranial window could be implanted for impedance recordings directly from the brain surface.

Another important consideration for fast neural EIT was injection frequency. The modelling performed by Liston et al. (2012) predicted the largest impedance decreases at DC which were estimated to be -0.06 − -1.7 % during cortical evoked activity in cats (Liston et al., 2012). These results were consistent with the fast impedance measurements in anaesthetised rabbits where impedance decreases of -0.01 − - 0.03 % were recorded with intracranial electrodes during somatosensory stimulation (Boone, 1995). However, at DC, noise due to the intrinsic EEG activity markedly interfered with the recordings. These observations lead to several studies which investigated the relationship between the carrier frequency and the amplitude of fast neural impedance changes in an attempt to identify the optimal frequency for fast neural EIT (Faulkner et al., 2018a; Oh et al., 2011; Vongerichten, 2015). The frequency response characterisations were performed in rats with subdurally implanted electrodes at 100 Hz – 10 kHz. The results of these studies showed a maximal impedance change of −0.13 % with the highest SNR at 1.5 – 2 kHz; therefore, frequencies within this range were exploited in further studies to probe the limits of the spatiotemporal and depth resolution of fast neural EIT (Faulkner et al., 2018a). A pioneering study by Aristovich et al. (2015) imaged fast neural impedance responses in rat somatosensory cortex following electrical whisker stimulation with a spatiotemporal resolution of < 200 µm and 2 ms and cross-validated them with the simultaneously recorded local field potentials (LFPs) (Aristovich et al., 2016). Unfortunately, the activity was limited to the superficial cortical layers (< 3 mm below the surface). A related modelling study confirmed that the outer third of the brain was the limit of depth sensitivity of fast neural EIT with epicortical electrodes for evoked responses (Faulkner et al., 2018b). The same study suggested that EIT imaging throughout the whole brain could still be achieved with a combination of epicortical and penetrating depth electrodes.

1.2.4.2 EIT of epilepsy

The main clinical application of EIT where it could prove exceptionally useful is epilepsy. Epilepsy is a neurological disorder characterised by predisposition to recurrent unprovoked seizures which are defined as signs of excessive synchronous neuronal discharges in the brain (Fisher et al., 2014). Based on the site of origin and extent of abnormal neural activity, epileptic seizures are categorized into focal and generalized (Berg et al., 2010; Sarmast et al., 2020). Focal seizures start within and remain confined to neural networks in one hemisphere with consistent ictal onset zone. Contrastingly, generalized seizures are bihemispheric and have the tendency to spread across neural networks with inconsistent localization and lateralization. Approximately two-thirds of epilepsy patients can control seizures by regular intake of anti-epileptic drugs (Kwan & Sander, 2004). However, the remaining population suffers from drug-resistant epilepsy (Laxer et al., 2014).

Fortunately, a proportion of patients with refractory focal epilepsy (5 – 50 %) qualify for another therapeutic approach: a surgical resection of epileptogenic tissue, which leads to a long-term remission in 40 – 80 % of patients (Krucoff et al., 2017; Ryvlin & Rheims, 2008). A patient’s eligibility for a surgical treatment approach is assessed through a series of criteria which include, but are not limited to, the identification of the epileptogenic zone (EZ). EZ precisely defines the minimum amount of brain tissue to be removed to achieve complete post-operative seizure control while sparing key brain areas and avoiding neurological deficits (Ryvlin & Rheims, 2008). The evaluation involves high-resolution MRI to identify the structural lesions, and video scalp EEG monitoring to detect the irritative and ictal onset zones which are later reconstructed with ESI. In some instances, where the preliminary results are ambiguous, other imaging techniques are employed, such as MEG, FDG-PET, or simultaneous EEG-fMRI (Baumgartner et al., 2019; Ryvlin & Rheims, 2008). If non-invasive monitoring fails to provide accurate information or if that information is divergent, intracranial EEG is performed using subdural grids, termed electrocorticography (ECoG), or depth electrodes, termed stereotactic EEG (SEEG) (Parvizi & Kastner, 2017).

Despite the stringency of the preoperative assessment, more than half of the patients experience seizure relapse which is often due to incomplete resection of epileptogenic brain tissue (Petrik et al., 2021). This can be attributed partly to the inherent limitations of the imaging techniques. Despite the unparalleled spatial resolution of fMRI, its temporal resolution is insufficient to discriminate the seizure onset and propagation while the opposite is true for non-invasive EEG and MEG. Additionally, ictal and interictal activity might be invisible to EEG and MEG if the orientation of the source is tangential or radial, respectively, or if multiple opposing sources are located along the sulci or gyri resulting in their cancellation (Ahlfors et al., 2010; Ebersole, 2003). Moreover, intracranial EEG carries the risk of haemorrhage, infarction, neurological dysfunction or even death (Wellmer et al., 2012; Wong et al., 2009). Therefore, there is an unfulfilled clinical need for a non-invasive imaging tool which could be used for long-term monitoring of epilepsy patients and in the preoperative assessment of ictal and interictal patterns with sufficiently precise spatiotemporal resolution.

Impedance changes during epilepsy

EIT has been proposed and investigated for imaging epileptic activity due to well-established changes in brain tissue impedance during seizures. Slow and large (~10 %) increases in the intracerebral impedance during ictal activity were first identified in animal studies (Elazar et al., 1966; Van Harreveld & Schadé, 1962). These conductivity changes were spatially and temporally correlated with the onset of seizures and lasted for several minutes after their termination. These slow impedance shifts were attributed to cell swelling observed in *ex vivo* and *in vivo* models of epilepsy (Colbourn et al., 2021; Federico et al., 1994; Hochman et al., 1995; Olsson et al., 2006).

Several mechanisms have been proposed to explain the cytotoxic oedema during seizures. Studies have shown that the sustained hypersynchronous neuronal depolarisation during ictal and interictal discharges results in energy deprivation akin to one during anoxic depolarisation (Dzhala et al., 2000; Fertziger & Ranck, 1970; Jensen & Wang, 1996). Glucose shortage and subsequently decreased ATP availability inhibits Na^+/K^+ pump which normally restores the ionic gradients across the neuronal membrane (Kager et al., 2000; Krishnan et al., 2015). This leads to ionic imbalance with intracellular accumulation of cations which are followed by the water molecules causing cells to swell (Olsson et al., 2006). Additionally, prolonged depolarisation of neurons results in sustained repolarising efflux of K^+ which leads to its accumulation in the extracellular space (Dufour et al., 2011; Köhling et al., 1995; Yaari et al., 1986). Increased extracellular K^+ plays a role in both, initiation and maintenance, of seizures by driving neuronal and glial depolarisation (Dichter et al., 1972; Du et al., 2016; Fertziger & Ranck, 1970; Hotson et al., 1973; Kager et al., 2000). Under physiological conditions, K^+ is buffered by astrocytes, however, in the absence of oxygen and glucose, astrocytes switch to anaerobic glycolysis which also encourages astrocytic swelling (Somjen, 1973). Therefore, impedance of the epileptogenic brain tissue prior to or during seizures increases due to the shrinkage of the extracellular space caused by the expansion of the swelling cells as the applied current is unable to cross the capacitive membrane barrier and remains confined extracellularly (Dietzel & Heinemann, 1986).

In addition to slow impedance changes, ictal and interictal spikes and discharges can directly cause impedance changes which are temporally aligned with neuronal activity. The mechanism of fast impedance decrease during seizures is analogous to that during normal neural activity in the brain. Coordinated opening of voltage- and ligand-gated ion channels which underlie the initiation and propagation of action potentials during both, physiological and pathological, brain activity cause transient decrease in impedance lasting milliseconds (Hanada, 2020; Hodgkin & Huxley, 1952).

Slow neural EIT of epilepsy

Early EIT studies focused primarily on imaging slow impedance changes during epilepsy. One of the first attempts were in anaesthetised rabbits using an original Sheffield Mark 1 EIT system (Rao, 2000). Slow impedance increases of ~7 % and ~5.5 % were recorded during electrically induced focal and generalised seizures, respectively, by injecting high frequency current (47 – 51 kHz) via intracranial electrodes placed directly onto the exposed cortex. Preliminary results in animals showing such remarkable impedance shifts encouraged an attempt to conduct slow EIT with scalp electrodes in parallel to video-EEG telemetry performed as a part of the pre-operative assessment in refractory epilepsy patients (Fabrizi et al., 2006). Unfortunately, no reproducible impedance changes of the expected magnitude (~0.1 %) determined *a priori* by modelling could be recorded. The detected variations in boundary voltages were a few orders of magnitude larger and, therefore, were attributed to an inconsistent electrode contact with the scalp due to subjects' movements. Moreover, using a single circuit for recording EIT and EEG introduced low-frequency 'switching' artefacts into EEG data which were caused by multiplexing of injection pairs and which obscured the important electrographic markers of seizures in EEG recordings.

To circumvent the issues related to serial data acquisition, Dowrick et al (2015) investigated frequency-division multiplexing for recording and imaging impedance changes during chemically-induced seizures in anaesthetised rats. Peak impedance changes of 6.28 % and 3.91 % were recorded in parallel using subdurally placed electrodes at 2.2 kHz and 2.6 kHz, respectively (Dowrick et al., 2015). However, the author concluded that more than two current sources were needed for reconstruction of accurate images.

Besides eliminating the switching artifacts, multifrequency EIT of slow changes during epileptiform activity has been shown to carry the potential of imaging their spatiotemporal propagation in real time. This was demonstrated in a study by Witkowska-Wrobel et al. (2021) who acquired images of slow impedance changes in benzylpenicillin model of epilepsy in anaesthetised pigs. EIT was performed with a combination of subdural grids and depth electrodes simulating a pre-surgical SEEG monitoring scenario in epilepsy patients (Witkowska-Wrobel et al., 2021). Maximal impedance changes of 6 %, 8 % and 9.5 % were recorded during focal, focal secondary generalized and generalized seizures, respectively, by injecting current through 32 current sources at 8.5 – 10 kHz. Even though reconstructed images had a relatively low temporal resolution (1 s), they correlated well with SEEG and ECoG recordings. This suggested that EIT could be used for improved localisation of epileptic foci in patients on telemetry wards with already implanted intracranial electrodes.

Successful EIT images of slow impedance changes have been recently acquired during electrically-induced neocortical and hippocampal seizures in rats (Hannan et al., 2021). A slow focal rise in impedance was observed in the somatosensory cortex and in the dentate gyrus with the peak values of 2.33 % and 0.52 %, respectively. The drawback of this study was the need for averaging across repeated seizures (≥ 30) as each EIT injection pair in the EIT protocol was used to record individual seizures. However, this study demonstrated that the slow brain activity during seizures spatially matched the EZ defined by ECoG, confirming the practicability of slow EIT in accurately detecting the ictal focus paired with the electrographic techniques currently used in standard clinical practice.

Fast neural EIT of epilepsy

EIT has also been investigated for imaging fast impedance changes during epilepsy. The first report of bidirectional impedance responses during seizures was presented by Vongerichten et al. (2016). This study used an acute chemical rat epilepsy model to record impedance changes during cortical seizures using subdurally implanted electrodes. Well-characterised slow impedance changes associated with epileptiform activity were preceded by transient impedance drops of -0.30 – - 0.64 % which temporally correlated with the peak of the interictal spikes (Vongerichten et al., 2016). Similarly, fast impedance changes were imaged during electrically-evoked cortical and hippocampal seizures in rats. (Hannan et al., 2020a; Hannan et al., 2018b). An upgraded 57-electrode epicortical array was used for recording fast EIT images. Impedance decreases of -0.3 % and -0.04 % were respectively detected during cortical and hippocampal epileptiform discharges with a spatiotemporal resolution of 2 ms and <400 μm. These studies demonstrated a unique capability of EIT to trace the trajectory of the cortical and subcortical seizures in 3D with an unmatched spatiotemporal precision.

1.2.4.3 EIT of other pathological brain activity

There are several other pathologies which cause slow brain impedance changes detectable by EIT. A marked increase (10 – 100 %) in the cerebral tissue impedance occurs in such conditions as cerebral ischemia and spreading depression due to anoxic depolarisation. When blood flow to the active brain regions is insufficient, neurons outrun the available energy and oxygen supply triggering an uncontrollable and progressive depolarisation of neural cells (Somjen, 2001). The lack of energy to maintain the transmembrane ionic gradients leads to the loss in the selective membrane permeability. As a result, ions and water move excessively from the extra- to intracellular compartment causing cell swelling at the expense of interstitial space which shrinks by > 30 % (Hansen & Olsen, 1980; Hansen & Zeuthen, 1981; Jing et al., 1994; McBain et al., 1990). This manifests as an increase in brain tissue impedance because the injected current travels predominantly in the reduced extracellular volume (Hoffman et al., 1973).

Multiple studies have been carried out imaging these large-scale events in animals using EIT. Impedance shifts of 10 – 20 % and up to 200 % have been recorded and later imaged during cerebral ischemia in anaesthetised rats using scalp and cortical electrodes, respectively (Holder, 1992b; Holder, 1992c). Similarly, cortical impedance changes up to 200 % were measured in the ischemic brain of cats, rabbits and monkeys (Gamache et al., 1975; Hossmann, 1971; Matsuoka & Hossmann, 1982). These lasted for tens of minutes upon the occlusion of a major cerebral artery and reversed upon the restoration of blood flow.

A similar mechanism underlies spreading depression, a phenomenon characterised by a wave of depolarisation propelled by the perpetual increase in the extracellular K^+ due to intense neuronal activity (Somjen, 1973; Ullah et al., 2015). Spreading depression has been proposed as a cause for migraine aura in humans and suggested to share the mechanistic pathways underlying cell volume changes in the brain during epileptic seizures (Charles & Baca, 2013; Olsson et al., 2006). Therefore, animal models of spreading depression were used to investigate the feasibility of non-invasive EIT of slow brain impedance changes with the applications in epilepsy and migraine. For example, impedance changes of around 40 % could be recorded in anaesthetised rats during experimentally-induced cortical spreading depression using scalp electrodes (Holder, 1992a). Intracranial recordings of slow impedance changes during spreading depression were also attempted. Successful EIT images of spreading depression in rabbits were obtained with an intracranial ring of 16 electrodes (Boone et al., 1994). Peak slow impedance changes of 5 – 25 % which propagated from the site of initiation towards the periphery could be recorded over several minutes.

Lastly, EIT has been investigated as a potential imaging tool in stroke. In principle, EIT could be used for long-term monitoring of structural brain changes which arise over hours after an intracranial haemorrhage or global cerebral ischemia. However, that requires prolonged stability of electrode and skin impedance which is unachievable with the current technology (Boone & Holder, 1996). Nonetheless, proof-of-concept studies were successfully performed in rabbits upon cerebral infarction, in rats after ischemic stroke and in an experimental model of subarachnoid haemorrhage in piglets (Cao et al., 2020; Dai et al., 2010; Yang et al., 2014). Additionally, multifrequency EIT was proposed for an acute stroke imaging and differentiation of its type for the purpose of early time-sensitive therapeutic intervention (Malone et al., 2014; McEwan et al., 2006). However, pronounced sensitivity of the present EIT image reconstruction models to the errors in the electrode position and shape necessitate further developments to validate EIT for this application.

1.2.4.4 Benefits and drawbacks of brain EIT

In the context of the current neuroimaging landscape presented in sections 1.1.1 and 1.1.2, EIT stands out as a uniquely versatile technique which can capture both fast (milliseconds) and slow (seconds to minutes) neural changes during regional activation of the brain. This is a significant benefit of EIT. Excluding combined imaging modalities (e.g., EEG/fMRI), no existing and widely-used neuroimaging tool has a similar imaging scope on its own. Therefore, EIT can offer an unmatched insight into brain neurophysiology at a level of neural circuits and beyond.

Furthermore, the principles of fast neural EIT which relies on changes in nervous tissue impedance during action potentials (~2 ms in duration) to trace the propagation of brain activity directly dictate the ultimate temporal resolution of brain EIT. Coupled with tomographic nature and image reconstruction principles which yield a spatial resolution of micrometres, EIT offers a combination of mesoscopic spatial and temporal resolution which is an important advantage over existing neuroimaging techniques.

1.3 Rationale, Purpose and Outline

The overall purpose of this PhD project was to develop EIT for imaging the three-dimensional propagation of physiological and pathological brain activity in real time. The main focus of this thesis was to investigate the feasibility of high-resolution single-shot imaging of aberrant neural circuit activity at a millisecond temporal resolution using penetrating intracranial electrodes and EIT in murine brain, one of the most common animal models in neuroscience, and establish the prospects of clinical EIT applicability. Successful intracranial fast neural EIT of epileptiform brain activity would provide an unparalleled insight into the functional connectivity of neural circuits everywhere in the brain and their alterations in such pathologies as epilepsy. Moreover, combining intracranial EIT measurements with deep brain stimulation (DBS) would yield a transformative high-precision therapeutic approach for clinical cases of pharmacoresistant epilepsy with contraindications for resective neurosurgery, such as mesial temporal lobe epilepsy (MTLE). Improving the localization of epileptogenic tissue with intracranial EIT in surgical epilepsy patients and optimising the protocols for targeted neuromodulation with DBS could lead to reduction in post-therapeutic seizure incidence rates and, therefore, tremendously improve the health span of those epilepsy patients for whom treatment options are limited.

Research detailed in this thesis was undertaken upon a thorough review and assessment of the current neuroimaging landscape which is summarised in Table 1.1. Having established the benefits and drawbacks of EIT with respect to other prominent brain imaging tools determined the overarching purpose and framework for the remainder to the work.

The first part of this thesis encompassing Chapters 2 and 3 was designed to assess the feasibility of using slow brain impedance changes as a marker for imaging functional brain activity in physiological and pathological cases. The rationale behind the first two studies was the extent of slow neural activity, including but not limited to neurovascular response, and a resulting intracerebral impedance change which is known to exceed the local fast transmembrane impedance drop during neuronal depolarisation by at least an order of magnitude. A theoretical increase in signal size was expected to yield a sufficient SNR for imaging functional brain activity non-invasively in real time (Chapter 2). An additional improvement in signal quality was predicted if an optimal carrier frequency for recording slow changes was identified. In this way, non-invasive EIT of slow neural changes during physiological stimulation of the brain was expected to produce images of haemodynamic activity which could serve as an inexpensive and portable substitute for fMRI in rodent studies of pathophysiological neural responses.

Table 1.1. Summary of the specifications and the key technical differences between EIT and other functional neuroimaging techniques forming the rationale for conducting the work detailed in this thesis.

Method	Basic principles	Key techniques	Benefits	Drawbacks	Spatial res.	Temporal res.
EEG	Detects extra- or intracranial voltage fluctuations caused by localised changes in neuronal activity.	EEG with scalp electrodes ECoG with subdural electrodes SEEG with depth electrodes	Non-invasive High temporal res.	Spatial accuracy Poor depth res. Motion artefacts	1 – 5 cm	≤1 ms
MEG	Detects magnetic field fluctuations arising from changes in localised neuronal populations.	MEG using SQUID sensors MEG using OPMs	Non-invasive High temporal res. Improved depth res.	Spatial accuracy Subpar depth res. Motion artefacts	≤ 1 cm	≤1 ms
fMRI	Detects changes in cerebral haemodynamics during neural activity based on magnetization/demagnetization of blood H_2O/Hb upon exposure to RF field.	ASL fMRI (ΔCBF) VASO fMRI (ΔCBV) BOLD fMRI (oxy-/deoxy-Hb)	Spatial res. Field of view Non-invasive	Temporal res. Indirect measure Costly	~0.1 – 1 mm	~50 ms – 1 s
PET	Detects localised neurometabolic changes ($CMRO_2$ and CMRGlu) upon brain stimulation using the rate of radiotracer decay as a marker.	FDG-PET	Field of view Non-invasive Complimentary info	Temporal res. Indirect measure Discontinuous	1 – 3 mm	1 – 15 min
OI	Exploits intrinsic differences in absorption/scattering of visible/infrared/UV light between blood and other brain tissues to trace functional haemodynamic changes.	NIRS OCT OISI DOI	Temporal res.	Invasive Modality-dependent spatial/depth res. Indirect measure	<10 µm – 10 mm	≤100 ms
EIT	Tracks localised changes in brain activity based on changes in neural tissue impedance.	Fast neural EIT Slow neural EIT	High temporal res. High spatial res. Versatile	Depth resolution Invasive Long recording time	~0.2 mm	≤2 ms – 2 sec

Failure to detect sufficient SNR of functional slow neural impedance changes using scalp electrodes prompted further investigation using intracranial epicortical electrodes (Chapter 3). The premise for the second study was an estimated increase in the signal amplitude due to the absence of the resistive skull barrier and a theoretical potential for a single-shot imaging of brain activity with a multifrequency parallel EIT. The rationale for this work was the potential utility of parallel slow neural EIT in behavioural rodent studies where skull can be replaced after implanting subdural electrodes. However, the findings indicated that, due to necessity for prolonged averaging, EIT of slow changes during physiologically evoked brain activity was impractical in its current state and, therefore, was not pursued further.

Epilepsy is a debilitating neurological disorder affecting approximately 50 million people worldwide (World Health Organization, 2022). A significant proportion of epilepsy patients suffers from its refractory form which is often treated with a surgical resection of epileptogenic tissue if the seizure focus is well-defined and discrete (Sultana et al., 2021). However, in cases where the EZ involves the eloquent cortex or resides in the subcortical structures, or where seizures are generalized, resective neurosurgery is not viable. DBS is a potential option for such patients and have shown promising results of significantly reducing or completely abolishing seizures in intractable epilepsy cases (Cukiert et al., 2014; Hodaie et al., 2002; Kim et al., 2017; Salanova et al., 2015; Son et al., 2016; Velasco et al., 2006). However, accurately delineating the spatiotemporal evolution of seizures with intracranial electrodes remains a challenge due to the limitations in the sampling volume and the orientation or the location of the source generators which are currently identified with invasive intracranial SEEG. EIT with depth electrodes has the potential to overcome these issues by detecting and imaging the onset and the evolution of epileptogenic activity in 3D with a millisecond and micrometre resolution. This formed the rationale for the remaining projects outlined in Chapters 4 to 6.

Intracranial depth EIT studies were further facilitated by the design of a novel stereo-electrode grid optimised specifically for recording functional intracerebral impedance changes at a mesoscopic resolution (Fitchett et al., 2022, 2023). The implementation of the 3D fast/slow neural EIT idea with this new electrode array required optimisation of an experimental method undertaken in Chapter 4. This also included the selection of an appropriate rat epilepsy model which was refined to suit the purpose of this thesis. Once a working principle and a suitable animal model were established, pilot studies were performed to determine the feasibility of real-time fast neural (Chapter 5) and slow neural EIT (Chapter 6) of ictal epileptiform activity in murine brain. In addition to investigating the spatiotemporal limits and the translational potential of intracranial EIT, these studies were intended to expand our understanding of the epileptogenic network activity during stereotypic ictal spike-wave discharges in rats. Hence, the work detailed in the last two experimental chapters was expected to add value from both the neural engineering and the broader neuroscientific perspectives.

1.4 Statement of Originality

The material presented in this thesis is my own work which has been completed and submitted for the degree of Doctor of Philosophy. To my knowledge, research outlined in this work has not been published elsewhere or by another person and contains only original material except otherwise stated. Notably, due to the interdisciplinary nature of the projects, I have received assistance in a few aspects of this work.

In Chapter 2, the forward modelling as well as the design and manufacturing of the scalp electrode array used in several scalp impedance recordings was undertaken by Kai Mason and Adam Fitchett.

In Chapter 3, the forward modelling and the calculation of the Jacobian matrix were performed by Adam Fitchett. A simulation control experiment was performed by Kai Mason. Epicortical electrode arrays were manufactured by both Adam Fitchett and Kai Mason according to the design in Faulkner (2019). A custom rack of parallel current sources was designed and made in-house by Adam Fitchett.

In Chapter 4, the depth probe and the apertured epicortical array were designed by Adam Fitchett. The manufacturing of the depth arrays used in Chapters 4, 5, and 6 was handled by an electrical engineering lab in Columbia University, USA, led by Prof. Ken Sheppard. The apertured epicortical arrays used for the same studies were produced by Adam Fitchett and Michael Lantin. All histological processing was performed by the laboratory staff from the IQPath group in UCL Queen Square Institute of Neurology. I also received assistance from Dr. Nicole Thompson on the interpretation of the histological findings.

In Chapter 5 and 6, the forward modelling for EIT and for SEEG inverse source localisation as well as the calculations of the Jacobian and the lead field matrices were performed by Yuval Gal-Shohet and Dr. Kirill Aristovich.

Lastly, although I performed all experimental work myself, including the animal experiments and data analysis, I received technical and engineering support from Adam Fitchett, Kai Mason and Dr Kirill Aristovich in all of my studies.

Chapter 2

Characterising slow impedance changes in the rat brain following evoked somatosensory activity using scalp electrodes

2.1 Introduction

EIT carries an unmatched potential to image functional brain activity non-invasively with a mesoscopic spatiotemporal resolution. However, the presence of the resistive barriers of the skull and the scalp results in significant attenuation of the recorded signal. In the case of fast neural activity, impedance changes are suppressed below the detection limit due to their small amplitude. On the other hand, slow functional intracerebral impedance changes, such as those produced by altered cerebral haemodynamics, are several orders of magnitude larger and, therefore, might be discriminated from the scalp. As such, EIT of slow brain activity has the prospect to serve as a convenient alternative to fMRI producing functional images of localised brain impedance changes during pathophysiological brain activity. To achieve that, it is desirable to understand the characteristics of slow impedance responses to physiological activation of the brain across the frequency spectrum as the magnitude of the observed signal is highly sensitive to the applied frequency. The study detailed in this chapter was conducted to assess the feasibility of non-invasive imaging of slow impedance changes in response to physiologically evoked activity in the rat brain. A broad-bandwidth frequency sweep of slow impedance responses was performed to establish their characteristics across the spectrum which could aid in the optimisation of the parameters for non-invasive slow brain EIT.

2.1.1 Background

There are functional changes in the brain which accompany increased neuronal activity evoked by the presentation of a physiological stimulus. Those changes primarily represent a neurovascular response to an increased metabolic demand imposed by the active neurons. This manifests as a sudden increase in CBF which overcompensates the energy requirements and therefore leads to a local increase in CBV developing over several seconds after the initiation of the response. A detailed account on the underpinning mechanisms can be found in 1.1.1.2.

2.1.1.1 Summary of the previous studies

Numerous neuroimaging techniques have utilised the functional change in CBF or CBV as secondary markers of functional brain activity. EIT has been similarly suggested for imaging these activity-related haemodynamic changes in the brain by recording a slow local decrease in brain tissue impedance upon the pathophysiological brain stimulation. The proposal was based on the hypothesis that a local accumulation of blood briefly changes the composition of the cerebral tissue in the active region. The proportion of highly conductive blood increases relative to the resistive grey matter, therefore, the total impedance of that brain region lowers. Hence, the activity-related neurovascular response should manifest as a decrease in transfer impedance on the peripherally placed EIT electrodes.

As reviewed in 1.2.4.1, EIT recordings of slow impedance changes during physiological brain activity were attempted in both animal and human studies (Holder et al., 1996; Tidswell et al., 2001; Witkowska-Wrobel, 2020). The initial studies were conducted in rabbits where slow impedance measurements following somatosensory and visual evoked activity were recorded directly from the cortical surface and successfully reconstructed into reliable images (Holder et al., 1996). Surprisingly, the changes, which were ~5 % in magnitude, were both positive and negative. This success prompted further investigations of physiologically evoked slow impedance responses in humans using scalp electrodes (Tidswell et al., 2001; Witkowska-Wrobel, 2020). Regrettably, both Tidswell et al. (2000) and Witkowska-Wrobel (2020) failed to replicate the results seen in rabbits. Although the single-channel slow impedance changes in response to sensory stimulation were successfully detected, no images could be reconstructed from the obtained data (Witkowska-Wrobel, 2020). The recorded changes in these studies were around 10 times smaller than those observed by Holder et al. (1996) and were riddled with motion artefacts making accurate EIT image reconstruction unachievable.

2.1.1.2 Deficits of the previous studies

The above studies were performed with an underlying assumption that the choice of the carrier frequency was not a significant factor in the slow impedance recordings if the observed impedance change was in fact due to the local build-up of the cerebral blood. Holder et al. (1996) and Tidswell et al. (2000) used 50 kHz whereas Witkowska-Wrobel (2020) used 1.725 kHz and 195 kHz with two different EIT recording systems. Conductivity of blood is roughly flat up to 1 MHz (Gabriel et al., 2009). Therefore, the amplitude of slow impedance changes was assumed to be independent of the injected frequency. However, what was likely not considered was the frequency-dependence of the bioimpedance of the nervous tissue which drops sharply with frequency (Gabriel et al., 2009; Gabriel et al., 1996). This decrease is the most notable between DC and 1 kHz as the conductivity difference between blood and brain changes approximately 5 times. Hence, the lower end of the frequency spectrum which has not been explored for slow impedance recordings might yield a bigger signal due to a larger impedance contrast between blood and brain. The increase in the SNR would substantiate the successful reconstruction of the slow neural activity images.

Another important consideration is the hardware used for data acquisition. The only previous animal study performing slow brain EIT employed an original Sheffield Mark 1 system (Holder et al., 1996). The limitation of Sheffield Mark 1 was a singular current injection pattern which permitted only adjacent injection pairs in a ring of 16 electrodes at a fixed injection frequency of 50 kHz (Brown & Seagar, 1987). This meant that non-invasive intracerebral impedance measurements were not practical as the current applied through neighbouring electrodes would be mostly shunted through the scalp. Hence, the system was used with electrodes placed directly onto the surface of the brain. Moreover, a high injection frequency in Sheffield Mark 1 was likely suboptimal for slow impedance measurements.

2.1.1.3 Expectations based the previous studies and underlying physiology

The working hypothesis of this study was that the slow impedance change in the rat brain evoked by somatosensory stimulation would lead to a maximal impedance change of -0.01 % on surface electrodes. The number was derived theoretically by a fellow PhD student Kai Mason using the published PET and fMRI data (Horitsugi et al., 2017; Mandeville et al., 2001). These studies have shown that CBV, which comprises approximately 4 % of brain tissue in rats, changed by around 25 % in the somatosensory cortex upon external stimulation (Horitsugi et al., 2017; Mandeville et al., 2001). Therefore, the local activity-induced change in CBV was estimated to be approximately 1 %. The resulting change in conductivity was then extrapolated from the difference in the weighted mean of the conductivities of blood and brain tissue before and after stimulation and calculated as follows. The conductivity values used for the calculations were 0.3 S/m and 0.6 S/m for brain and blood, respectively (Gabriel et al., 2009; Latikka et al., 2001):

(1) Before the stimulation, the conductivity of a brain volume where 96 % comprises brain tissue and 4 % of blood was estimated:

$$\rho_1 = 0.96 \times 0.3 \; {}^{S}\!/\!{}_{m} + 0.04 \times 0.6 \, {}^{S}\!/\!{}_{m} = 0.312 \; {}^{S}\!/\!{}_{m}$$

(2) After the stimulation, the volume of blood increases by 1 % (5 % in total), resulting in the decrease of the fraction of neural tissue (95 %) in the active brain volume. Therefore, the conductivity of the region changes was calculated as follows:

$$\rho_2 = 0.95 \times 0.3 \; {}^{S}\!/\!{}_{m} + 0.05 \times 0.6 \; {}^{S}\!/\!{}_{m} = 0.315 \; {}^{S}\!/\!{}_{m}$$

(3) Hence, the change in the conductivity ($\delta\rho$) of the brain volume of interest after its stimulation (ρ_2) if expressed as a percentage (%) of the starting conductivity of the same region pre-stimulation (ρ_1) was predicted to be:

$$\delta\rho \;=\; \frac{\rho_2 - \rho_1}{\rho_1} \times 100\% = \frac{0.315\ {}^{S}/_{m} - 0.312\ {}^{S}/_{m}}{0.312\ {}^{S}/_{m}} \times 100\% = 0.96\% \;\approx 1\%$$

(4) Based on the previous modelling studies, the skull was predicted to attenuate the signal around 100 times resulting in a maximal impedance change of -0.01 % recorded with the scalp electrodes (Gilad et al., 2009; Liston et al., 2012).

The slow impedance changes were expected to correlate negatively with the carrier frequency. The prediction was that the physiological change would be largest at low frequencies (< 1 kHz) where the contrast between the bioimpedance of blood and brain is the most pronounced. However, the spontaneous EEG noise was also expected to amplify below 1 kHz and blunt the signal. Therefore, similarly to the findings in the frequency sweep of fast impedance changes conducted by Faulkner et al. (2018a), the frequency sweep of slow changes was expected to reveal a ‘sweet-spot’ for recording EIT of slow neural activity from the scalp with the highest SNR.

2.1.2 Purpose

The purpose of this work was to determine whether slow impedance changes during physiological brain activity in rats can be recorded non-invasively with a broader goal of developing an fMRI-like imaging system comprising EIT recording equipment and scalp electrodes. In this study, I aimed to answer the following questions: (1) Is it possible to measure slow impedance changes following somatosensory stimulation using scalp electrodes in anaesthetised rats? (2) What are the characteristics and the size of this impedance change when recorded non-invasively? (3) What carrier frequency is optimal for detecting slow impedance changes during physiologically evoked responses when using scalp electrodes? (4) Is non-invasive imaging of slow neural changes during normal brain activity possible with EIT and scalp electrodes using the present experimental set-up?

2.1.3 Experimental Design

Experiments were conducted in 16 anesthetized rats. The data from nine animals was used in method development and optimisation. The remaining seven animals were used for the collection and analysis of the final dataset. Single-channel slow impedance responses to somatosensory stimulation were recorded with extracranial electrodes whilst electrically stimulating the contralateral forepaw at 11 Hz. The frequency response of these impedance changes was recorded at four EIT injection frequencies spanning the range between 200 Hz – 100 kHz. The lower frequency limit was chosen such that when the carrier signal was filtered with a 100 Hz bandwidth most of the noise at the mains harmonics and the resting state EEG activity could be removed. The upper frequency band was determined by the hardware limitations.

2.1.3.1 Forepaw stimulation paradigm

To characterise the slow intracerebral impedance change during physiological brain activation, a model system of electrical forepaw stimulation in rats was employed. This model relies on the activation of an established neural circuit which propagates peripheral sensory inputs from the median nerve in the rat's forepaw to the contralateral primary somatosensory cortex (S1) with the fibres decussating at the ventral posterolateral nucleus of the thalamus (VPL) (Dawson & Killackey, 1987; Fabri & Burton, 1991). Activation of this circuit elicits well-characterised somatosensory evoked potentials (SEPs) in the forelimb region of S1 (Rojas et al., 2006; Sakatani et al., 1990). A fast neural response is accompanied by a slower local increase in CBF and CBV (Goloshevsky et al., 2008; Silva et al., 2000; Silva et al. 2007). I expected that this regional change in CBV would produce a local change in brain impedance which could be measurable with the scalp electrodes as a slow impedance change.

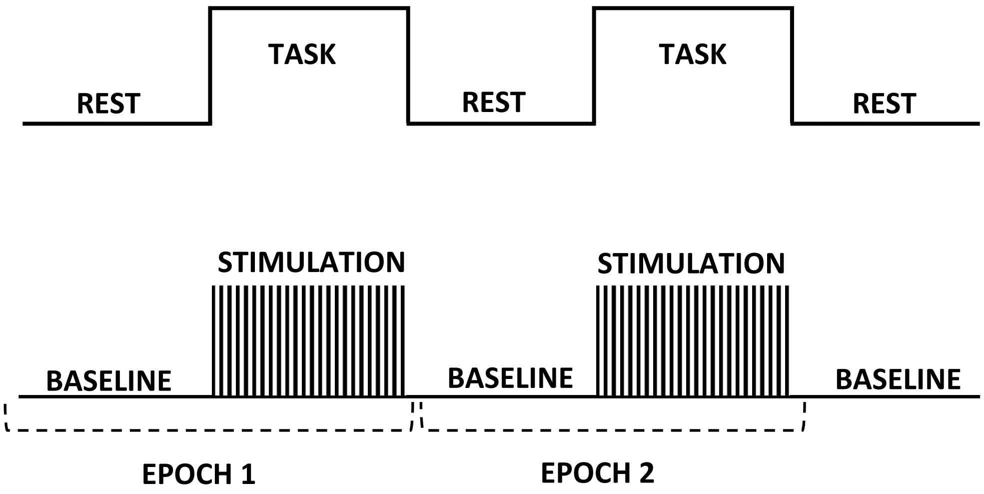

Figure 2.1. A classical 'boxcar' experimental design used for recording event- or task-related brain activity changes with respect to a resting state activity. Developed for low-resolution functional neuroimaging studies, block experimental design enables evaluation of slow neural activity changes in the brain between unstimulated and stimulated conditions. Baseline-stimulation epochs are averaged together to maximise the SNR.

Somatosensory stimulation was delivered in a ‘block’ paradigm (Fig. 2.1). Epoch-based, or ‘boxcar’, design originated from low temporal resolution functional imaging studies and combined alternating periods (‘blocks’) of stimulation and rest into epochs which were repeatedly administered and then averaged together to boost the SNR (Bandettini & Cox, 2000; Blamire et al., 1992; Fox & Raichle, 1984). The recorded signal could then be evaluated relative to the baseline established during periods of rest (Fox et al., 1984; Fox & Raichle, 1984).

In this study, a total of three stimulation paradigms were tested (Table 2). The first two paradigms were part of a method development while the last paradigm was used in the final data acquisition. Initially, epochs contained a prolonged cortical stimulation (30 s) at low frequency (3 Hz) which was expected to induce a longer-lasting haemodynamic change (Huttunen et al., 2008; Kim et al., 2010; Silva et al., 2000). However, long epoch duration limited the number of repetitions which could be collected per unit time and consequently restricted the maximal SNR of impedance recordings proving suboptimal for the purpose of this study.

Based on known non-linearities of cerebral haemodynamic response, further experiments were carried out using a combination of high stimulus frequency and short stimulus duration (Table 2.1) (Hirano et al., 2011; Liu et al., 2010; Pfeuffer et al., 2003). The exact parameters were guided by the findings of Kim et al. (2010) and Hirano et al. (2011). The former study demonstrated that the haemodynamic changes evoked by a short forepaw stimulation (< 10 s) were maximised at stimulation frequencies 8 – 12 Hz (Kim et al., 2010). Moreover, the amplitudes of the CBF and BOLD responses reached saturation for stimuli longer than 1 s and 2 s, respectively (Hirano et al., 2011). Therefore, in the final experimental design, the electrical stimulus was delivered for 2 s at 11 Hz at a maximum amplitude of 2 mA to avoid causing nociceptive response which could distort the spatial distribution of the recorded impedance response (Lowe et al., 2007). Somatosensory stimulation was enveloped by a 5 s pre-stimulus baseline period and 13 s post-stimulation recovery (5 s OFF – 2 s ON – 13 s OFF) to allow sufficient time for locally increased CBV to return to baseline before the next epoch begins (Hirano et al., 2011).

Table 2.1. Forepaw stimulation paradigms tested during the method development phase.

Stimulation design	Stimulation frequency
30 s ON – 60 s OFF	3 Hz
8 s OFF – 2 s ON – 20 s OFF	3 Hz and 11 Hz
5 s OFF – 2 s ON – 13 s OFF	11 Hz

The number of epochs collected during each recording was dictated by the expected size of the signal and the noise observed in the preliminary data during the method development phase. The initial recordings showed that the average peak-to-peak noise of the filtered and demodulated signal was ~0.3 %. With the SNR of 2 defining the visual detection limit, to distinguish an impedance change of 0.01 %, the maximal noise amplitude quantified as the standard deviation of the baseline in the averaged signal needed to be ≤0.005 %. Assuming the Gaussian distribution of noise which would decrease with the square root of the number of repetitions, to achieve the satisfactory noise levels for the smallest expected signal amplitude, at least 144 epochs needed to be collected yielding a total time of approximately 50 min per recording.

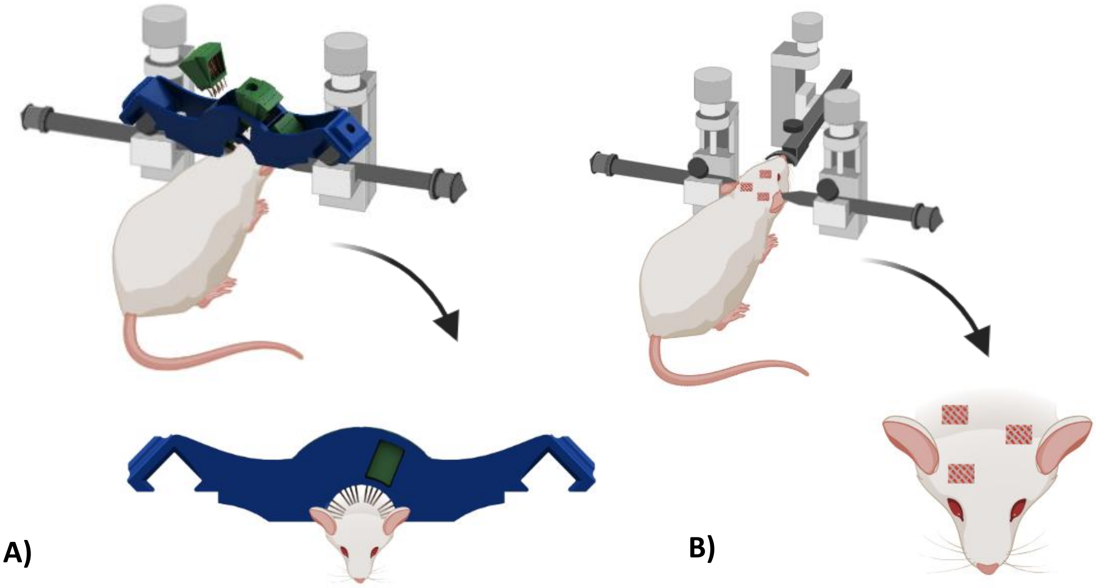

Figure 2.2. The experimental framework for recording single-channel slow impedance changes from the scalp in this study. (**A**) The first part of the study was undertaken using the scalp electrode array containing 24 stainless-steel probes coated with PEDOT:PSS. Current was injected through a pair of diametrically opposed electrodes chosen *ad hoc* and recorded with the remaining electrodes. (**B**) An alternative experimental design employed custom-sized hydrogel electrodes which were applied to shaved and abraded scalp in the geometry represented in the picture. All impedance measurements were taken with respect to a circular reference Ag-AgCl electrode placed at the back of the head underneath the skin (not shown in the picture). Figure created with BioRender.com.

2.1.3.2 Electrodes

The study was performed using two electrode designs, namely spring-loaded rod electrodes and sticky hydrogel electrodes (Fig. 2.2). The reason for utilising two electrode designs was their respective benefits and drawbacks which differentially affected the degree of experimental error. The first recordings were undertaken with a rigid rod-electrode array mounted onto the stereotaxic frame (Fig. 2.1A). The advantage of this type of array was a stable and consistent electrode contact with the skin. However, the pressure from the spring-loaded rods caused time-dependent skin swelling at the edges of the array which was likely to impact the propagation of injected current. Furthermore, electrically conductive gel had to be applied to shaved and abraded skin before fixing the probes onto the scalp to improve the contact impedance. Due to long duration of experiments (up to 12 hours), the gel frequently dried out causing a gradual drift in electrode-skin contact impedance throughout the recordings.

To overcome the above issues, the rod electrode array was replaced by planar hydrogel electrodes which were used for both, the current injection and the recording of the boundary voltages. These electrodes were sufficiently soft and flexible to avoid causing skin oedema. However, due to the lack of firmness and rigidity, electrode-skin contact was uneven which also affected the contact impedance. To circumvent the issue, hydrogel electrodes were glued with collodion.

2.1.3.3 Simulation

Preliminary results from the method development suggested that the expected size (-0.01 %) of slow impedance change from the scalp was likely an overestimate. Therefore, forward modelling was conducted by a fellow PhD student Kai Mason in parallel to *in vivo* experiments to simulate the predicted boundary voltage changes at the scalp electrodes which would result from 1 % conductivity perturbation in the forelimb S1. This simulation was performed using an anatomically realistic rat head mesh incorporating five distinct conductivity layers which were segmented from a CT scan of a rat's head. The known conductivity values of the relevant intra- and extracranial tissues allowed the prediction of the boundary voltage measurements directly proportional to transfer impedance on the scalp electrodes when a low-resistivity perturbation was inserted in the cerebral cortex of a rat. The simulated electrode geometry mimicked the experimental setup with hydrogel electrodes with the simulation containing an additional electrode in the rat's mouth (Fig. 2.2). All possible injection and recording electrode combinations were tested yielding 20 boundary voltage measurements. The measurements recorded from the injecting electrodes were not considered.

2.2 Materials and Methods

2.2.1 Animal preparation and surgery

Adult Sprague-Dawley rats weighing between 300 – 450 g were used for the experiments. All animals used for completing the experimental work detailed in thesis were previously housed under a standard 12-hour light/dark cycle in groups of two to four in open-shelf caging. Each cage contained lignocel bedding and tissue serving as nesting materials as well as an Aspen wood chew block and two cardboard tunnels for additional enrichment. The rats were fed Teklad Global Rodent Diets® pellets with an *ad libitum* access to both food and water. Before the experimental procedures were undertaken, the rats were anaesthetised with an intraperitoneal (IP) injection of 1.3 – 1.5 g/kg urethane. The onset and the depth of anaesthesia was determined and continuously monitored by checking the pedal withdrawal reflex. Once areflexic state was reached, the animal was placed in dorsal recumbency on a Perspex platform tilted at 45 degrees to the optical table. A wire loop attached to the top of the platform was hooked under the superior incisors enabling the visualisation of the larynx and vocal cords transilluminated with an external light source. Endotracheal intubation was then performed using a 14-gauge polyethylene catheter with a flexible blunt-tip stylet inserted a few millimetres past the tip of the endotracheal tube while compressing the tongue with a laryngoscope (Vongerichten et al., 2014). The stylet was introduced into the trachea guiding the endotracheal tube and, once past the vocal cords, the stylet was retracted. The endotracheal tube was then connected to the Y-piece sutured to the mandibular skin to prevent extrication. The animals were allowed to breath spontaneously a supplemental gas mixture of 70/30 % air/oxygen. To prevent dehydration, a butterfly needle was also inserted IP for continuous administration of 0.9 % sterile saline at 1ml/hr.

Next, the rats were fixed within ear bars in a stereotaxic frame (Narishige International Ltd, London, UK). The scalp was shaved with Veet® depilating cream and abraded using Nuprep gel prior to the application of electrodes. When the copper electrode array was used, the tip of each probe was individually covered with conductive gel (Tower Health, UK). Alternatively, hydrogel electrodes were glued to the scalp with collodion and then covered with a cling film to retain the moisture of the skin. Throughout the duration of each experiment, electrocardiogram (ECG), heart rate, respiratory rate, end-tidal CO_2, and SpO_2 were monitored using Vetronics Lightning monitor (Vetronic Services Ltd, Abbotskerswell, UK). The core body temperature was maintained using a homeothermic heating unit comprising a blanket and a rectal thermometer which continuously sampled the temperature and fed the measurements back to the system which then adjusted the warmth of the blanket accordingly (Harvard Apparatus, Edenbridge, UK). All animal handling and experimental work complied with the UK Home Office regulations detailed in the Animals (Scientific Procedures) Act 1986.

2.2.2 Hardware and data collection

2.2.2.1 Hardware

Data was collected using the ScouseTom EIT system (Avery et al., 2017) with either an actiCHamp amplifier (Brain Products GmbH, Gilching, Germany) used for carrier frequencies up to 10 kHz, or a NL106 AC/DC amplifier (NeuroLog^{TM}, Digitimer, Letchworth, UK) and a National Instruments Data Acquisition device (NI DAQ; National Instruments Corp., Austin, TX, USA) for carrier frequencies up to 100 kHz. Detailed hardware specifications for each data acquisition system are included in Appendices A and B. The contralateral forepaw was stimulated using a NL800A (NeuroLog^{TM}, Digitimer, Letchworth, UK) stimulator at a frequency of 11 Hz in 300 µs pulses which had a maximum amplitude of 2 mA. Impedance recordings were performed using two different electrode designs, namely spring-loaded rod electrode array and sticky hydrogel electrodes. In both cases, re-usable Ag-AgCl EEG cup electrodes (8 mm in diameter) were used as reference and ground electrodes.

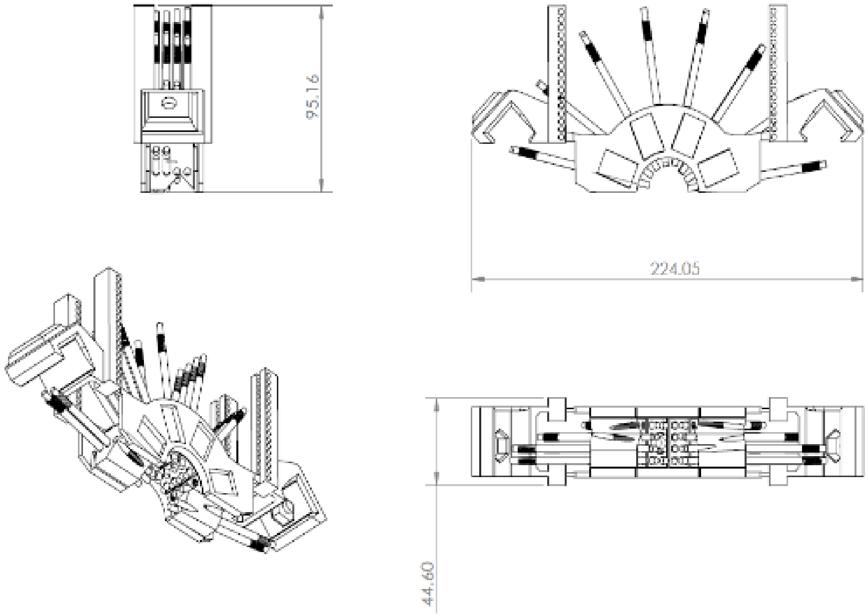

Figure 2.3. Design of the scalp electrode array made of spring-loaded stainless-steel rods in a 3D-printed PLA case. The dimensions are indicated in millimetres.

A rigid rod electrode array was designed and fabricated in house (Fig. 2.3). The frame and the modules for holding the probes were 3D-printed from polylactic acid (PLA). The frame was designed to attach to the stereotaxic frame once vertically lowered onto the scalp. The probes were made from the stainless-steel rods placed through brass tubing and soldered to the extension springs. The probes were held in six 3D-printed modules, each of which could house up to eight probes. The modules were longitudinally stacked within the frame forming an array of electrodes which covered the dorsal and temporal head surface. Prior to the experiments, the tip of each probe was individually coated with PEDOT:PSS to reduce the contact impedance. The diameter of the individual contacts was 3 mm.

An alternative electrode design involved disposable hydrogel electrodes typically used for clinical ECG recordings (Electrode Store, USA). The electrodes were manually re-sized to the appropriate dimensions. To ensure the sufficient coverage of the active area, both injecting and recording electrodes were cut in a rectangular shape and measured c. 5 x 5 mm (Figure 2.2).

2.2.2.2 Data acquisition

Recordings at carrier frequencies up to 10 kHz were made from a single channel at a sampling frequency of 100 kHz using a 24-bit actiCHamp amplifier (Brain Products GmbH, Germany). The data acquisition system used to obtain recordings at 100 kHz comprised the NL106 AC/DC amplifier (NeuroLog^{TM}, Digitimer, Letchworth, UK) and a 16-bit DAQ (National Instruments Corp., Austin, TX, USA). The Keithley 6221 current source (Keithley Instruments Ltd, Solon, OH, USA) was used for injecting current at all four carrier frequencies, namely 200 Hz, 1 kHz, 10 kHz and ~100 kHz. Due to low frequency interference observed in some of the experiments, recordings at the highest carrier frequency were taken in a frequency range 99.8 – 100 kHz. The amplitude of the injected current was adjusted according to the injection frequency and ranged between 1 – 10 mA with higher amplitude used for higher frequency recordings. In both instances, the location of the injection electrodes was selected to maximise the amount of current travelling through the active area and were located on diagonally opposite sides of the scalp (Fig. 2.2). When the rod electrode array was used, the electrode exhibiting the greatest sensitivity to somatosensory stimulation was chosen for recording impedance changes on case-by-case basis in each rat (Fig. 2.2A). Alternatively, the recording hydrogel electrode was fixed arbitrarily aiming for the maximal coverage of the active cortical area (Fig. 2.2B). A full sweep of all four injection frequencies was not conducted in a single animal due to the long duration of individual impedance recordings.

2.2.3 Data processing and analysis

Recordings of forepaw SEPs and slow impedance changes were acquired separately. SEPs were extracted by averaging the raw EEG signal to the repeated stimulation trigger administered at 11 Hz. The averaged data was then filtered with a 5 Hz high-pass filter (1st order, Butterworth) followed by a 200 Hz low-pass filter (5th order, Butterworth). The averaged traces were visually inspected to ensure the presence of reliable forepaw SEPs with reproducible characteristics. The latency of the recorded SEPs was calculated by identifying the timing of the first positive (P1) or negative (N1) voltage response following the stimulation.

Raw voltage recordings, which were directly proportional to transfer impedance due to injection of a constant current, were first filtered with a 100 Hz band-pass filter (3rd order, Butterworth), 50 Hz each side of the carrier frequency. The data was then demodulated using the Hilbert transform. To extract the slow impedance change, the demodulated signal was filtered with a 1 Hz low-pass filter (3rd order, Butterworth). This cut-off was chosen to account for the predicted frequency of the slow cortical impedance changes (~0.1 – 0.5 Hz). The low-pass filtered signal was subsequently segmented into 20 s epochs, - 5 to +15 seconds, with 0 s timepoint corresponding to the start of somatosensory stimulation. Outlying epochs were removed before further processing of the data. Outliers were defined as epochs containing a datapoint greater than the 75th percentile plus five times the interquartile range or a datapoint lower than the 75th percentile minus five times the interquartile range, except for filtering artefacts which occupied <1 second of the epoch. The remaining epochs were averaged together to compute a mean impedance change.

Residual noise in the averaged and filtered signal was determined by computing the standard deviation of the baseline signal (-5 to 0 seconds of the epoch). Only recordings with noise level below the cut-off of 0.005 % derived in 2.1.3.1 were displayed and analysed further. The average baseline noise across all recordings acquired at the same carrier frequency was then calculated by taking the mean of the noise figures from the selected recordings. The mean impedance change at each carrier frequency was expressed as a percent change of the mean demodulated data (dZ, %) and calculated by averaging all epochs from one single-channel recording (n = 1) in one rat (N = 1) and displayed with the standard error (S. E.) of the mean.

2.2.4 Statistical analysis

Statistical tests were used to establish whether the averaged signal contained any significant changes in voltage across epochs when compared to the baseline potential centred at 0 µV. A series of one-way t-tests were performed for each timepoint across all epochs within each recording. The resulting p-values were adjusted using Bonferroni correction to control familywise error rate. A significance level α = 0.05 was used for these analyses. The recorded impedance change was considered significant only if it met the statistical criteria in more than one recording at the same carrier frequency.

2.2.5 Forward modelling

The forward modelling was computed using PEITS forward solver (Jehl et al., 2015) on a 3D anatomically realistic rat head mesh containing 9 million tetrahedral elements. The mesh comprised five conductivity layers. The conductivity values assigned to brain, CSF, skull and scalp were 0.3, 1.79, 0.025, and 0.4 S/m, respectively (Vorwerk et al., 2014). Sinuses were modelled as air-filled cavities with an infinite resistivity (Montes-Restrepo et al., 2014).

A perturbation with 1 % change in conductivity and occupying a volume of c. 10 mm^3 was inserted into a head mesh in the relative location of the forelimb S1. The volume of the perturbation encompassed the whole forelimb S1 region (dimensions at maximal distances: AP axis = 3.6 mm, ML axis = 2 mm) across all six cortical layers with a combined thickness of 1.5 mm (Paxinos & Watson, 2013). The simulated local conductivity change was assumed to be purely haemodynamic and yield a uniform increase in conductivity in the brain volume of interest. To compute the forward solution, four circular electrodes with a diameter of 5 mm were equidistantly spaced on the rat head mesh and one circular electrode with diameter of 10 mm placed in the mouth. The reference electrode was located at the back of the head.

2.3 Results

2.3.1 Extracranial forepaw somatosensory evoked potentials

Electrical stimulation of the left forepaw at 11 Hz reliably evoked somatosensory potentials on the scalp electrodes in rats anaesthetised with urethane (Fig. 2.4). The latency of the first response was 5 – 7 ms with an amplitude of <~1.0 µV (Fig. 2.4).

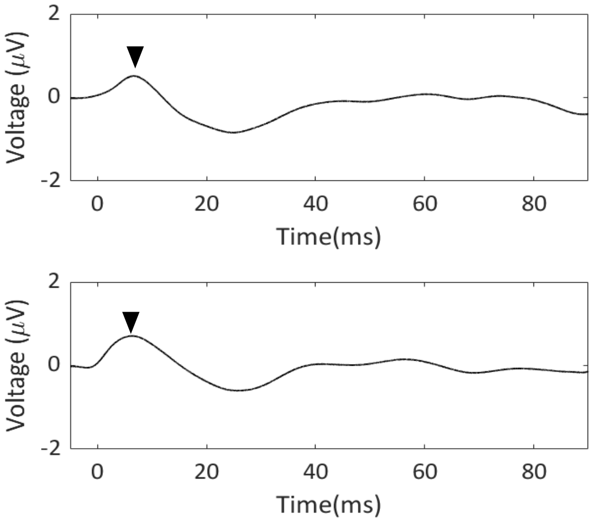

Figure 2.4. **Representative examples of reproducible averaged forepaw SEPs at 11 Hz recorded with the scalp electrodes in two rats.** Electrical stimulation of the contralateral forepaw reliably evoked somatosensory responses on the extracranial electrodes placed on the shaved and abraded scalp of anaesthetised rats. The timepoint of 0 ms marks the stimulation. The peak latency of the first response P1 (marked ▼) in the shown SEPs was 6.3 – 6.7 ms. The amplitude of the P1 was 0.51 and 0.71 µV, respectively.

2.3.2 Single-channel recordings of slow impedance responses across frequencies

Single-channel impedance recordings (n = 23) were obtained in seven rats (N = 7) across all carrier frequencies. Four recordings were respectively obtained at 200 Hz and 1 kHz in four rats. All recordings met the baseline noise threshold of <0.005 % at these frequencies. Eight recordings were obtained at 10 kHz in six rats. One recording was dismissed due to a corrupted data file. Four of the remaining seven recordings were discarded due to either a prolonged (>1 sec) filtering artefact (n = 2) which contaminated impedance data, or due to unfavourable noise characteristics (n = 2). The last seven recordings were obtained at 99.8 – 100 kHz carrier frequencies in six rats. Three of these recordings were discarded. One recording contained corrupted data whereas two other recordings contained baseline noise of >0.005 %. After thresholding, the mean baseline noise across the remaining averaged impedance recordings was 0.003 % at 200 Hz (n = 4 recordings, N = 4 rats) and ~100 kHz (n = 4 recordings, N = 4 rats), and 0.002 % at 1 kHz (n = 4 recordings, N = 4 rats) and 10 kHz (n = 3 recordings, N = 3 rats).

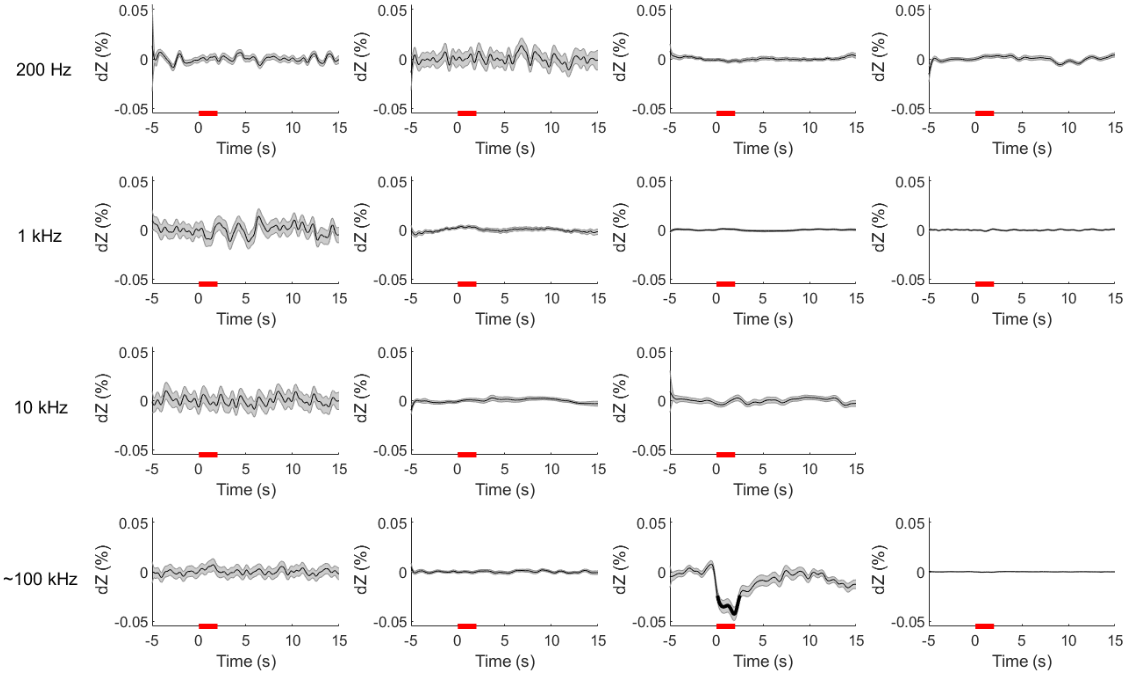

Figure 2.5. Single-channel averaged slow impedance changes at 200 Hz – 100 kHz in response to somatosensory forepaw stimulation in anaesthetised rats. Each row represents the mean dZ ± S.E. (shaded area) with acceptable baseline noise (≤0.005 %) extracted from individual recordings at one carrier frequency labelled on the left. No reproducible impedance changes could be recorded in response to somatosensory stimulation at any carrier frequency (n = 15 recordings, N = 7 rats). The red line on the x-axis marks the period of somatosensory stimulation.

No physiologically significant impedance changes could be reproducibly recorded at any of the tested frequencies despite acceptable noise characteristics (Fig. 2.5). An isolated slow impedance decrease of -0.0425 ± 0.007 % was recorded at ~100 kHz in one rat ($p < 0.05$, one-way t-tests with Bonferroni correction). This impedance change commenced 0.1 s after the onset of somatosensory stimulation and lasted for 2.4 s. However, this pattern was not reproduced in other rats; therefore, the change was not considered significant.

2.3.3 Forward modelling of slow impedance changes from the scalp

Forward modelling indicated that intracerebral conductivity change of 1 % occupying an entire volume of forelimb S1 (~10 mm^3) would yield a maximal voltage decrease of -0.004 % on the scalp electrodes. A change of this magnitude exceeded the average baseline noise (0.0015 – 0.0031 %) recorded *in vivo* and was theoretically detectable with electrodes placed on the rat's head.

2.4 Discussion

2.4.1 Summary of results

This study showed that, in the presence of reliable forepaw SEPs, slow impedance changes in the rat brain cannot be reproducibly recorded using scalp electrodes at carrier frequencies of 200 Hz – 100 kHz. A single negative slow impedance response of -0.0425 % to somatosensory stimulation was observed at 100 kHz (Fig. 2.5); however, the finding could not be reproduced in further animals suggesting that this response was artefactual. Nonetheless, simulations conducted in parallel to *in vivo* recordings indicated that, with the noise level observed in the current data, a maximal slow impedance change of -0.004 % was expected on the scalp electrodes if originating from the neurovascular response in the active brain area as hypothesised. With the baseline noise levels observed in this study (0.002 – 0.003 %), the modelled change was theoretically measurable in all recordings. Therefore, the negative findings of this study suggest one of the following. Either the predicted change was markedly overestimated, or perhaps the biological mechanisms generating slow impedance changes in the brain during evoked responses are more intricate than hypothesised and require alterations to the experimental setup to be accurately measured.

2.4.2 Technical considerations

When interpreting the results of this chapter, the following technical limitations and confounding factors should be considered.

2.4.2.1 Electrode design

The main limitation of this study was the scalp electrodes used for single-channel impedance recordings. Both electrode designs posed unique issues which compromised recording quality and introduced experimental error.

The first array made from firm stainless-steel probes exerted significant pressure on the scalp and, therefore, caused pronounced skin oedema at the perimeter of the scalp. The degree of swelling correlated with the duration of the recordings indicating that this electrode design was not suitable for prolonged use. In this study, gradual scalp swelling could have substantially impacted the results by causing the shunting of the injected current through the swollen skin, the path of lowest resistance, and preventing the current from penetrating the skull.

The second issue with this electrode design was the need for the electrically conductive gel. The gel was applied at the beginning of each experiment to reduce the electrode-skin contact impedance which is of a particular concern at frequencies < 10 kHz (McEwan et al., 2007). Poor electrode-skin contact can result in higher contact impedance which can negatively impact the common-mode rejection of the impedance measuring system and introduce measurement errors (McEwan et al., 2007; Petrova, 1999). In this study, the cumulative duration of impedance recordings was frequently 6 – 8 hours which meant that the conductive gel dried out causing fluctuations in the electrode-skin contact impedances and significantly impacting the recording quality.

The alternative electrode design utilised sticky hydrogel electrodes which eliminated the issue of the swollen scalp. However, the problem with this electrode type was their unstable adherence to the skin which similarly compromised the contact impedance. Despite being covered with collodion, the electrodes tended to gradually peel off over the course of the experiment. In addition to that, the crocodile clips used to connect the hydrogel electrodes to the current source and the recording system exerted tension onto the scalp and caused the formation of the skinfolds which could have had an analogous effect on the injected current path as the skin swelling.

All in all, the imperfect electrode design might have compromised the ability to detect reliable impedance changes. In future studies, a new electrode design should be adopted for non-invasive slow neural EIT in rats. A flexible and soft electrode cap similar to the one used in human EEG recordings could be manufactured for rat studies. Electrodes could be imprinted into a flexible material such as silicone rubber which could be wrapped around the rat's head and secured under the lower jaw. This would provide a more even electrode-skin contact without exerting too much force onto the soft tissues.

2.4.2.2 Extrapolating the resistive impedance component

In this study, a change in the transfer impedance associated with somatosensory stimulation was extracted by demodulation of the signal and by obtaining the modulus of the resulting complex impedance change. This procedure provides an accurate measure of the resistive component of the complex impedance if the phase angle between the injecting and the recording electrodes remains minimal (see Fig. 1.1 for reference). Several studies have estimated the phase angle of the nervous tissue at injection frequencies up to 10 kHz which was consistently demonstrated $<10^{o}$ making impedance modulus a representative approximation of its resistive component at these frequencies (Faulkner et al., 2018a; Oh et al., 2011). However, in this study, carrier frequencies extended up to 100 kHz, a frequency at which the phase angle may have been significantly increased due to the capacitive tissue properties. In that case, the modulus of the complex impedance may have reflected a composite measure of both the real (resistive) and the imaginary (reactive) parts of impedance and, therefore, prevented accurate estimation of the true changes in intracerebral resistance arising from neural activity. To avoid errors in the future, studies using EIT injection frequencies above 10 kHz should calculate functional neural impedance changes by decomposing the signal into its resistive and reactive components instead of calculating impedance modulus.

2.4.2.3 Stimulation artefacts

The findings of this study showed an isolated slow impedance decrease detected at 100 kHz (Fig. 2.5). However, the result was not replicated in further experiments suggesting its artefactual nature. Another indication was the latency and the duration of the observed change. The impedance drop correlated almost precisely with the stimulation period and did not extend beyond its time limits. Based on the physiological mechanism of neurovascular response, the onset of slow neural response was expected to be delayed by at least 0.5 – 1 seconds and last several seconds beyond the cessation of the stimulus (Hirano et al., 2011; Silva et al., 2000). Therefore, it was likely that the observed impedance change was not of biological origin. Electrical stimulation of the peripheral nerves to evoke somatosensory potentials is known to cause a stimulus artefact which can distort the shape of the measured signal (Mcgill et al., 1982; Scott et al., 1997). The current injected into the paw through the needle electrodes flows in all directions and can propagate through the skin up to the scalp. The extent and the magnitude of the artefact is amplified when the recording electrodes are close to the stimulating ones such as in the case of forepaw stimulation in rats where the distance between the upper limbs and the scalp is short (Scott et al., 1997). In addition to the spreading stimulus current, the stray capacitances of the stimulator and the capacitive coupling between the stimulating and recording leads can also contribute to the stimulus artefact. It is plausible that the apparent slow impedance change recorded in this study was the result of a stimulus artefact which independently modulated the recorded voltage signal during the period of electrical stimulation and manifested as an impedance change through the application of low-pass filters.

To circumvent these issues, several methodological principles were previously proposed, including but not limited to using a constant-current rather than a constant-voltage stimulator, keeping the stimulating and the recording cables short and distant, and regularly replacing the electrodes with the deteriorated plating (McGill et al., 1982)**.** Although these measures were implemented in the experimental set-up of this study, it is possible that the artefact could not be prevented, and the nature of the observed response should be interpreted with caution. Future experiments could be performed with an updated scalp electrode design with appropriate controls in place to confirm the origin of the observed response.

2.4.3 Answers to questions

2.4.3.1 Is it possible to measure a slow impedance change following the somatosensory stimulation using scalp electrodes in rats?

No significant slow impedance changes of physiological origin as well as expected magnitude could be recorded in this study. A singular example of slow impedance response of -0.045 % was captured at 100 kHz (Fig. 2.5); however, it was subsequently attributed to a stimulation artefact due to a lack of reproducibility. Albeit in broad agreement with an *a priori* prediction (~-0.01%), the peak value of the recorded change was 10 times that suggested by the modelling which showed that the activation of the entire volume of the forepaw S1 would yield an impedance change of -0.004 %. With no reproducible changes and low noise (<0.005%), the data suggested that slow brain impedance changes following the electrical stimulation of the rat's forepaw could not be accurately measured with the existing experimental setup.

2.4.3.2 What is the size of the slow impedance change when recorded non-invasively?

Forward simulations suggested that a maximal slow impedance change which could be recorded with scalp electrodes upon the supramaximal somatosensory stimulation of the forepaw would be an order of magnitude smaller than initially predicted from the calculations based on the underlying physiology and the results of other functional imaging studies. The noise figures achieved in this study were theoretically conducive to scalp slow impedance recordings suggesting that the real physiological change might be even smaller. Empirically, this could be attributed to higher-than-expected signal attenuation by the skull. On the other hand, the conductive layers of the scalp and the CSF which sandwich the skull might shunt the current preventing its penetration. Studies using transcranial current stimulation show that all three head layers impose a significant barrier to the delivery of the current and lead to a reduced current density in the brain (Holdefer et al., 2006; Miranda et al., 2013; Salvador et al., 2010). When recording impedance changes with EIT, poor concentration of the injected current in the region of interest (ROI) leads to significant reduction in the SNR of the signal (Faulkner et al., 2017). This can be overcome by increasing the inter-electrode distance, however, at the expense of the reduced electrode diameter which would increase the electrode-skin contact impedance (Faria et al., 2011). In this study, the electrode sizes for both experimental setups were based on practicability and the arbitrary balance between their diameter and the spacing.

In silico simulations for predicting impedance change at the scalp electrodes were conducted by inserting a perturbation which provided a 1% uniform conductivity increase in the full volume of forepaw S1. However, electrical stimulation of the forepaw was unlikely to activate the entire forepaw S1 region but rather the specific subfields corresponding to smaller somatotopic regions of the forelimb (Waters et al., 1995). This would be expected to induce a smaller CBV change than the activation of the entire forelimb S1 area. Functional MRI studies are in agreement with this and show that the activation of the individual whiskers and forepaw digits can be discriminated with the high-resolution BOLD-fMRI of the rat somatosensory cortex (Weng et al., 2011; Yang et al., 1996). Therefore, the slow impedance change produced by the local increase in CBV due to the activation of a forelimb S1 subfield would likely be smaller than that predicted by the forward modelling. Considering the average baseline noise of 0.002 – 0.003 % observed in this study, impedance changes of <-0.004 % were hardly detectable. Moreover, statistical tests performed to establish significant voltage deviations from the baseline across all averages showed no significant changes supporting the hypothesis of lower-than-anticipated signal amplitude.

The only successful slow EIT study during evoked physiological activity in anaesthetized rabbits used an intracranial ring of electrodes placed on the exposed cerebral cortex (Holder et al., 1996). Hypothetically, the open craniotomy might have allowed the brain to expand upon the accumulation of excess blood in the active brain area. Thus, it is feasible that in the present study the skull prevented the distension of the brain limiting the amount of CBV which could be delivered to the active brain region. Consequently, the slow impedance change on the scalp was negligible compared to that with an open skull.

2.4.3.3 What carrier frequency is optimal for detecting evoked slow impedance changes from the scalp?

The findings of this study showed that the noise across the injection frequencies was relatively uniform (Fig. 2.5). This observation was surprising as higher noise was predicted at <1 kHz with increased proximity to the EEG bandwidth. Moreover, in contrast to the predictions, the larger difference between the blood and brain impedance at low injection frequencies did not sufficiently increase the SNR. This was in agreement with the previous recordings of fast neural impedance changes in the rat brain across the carrier frequencies up to 10 kHz which showed decreased SNR below 1 kHz (Faulkner et al., 2018a; Oh et al., 2011). Therefore, this study reinforced the idea that low frequencies were suboptimal for EIT of brain activity, fast or slow. Similarly to the low frequency band, the suitability of high frequencies for EIT of slow brain activity is questionable due to significantly reduced resting brain impedance. Because of the probable artefactual nature of the slow impedance change recorded at 100 kHz in this study, the result cannot be generalised for future slow EIT applications. Collectively, these results suggest that the optimal frequency for slow neural EIT might lie somewhere between 1 – 10 kHz where the balance between the noise and high signal amplitude could be achieved.

2.4.3.4 Is non-invasive imaging of slow neural changes during normal brain activity possible with EIT and scalp electrodes using the present experimental set-up?

Current neuroscientific studies in rodents exploring functional changes in brain activity utilise fMRI as a primary means for visualising regional activation patterns. Albeit equipped with impeccable spatial resolution, fMRI is stationary, making behavioural task-based studies in unrestrained animals extremely challenging with cognitive paradigms merely impossible to execute (Chang et al., 2016; Lu et al., 2022). Alternative neuroimaging techniques with comparable spatiotemporal resolution, such as functional ultrasound, which can be applied in freely-moving animals, are generally invasive and require a craniotomy (El Hady et al., 2024; Urban et al., 2015). Slow neural EIT with scalp electrodes can theoretically circumvent these limitations and provide a cheap and portable alternative to fMRI. Therefore, this chapter focused on investigating the feasibility of functional imaging of slow neural changes during physiological brain activity in the rat brain with EIT and externally applied electrodes. The results showed that, unlike hypothesised, slow impedance changes due to non-pathological activation of the brain cannot be accurately measured using existing electrode geometries. This therefore makes non-invasive slow neural EIT currently unattainable without further hardware modifications.

2.4.4 Future work

Based on the results acquired in this study, future work should be focused on the development of scalp electrode arrays for non-invasive rat brain EIT recordings. The aim should be to improve the stability of the electrode contact with the skin which would not damage the tissues compromising the recording quality. That could be attempted with the electrodes imprinted into a flexible fabric which could be used to make a cap with electrodes embedded in the material. Improvements in the electrode design could further reduce the noise and, consequently, shorten the averaging time. Moreover, lower electrode-skin contact impedance could in principle enhance the current penetration to the brain yielding a larger current density in the ROI. Nonetheless, at present, it is unlikely that non-invasive slow EIT of physiological brain activity could lead to a viable imaging technique due extremely low signal amplitude and necessity for prolonged averaging. Hence, effort should be shifted to developing non-invasive slow EIT of pathological brain activity such as epilepsy where changes are an order of magnitude larger and could potentially be detected even with the attenuating effect of external head tissues. Otherwise, slow EIT of physiological brain activity could be attempted with intracranial electrodes as the signal would be significantly larger and impedance change might be apparent in real time. Even with invasive placement of the electrodes, slow brain EIT would be a useful tool in a research setting where electrodes could be inserted through a wide craniotomy with skull replaced afterwards. Therefore, this sets the rationale for the study conducted in the next chapter.

Chapter 3

Characterising and imaging slow impedance changes in the rat brain following evoked somatosensory activity using epicortical electrodes and parallel EIT

3.1 Introduction

The study presented in Chapter 2 confirmed that non-invasive functional imaging of slow neural activity during evoked responses in the rat brain is not feasible with the current EIT technology. Following from these results, in the study presented in this chapter, I investigated the feasibility of imaging slow functional brain activity with invasive subdural electrodes. In the first part of the study, I characterised the frequency response of slow impedance changes following physiological activation of the rat brain using epicortical electrodes. The characterisation of the frequency spectrum was followed by imaging of slow brain activity with parallel multifrequency EIT and a subdural electrode mat serving as a proof-of-principle for slow EIT of physiologically evoked brain activity. The suitability of EIT for invasive functional imaging of the brain was assessed in the context of the practicality and the intricacies of the imaging set-up, data collection and accuracy.

3.1.1 Background

Imaging of slow neural changes in the brain evoked upon its regional activation is the mainstay of functional neuroimaging. The current gold-standard in neuroimaging field, BOLD-fMRI, utilises activity-related blood oxygenation changes as an endogenous marker of localised increase in neuronal activity. Although indirect, this way of measuring brain activity has recently reached a spatiotemporal resolution of tens of milliseconds and hundreds of micrometres in high magnetic field rodent studies (Jung et al., 2021). The remarkable increase in the temporal accuracy of fMRI has brought it closer to the resolution of the electrophysiological neuroimaging techniques providing a direct representation of brain activity over time.

However, the use of fMRI in research is still limited. The equipment is expensive and stationary; therefore, task-based behavioural neuroscience studies which often employ rodent models cannot be performed. This leaves an unmet need for an inexpensive and portable imaging technique with a comparable spatial and temporal resolution which could be used in place of fMRI for functional neuroscience studies with rodent models.

EIT of slow brain activity can potentially fulfil these criteria. As evidenced by the results from Chapter 2, non-invasive slow EIT is not currently possible due to insufficient SNR. However, EIT with electrodes placed directly on the surface of the brain could provide a necessary increase in the SNR to yield high resolution images of slow impedance changes produced by localised fluctuations in CBV. In behavioural studies with rodents, a wide cranial window could be opened for implanting an epicortical electrode array and then carefully closed by replacing the skull and/or suturing the opening. A similar method is widely applied for chronic brain imaging with such techniques as optical microscopy or photoacoustic imaging during mobile tasks (Czajkowski et al., 2014; Scott et al., 2018; Wang et al., 2021). EIT for intracranial imaging of slow brain activity could be arranged in a similar principle but yield fMRI-like images with a mesoscopic resolution.

3.1.1.1 Summary of the previous studies

The only successful invasive EIT imaging study which depicted spatiotemporal evolution of slow impedance changes during physiological brain activity was performed in anaesthetized rabbits (Holder et al., 1996). The study utilised an intracranial ring of electrodes, which, therefore, required a large craniotomy. To the authors' surprise, the images of brain activity following visual and somatosensory stimulation showed both decreases and increases in brain impedance which were localised to the active brain region and surrounding areas, respectively. While resistivity decreases could be easily attributed to the pooling of cerebral blood in the activated cortical area, the concurrent drops in impedance in the neighbouring regions were of unknown origin. This study was not followed up with further investigations as the technique was invasive and required prolonged averaging of evoked responses for acquisition of a single EIT image.

The above study was performed with an initial EIT prototype, Sheffield Mark 1, which assumed a 2D imaged object and employed a crude back-projection reconstruction algorithm. Since then, significant advances have been made in the imaging methods, including improvements in hardware, intracranial electrode design and more sophisticated 3D image reconstruction algorithms. These approaches enabled more accurate visualisation of slow neural changes in the rat brain during ictal and interictal activity but not, until now, physiologically evoked brain activity (Hannan et al., 2021; Vongerichten et al., 2016). These studies used epicortical arrays with 30 – 57 contacts, therefore, also required a wide cranial window to implant the electrodes. These studies showed a pronounced slow rise in impedance in epileptogenic brain tissue which reflected transient cell swelling in response to an abnormally aggravated neuronal activity (Olsson et al., 2006). Therefore, any impedance changes due to the redistribution of cerebral blood flow and volume were likely to be overwhelmed by a much larger shift in water balance from the extra- to intracellular space resulting in an overall local increase in brain impedance.

3.1.1.2 Limitations of the previous research and Rationale

There are several deficiencies of the previous studies which are addressed in this study. First, as discussed in Chapter 2, the carrier frequencies used for EIT of slow changes during both pathological and physiological brain activity might have been suboptimal. Second, all three previous studies used a serial data acquisition system which multiplexed the injection pairs sequentially and, therefore, required averaging of the recorded activity (Hannan et al., 2021; Holder et al., 1996; Vongerichten et al., 2016). Third, whilst imaging of intracerebral slow changes associated with epileptic activity was performed using updated 3D reconstruction methods, slow neural activity during evoked responses in rabbits was imaged in 2D using a back-projection algorithm. Lastly, no study to date comprehensively characterised slow neural changes following evoked activity in the rat brain using updated hardware and epicortical electrodes.

In this study, the use of a parallel data acquisition system is proposed for imaging slow brain activity to shorten the recording time. Frequency-division multiplexing EIT has been previously investigated for imaging slow neural activity in a swine model of epilepsy with a combination of subdural and depth electrodes (Witkowska-Wrobel et al., 2021). Images of seizure propagation with a temporal resolution of seconds were reconstructed in real time. However, the use of penetrating depth electrodes was a major limitation of this study restricting its translatability to a confined population of surgical epilepsy patients with already implanted intracranial electrodes. The current study aimed to extend the application of parallel EIT with epicortical electrode arrays for recording slow changes induced by physiological brain activity in a rat model of physiologically evoked responses. If successful, this could provide a system suitable for producing fMRI-like images in real time without the need for averaging. This type of imaging paradigm could be used for cognitive and behavioural neuroscience studies in rodent models. Compared to fMRI, EIT studies would provide a convenient low-cost option for repeated imaging with chronically implanted subdural electrodes over several months.

3.1.1.3 Expectations based on previous studies and modelling

Based on the results of the study in Chapter 2, the expectation was that the surgical ablation of the scalp, the skull and the dura with subdurally circulating CSF would increase the signal by at least 100 times. To verify these predictions, forward modelling of the boundary impedance measurements at the cortical surface was conducted prior to this study by a fellow PhD student Kai Mason. As in Chapter 2, a conductivity perturbation of 1 % was inserted into a forelimb region of S1 in an anatomically realistic rat brain mesh segmented from a CT scan. The simulation predicted a maximal impedance change of -0.1 % at the epicortical electrodes. A 25 times larger signal, compared to that on the scalp electrodes, coupled with an improved quality of recording electrode contact was expected to yield a sufficient SNR within at least half the averaging time used for scalp recordings.

3.1.2 Purpose

The purpose of this study was to image slow impedance changes in rats during evoked brain activity with EIT and epicortical electrodes. Questions to be answered were: (1) What are the characteristics of epicortically recorded single-channel slow impedance changes in response to evoked somatosensory activity? (2) What is the optimal carrier frequency yielding the best SNR for recording slow neural activity from the cortical surface? (3) Can slow neural changes be reliably and reproducibly imaged using parallel multifrequency EIT and epicortical electrodes?

3.1.3 Experimental Design

Experiments were conducted in 13 anaesthetised rats. Seven rats were used during the method development phase for collecting preliminary data and for performing control experiments. Once an optimal experimental protocol and method was achieved, eight full frequency sweeps spanning 200 Hz – 10 kHz were obtained in three rats. Three successive frequency sweeps were performed in the first and in the second rat. Two spectral sweeps were conducted in the last rat. Once the single-channel impedance data was analysed, additional three rats were used for collecting EIT images with a parallel data collection system. Four EIT recordings were obtained in the first and in the second rat. Five recordings were collected in the third rat. All voltage measurements were undertaken using a 57-electrode epicortical array implanted on one hemisphere.

Somatosensory activity was evoked by electrical stimulation of the rat's forepaw at 11 Hz administered in the same boxcar design described in Chapter 2 (5 s OFF – 2 s ON – 13 s OFF). Single-channel impedance changes were recorded at five carrier frequencies, namely 200 Hz, 500 Hz, 1 kHz, 5 kHz, and 100 kHz. The lower frequency band was chosen as in the previous study (Chapter 2). The upper frequency limit was defined by the specifications of the amplifier used for data collection. Current injection pairs were selected *ad hoc* in each rat based on the electrode detecting the largest SEP which was considered to mark the centre of the ROI (Fig. 3.1). To maximise the injected current density in the active region, current was applied between the electrodes on the diametrically opposite regions of the ROI. The duration of individual single-channel impedance recordings was optimised based on the noise in the preliminary data which showed that 50 epochs were enough to yield a minimum SNR of 4 on the most sensitive contacts.

Slow neural changes were imaged using a parallel EIT system which utilised 20 simultaneous injection pairs centred around 5 kHz and separated by approximately 50 Hz. This narrow bandwidth was possible as these slow changes occurred over several seconds. Thus, a bandwidth of ±10 Hz around each carrier frequency permitted accurate characterisation of slow impedance changes over time. The centre frequency of 5 kHz was chosen for parallel EIT due to significantly higher SNR of significant positive impedance changes at this carrier compared to the other tested frequencies in the single-channel impedance recordings. The injection protocol was optimised as per Faulkner et al. (2017) and concentrated the maximal current density in the ROI, that is, forelimb S1 area, according to the coordinates in the rat brain atlas (Paxinos & Watson, 2013). The recording duration was doubled (100 averages) to account for expected increase in noise due to multiple simultaneous injection pairs.

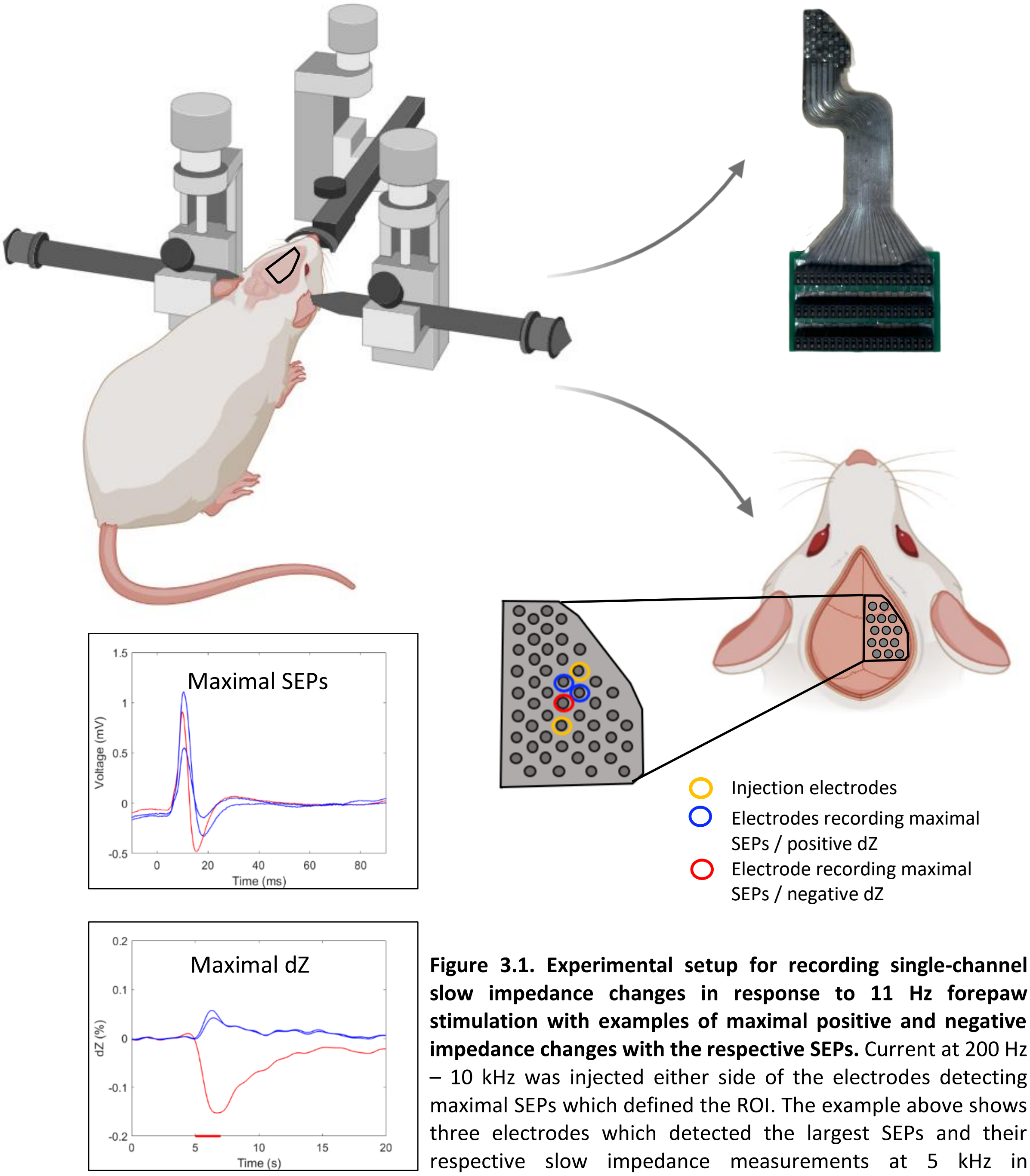

Figure 3.1. Experimental setup for recording single-channel slow impedance changes in response to 11 Hz forepaw stimulation with examples of maximal positive and negative impedance changes with the respective SEPs. Current at 200 Hz – 10 kHz was injected either side of the electrodes detecting maximal SEPs which defined the ROI. The example above shows three electrodes which detected the largest SEPs and their respective slow impedance measurements at 5 kHz in corresponding colours. Figure created with BioRender.com

3.1.3.1 Controls

A series of controls were performed to ensure that the observed impedance changes were not confounded with known data artefacts.

The current level control was conducted to investigate whether the size of the observed impedance changes was independent of the injected current level. According to Ohm's law, raw impedance changes (expressed in microvolts; dV, µV) should increase proportionally to the injected current while the proportional impedance changes normalised to the standing voltage of the recording electrode (expressed in percent; dZ, %) should stay flat across current levels. Violation of this relationship might indicate that the observed impedance changes were artefactual.

Two experiments were conducted to check for artefacts arising from evoked activity. A simulation analysis was designed and conducted by a fellow student Kai Mason to investigate whether the forepaw SEPs were independently modulating the carrier signal in a way that would yield an artefactual impedance change through imperfect signal processing. Furthermore, a potential phase-coupling between the SEPs and the carrier signal was investigated by manipulating the forepaw stimulation frequency ±0.5 Hz. The underlying hypothesis was that the evoked responses phase-coupled to the carrier wave could produce an artefactual impedance change through data filtering.

The presence of a stimulation artefact, a known confounding factor in animal and human studies of evoked responses, was checked by performing impedance recordings in a dead rat. Slow impedance changes in the absence of physiological responses would suggest that the recorded signal arose from the stimulus current electrically conducted from the forepaw to the epicortical array.

The myogenic artefacts were also evaluated by introducing neuromuscular blockade which eliminated any involuntary muscle contractions potentially producing artefactual impedance changes in the recorded signal.

Lastly, recordings were performed and compared under two different anaesthetics, namely isoflurane and urethane, to ensure that the features of the observed slow impedance changes were not anaesthetic-dependent. The rationale for this control was based on known differences in the shape and the spatiotemporal characteristics of the SEPs under different anaesthetics (Huttunen et al., 2008; Rojas et al., 2006). I hypothesised that slow impedance responses might exhibit a similar tendency and, therefore, the recordings were collected both under an inhalational (isoflurane) and an injectable (urethane) anaesthetic to account for their different pharmacokinetics and effects on the CNS.

3.1.3.2 Parallel EIT system

To image slow impedance changes during evoked brain activity, a parallel EIT system which employs frequency-division multiplexing was chosen. This system was designed by a fellow PhD student Adam Fitchett and manufactured in-house. Serial current injection and data acquisition was not practicable due to a necessity for averaging impedance changes recorded with each injection pair (~15 - 30 min) to reach an acceptable SNR. With a typical EIT protocol comprising tens of injection pairs, a single slow EIT image frame would be serially acquired within several hours. Therefore, to increase the frame rate, EIT recordings were collected in parallel by simultaneously injecting multiple frequencies and recording the transfer impedances with the same electrodes. The principles and hardware requirements for the parallel EIT system are explained in Dowrick et al. (2015). The innovation of the system used in this study was a custom-made rack of five parallel current sources used for simultaneous injection of up to 30 frequencies centred around the selected frequency of 5 kHz.

3.2 Materials and Methods

3.2.1 Animal preparation and surgery

Adult Sprague-Dawley rats weighing between 300 – 450 g were used for all experiments in this chapter. During the method development stage and in the control experiments, seven rats were anaesthetised with an IP injection of 1.3 - 1.5 g/kg urethane. If an areflexic state was not achieved within 30 min, urethane was supplemented *ad hoc* up to a maximum total dose of 1.6 g/kg. Due to a high dose of irreversible injectable anaesthetic used in these experiments, SEPs could not always be detected in a consistent manner. This was attributed to the urethane's depressive effect on the CNS. For improved control of the achieved anaesthesia level in the frequency sweep experiments and in EIT imaging experiments, isoflurane was introduced instead. Six rats were anaesthetised in a Perspex box with 4 – 5 % isoflurane in 2 L/min O_2 and 0.5 L/min air. Endotracheal intubation was performed as detailed in section 2.2.1 to enable continuous delivery of the vaporised anaesthetic and supplemental gas. The endotracheal tube was sutured to the skin on the lower jaw for preventing extubation and connected to the Y-piece which enabled the delivery of isoflurane and supplemental gases. The animals were allowed to breath spontaneously or with the assistance of mechanical ventilation when needed (SAV04 Small Animal Ventilator, Vetronic Services Ltd., Abbotskerswell, UK) using a 50/50 % mixture of nitrous oxide (N_2O) /O_2 and 2 – 2.5 % isoflurane. The depth of anaesthesia was determined and continuously monitored by ensuring the absence of the pedal withdrawal and corneal reflexes. Cannulation of the right femoral artery was then undertaken to allow for the monitoring of the intra-arterial blood pressure (IBP). The right femoral vein was also catheterised to enable continuous administration of 0.5 – 1 ml/hr saline IV. Where IV access could not be gained, saline was administered IP via a butterfly needle. Throughout the duration of each experiment, ECG, IBP, heart rate, respiratory rate, end-tidal and inspired CO_2 were monitored using Vetronics Lightning monitor (Vetronic Services Ltd, Abbotskerswell, UK). The core body temperature was maintained and regularly sampled using a system described in section 2.2.1.

Following the femoral cannulations, the rats were fixed in a stereotaxic frame using ear bars which restrained the head movement in the horizontal and vertical axes (Narishige International Ltd, London, UK). The scalp was then shaved and incised incised horizontally at the base of the head followed by a cut along the midline to expose the skull. The epicranial aponeurosis and connective tissues were thoroughly removed with cotton buds. The right temporal muscle was subsequently separated from the skull and excised whilst cauterising the insertion site with a bipolar coagulation tool (Codman Malis CMC-II; Codman, Raynham, MA, USA). A trapezoidal craniotomy was performed on one hemisphere using a veterinary bone drill (Ideal Micro-Drill; Harvard Apparatus, Edenbridge, UK). To minimise bleeding from the bone, the skull was regularly washed with room temperature sterile saline. When the drill penetrated the soft bone, only warm (38^{o}C) saline was applied. The cranial window extended from 1 mm anterior to lambda to 5 mm posterior of bregma in AP axis and from 1.5 mm lateral to sagittal sinus to 3 mm lateral of the zygomatic arch in ML axis. These markings ensured that the cranial window was sufficiently large to fit the array but did not leave any regions of the exposed hemisphere uncovered. The excised bone fragment was removed using the micro-dissecting forceps whilst steadily grasping the opposite sides of the bone flap and slowly lifting to allow atraumatic separation of bone and dura. Durotomy was performed using a dura hook and micro-scissors whilst frequently irrigating with 38^{o}C artificial CSF (aCSF) solution (recipe from Sutherland et al., 2014). After the completion of the surgical procedures, the concentration of isoflurane was incrementally lowered to ~ 1 % before commencing the recordings.

A planar epicortical array containing 57 PEDOT-coated electrode contacts, 0.6 mm in diameter and 1.3 mm centre-to-centre distance, arranged in a trapezoidal geometry (detailed description in Faulkner, 2019) was implanted on the cortical surface using a micromanipulator (Narishige International Ltd., London, UK) and a custom-made holder. The array was then covered with a cotton wool ball soaked in warm aCSF and wrapped in cling film to retain the moisture on the brain surface. The array measured approximately 9 mm and 13 mm at its furthest edges along ML and AP axes, respectively, and was designed to conform around the temporal convexity of the brain allowing even contact with the exposed hemisphere. To avoid abrasion of brain surface, the array was not repositioned after the implantation. The reference and ground electrodes, made of Ag-AgCl and measuring ~8 mm in diameter, were placed under the nuchal skin with a separation distance of approximately 2 cm. Lastly, silver needle electrodes used for somatosensory stimulation were inserted into the contralateral forepaw. One electrode was positioned in between the third and the fourth digit whereas the second electrode was inserted through the middle of the ventral pads to ensure a reliable contact with the median nerve and the activation of a large region in the forelimb area of S1. In the muscle artefact control experiments, 1 mg/kg pancuronium bromide was infused IV prior to the start of the impedance recordings. All procedures were undertaken on a Nexus® optical table (Thorlabs Inc., Newton, NJ, USA). Animal handling and experimental work complied with the regulations set out by UK Home Office and detailed in the Animals (Scientific Procedures) Act 1986.

3.2.2 Hardware

Single-channel data was collected using the ScouseTom EIT system (Avery et al., 2017) including the actiCHamp EEG amplifier with 64 channels (Brainproducts GmbH, Gilching, Germany; see Appendix A for detailed specifications) and the Keithley 6221 current source (Keithley Instruments Ltd, Solon, OH, USA). The contralateral forepaw was stimulated using the NL800A stimulator (NeuroLog$^{\mathrm{TM}}$, Digitimer, Letchworth, UK) at a frequency of 11 Hz in 300 µs pulses which had an amplitude of 2 mA. Imaging was performed using a modified ScouseTom EIT system containing the same amplifier but a novel current source. This current source comprised a custom-made rack of five parallel current sources producing up to 30 separate currents. These current sources each contained six channels. Each channel consisted of a direct digital synthesiser generating a sinusoidal voltage (centred at zero) which was

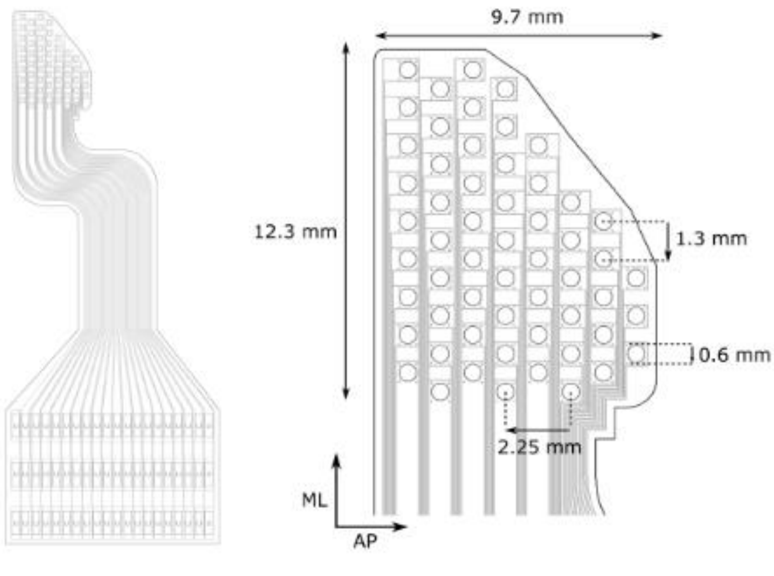

Figure 3.2. The design and dimensions of the epicortical electrode array used for this study. Array design and figure taken from Faulkner (2019).

filtered and then delivered as a sinusoidal current by a mirrored Howland current pump. This allowed for the generation of 30 separate currents separated by approximately 50 Hz with amplitudes up to 250 µA and a compliance of +/-3.3 V. Single-channel recordings were performed with a 57-electrode epicortical array manufactured from stainless-steel and silicone rubber with individual contacts coated with PEDOT:PSS (Fig. 3.2).

3.2.3 Data Collection

3.2.3.1 Frequency sweep of single-channel impedance recordings

In frequency sweep experiments, single-channel impedance recordings were collected at 200 Hz, 500 Hz, 1 kHz, 5 kHz, and 10 kHz. Frequencies were administered in random order in each rat and repeated twice in the first rat and three times in the subsequent rats yielding a total of eight comprehensive frequency sweeps. Electrodes for current injection were located either side of the electrode detecting the largest SEPs in each rat. The amplitude of the injected current was 50 µA when injection frequency was 200 Hz and 500 Hz and was increased to 100 µA for the remaining frequencies. Voltage changes were recorded on all electrodes in the array and digitised at 50 kHz. This yielded 57 voltage measurements per recording at each frequency in each rat. According to Ohm’s law, impedance was considered directly proportional to voltage due to injection of a constant current. Impedance herein refers to the magnitude of the complex impedance change. Since the phase angle of the nervous tissue at frequencies up to 10 kHz has previously been estimated <10°, the modulus of the complex impedance was considered representative of the resistive component as the influence of the capacitive component can be neglected at these phase angles (Faulkner et al., 2018a). Therefore, all voltage measurements collected during this study were represented as impedance recordings (dV, µV).

3.2.3.2 Controls

Current controls were performed by injecting a constant current oscillating at 1 kHz. The current amplitude was alternated between 10 µA, 25 µA, 50 µA, and 100 µA in a randomised order. Each recording comprised 50 – 100 epochs. The data was sampled at 50 kHz.

Forepaw stimulation control was performed by recording slow impedance responses to forepaw stimulation at 10.5 Hz, 11 Hz or 11.5 Hz delivered in the same boxcar paradigm as in the other slow impedance recordings. Each recording was obtained at a carrier frequency of 1 kHz and consisted of 100 epochs.

3.2.3.3 Imaging with EIT

Slow EIT images were collected whilst injecting a constant AC with an amplitude of 50 µA through 20 electrode pairs in parallel at frequencies 4.3 – 5.8 kHz. Individual injection pairs were spaced by ~50 Hz. Boundary voltage measurements were obtained on all electrodes in the array simultaneously. The current injection protocol was optimised such that the maximal current density was concentrated in the ROI, that is the forelimb region of the S1 (Faulkner et al., 2017). A full protocol, containing 20 injection pairs, was generated *de novo* in each rat after excluding saturated channels. Each voltage measurement was obtained by continuously recording impedance responses during successive 20 s-epochs of stimulation-rest (described in Chapter 2). Each EIT recording comprised 100 repeats which took ~40 min to collect.

3.2.4 Data processing and analysis

There was a total of 40 single-channel impedance recordings collected in three rats. This dataset consisted of eight sweeps at each of five carrier frequencies (200 Hz, 500 Hz, 1 kHz, 5 kHz, 10 kHz). In each of recording at each frequency, 57 impedance measurements were obtained by all available electrodes. Those impedance measurements were considered independent and with equal variance based on the analysis of the background noise, which was uncorrelated and had similar standard deviations. Collectively, all sweeps and recordings yielded 2280 independent impedance measurements available for further processing and analysis.

There were 13 parallel EIT recordings collected in another three rats. Each recording represented a single EIT image of averaged slow neural impedance changes following a 2-second somatosensory stimulation period.

Henceforth, the number of rats is represented by an uppercase ‘N’. In the context of single-channel recordings, a lowercase ‘n’ represents the number of independent impedance measurements. When discussing EIT images, a lowercase ‘n’ pertains to the number of discrete parallel EIT recordings.

3.2.4.1 Somatosensory evoked potentials

SEPs were extracted by averaging the raw impedance signal triggered off the repeated stimulus from all stimulation intervals in each single-channel recording. The averaged data was then filtered with a 100 Hz low-pass filter (5th order, Butterworth) if the recording was performed at 200 Hz and with 200 Hz low-pass filter (5th order, Butterworth) if the recording was performed at frequencies > 200 Hz. The SEPs with the largest amplitude across all channels within each recording were identified and averaged together to yield the mean SEP amplitude and latency. The data is displayed as a mean ± standard deviation (S. D.) between the SEPs extracted from individual recordings.

3.2.4.2 Single-channel impedance recordings

Data from each recording and each measurement electrode were first filtered with a 40 Hz band-pass filter (3rd order, Butterworth), 20 Hz each side of the carrier frequency. The data was then demodulated using the Hilbert transform and segmented into 20 s epochs as described in 2.2.3. Each epoch spanned from -5 to 15 seconds with the 0 s timepoint signifying the start of somatosensory stimulation. Epochs were subsequently filtered with 1 Hz low-pass filter (3rd order, Butterworth) to isolate voltage changes of the expected frequency (< 0.5 Hz). The epoch data was assessed for the presence of outliers which were removed from further analysis. An epoch was considered an outlier if it contained a data point that was greater than the upper quartile plus five times the interquartile range or less than the lower quartile minus five times the interquartile range. To account for the differences in the standing voltage between the electrodes, the change in voltage was normalised to the average amplitude of the carrier signal and expressed as a percent impedance change of the mean demodulated data (dZ, %) and normalised to the baseline (-5 to 0 seconds). Injecting electrodes and electrodes with a standing voltage of <1 mV were excluded from further analysis to avoid data from saturated channels. This eliminated 50 ± 0.5 % (mean ± S. D.) of independent impedance measurements collected in each recording from the available 57.

Electrodes detecting statistically significant positive or negative impedance changes with respect to baseline were then identified by statistical analysis. Statistically significant impedance changes with noise, defined as the standard deviation of the baseline, of >0.01 % were discarded to avoid false-positives from noisy data. The SNRs of the remaining impedance changes were computed by dividing the peak amplitude of impedance change by the noise. These impedance measurements obtained from individual electrodes were then grouped by injection frequency and the direction of change (positive or negative). The results show significant proportional impedance changes (dZ, %) from individual recording channels across all rats and all recordings. A mean (%) of these dZs ± S. D. between different impedance measurements is also displayed.

3.2.4.2 EIT recordings

The EIT recordings acquired with a parallel current injection protocol were first filtered around each carrier frequency using a ±10 Hz bandpass filter (4th order, Butterworth). The data was then processed in the same manner as the single-channel impedance recordings by demodulation and segmentation into 20 s-long epochs. The epochs were then filtered with a 1

Hz low-pass filter (3rd order, Butterworth) providing a minimal temporal resolution of 1 second. The filtered epochs from each recording channel and each carrier frequency were averaged yielding 1,140 transfer impedance measurements per EIT recording (20 current injection pairs x 55 recording electrodes). Impedance measurements from injecting channels were discarded from the dataset obtained at the corresponding carrier frequency. For reconstructing EIT images, the averaged data was downsampled and a change in impedance with respect to baseline was computed in 100 ms intervals across the whole epoch for each injection-measurement electrode combination. These impedance measurements were thresholded by the noise level in the bandpass filtered and averaged signal during periods of inactivity which included up to 5 seconds at the start and at the end of each epoch. The chosen noise cut-off value for the averaged impedance traces was between 0.3 – 0.4 µV achieved upon the application of a 20 Hz bandpass filter. This range was based on impedance measurements detecting the largest absolute impedance changes and which eliminated measurements with abnormal voltage spikes in inactivity periods. The raw, as opposed to proportional, voltage threshold ensured unbiased selection of transfer impedance measurements for reconstruction without excluding significant dZs from channels with a large standing voltage. The amplitude range of the positive and negative impedance changes detected across the remaining impedance measurements in all suitable EIT recordings obtained and expressed as a mean dZ (%) ± 1 S. D. between the maximal/minimal values across EIT recordings in all rats.

3.2.5 Simulation controls

A simulation analysis was conducted to assess for potential presence of an EP artefact. A 2 s section extracted from an EP recording obtained independently during one of the experiments was added to an artificially generated sine wave with a standing potential of 10 mV. The carrier was simulated to oscillate at frequencies between 100 Hz – 10 kHz at 100 Hz steps. The simulated signal was processed in the same way as the experimentally obtained impedance recordings. The resulting trace was inspected for any significant change that would resemble the shape and size of impedance changes observed in the impedance experiments. The apparent impedance changes induced by the EPs were quantified at each carrier frequency and plotted against the carrier frequency. The proportional changes were expressed in percent (dZ, %) by normalising to the mean amplitude of the carrier wave.

3.2.6 Image reconstruction

The forward solution of the boundary voltages which result from the injection and recording electrode combinations defined in the protocol was computed with the PEITS forward solver (Jehl et al., 2015) on an anatomically realistic FEM rat brain mesh composed of 3 million tetrahedral elements. Each boundary impedance measurement was obtained with reference to a 9 mm-diameter electrode positioned over the cerebellum. The mesh comprised three conductivity layers, namely grey matter, white matter, and CSF, with corresponding conductivity values of 0.3 S/m, 0.15 S/m and 1.79 S/m (Horesh, 2006). The inverse problem was solved by calculating and inverting the Jacobian matrix. The reconstruction was performed on a coarser mesh composed of 80,000 hexahedral elements with size of 300 µm using zeroth-order Tikhonov regularisation. Noise-based correction was performed upon selection of the regularisation parameter through generalized cross-validation (Aristovich et al., 2014). For visualisation, the reconstructed conductivity changes in each voxel were expressed as a significance Z-score of conductivity change ($Z_{\delta\sigma}$) (Mason et al., 2024). $Z_{\delta\sigma}$ was derived by dividing the reconstructed conductivity values by the standard deviation of the conductivity changes predicted to result from random Gaussian noise in the voltage measurements. Forward and inverse solutions were calculated on a research workstation (Dell Precision, Dell Inc., UK, 256GB RAM, 16 Intel Xeon CPU cores). It took 120 – 360 min to compute the forward solution and <10 min for the inverse solution per EIT recording.

3.2.7 Image analysis

Each EIT recording was analysed independently (n = 13 recordings, N = 3 rats). Any positive or negative impedance changes which occurred between the start (0 s) of the somatosensory stimulation and 10 s after the start were regarded as significant impedance changes. To visualise these changes, two thresholds were applied to the reconstructed conductivity Z-score values. Significant negative impedance changes were visualised by displaying voxels with positive $Z_{\delta\sigma}$ values which exceeded those reconstructed in the inactivity periods (defined in 3.2.4.2). Significant positive impedance changes were visualised by displaying voxels with negative $Z_{\delta\sigma}$ values exceeding those reconstructed in the inactivity periods. Presumed conductivity changes due to filtering artefacts in the raw voltage recordings were not considered.

After the thresholding, the start, the end and the peak activity times in each EIT recording were identified by visual inspection. To assess the spatial specificity of the reconstructed conductivity changes as well as their 3D propagation over time, the images were overlaid onto the anatomically accurate boundaries of the cortical volume occupied by the forelimb S1 (Faulkner, 2019).

3.2.8 Statistical analysis

3.2.8.1 Somatosensory evoked potentials

To assess whether the amplitude of the SEPs was different across injection frequencies, a one-way ANOVA test was conducted. The dataset contained the peak amplitudes of the maximal SEPs captured during each of the 40 single-channel impedance recordings (n = 40) performed in three rats (N = 3). A significance level of α = 0.05 was used for this analysis.

3.2.8.2 Impedance data

When assessing the statistical significance of the results, positive and negative impedance responses were treated independently. A significance level of α = 0.05 was used for all statistical analyses detailed below.

In all frequency sweeps and control recordings, significant impedance changes were determined by analysis of impedance measurements obtained by individual epicortical electrodes. A series of one-way t-tests were performed for each timepoint of the epoch across all epochs (50 – 100) acquired within each impedance measurement at each injection frequency or current level. The resulting p-values were adjusted with Bonferroni correction.

Four one-way ANOVA tests were performed to evaluate any statistically significant differences in impedance responses and their SNRs across frequencies: amplitude of positive dZs vs carrier frequency, SNR of positive dZs vs carrier frequency, amplitude of negative dZs vs carrier frequency, SNR of negative dZs vs carrier frequency. Where significant differences between frequencies were detected with one-way ANOVA, multiple comparisons were performed using a post-hoc Tukey-Kramer test. The datasets comprised the amplitudes of all significant positive and all significant negative impedance changes and their SNRs at each injection frequency across eight frequency sweeps in three rats. This yielded a sample size of n = 540 measurements of significant positive dZs and their respective SNRs from individual electrodes, and n = 62 significant negative dZs and their SNRs from individual electrodes.

To evaluate the correlation between the amplitude of the SEPs and the amplitude of the significant peak positive (n = 39 impedance measurements, N = 3 rats) and peak negative slow impedance changes (n = 39 impedance measurements, N = 3 rats), linear regression analyses were performed using the largest SEPs and the maximal impedance responses detected in each recording.

3.2.8.3 Controls

Current level control experiments were performed at 1 kHz injection frequency in two rats (N = 2 rats). Each current level, namely 10, 25, 50 and 100 µA, was tested twice in the first rat and once in the second rat. Significant impedance changes were identified on individual electrodes in each recording. A series of one-way t-tests were used to determined significant timepoints with respect to baseline within each impedance measurement. Type I error was controlled by performing Bonferroni correction of the resulting p-values. The proportional (%) amplitudes of significant dZs were then compared across different current levels using one-way ANOVA with post-hoc pairwise comparisons using a Tukey-Kramer test.

To assess the difference in the amplitude of impedance changes at different forepaw stimulation frequencies, one-way ANOVA was performed. The dataset comprised the amplitudes of all significant proportional impedance changes detected by individual electrodes at each stimulation frequency in one rat (n = 17 impedance measurements, N = 1 rat). A significance level of α = 0.05 was used for the analysis of all controls.

3.2.8.4 EIT images

The brain area with significant activity across rats was quantified by creating a binary mask for each EIT recording. Significant positive and significant negative impedance changes were evaluated separately. Mask pixel values of 1 were assigned to elements of the mesh which contained a conductivity Z-score value below the negative threshold or above the positive Z-score threshold for positive and negative impedance changes, respectively. Mask pixel values of 0 were assigned to the remaining elements which were considered to display background activity. Binary masks corresponding to each of 13 recordings were then summed together to obtain a significance map where the elements contained values ranging from 0 to 13. Significant activity was evaluated by computing the p-values for each pixel value in the sum of 13 binary masks:

(1) the p-values for the pixel values of 0 and 13 equalled the probabilities of all zeros and all ones occurring in the respective pixels across 13 repeats:

$$p = \left(\frac{1}{2}\right)^{13}$$

(2) the p-values for the summed pixel values of 1 – 12 were computed by multiplying the p-value calculated above by the number of all possible combinations of zeros and ones in that pixel across 13 binary masks yielding each intermediary pixel value:

$$p_k = \left(\frac{1}{2}\right)^{13} \times \frac{13!}{k!\,(13-k)!}$$

where k is a value between 1 to 12. Voxels with a summed value > 50 % of maximal and a p-value < 0.05 were considered to display common statistically significant activity. Voxels with a sum value of 0 represented significant inactivity.

3.2. Results

3.3.1 Characteristics of forepaw somatosensory evoked potentials at 11 Hz

Somatosensory stimulation of the contralateral forepaw at 11 Hz evoked consistent SEPs in each recording detectable within 1.5 mm radius of the most sensitive electrode which displayed the largest SEP. This area was considered to define the ROI. All SEPs were composed of two sequential positive and negative peaks (Fig. 3.3). The mean latency of the maximal SEPs detected across all impedance recordings was 10.1 ± 0.5 ms (mean ± S. D.). The average amplitude of the initial peak was 0.32 ± 0.02 mV (mean ± S. D.). There was no significant difference in the amplitude of the maximal forepaw SEPs recorded at different carrier frequencies (p > 0.05, one-way ANOVA).

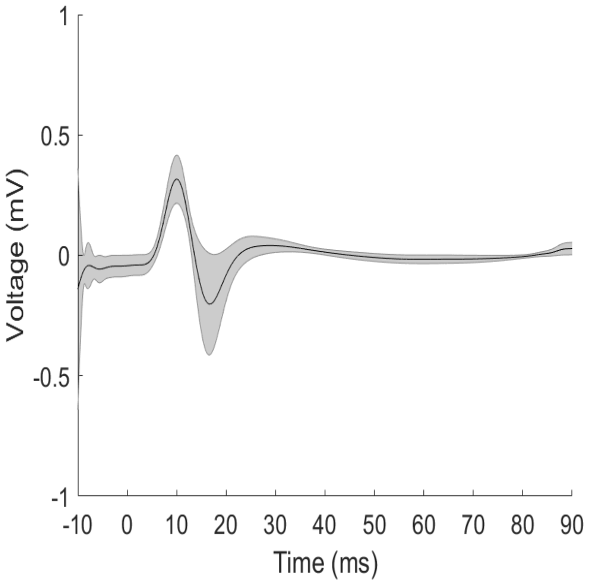

Figure 3.3. Somatosensory potential evoked by 11 Hz stimulation of the contralateral forepaw. The average amplitude of the maximal forepaw SEPs was 0.32 ± 0.02 mV (mean ± S. D.).

3.3.2 Characteristics of single-channel impedance responses across frequencies

Significant positive and negative slow impedance changes were observed in response to electrical stimulation of the forepaw in three rats across all carrier frequencies in 602 out of 2280 impedance measurements ($p < 0.05$, one-way t-tests with Bonferroni correction; Fig. 3.4). Overall, significant positive changes were more abundant than the negative ones with the former comprising 90 % of impedance measurements with significant changes ($n = 602$ impedance measurements, $N = 3$ rats; Fig. 3.4). The mean amplitude of all significant positive changes was 0.049 ± 0.045 % (range 0.012 – 0.361 %; $n = 540$ impedance measurements, $N = 3$ rats) whereas the mean amplitude of all significant negative changes was -0.093 ± 0.055 % (range -0.022 – -0.233 %; $n = 62$ impedance measurements, $N = 3$ rats) across carrier frequencies. However, when comparing only the peak impedance changes detected within the same single-channel recordings, the magnitude of impedance increases was consistently larger than the magnitude of impedance decreases irrespective of the carrier frequency ($n = 78$ impedance measurements with peak positive/negative changes, $N = 3$ rats; $p < 0.001$, paired sample t-test).

The observed slow impedance changes following sensory stimulation could be characterised by a rapid onset which occurred within one second from the start of the somatosensory stimulation, a sharp peak 1.3 – 1.6 s after the start of the stimulation and a slow return to baseline (Fig. 3.4). Positive changes subsided faster than negative ones with an average duration of seven and ten seconds, respectively

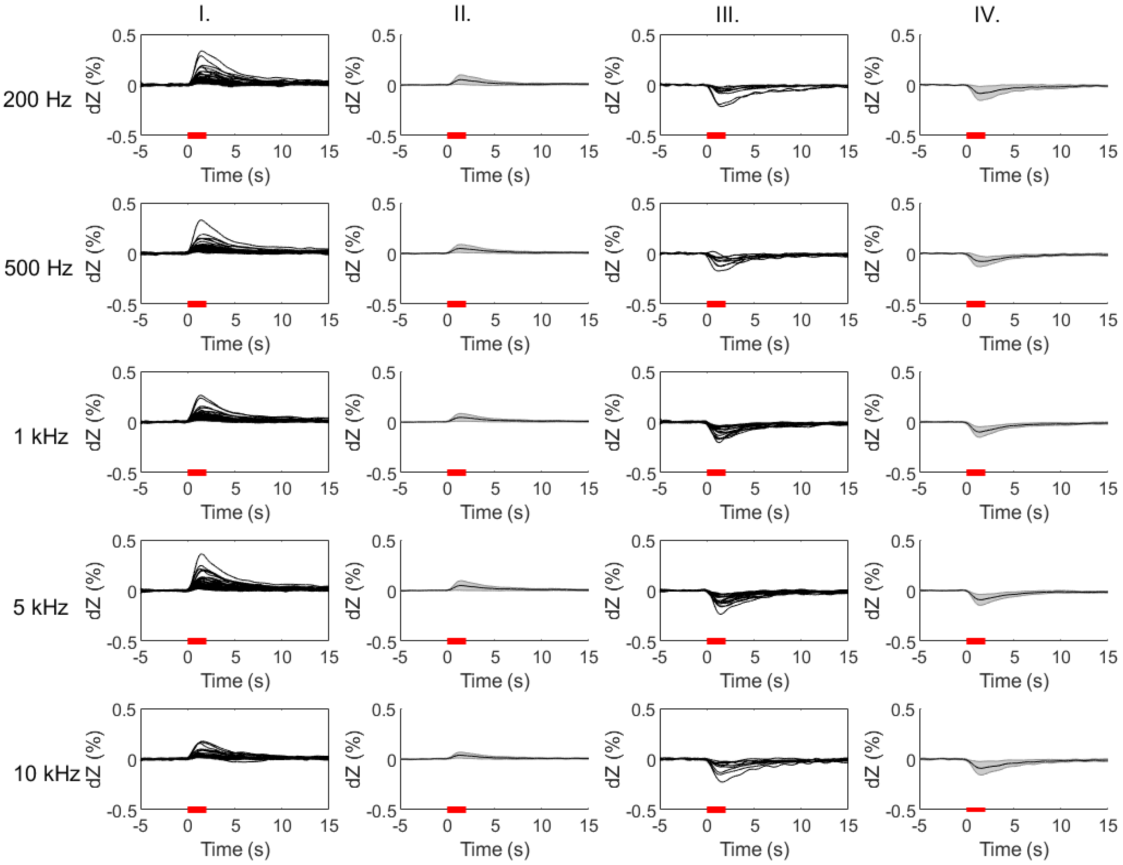

Figure 3.4. Positive and negative slow impedance changes in the rat brain following evoked somatosensory forepaw activity at injection frequencies of 200 Hz – 10 kHz. Column I contains all significant positive single-channel impedance measurements obtained at 200 Hz (n = 113 measurements), 500 Hz (n = 105), 1 kHz (n = 107), 5 kHz (n = 126) and 10 kHz (n = 89) injection frequencies across 39 sweeps in three rats (N = 3 rats; $p < 0.05$, one-way t-tests with Bonferroni correction). Column II shows all significant negative single-channel impedance measurements obtained at 200 Hz (n = 9 measurements), 500 Hz (n = 9), 1 kHz (n = 16), 5 kHz (n = 19) and 10 kHz (n = 9) across 39 sweeps in three rats (N = 3; $p < 0.05$, one-way t-tests with Bonferroni correction). Columns II and IV represent the mean ± S. D. (grey area) of these positive and negative impedance changes. There was no statistically significant difference between the amplitudes of significant positive and negative impedance changes between frequencies ($p > 0.1$ and $p > 0.5$, respectively; one-way ANOVA). The red band in the graphs represent the period of somatosensory stimulation.

3.3.3 Frequency response of slow impedance changes and their SNR

There was no statistically significant difference in the amplitude of neither positive, nor negative slow impedance changes between different carrier frequencies ($p > 0.1$, one-way ANOVA tests).

On the other hand, whilst there was no statistical difference in the SNR of the negative impedance changes across frequencies ($p > 0.1$, one-way ANOVA), the SNR of the positive ones depended significantly on the injection frequency ($p < 0.001$, one-way ANOVA). Multiple comparison post-hoc analysis showed that the SNR was significantly greater at 5 kHz than 200 Hz, 500 Hz and 10 kHz ($p < 0.001$, Tukey-Kramer post-hoc test) but not when compared to 1 kHz ($p > 0.1$, Tukey-Kramer post-hoc test). On the other hand, the SNR at 1 kHz was significantly higher than the SNR at 10 kHz ($p < 0.001$, Tukey-Kramer post-hoc test) but not at 200 Hz or 500 Hz ($p > 0.1$, Tukey-Kramer post-hoc test).

3.3.4 Relationship between the SEP amplitude and the magnitude of slow impedance changes

A linear regression analysis showed that there was a significant correlation between the amplitude of the SEPs and the amplitude of the maximal positive impedance changes ($n = 39$ impedance measurements, $N = 3$ rats, $p < 0.001$; Fig. 3.5A). A linear fit could explain >50 % of variability in the dataset ($R^2 = 0.56$). In contrast, negative impedance changes did not display a linear relationship with the size of the SEPs ($n = 39$, $N = 3$; $p > 0.05$; $R^2 = 0.06$; Fig. 3.5B).

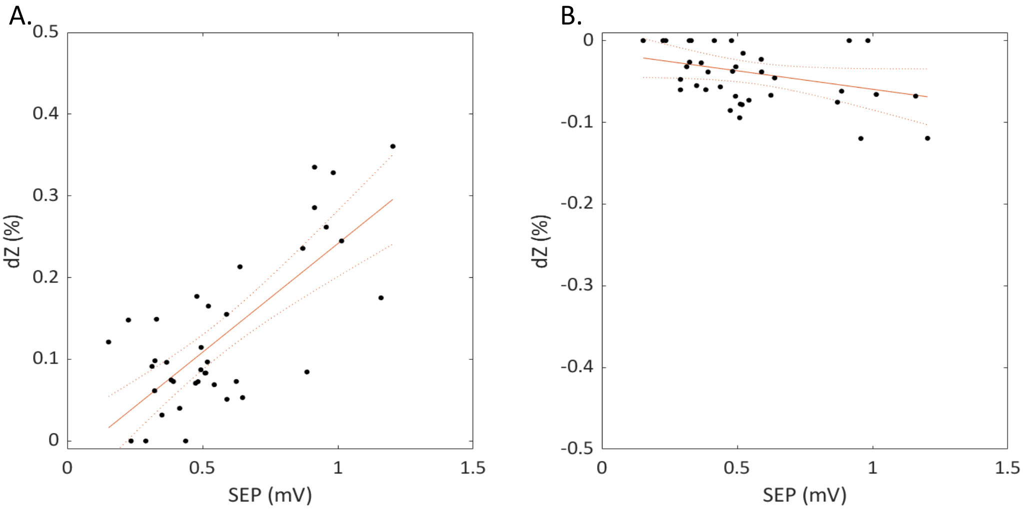

Figure 3.5. The amplitudes of positive, but not negative, slow impedance changes following somatosensory forepaw activity were linearly dependent on the size of forepaw SEPs at the time of recording. The plots demonstrate the relationship between the size of the maximal SEP and the size of the corresponding maximal positive (A) and the maximal negative (B) slow impedance changes from the same recordings. Slow impedance increases were positively correlated with the amplitude of forepaw SEPs ($p < 0.001$, $R^2 = 0.56$; $n = 39$ impedance measurements, $N = 3$ rats) whereas slow impedance decreases displayed no significant relationship with evoked responses ($p > 0.05$, $R^2 = 0.06$; $n = 39$ impedance measurements, $N = 3$ rats). The red line shows the best linear fit of the data.

3.3.4 Controls

3.3.4.1 Current level control

Between 10 – 100 µA, the level of injected current did not significantly impact the amplitude of the positive slow impedance changes (n = 133 measurements, N = 2 rats; p = 0.05, one-way ANOVA; Fig. 3.6). More detailed pairwise comparison showed that the difference in the size of the detected positive changes between the lowest and the highest current levels was close to the limit of statistical significance (n = 58 measurements, N = 2 rats; p = 0.04, Tukey-Kramer post-hoc test; Fig. 3.6). However, no differences were detected between 25 – 100 µA (n = 75 measurements, N = 2 rats; p > 0.05, Tukey-Kramer post-hoc test). Similarly, the amplitude of the negative impedance changes stayed flat between 25 – 100 µA (n = 29 measurements, N = 2 rats; p > 0.5, one-way ANOVA; Fig. 3.6). Negative impedance responses at 10 µA could not be examined due to an insufficient sample size of significant negative changes at this current level (n = 1).

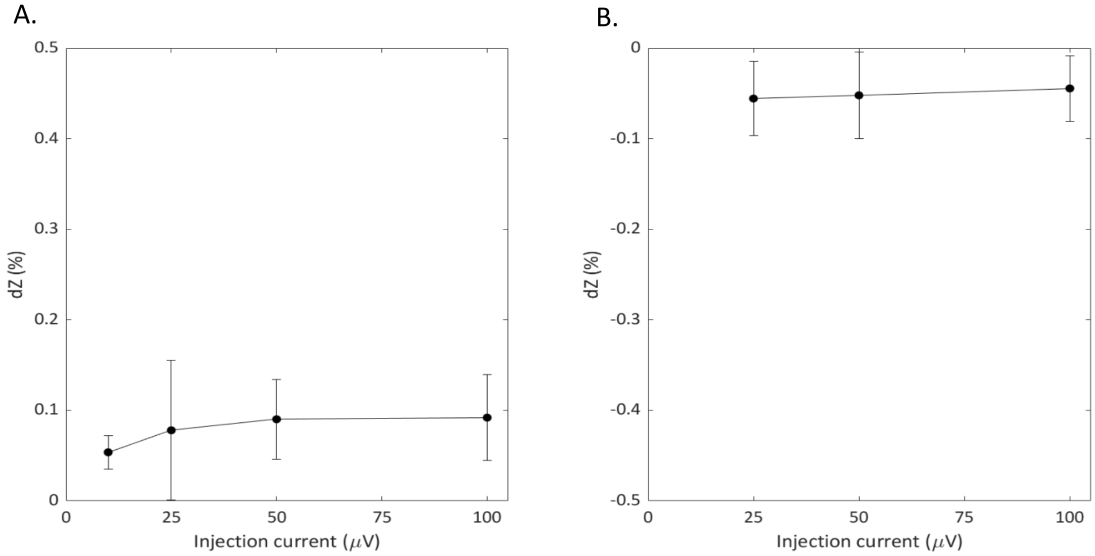

Figure 3.6. The peak amplitude of significant positive (A) and negative (B) slow impedance changes did not depend on the injected current level. (A) The plot shows the mean of significant positive dZs ± S. D. identified in 133 out of 660 single-channel impedance measurements across two rats (n = 133, N =2). There was no significant difference between positive impedance changes detected at different injection current amplitudes (p = 0.05, one-way ANOVA). (B) The plot shows the mean of significant negative dZs ± S. D. detected in 29 out of 660 single-channel impedance measurements across two rats (n = 29, N =2). Negative impedance changes did not differ when injection current increased between 25 – 100 µA (p > 0.5, one-way ANOVA).

3.3.4.2 *Simulation of SEP artefact*

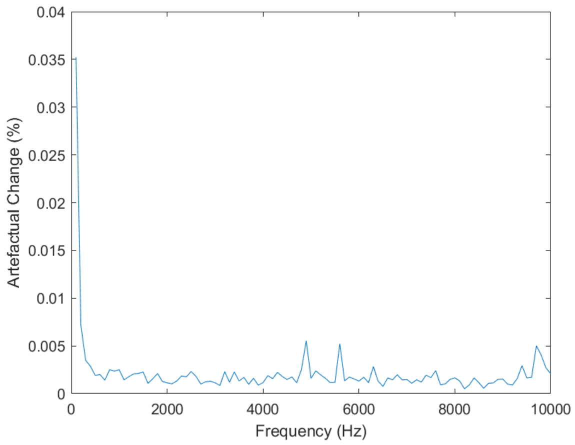

Figure 3.7. The relationship between the size of the EP artefact and the frequency of the simulated carrier signal. The size of the EP artefact was normalised to the amplitude of the simulated carrier signal of 10 mV and expressed in percent.

A quantitative analysis of the simulated modulation of the carrier signal by an SEP showed that EP contribution to the observed slow impedance change was largest at the carrier frequency of 100 Hz and dropped sharply at higher frequencies (Fig 3.7). For a simulated standing voltage of 10 mV, the largest EP-induced impedance change was 0.035 % at 100 Hz. Beyond 100 Hz, the EP-induced artefactual impedance changes did not exceed 0.0050 % which was > 5 times smaller than the smallest impedance change observed in this study.

3.3.4.3 *SEP-carrier signal coupling control*

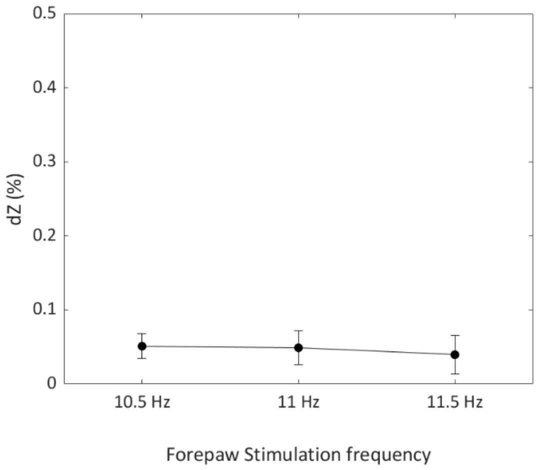

Figure 3.8. The amplitude of slow impedance changes was not affected by variation in stimulation frequency. The plot shows the mean dZ amplitude ± S. D. of significant positive impedance changes detected in response to forepaw stimulation at 10.5, 11 and 11.5 Hz (n = 17 impedance measurements, N = 1 rat). There were no statistically significant differences between these groups (one-way ANOVA, p > 0.5).

17 significant positive impedance changes were detected across 165 impedance measurements in one rat from recordings at 10.5 Hz, 11 Hz, 11.5 Hz forepaw stimulation frequencies (n = 165 measurements, N = 1 rat; one-way t-tests with Bonferroni correction, $p < 0.05$). No significant negative impedance changes were detected in these recordings (n = 165 impedance measurements, N = 1 rat; one-way t-tests with Bonferroni correction, $p < 0.05$). The magnitude of significant impedance changes did not change with the stimulation frequency (one-way ANOVA, $p > 0.5$; Fig. 3.8). Qualitative evaluation of the other electrographic characteristics of the detected impedance changes, such as the shape, the latency, and the duration, confirmed no apparent differences between the slow impedance changes evoked at different stimulation frequencies.

3.3.4.4 Dead rat control

There were no significant slow impedance changes following somatosensory forepaw stimulation in a dead rat at any of the tested injection frequency (n = 165 impedance measurements, N = 1 rat; one-way t-tests with Bonferroni correction, p > 0.8).

3.3.4.5 Muscle artefact control

The magnitude of significant slow impedance changes did not change after the administration of a paralysing agent when compared to slow changes detect prior to neuromuscular blockade (n = 11 impedance measurements, N = 1 rat; one-way t-tests with Bonferroni correction, p > 0.5). Moreover, there were no qualitative differences in the appearance and the spatiotemporal pattern of these slow changes.

3.3.4.6 Anaesthetic control

Visual inspection and qualitative comparison of significant slow impedance changes recorded under isoflurane and under urethane anaesthesia throughout the study confirmed no differences in the electrographic presentation of the observed impedance changes between the anaesthetics.

3.3.4 EIT images of slow neural activity

EIT images of slow neural activity during somatosensory forepaw response showed reproducible positive and negative impedance changes in all rats (Fig. 3.9). Peak positive and negative voltage changes used for image reconstruction ranged respectively between 2.6 – 8.4 μV and -1.4 – -3.5 μV with corresponding proportional dZ values of 0.031 – 0.11 % and -0.049 – -0.38 % (n = 13 recordings, N = 3 rats). Examples of successive reproducible slow EIT recordings with images of peak activity from one rat are shown in Fig. 3.9.

Bidirectional slow changes in the ROI developed concurrently (Fig. 3.10). The onset time varied between 0.4 – 0.7 seconds with activity peaking 2.0 – 3.0 s after the start of somatosensory stimulation. Positive slow changes were more spatially confined and consistent than negative changes which were topographically dispersed. Spatiotemporal evolution of slow impedance changes reconstructed from individual EIT recordings in different rats is compared in Fig. 3.10.

Population statistics showed that only positive impedance changes were significantly co-localised across animals (Fig. 3.11). Common active voxels reliably featured slow neural activity in the posteromedial region of the forelimb S1. Significant increase in cerebral tissue impedance commenced at 0.9 s following the start of forepaw stimulation, peaked at 2 s, and completely subsided by 3.4 s post-stimulus. Activity developed only in the superficial layers of the cortex. No significant changes could be reconstructed in the subcortical structures.

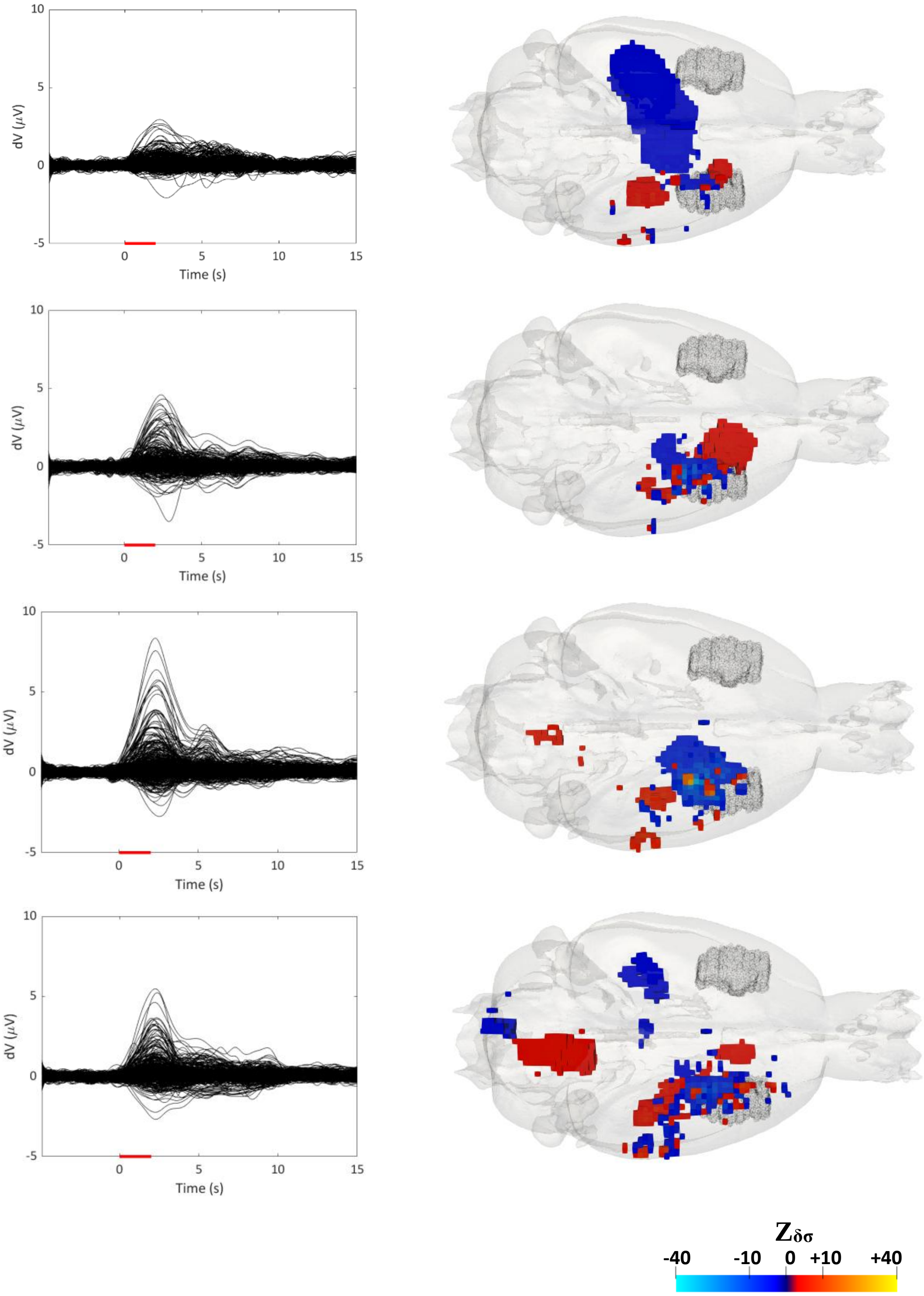

Figure 3.9. A representative example of reproducible transfer impedance changes recorded with a parallel EIT system following evoked forepaw activity in one rat with corresponding reconstructions of peak slow neural activity in EIT images. A consistent pattern of concurrent positive and negative voltage changes (dV, µV) with peak amplitudes of 2.6 – 8.4 µV (0.031 – 0.11 %) and -1.4 - -3.5 µV (-0.049 − -0.38 %) were recorded across rats (N = 13 recordings, n = 3 rats). These boundary voltage measurements translated into reproducible positive impedance changes in the forelimb S1 (blue) with more dispersed negative impedance changes in the surrounding areas (red). $Z_{\delta\sigma}$ represents the Z-score of the conductivity change reconstructed from the voltage measurements on the left-hand side. The black outline defines the boundaries of the forepaw S1. The red band on the x-axes of the plots signifies the period of somatosensory stimulation.

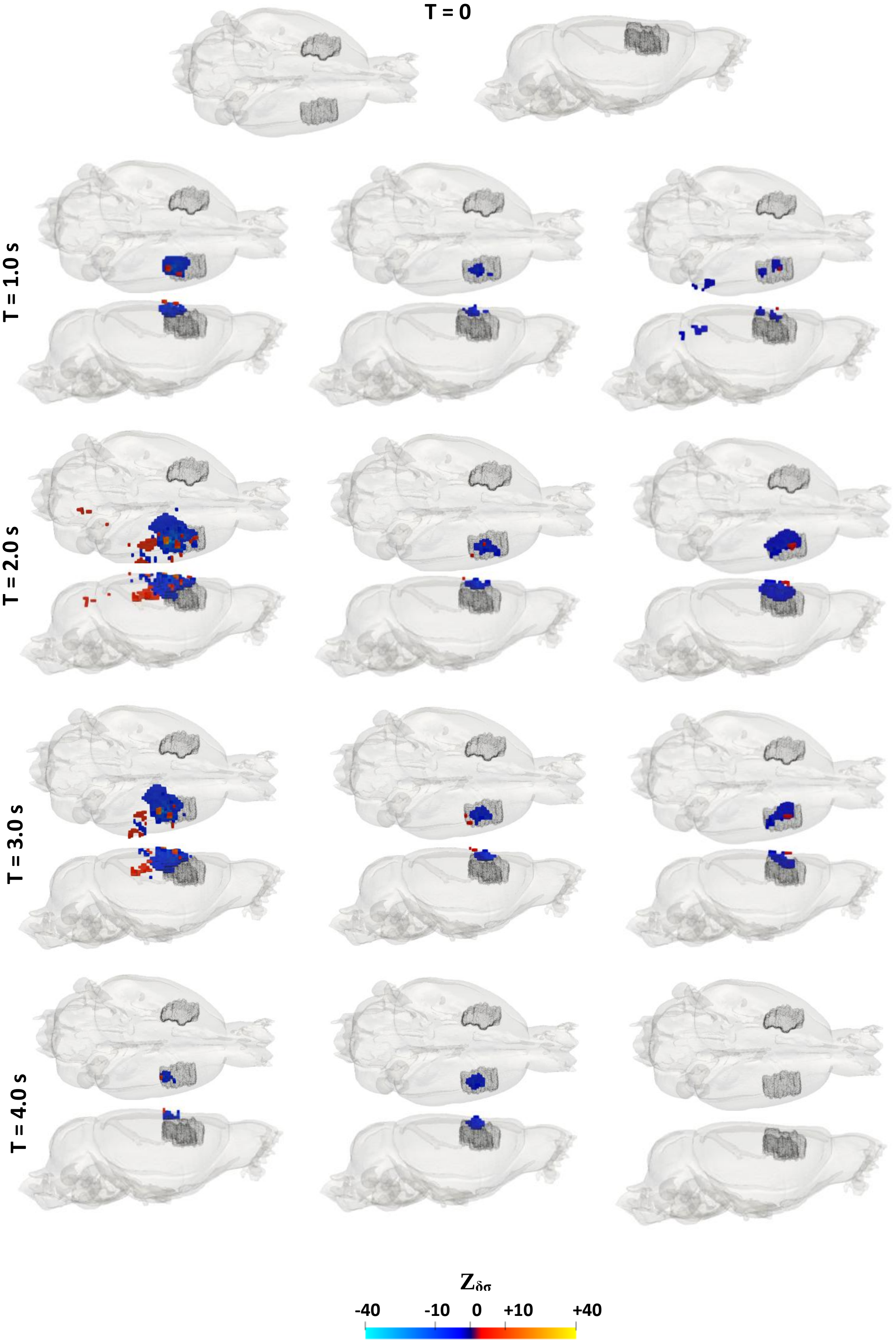

Figure 3.10. A reproducible spatiotemporal pattern of intracerebral slow impedance changes in response to 11 Hz somatosensory forepaw stimulation could be reconstructed in EIT images. Each column represents slow neural activity detected in different recordings from different rats across a series of timepoints (n = 3 recordings, N = 3 rats). The start of somatosensory stimulation is marked by 0 s. The black outline defines the boundaries of the forepaw S1. $Z_{\delta\sigma}$ represents the Z-score of the conductivity change.

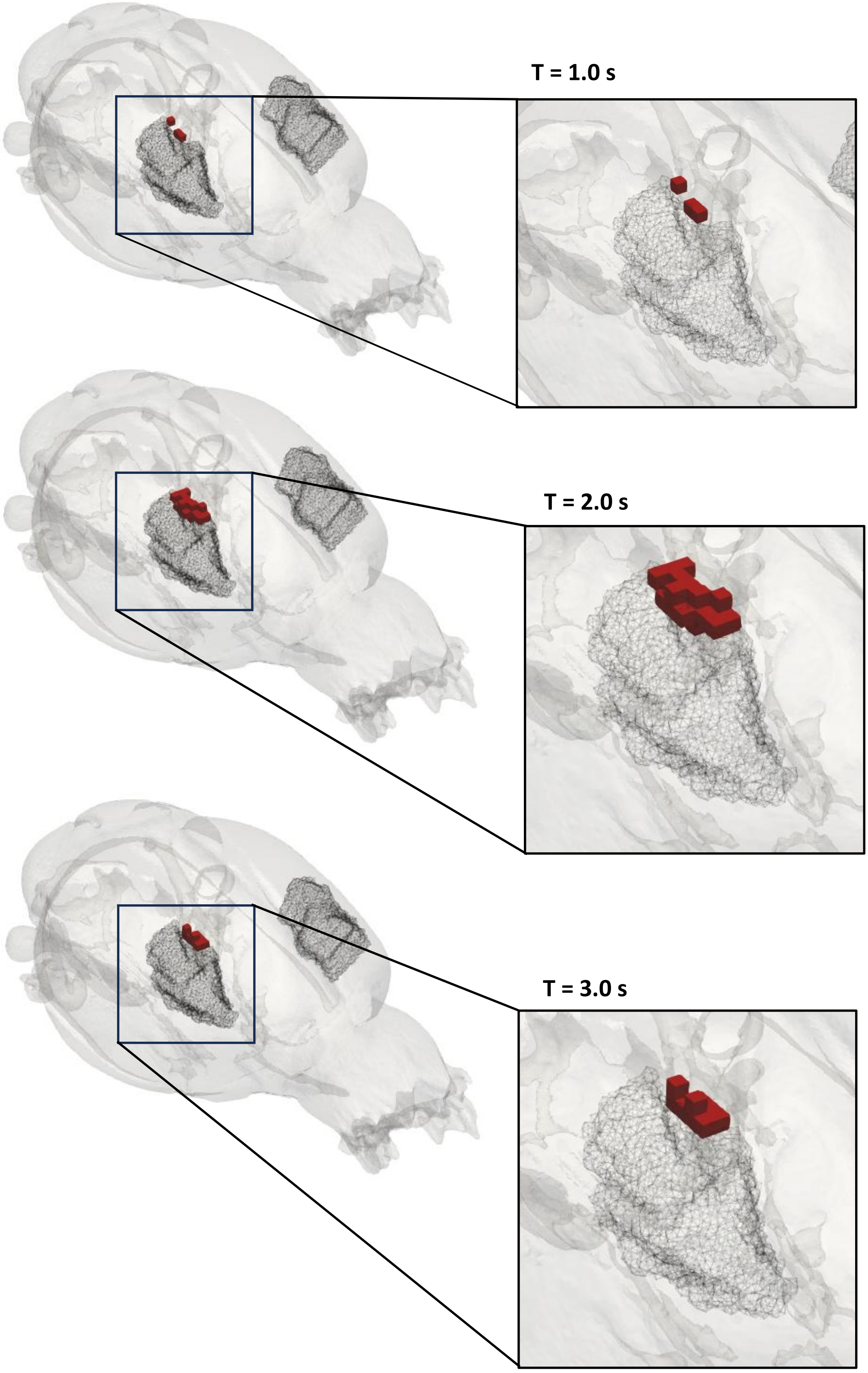

Figure 3.11. Population statistics of slow neural EIT images depicted a transient localised increase in cortical tissue impedance. Images display a time-series of common active voxels (shown in red) in the reconstructed $Z_{\delta\sigma}$ across all recordings in all rats ($p < 0.05$, $n = 13$ recordings, $N = 3$ rats). Activity was confined to a small sub-field of a forepaw S1 area (black mesh) with a slight eccentric spread in a transverse plane. Significant tissue conductivity change lasted for ~3 s (0.9 – 3.3 s from the onset of stimulation).

3.4 Discussion

3.4.4 Summary of results

The results of this study showed that both, positive and negative, slow impedance changes could be detected in single-channel impedance recordings with epicortical electrodes upon physiological stimulation of the rat brain. Regardless of the direction, the observed changes exhibited identical temporal and electrographic characteristics. The changes started and peaked within the course of somatosensory stimulation administered for 2 s and gradually approached baseline within 10 s post-stimulus (Fig. 3.4). The amplitude of both positive and negative changes was around +/- 0.1 % with no statistically significant difference between injection frequencies of 200 Hz – 10 kHz (Fig. 3.4). Positive impedance changes were more numerous across impedance measurements and, at their maximum values, were consistently larger than negative ones. Moreover, the SNR of positive changes significantly increased with injection frequency. The largest SNR was registered at 5 kHz which was subsequently chosen as a carrier frequency for parallel slow EIT. Cumulatively, these findings suggested that positive slow impedance changes were likely more physiologically relevant than negative ones; however, EIT imaging was necessary to confirm the updated hypothesis.

Following the epicortical characterization of intracerebral slow impedance changes, they were imaged using the parallel EIT system with frequency-division multiplexing and subdural electrodes ($n = 13$ recordings, $N = 3$ rats). EIT images showed a reproducible pattern of slow neural activity developing in and around the activated S1 region (Fig 3.9 and 3.10). Population statistics confirmed that only the slow impedance increase was consistent across the recordings in different rats ($p < 0.05$; Fig. 3.11). Common voxels with significant conductivity Z-score values highlighted a posteromedial portion of forelimb S1 which was active for ~3 s following the onset of stimulation (Fig. 3.11). As expected, negative impedance changes did not localise to the overlapping brain regions and, therefore, were unlikely to be physiologically meaningful. All in all, the findings of this study were not in agreement with the initial hypothesis that the imaged activity was of haemodynamic origin and implied an existence of slow changes in the cerebral tissue arising from an alternative neurophysiological pathway.

3.4.5 Technical considerations

3.4.5.1 Anaesthetics

Anaesthesia is known to have profound effects not only on the electrical brain activity but also cerebral perfusion which was initially hypothesised to produce the observed slow impedance changes. In this study, most data was acquired in rats anaesthetised with isoflurane as it allowed precise and continuous control of the depth of anaesthesia due to its fast pharmacokinetics (Yasuda et al., 1991). Isoflurane is an inhalable anaesthetic commonly used in rodent neuroimaging studies because of its versatile applicability to both terminal and recovery experiments. The main drawback of isoflurane is its tendency to suppress the electrical brain activity with distinct effect on the amplitude and the shape of evoked potentials (Porkkala et al., 1994; Rojas et al., 2006). Fortunately, the effect is dose-dependent and reversible because of the short half-life of isoflurane.

In addition to suppressing neural activity, isoflurane is a potent vasodilator leading to global changes in blood flow (Iida et al., 1998; Matta et al., 1999). Therefore, isoflurane anaesthesia can impact the size of the observed changes in CBF and CBV associated with localized brain activation. The effects of isoflurane anaesthesia on the haemodynamic parameters recorded during spontaneous or evoked brain activity have been examined in rats in multiple studies (Kim et al., 2010; Masamoto et al., 2007; Masamoto et al., 2009; Tsurugizawa et al., 2016). An isoflurane dose-dependent increase in the cortical blood flow following electrical forepaw stimulation was observed by Masamoto et al. (2009). Increase in the concentration of this anaesthetic from 1.1 % to 2.1 % resulted in more than doubling of the CBF (Masamoto et al., 2009). However, the effect appeared to also depend on the frequency of electrical stimulation shown in a separate study which compared CBF changes evoked by the stimulation of the rat's forepaw under isoflurane and α-chloralose anaesthesia (Masamoto et al., 2007). Low frequency stimulation (3 – 8 Hz) was shown to yield smaller CBF changes than higher frequency (~12 Hz) stimulation if the duration was adjusted to avoid neural adaptation (Kim et al., 2010; Masamoto et al., 2007; Sommers et al., 2009).

To balance the depressive effect of isoflurane on neural activity and its vasodilatory quality, in this study recordings were carried out after the isoflurane concentration was gradually reduced to ~1 %. A low level of isoflurane for maintaining appropriate depth of anaesthesia was enabled by the replacement of air vehicle with N_2O. Although some human studies reported a more pronounced suppression of evoked activity when isoflurane was used in combination with N_2O, this was not observed in this study (Pechstein et al., 1998; Porkkala et al., 1997). It was noticed that the effective isoflurane dose could only be reduced below ~1.5 % if N_2O vehicle was used. Moreover, the recordings were not commenced until at least 30 min after reducing the isoflurane concentration to allow its partial clearance from the brain (Wyrwicz et al., 1987).

Nonetheless, N_2O also displays effects on the vascular diameter and, when used in combination with isoflurane, can enhance cerebral perfusion (Algotsson et al., 1992). Therefore, if the slow impedance changes observed in this study were indeed caused by haemodynamic alterations, then the choice of the anaesthetic used for the single-channel recordings and EIT imaging might have exaggerated the magnitude of the response. Although the control single-channel recordings performed under urethane anaesthesia to compare the effect of two anaesthetics showed no differences in the electrographic features of the observed impedance responses, the known effects of N_2O and isoflurane on systemic blood pressure should be taken into account when interpreting the results of this study.

3.4.5.2 Placement of paw electrodes

The extent of the slow changes in brain tissue which accompany evoked neural activity is dependent on the proportion of activated neurons. This is determined by the location of the peripheral stimulation which is represented in the topographic arrangement of the forelimb S1 containing the somatotopic divisions representing each digit, dorsal and ventral surfaces of the paw (Waters et al., 1995). In this study, the needle electrodes were inserted in parallel with each other along the horizontal axis of the paw such that the maximal excitation of the median nerve was achieved during the forepaw stimulation. In this way, the maximal area in the forelimb S1 was expected to be activated and, consequently, yield the largest haemodynamic change. However, minor inconsistencies in the placement of needle electrodes between rats could have resulted in the activation of unequal regions in the S1 which could have impacted the size of the detected impedances changes due to inconsistencies in the populations of neurons involved in the response. These inaccuracies could have contributed to the large variance in the amplitude of the detected impedance changes across rats which ultimately rendered the results between the different frequencies not statistically significant.

3.4.6 Answers to questions

3.4.6.1 What are the characteristics of single-channel slow impedance changes in response to evoked somatosensory activity in rats?

This study showed that 11 Hz electrical stimulation of the contralateral forepaw in anaesthetised rats evoked biphasic slow impedance responses in the somatosensory cortex. The observed impedance changes had distinct characteristics which remained consistent across the injection frequencies. The mean positive and negative impedance changes were 0.049 ± 0.045 % and -0.093 ± 0.055 %, respectively, and were temporally aligned. The figures agreed with the forward simulation suggesting that a 1 % local conductivity increase in the entire forepaw S1 region (~10 mm^3) should result in a negative slow impedance change with a magnitude of ~-0.1 % at the boundary. However, the findings of this study showed concomitant positive slow impedance changes in neighbouring cortical areas. Whilst unexpected, these results echoed the previous slow brain EIT studies in anaesthetized rabbits and single-channel slow impedance recordings in humans (Holder et al., 1996; Tidswell et al., 2001). The shape, size, and the temporal characteristics of both positive and negative slow impedance responses detected in this study resembled the corresponding features of BOLD and CBV signals recorded in rats upon 2 s forelimb stimulation (Hirano et al., 2011). This initially suggested that the negative slow impedance changes potentially occurred due to the heightened CBF producing a local change in the CBV.

Nonetheless, the abundance of positive changes detected across impedance recordings and animals suggested that impedance increases, rather than decreases, arose from neurophysiological changes. A localized decrease in conductivity conflicted with my hypothesis and with a proposed mechanism for slow neural impedance changes (Holder, 2021a; Holder et al., 1996). Therefore, control experiments and EIT imaging were needed to investigate whether the observed changes were genuine and did not arise from artefacts often encountered in EEG and other electrophysiological recordings (Aristovich et al., 2015; Scott et al., 1997; Tatum et al., 2011). Controls were performed prior to imaging and suggested that both types of impedance changes were unlikely to be artefactual. Therefore, EIT imaging was required to confirm the physiological nature of the bidirectional slow changes and to ascertain that they did not cancel out when multiple injection pairs were implemented.

3.4.6.2 What is the optimal carrier frequency yielding the best SNR for recording slow neural activity?

The frequency sweep of slow impedance responses to physiologically evoked brain activity showed a flat relationship of the injection frequencies with the amplitude of both negative and positive slow changes between 200 Hz – 10 kHz. A larger signal predicted at low frequencies (< 1 kHz) due to a wider gap between the conductivities of blood and brain was not observed suggesting an alternative pathway at play. On the other hand, the SNR of positive, but not negative, impedance changes increased significantly with the carrier frequency up to 5 kHz with a further statistically significant drop at 10 kHz. Coupled with the higher prevalence of positive impedance responses, the observed trend suggested that slow impedance changes seen in these experiments might have arisen from neuromorphological responses distinct from the mechanisms of neurovascular coupling and associated with water movement during neural activation. Similar slow changes have been observed in optical imaging studies with stimulated nerve fibres and brain slices and were attributed to neuronal cell volume changes due to an influx of cations during the electrical activity (Lee & Kim, 2010; Lipton, 1973; Rector et al., 2001; Tasaki & Byrne, 1992). Transient volumetric fluctuations could have theoretically generated localised short-lived peaks in cerebral tissue impedance lasting several seconds beyond the duration of external stimulus. However, theoretically, the frequency-dependence would be expected to hold in this instance as the injected current would preferentially travel in the extracellular space at low frequencies.

It is possible that the lack of a statistically significant trend in the magnitude of the observed slow changes with the carrier frequency was not representative of the true relationship between these variables due to a large inter-sample variability. Individual impedance recordings showed values ranging between 0.012 – 0.361 % and -0.022 – -0.233 % for positive and negative changes, respectively (Fig. 3.4). Such a wide range of response values could have resulted from experimental errors or could have tightly correlated with the amplitude of the forepaw SEPs at the time of recording (Huttunen et al., 2008). Consistent with the known dose-dependent reduction in the amplitude of the SEPs under isoflurane anaesthesia, it was noticed post-processing that the magnitude of slow impedance responses increased towards the end of the experiments when the isoflurane concentration was < 1 % (Kameyama, 1994; Rojas et al., 2006). This finding encouraged the investigation whether the recorded slow impedance changes correlated with the amplitude of the forepaw SEPs which was affected by the depth of anaesthesia. The linear regression analysis showed that there was a strong positive correlation between the size of the SEPs and the peak positive but not negative slow impedance changes ($p < 0.001$ and $p > 0.05$, respectively; Fig. 3.5). This suggested that the lack of significant frequency dependence of positive slow impedance responses was potentially confounded by the amplitude variability of the SEPs between the different states of anaesthesia. However, the frequency relationship of negative impedance responses should not have been affected by the basal neural activity. Moreover, this finding reinforced the physiological relevance of the positive, but not the negative, impedance responses and suggested that they represented slow neural changes of other than haemodynamic origin.

Nevertheless, the selection of the optimal frequency for EIT of slow changes was based on the comprehensive picture of slow impedance responses across frequencies and the convenience of using the chosen frequency with the parallel system. As the magnitude of impedance responses appeared to be relatively even across frequencies, the choice of EIT injection frequency for imaging was made on the SNR of the recorded changes across all experiments. Significantly higher SNR of positive impedance changes observed at 5 kHz encouraged the choice of this frequency for parallel EIT of slow brain activity.

3.4.6.3 Can slow changes be reliably and reproducibly imaged using EIT and epicortical electrodes?

This study demonstrated that slow neural activity in the rat brain following evoked somatosensory activity of the contralateral forepaw could be successfully imaged with parallel EIT which tracked the three-dimensional propagation of slow changes in the rat brain with a temporal resolution 1 s. EIT images showed that only the increase in the cerebral tissue impedance following the stimulation of the rat somatosensory cortex was spatially consistent and reproducible within and across animals (Fig. 3.9, 3.10, 3.11). Even though single-channel impedance recordings depicted bipolar impedance changes in neighbouring subfields of S1, EIT images showed that slow impedance decreases were irregular and not statistically significant. On the other hand, this finding was consistent with the marked abundance of positive changes in single-channel impedance measurements (Fig. 3.4). Therefore, an *a priori* assumption that slow impedance changes during regional brain activation by non-pathological stimuli reflected fluctuating cerebral haemodynamics could not explain the results.

The observed activity pattern fits the model of the neuromorphological, or neuromechanical, coupling which connects the electrical activity of neurons to their microstructural changes induced by cell swelling and transmembrane water transport in the active tissue (Le Bihan, 2014; Pan et al., 2018; Tsurugizawa et al., 2016). As discussed in Chapter 1, in pathological cases, intense uninterrupted neural activity results in the disruption of an electrochemical balance of Na^+, K^+ and Ca^{2+} ions leading to an intracellular accumulation of water (Raimondo et al., 2015). As a result, extracellular space shrinks and, therefore, the impedance of the active brain tissue increases (Hannan et al., 2021). This process is prominent during epileptic seizures when hypersynchronous neuronal firing depletes the available energy stores and prevents the reinstatement of the transmembrane ionic gradient which is otherwise restored during physiological brain activity. However, the initiation and propagation of the action potentials in the active brain regions are accompanied by smaller-scale transient decreases in the extracellular Na^+. Moderate fluctuations in extracellular osmolality which mimic changes during the action potentials have been shown to reduce interstitial volume in brain slices which suggested that non-pathological neuronal activity could be similarly coupled to changes in the active cell volume, the phenomenon termed neuromorphological coupling (Fayuk et al., 2002; Lipton, 1973; Pan et al., 2018). Numerous *ex vivo* and *in vivo* studies have explored this idea by looking at light scattering or water diffusion changes during functional brain activity using IOI or diffusion fMRI (dfMRI), respectively (Darquié et al., 2001; Holthoff & Witte, 1996; Le Bihan et al., 2006; Lee & Kim, 2010; Pan et al., 2018; Tsurugizawa et al., 2013). *In vivo* studies in this field were pioneered by Denis Le Bihan and colleagues who employed dfMRI to probe the fast-onset biophysical changes in the activated neural cells as a reliable marker of brain activity in humans and rodents upon sensory stimulation (Darquié et al., 2001; Kohno et al., 2009; Komaki et al., 2020; Le Bihan et al., 2006; Tsurugizawa et al., 2013). In comparison to a stereotypically slow BOLD response characterised by the initial dip and post-stimulus undershoot, the dfMRI signal was consistently shown to exhibit a sharper onset and shorter time-course, albeit the intensities were similar (Kohno et al., 2009; Le Bihan et al., 2006). The most recent work by Nunes et al. (2021) extended these finding to demonstrate an unparalleled capability of dfMRI signal to track both, fast- (< 100 ms) and slow-onset (4.5 s), secondary changes in the active brain tissue elicited by increased neural activity. Notably, the fast component of dfMRI signal followed the dynamics of IO signal in electrically-stimulated brain slices, where haemodynamic response was absent, and was insensitive to hypercapnic challenge, known to dampen the haemodynamic response. Collectively, this data corroborated the rapid-onset neuromorphological alterations imparted by neural activity which modulated cellular and extracellular volume on a timescale preceding that of haemodynamic changes (Lee & Kim, 2010).

Considering the available evidence, slow impedance increases observed in this study are likely to reflect the transient cell volume changes described above which distinctly differ from the typical haemodynamic response. The recorded signal displays an immediate stimulus-locked onset and a sharp peak with a gradual decline without the post-stimulus undershoot (Fig. 3.4). The significant change in cerebral impedance is also confined to the first 3 s after the onset of somatosensory stimulation suggesting that the response does not involve vasculature as its recruitment has been shown to lag by several seconds (Huber et al., 2019; Kohno et al., 2009).

Lastly, the lack of qualitative differences between slow impedance responses under urethane and isoflurane anaesthesia observed in this study further supports the non-vascular origin of the recorded impedance signal (Tsurugizawa et al., 2016). Local haemodynamic response under isoflurane would be expected to increase in magnitude relative to that under urethane whereas the effect on cell swelling would be minimal. This has been shown by Abe et al. (2017) in a study comparing the effects of isoflurane and medetomidine anaesthesia on BOLD-fMRI and dfMRI signals. Unlike the BOLD signal, water diffusion coefficient was affected in a dose-dependent manner irrespective of the anaesthetic agent used. This indicated that both, medetomidine and isoflurane, anaesthesia respectively affected the degree of cell swelling by neuronal deactivation or suppression whereas the haemodynamic response parameters were additionally modulated by the corresponding vasodilating or vasoconstricting effects of the anaesthetics (Nasrallah et al., 2014; Sicard et al., 2003). Combined with the known minimal effects of urethane on cardiovascular system, these results agree with the hypothesis that the slow intracerebral impedance changes detected in this study arose as a result of transient changes in cell volume.

Nonetheless, as the direct evidence for neuromorphological changes in slow EIT images is missing, it is still plausible that the observed activity represents a blood ‘stealing’ effect. It refers to a solely vascular phenomenon during which CBF is redistributed from the passive to the active brain regions to enable an efficient response to an acute increase in local metabolic demands by the actively firing neurons (Woolsey et al., 1996). Haemodynamic ‘stealing’ has long been suggested as an underlying cause for the negative BOLD response often seen in brain regions adjacent to those experiencing BOLD signal increase (Harel et al., 2002). Using direct measurements of CBF with Laser-Doppler flowmetry, it was demonstrated that while CBF increased in microvasculature, there was a parallel negative shift in CBF in larger feeding vessels during the functional activation of rat whisker barrel cortex diverting the CBF away from the inactive barrel subfields (Kannurpatti & Biswal, 2004). This negative haemodynamic response associated with evoked brain activity upon sensory stimulation was shown to occur in the absence of neuronal deactivation supporting its vascular origin to account for regional changes in neuronal activity (Hu & Huang, 2015; Ma et al., 2017). In this context, the EIT images of slow brain activity could represent the ‘perfusion steal’ from the superficial pial vessels to the parenchymal vessels located in the deeper cortical layers. The sudden shunting of blood from the large distal feeding arteries to the smaller proximal arteries and arterioles and to capillaries endowing the active population of neurons could potentially cause a sharp increase in impedance which would gradually dissipate as the myogenic forces would restore the appropriate CBF (Bevan & Hwa, 1985; Harder et al., 2011; Pohl & de Wit, 1999). This would explain the existence of the collateral negative impedance responses seen in single-channel recordings, however, would not account for their incoherent distribution in EIT images.

3.4.7 Future work

The results of this study serve as a proof-of-concept showing that imaging of slow brain activity in rats is possible using parallel multifrequency EIT and epicortical electrodes. Tomographic images of a cerebral impedance increase likely capture a brief change in the active cell volume upon physiological brain stimulation, albeit the underlying physiology is under debate. Therefore, future work could involve collecting images of these slow impedance changes using additional imaging modalities, such as IOI or (d)fMRI, which would help to discern the nature and the source of the observed activity. Delineating the underlying physiological mechanism of the slow neural activity detected here would aid in the exposure of the parallel EIT to researchers as a useful imaging method for tracking neural activity in rodent studies.

Unfortunately, poor depth resolution and slow frame rate of parallel EIT at its current state significantly limits its plausible applications until further technical improvements are made. Therefore, future studies could also focus on extending this work to imaging slow impedance changes in rodents during epileptic seizures where impedance of brain tissue increases by at least an order of magnitude more than during physiological brain activity (Hannan et al., 2021). With the use of parallel EIT system, this would theoretically enable the imaging of cell volume changes during epileptiform activity in real-time without the requirement for averaging. Moreover, if the exogenous and endogenous sources of noise could be reduced, parallel EIT could potentially image a three-dimensional propagation of seizures across the rat brain without the requirement of penetrating depth electrodes (Witkowska-Wrobel et al., 2021). If successful, parallel EIT of slow changes during epileptogenic activity in the rat brain could serve as a useful tool for studying the origin and the spatiotemporal propagation of ictal and interictal events in the rodent models of epilepsy.

Chapter 4

Method development for imaging pathophysiological brain activity in an acute rat epilepsy model using a custom stereo-electrode array and EIT

4.1 Introduction

The main purpose of this thesis was to develop EIT for high-resolution imaging of pathophysiological neural changes anywhere in the brain using surgically-anaesthetised rats as a model organism. Since achieving sufficient spatial coverage and depth resolution with electrodes placed on the scalp and on the cerebral cortex in earlier chapters proved challenging with the current technology, the focus of the remainder of my thesis was combining fast and slow neural EIT with implantable 3D depth electrode arrays. The rationale behind the use of the penetrating depth electrodes was increased signal and, consequently, SNR due to the proximity of the local neural changes to the recording device. This increase in SNR was expected to substantially improve the feasibility of accurate fast neural EIT (hereafter abbreviated fnEIT) recordings which were the focus of this chapter due to a scientific value of successful fnEIT. Successful fast neural depth EIT would carry immense translational potential as it would allow tracing of the precise trajectory of the epileptic circuits during surgical monitoring in epilepsy patients with pre-implanted depth electrodes. Accurate reconstruction of ictal activity in a seizure onset zone (SOZ) and surrounding epileptogenic areas using unique fnEIT data would have the prospect of improving the resection outcomes and increasing the proportion of surgical patients with complete seizure freedom. Moreover, information about the precise recruitment of neural networks during epileptic attacks extracted from fnEIT data could be used to instruct closed-loop DBS protocols. Overall, fnEIT with depth arrays would be transformative in the realm of the available therapeutic tools for patients with pharmacorefractory epilepsy and decrease the societal impact of debilitating epilepsy cases. Additionally, complementary slow neural EIT recordings which could be obtained with the same recording setup would provide insight into larger-scale neurometabolic responses occurring over the course of the same seizures further refining the treatment strategies for these patients. Therefore, this chapter is dedicated to developing a robust and reliable method for investigating the feasibility of imaging pathological neural circuit activity during ictal epileptiform discharges in an acute murine epilepsy model using highly optimised stereo-electrode arrays and EIT.

4.1.1 Background

Epilepsy is a neurological disorder defined by the tendency towards recurrent unprovoked seizures with associated clinical symptoms and cognitive as well as psychosocial repercussions (Fisher et al., 2014). Whilst epilepsy affects less than 1 % of the world's population, each individual has a 10 % chance of experiencing an isolated seizure in their lifetime (Falco-Walter, 2020). An epileptic seizure therefore is a collection of signs and symptoms attributed to a transient period of excessive and abnormally synchronous neuronal activity with mixed aetiology (Fisher et al., 2005). In cases where epilepsy diagnosis is confirmed, anti-seizure medication is commonly initiated based on seizure severity and frequency. However, around one third of epilepsy patients are resistant to pharmacotherapy and are evaluated for other treatment strategies, such as surgical resection of epileptogenic area or responsive neurostimulation with implantable electrodes. Both alternatives rely on successful localisation of EZ currently mapped using a combination of invasive (intracranial EEG) and non-invasive (MRI) electromagnetic techniques. However, complete post-therapeutic seizure freedom is extremely rare, and most patients experience only ~50 % reduction in seizure frequency with a significant proportion of relapse within the first few years after the surgery (Gouveia et al., 2024; Halford & Edwards, 2020; Téllez-Zenteno et al., 2005; Yoon et al., 2003). This suggests that current techniques for predicting the SOZ as well as its spatial development are still largely limited (Kudlacek et al., 2021; Kuhlmann et al., 2018; Proix et al., 2021). Intracranial fnEIT has already demonstrated its potential to fill this gap by generating 3D images of ictal epileptiform activity originating in the hippocampus and the cerebral cortex when using epicortical electrode mats (Hannan et al., 2020b; Hannan et al., 2018b). The study detailed in this chapter builds on the previous results by introducing a 3D stacked depth electrode array optimised specifically for EIT recordings in order to improve the field of view and the depth resolution of brain EIT (Fitchett et al., 2023). To fulfil the objectives, a method development is undertaken for assessing the feasibility of imaging the spatiotemporal development of electrical seizures in the rat brain with a resolution of milliseconds and micrometres using fnEIT and stereo-electrode arrays. If successful in animal studies, this imaging method could be incorporated clinically as an adjunct diagnostic and/or therapeutic tool enabling a detailed functional characterisation of the epileptogenic and irritative zones with currently unmatched precision.

4.1.1.1 Epilepsy model

The first pre-requisite in achieving clinical implementation of intracranial depth EIT are proof-of-concept studies in animals. Rodent epilepsy models are some of the most common animal models in neuroscience research for investigating the pathogenesis of seizures and epilepsies as well as developing diagnostic modalities and effective treatment forms. The groundwork for fast neural EIT in an acute rat model of epilepsy was laid by Sana Hannan (Hannan et al., 2020b, 2020a; Hannan et al., 2018b). The researcher developed and employed protocols for induction of on-demand electrical seizures in the murine neocortex and hippocampus (Hannan et al., 2020b). The experimental model was specifically tailored to serial image acquisition with EIT and epicortical arrays in terminally anaesthetised rats as the electrical seizure induction method permitted controlled acquisition of reproducible focal ictal discharges of relatively similar morphology (Hannan et al., 2018b, 2020a). This epilepsy model permitted serial acquisition of the full fnEIT protocol as each current injection pair could be recorded during separate but electrographically similar seizures. This seizure induction method was based on electrical stimulation mapping (ESM) used in pre-surgical assessment of epilepsy patients as a means of localizing eloquent cortical areas, outlying the boundaries for EZ and identifying the overlap between the two. In standard clinical practice, ESM parameters are iteratively adjusted for each patient by determining the threshold for electrographic or functional responses which are marked by the severity of afterdischarges (ADs) defined as rhythmic runs of stereotypic aberrant EEG/ECoG/SEEG waveforms, consisting of distinct spikes and sharp waves, or a combination of both, in response to electrical stimulation (Blume et al., 2004; Kalamangalam et al., 2014). Due to increased susceptibility to hypersynchronisation and uncontrolled spread of neuronal depolarisation, EZ is considered to have a lower threshold for ADs with the propensity to develop into iatrogenic seizures, substantiating ADs as markers for the region of spontaneous seizure onset in epilepsy patients (Bernier et al., 1990; Cuello Oderiz et al., 2019; Wyler & Ward, 1981). Although correlation between the location of ADs and habitual seizures is ambiguous, shared cellular mechanisms support the use of electrical ADs as a model of human epilepsies for acute assessment of neural circuit dynamics (Liu et al., 2017; McCormick & Contreras, 2001).

Stimulation protocols defined by Hannan et al. (2020b) were tailored to the respective electrode geometries for inducing focal seizures in targeted brain regions. Neocortical epileptic ADs were provoked using planar circular epicortical electrodes (0.6 mm in diameter) separated by ~3 mm and located over the boundary between forelimb and hindlimb S1. In contrast, hippocampal ADs were elicited by stimulating the angular bundle of the perforant path using a penetrating wire electrode (~0.2 mm in diameter). In both cases, square biphasic symmetric charge-balanced pulses with a duration of 1 ms and maximal amplitude of 1.5 – 2 mA were delivered to elicit reliable and reproducible ictal activity. Stimulation duration differed between the brain areas as a shorter stimulus was shown to be sufficient to cause hippocampal but not cortical ictal activity (Hannan et al., 2020b, 2020a). Considering the known response heterogeneity across brain regions and distinct biophysical properties of neural tissues as well as cellular interactions with the stimulating current, the effects of its intensity and polarity, the seizure induction protocols, developed by Hannan et al. (2020b), were specific to the experimental set-up. Since a novel stereo-electrode array was implemented in this part of my thesis for recording EIT of epileptiform activity, the electrical seizure induction method needed to be modified and adapted to a new electrode geometry.

4.1.1.2 Stereo-electrode arrays

Commercially available depth probes are mostly suited for passive voltage recording, yielding information about multi- or single-unit activity. Striving for whole-brain coverage with high spatial granularity, the manufacturers of the most advanced probes in the market has focused on scaling the number of electrodes with minimal brain tissue damage. This developmental pathway led to thin probes (<100 µm) containing small densely packed electrodes (Ghane-Motlagh & Sawan, 2013; Wijdenes et al., 2021; Yi et al., 2024). For example, in their updated design, Neuropixels silicone probes, which comprise four 10-mm long shanks, have condensed 5,120 recording sites spanning a plane of 750 µm by 720 µm (Steinmetz et al., 2021). The electrodes measure 12 x 12 µm with inter-electrode spacing of 15 µm and 32 µm in longitudinal and transverse axes, respectively. Such electrode geometry inevitably leads to high contact impedance on the order of 100 kΩ contraindicating it for EIT due to unfavourable noise characteristics. Moreover, the dense electrode distribution raises the likelihood of shunting between injection electrodes with an additionally increased risk of tissue damage due to the small surface area (Atkinson et al., 2022). Therefore, the specifications of the existing depth arrays were mostly incompatible with EIT for neural applications and necessitates a unique design with a balanced geometry and impedance characteristics.

EIT depth probe design and fabrication

The ideal EIT depth array should enable injection of an appropriate and safe current level but also have a noise floor low enough for recording neural impedance changes with a size of 1/100th of the standing wave, or smaller (a few microvolts). Thus, the electrode diameter and spacing must be as large as possible to maximise the injected current and avoid shunting. On the other hand, these parameters need to be small enough for mesoscopic spatial resolution. The same applies for the spacing between the shanks with brain damage being an additional factor limiting the electrode count.

A comprehensive in silico study was undertaken by a fellow PhD student Adam Fitchett to determine the best specifications for the depth probe tailored to fast neural EIT in the murine brain (Fitchett et al., 2022, 2023). Using MATLAB and COMSOL Multiphysics, 766 possible depth arrays were simulated and tested by running a forward model of the boundary voltage changes with a 0.4 % conductivity perturbation inserted halfway between two shanks at a depth of 5 mm or deeper. Based on an objective function which ranked the simulated arrays on their performance under different noise levels, the best candidate containing 36 relatively large (0.007 mm^2 surface area) but narrow (0.01 mm width) electrodes was selected and used as a template for manufacturing an optimal array in Bioelectronics Systems Lab at Columbia University. Due to practical limitations in fabrication process, the preferred array design was minimally adjusted with the modifications including increase in the shank width (from 100 to 120 µm), a minor reduction in the electrode height (0.666 mm to 0.5 mm) and inter-electrode spacing (from 2.11 to 2.00 mm) as well as a significant decrease in the inter-shank pitch (from 3 to 1 mm). The finalised array was made from silicon and assembled from three separate layers with three shanks in each layer and four tantalum-gold alloy contacts exposed on each shank (36 contacts in total). The shank layers were attached to an interposer board which was wire-bonded to the contact pads giving a fixed geometry (Fig. 4.1). The electrode surface was coated with PEDOT:PSS which consistently produced ≤1 kΩ impedance on at least 80% of the contacts across multiple probes assessed during array development.

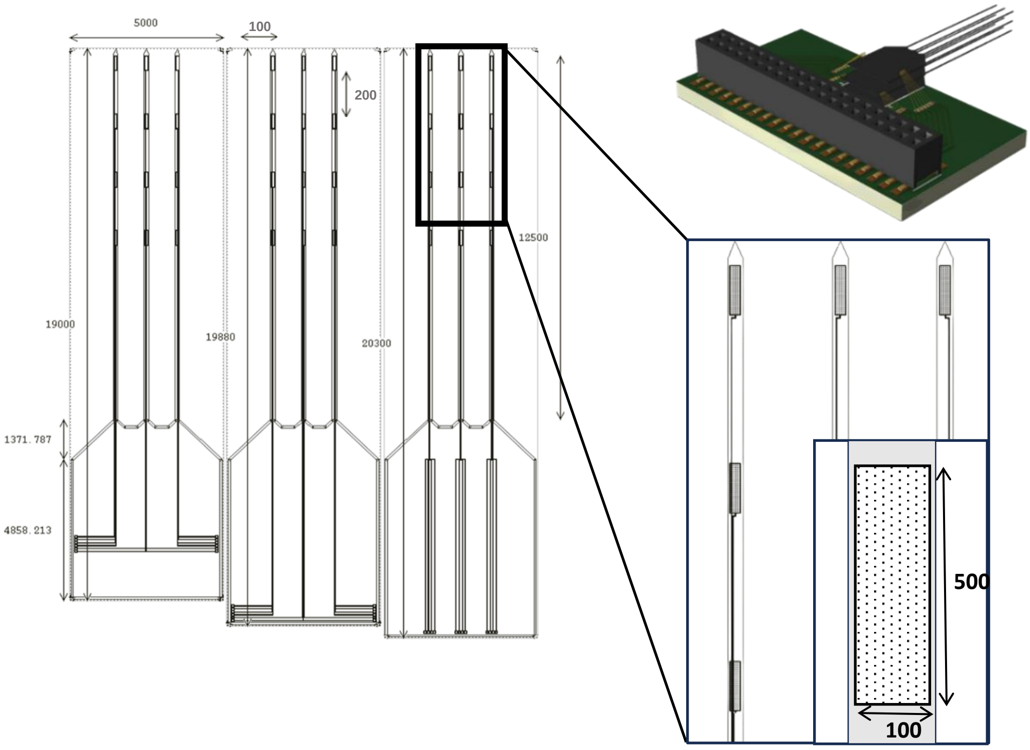

Figure 4.1. The final design and the dimensions of the optimal EIT depth probe. Optimal depth array comprised three layers, each containing three equidistant probes. Each probe had four 0.1 X 0.5 mm electrodes spaced by 2 mm along the vertical axis. The total probe width was 0.12 mm, providing 10 µm clearance from the shank edges. Probe length from the top edge of the electrodes to the shank base was 12.5 mm and was inserted ~8 mm deep into the brain. Dimensions in the picture are provided in micrometres.

Selection of a universal probe insertion site

To fulfil an objective of whole-brain imaging of physiological and pathological activity in the rat brain with intracranial depth EIT, a suitable insertion site had to be selected. For successful proof-of-concept studies, the depth probe had to penetrate brain regions where a stereotypical neurophysiological signal could be evoked in response to a controlled external stimulation. Additionally, the brain areas proximal to the insertion site had to exhibit heightened susceptibility to pathological hyperexcitability which would facilitate the generation of on-demand electrical seizures in the cortical and subcortical structures.

With the above requirements in mind, the selected insertion site was centred in the middle of the forepaw S1 with the other superficial electrodes landing in the hindlimb and whisker S1 areas and the deeper electrodes in the middle and the posterior shank layer placed in the thalamus (Fig. 4.2). This placement was expected to enable the imaging of neural changes in the thalamocortical (TC) loop during evoked forepaw, hindpaw and whisker activity (Fitchett et al., 2023). As described in the previous chapter, this model of non-pathological brain activity is well-established and has been characterised using multiple imaging techniques with a spatiotemporal resolution spanning from microscopic to macroscopic. The *a priori* knowledge of the expected activity pattern could therefore be used to verify the accuracy and specificity of depth EIT recordings with the optimised array. From the perspective of imaging pathological neural circuits, the thalamus was an important insertion point due to its widespread connectivity to cortical and subcortical regions and its role as a rhythm generator and pacemaker involved in the onset, progression, and maintenance of epileptic seizures, especially ictal spike-and-wave discharges (SWDs) (Fan et al., 2017; Pizzo et al., 2021).

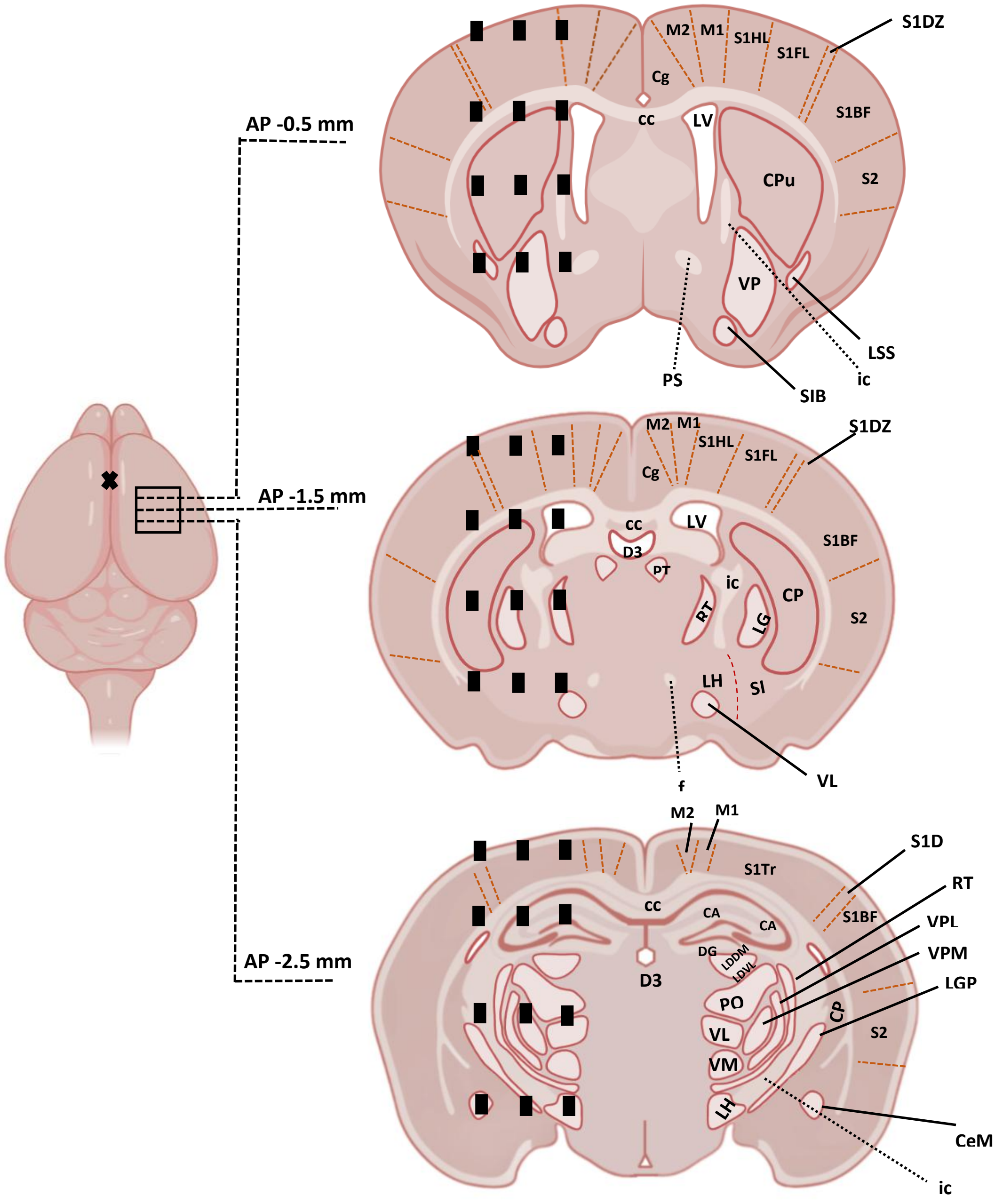

Figure 4.2. Schematic representation of the insertion sites for each of the layers in the depth probe. In all experiments, depth probe was inserted such that the most anterior layer A was located 0.5 mm posterior to bregma (marked by x) with the most medial shank 2 mm lateral to the midline. Layers B and C were therefore respectively located 1.5 mm and 2.5 mm posterior to bregma. Each probe penetrated the brain approximately 8 mm. Individual depth electrodes are represented by black squares. (Continued overleaf)

The key brain structures and coordinates are marked by the following abbreviations: AP - antero-posterior axis; CA1, CA2 and CA3 hippocampal regions; cc - corpus callosum; CeM - central amygdaloid nucleus, medial part; Cg - cingulum; CPu - caudate putamen; D3V - dorsal third ventricle; DG - dentate gyrus; f - fornix; ic - internal capsule; LGP - lateral globus pallidus; LDDM - laterodorsal thalamic nucleus, dorsomedial part; LDVL - laterodorsal thalamic nucleus, ventrolateral part; LH - lateral hypothalamus; LSS - lateral stripe of the striatum; LV - lateral ventricle; M1 - primary motor cortex; M2 - secondary motor cortex; PO - posterior thalamic nuclear group; PS - parastrial nucleus; PT - paratenial thalamic nucleus; RT - reticular nucleus of the thalamus; S1BF - primary somatosensory cortex, barrel field; S1DZ - primary somatosensory cortex, dysgranular zone; S1FL - primary somatosensory cortex, forelimb region; S1HL - primary somatosensory cortex, hindlimb region; S1Tr - primary somatosensory cortex, trunk region; S2 - secondary somatosensory cortex; SI – substantia innominata; SIB - substantia innominata, basal part; VL - ventrolateral thalamic nucleus; VLH - ventrolateral hypothalamic nucleus; VM - ventromedial thalamic nucleus; VP - ventral pallidum; VPL - ventral posterolateral thalamic nucleus; VPM - ventral posteromedial thalamic nucleus. Figure was created using BioRender.com according to Paxinos and Watson (2013) rat brain atlas. The elements of this figure are not to scale.

Probe insertion guided by an apertured planar epicortical array

Depth probe insertion requires a craniotomy which is typically restricted to the diameter of the implanted array to minimise the risks of bleeding, infection, brain dehydration and inflammation, all of which can adversely impact electrophysiological recordings (Shimizu et al., 2020; Xu et al., 2007). At an early developmental stage, EIT probe insertion was trialled through a rectangular craniotomy, 4 x 4 mm, centred at 2 mm posterior and 3 mm lateral to bregma. However, this setup proved impractical because brain health could not be assessed independently of the probe which was crucial when monitoring the neurophysiological impact of the procedure. Moreover, it proved difficult to ensure that no sharp bone dust from the drilling settled in such a small cranial window and damaged the cortical surface.

Therefore, an alternative probe implantation strategy was designed. The epicortical array used in Chapter 3 was altered by a fellow PhD student Adam Fitchett to include a 4 x 4 mm square opening 4 mm below the tip of the anterior edge (Fig. 4.3). There were 37 intact epicortical contacts around the aperture for recording brain activity from the cortical surface. Placement of this apertured epicortical array through a wide cranial window was deemed safer due to a well-established surgical technique and offered additional advantages. The aperture was positioned such that, when on the cortical surface, it was centred 3 mm lateral and 1.5 mm posterior to bregma. This assured that the probe penetrated the relevant somatosensory and motor cortices as well as the thalamic and striatal nuclei. Additionally, epicortical electrodes could be used for monitoring spontaneous and task-related brain activity before and after probe insertion informing on the functional impact of the procedure.

Lastly, the chosen recording setup permitted good control of brain hydration. Small cotton wool balls soaked in warm aCSF could be arranged around the aperture and, with the depth probe in place, aCSF could be frequently applied to the aperture or to the cotton wool balls leaching the solution into the opening.

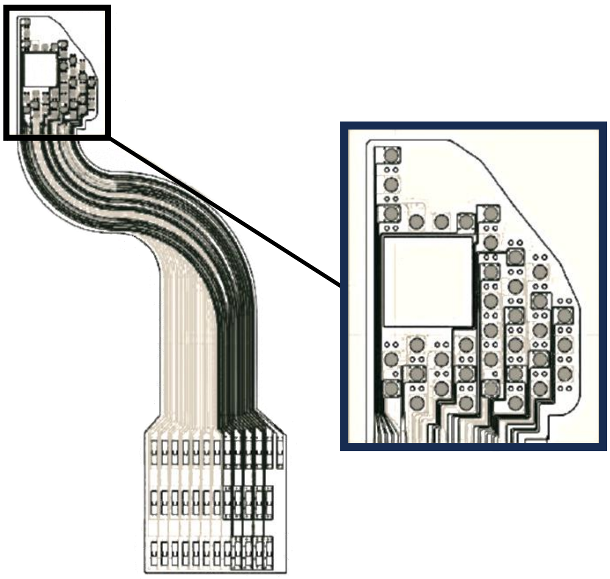

Figure 4.3. Apertured epicortical array designed to guide the insertion of EIT depth probe. This design was based on the epicortical array used in Chapter 3. A 4 x 4 mm aperture was opened above the forelimb S1 region which was localised on the basis of previous epicortical recordings of forelimb and hindlimb SEPs. The dimensions of the electrodes were maintained as before (Faulkner, 2019). The additional modification included separating the electrodes with neighbouring tracks into two layers with a silicon insulation in between (contrasted by grey and black colours).

4.1.2 Purpose

The purpose of this chapter was to develop and optimise a viable method for recording neural changes during cortical and subcortical electrical seizures in the rat brain using EIT and a 3D custom electrode array. The aim of the method development was to answer the following questions:

1. Assessment of depth probe quality and mechanical stability:
    a. What is the depth electrode impedance after coating?
    b. How does the impedance change upon repeated use?
2. Depth probe insertion rigor:
    a. What is the reproducibility of the anatomical insertion site between animals?
3. Depth probe implantation safety:
    a. Does depth probe insertion cause significant bleeding?
    b. Does probe insertion negatively impact neurophysiology?
    c. Does probe implantation lead to aberrant histological changes in the brain?
4. Induction of reproducible electrographic seizures in cortical and subcortical structures:
    a. What are the criteria for acceptable epileptiform activity for imaging with EIT and depth electrodes?
    b. Which cortical and subcortical stimulation pairs yield the best electrographic seizures?
    c. What are the optimal stimulation parameters for inducing reproducible seizures?
5. Data analysis technique for extracting fast impedance changes:
    a. What is the best method for locating and applying the trigger markers to effectively isolate fast neural impedance changes associated with individual ictal ADs on the depth electrodes?

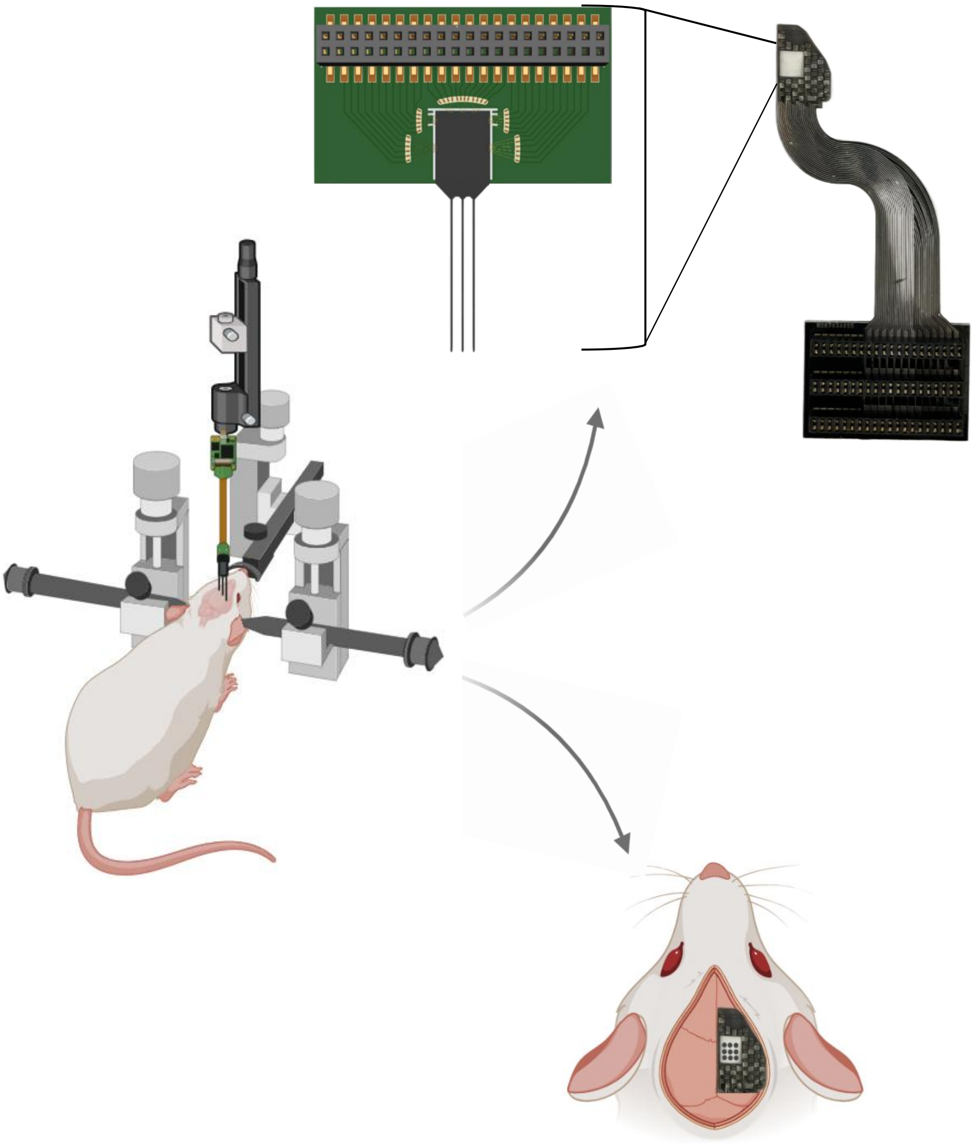

Figure 4.4. Experimental setup for inducing electrical seizures and recording their spatiotemporal propagation in the rat brain using optimised stereo-electrode arrays. Anaesthetised rats were firstly immobilised in a stereotaxic frame. Then a hemisphere-wide craniotomy was opened for the implantation of an apertured subdural electrode array which permitted independent monitoring of brain health and guided the insertion of the EIT depth array. Individual elements in this figure are not to scale. Figure was created using BioRender.com.

4.1.3 Experimental Design

A total of 23 anaesthetised rats were used for method development and preliminary impedance recordings. Experiments could not be completed in six rats due to one of the following reasons: inadvertent brain damage during the placement of the epicortical array, damage to the depth probe, unstable vital signs, or inability to evoke seizures. The remaining 17 rats were used for conducting different stages of the method development. The precise animal numbers used for each test and procedure are detailed in appropriate methods sections. The experimental set-up used throughout this study is represented in figure 4.4.

4.1.3.1 Depth probe quality testing

The first stage of the method development included the electrical testing of the available depth arrays to ensure that they were suitable for the purpose of this project. Since these arrays were designed to capture very small voltage modulations in the frequency bandwidth of ~100 – 1000 Hz, maintaining low contact impedance was paramount. A recent human study comparing the noise characteristics between low- and high-impedance intracranial arrays demonstrated superior performance of electrodes with impedance of approximately 3 – 5 kΩ with a median noise level consistently <1 µV (Dimakopoulos et al., 2023). Notably, the researchers used platinum-coated electrodes which have shown inferior electrical characteristics in comparison to PEDOT used in this study (Dijk et al., 2023; Sharafkhani et al., 2022). Experience with PEDOT-coated subdural arrays in the previous chapter together with examples in the literature indicated that impedance of ≤2 kΩ was achievable at 1 – 2 kHz; however, the surface area of previously used epicortical electrodes was six times larger which contributed to low contact impedance (Blad et al., 2005). Unfortunately, delamination of epicortical electrodes was notable after a single use rendering arrays non-reusable. Since the goal for the current experimental setup was extended durability, it was also important to investigate the stability of the depth electrode impedance across experiments. It was unclear whether the depth contacts would be able to withstand both repeated high-intensity (mA) current injections to induce seizures and simultaneous EIT recordings with continuous injection of low-amplitude currents (µA). Nonetheless, favourable evidence of prolonged stability of PEDOT coating when deposited on gold electrodes was encouraging as gold formed part of the alloy used to make the depth electrodes for this study (Schander et al., 2016).

4.1.3.2 Functional confirmation of depth probe insertion site reproducibility

The accuracy and the precision of the anatomical depth probe insertion location across animals was an important metric in validating the model. The degree of implantation precision could later be correlated with variability in seizure induction outcomes or cross-checked with the results of fast and slow neural impedance recordings. To address this aim, the repeatability of evoked forelimb and hindlimb activity on the same depth electrodes between animals was used as a proxy for insertion site reproducibility between experiments. A distribution map of averaged forelimb and hindlimb SEPs on all depth electrodes was produced and the reoccurence of the maximal SEPs on the same depth electrodes was assessed. To account for the variability in the amplitude of the SEPs between rats due to changes in experimental conditions, somatosensory stimulation amplitude and/or anaesthesia level, an arbitrary measure, termed ‘SEP intensity’, and its scoring system were derived. The SEP intensity combined both the amplitude of forelimb and hindlimb SEPs and their recurrence frequency on the same depth electrodes between recordings and animals. A detailed explanation of the calculations and the scoring system is provided in the methods section 4.2.3. This arbitrary intensity measure was used as a proxy for probe position with respect to the epicentre of evoked forelimb and hindlimb activity defined by maximal SEPs in the respective S1 regions. Such functional probe localisation therefore served as an indirect assessment of both the accuracy and the reproducibility of the probe insertion site *in vivo* and with respect to its expected, or target, insertion site.

4.1.3.3 Optimising an acute electrical epilepsy model in rats

To ensure the validity of depth fnEIT of epileptiform activity, the imaged seizures needed to (1) be comparable to those recorded with the previous techniques and (2) accurately approximate electroclinical seizures observed in human epilepsies. The method for inducing repeatable on-demand ictal epileptiform discharges suitable for serial fnEIT was firstly developed by Hannan et al. (2020b) using epicortical arrays to induce epileptiform ADs in the neocortex and the hippocampus. This model was used a framework for creating an equivalent experimental preparation utilising EIT depth probes for inducing seizures anywhere in the rat brain. Depth probe insertion location permitted stimulation of a range of brain regions; however, all permutations of possible stimulation pairs could not be investigated due to time constraints. Stimulation sites of interest were grouped into cortical and subcortical, and a subset of each with variable inter-electrode distance were tested further.

Electrical stimulation of sensitive regions, e.g., sensorimotor cortex, thalamus, basal ganglia, was expected to yield consistent bouts of stereotypical ADs after the cessation of stimulus as defined in 4.1.1.1. (Kalamangalam et al., 2014). Due to the proximity of the neural activity to the depth electrode array, the amplitude of fast impedance changes associated with individual ADs was predicted to be ~1 % of the standing voltage on the recording channels (Liston et al., 2012). Therefore, averaging of these changes was expected to be necessary in order to achieve an SNR of at least 3 – 5 necessary for image reconstruction (Aristovich et al., 2014; Gilad & Holder, 2009). Therefore, temporal markers corresponding to reproducible ictal ADs occurring within each seizure could be used to average the recorded raw impedance signal and yield a representation of millisecond changes in the electrical impedance of epileptogenic brain tissue associated with the opening of voltage-gated ion channels.

The noise within a signal is known to decrease with the square root of the number of averages. Therefore, the duration of a seizure and the number of identical ictal ADs it contained, directly would impact the SNR of an impedance change. To ensure that the SNR remained consistently at or above ~3 – 5, the shortest acceptable seizure duration was calculated as follows:

(1) The standing voltage on the depth channels typically ranges between 1 – 10 mV. Therefore, the smallest local fast neural impedance changes (~1 %) would be expected to have an amplitude of 10 – 100 µV:

   i. Lower limit:

$$dZ = 1\,mV \times 0.01 = 10\,\mu V$$

   ii. Upper limit:

$$dZ = 10\,mV \times 0.01 = 100\,\mu V$$

(2) The demodulated data was empirically predicted to contain noise of up to 10 µV before averaging.

(3) With these noise characteristics, for the smallest predicted impedance change (10 µV) to have an SNR of ~5 which falls at the upper end of the range reported in the section above, a minimum of 25 fast impedance changes needed to be averaged together:

   i. $SNR = \frac{dZ}{noise\ after\ averaging}$

   ii. $5 = \frac{10\ \mu V}{noise\ after\ averaging}$

   iii. $noise\ after\ averaging = \frac{10\ \mu V}{5} = 2\ \mu V$

   iv. $\sqrt{number\ of\ dZs\ for\ averaging} = \frac{noise\ before\ averaging}{noise\ after\ averaging} = \frac{10\ \mu V}{2\ \mu V} = 5$

   v. $number\ of\ dZs\ for\ averaging = 5^2 = 25$

(4) The most consistent and prevalent form of ADs seen in Hannan et al. (2020b) model was 1 – 5 Hz SWDs. A similar seizure morphology and composition was expected in the epilepsy model developed in this chapter. Based on the frequency of ictal SWDs typically reported in the range of 3 – 4 Hz with values up to ~8 – 10 Hz in some literature sources, and considering that seizures had to contain at least 25 reproducible SWDs, only electrical stimulation events which yielded ≥6 s trains of ADs in this study could be considered successful for the purpose of imaging with depth fnEIT (Blume et al., 2004; Blumenfeld, 2005; Meeren et al., 2002; Timofeev & Steriade, 2004; van Luijtelaar & Coenen, 1986):

$$Seizure\ duration\ (s) = \frac{No.of\ SWDs}{Frequency\ of\ SWDs\ (Hz)} = \frac{25}{4^{*}\ Hz} = 6.25\ s\ \approx 6\ s$$

* - 4 Hz was chosen for the purpose of the calculation as an appropriate mid-point in the range of frequencies at which SWDs typically occur.

Selection of stimulation sites

The first set of depth stimulation sites on the depth probe were directed at the S1. Once reliable seizures could be evoked in the neocortex, additional stimulation sites in the thalamus and in the basal ganglia where investigated.

Cortical ADs are a common type of epileptiform activity in both clinical and iatrogenic seizures lending themselves an acceptable acute model of frontal lobe epilepsy (FLE). FLE is considered the second most common type of epilepsy following the temporal lobe epilepsy, and accounts for 20 – 30 % of extratemporal cases (Hosking, 2003). FLE involves widespread seizure foci with complex and diverse semiology and aetiology. Based on the anatomical location, some of the most common seizures seen with FLE are focal motor seizures originating in the somatosensory and motor areas. Typical symptoms include unilateral clonic or tonic-clonic activity with preservation of consciousness generally lasting for <1 min. The ictal electrographic pattern is often obscured; however, interictal activity is frequently observed in the form of bilateral SWDs (Ramakrishnan et al., 2024). The rat model of stereotypical on-demand electrical ADs induced in the somatosensory cortex can replicate these electrographic features and clonic symptoms of focal motor seizures in humans. More specifically, electrical ADs can be easily elicited by the stimulation of sensorimotor area of the rat cortex likely owing to a large proportion of intrinsically burst-generating neurons which have a heightened susceptibility to epileptogenesis (Franceschetti et al., 1998; McCormick & Contreras, 2001).

Neocortical SWDs are also a signature of non-motor generalised seizures occurring in absence epilepsies and syndromes with strong genetic predisposition, such as juvenile absence epilepsy or Lennox-Gastaut syndrome (Nolan et al., 2005; Sakurai et al., 2010). Absence seizures feature behavioural arrest and unresponsiveness accompanied by rhythmic bilateral 3 Hz-SWDs (Destexhe et al., 1999). This electrographic pattern is known to arise from the integrated synaptic activity in the cortico-thalamic-cortical loop also implicated in sleep spindles (Kandel & Buzséki, 1997; McCormick & Bal, 1997; McCormick & Contreras, 2001). The precise dynamics of the underlying neural pathways are complex and involve an ongoing interaction between the thalamocortical relay cells and the intrinsic inhibitory thalamic circuits, particularly the reciprocal connections between the thalamic reticular neurons (Destexhe et al., 1999; Fan et al., 2017). Interestingly, despite the established pacemaker role of the thalamus in the synchronisation of the cortical rhythms, some experimental evidence in the feline epilepsy models indicates that cortex is the leading structure in the ictogenesis of 3 Hz-SWDs (Avoli & Gloor, 1982a, 1982b; Steriade & Contreras, 1998). The alternative hypothesis suggests that an imbalance between the excitation and inhibition within the cortical networks leads to coherent oscillations which subsequently entrain the thalamus (Timofeev & Steriade, 2004). This leads to the spike-bursts in reticular cells and ensuing inhibitory PSPs in

TC cells with a time constant of 150 – 300 ms which accounts for the frequency of the ictal SWDs. The depth probe insertion site in my experimental preparation not only enabled the penetration of the cortical regions with high excitability and proclivity to develop abnormal oscillations but also positioned the shanks in the immediate vicinity of the thalamic reticular nucleus implicated in the initiation and maintenance of epileptiform SWDs (Fig. 4.2). Therefore, induction of ictal SWDs by the stimulation of both the neocortex and the thalamus using the EIT stereo-array could serve as a model of absence seizures in rodents. Moreover, fnEIT images of electrically-induced SWDs would help to decipher the temporal dynamics and the hierarchy of the TC circuits in progression of SWD seizures, a matter still under debate (Danober et al., 1998).

Widespread connectivity between the cortex, the thalamus and the basal ganglia highlights another subcortical network with strong epileptogenic potential. The basal ganglia is a system of interconnected subcortical nuclei which send bidirectional projections to the cortex via direct and indirect neuronal pathways relayed via the thalamus (Graybiel, 2000). Direct cortical efferents terminate in the striatum and subthalamic nuclei, both of which send polysynaptic projections via the globus pallidus, substantia nigra and the thalamus back to the cortex forming a cortico-striatal-thalamo-cortical loop (Vuong & Devergnas, 2018). Complex anatomical relationship with the cortex and the thalamus with high epileptogenic potential has prompted interest in the role of basal ganglia in the onset and propagation of epileptic seizures. Multiple *in vivo* studies have since confirmed that virtually all structures within the basal ganglia participate in some form of epileptic activity including but not limited to absence and sensorimotor seizures (Vuong and Devergnas, 2018). More specifically, experimental evidence from the genetic and electrochemical rodent models of epilepsy have revealed the importance of intact corticostriatal pathways in the development of both, motor and non-motor, seizures (Miyamoto et al., 2019; Ono et al., 1987; Slaght et al., 2004). Moreover, in a primate model of electrical ADs, abnormal spike-wave activity was recorded in the caudate nucleus in synchrony with the ADs in the frontal cortex (Poggio et al., 1956). Heightened caudate activity was also detected during penicillin-induced cortical epileptiform discharges in cats (Neafsey et al., 1979). However, no comprehensive study has been conducted to date detailing the precise spatiotemporal trajectory of ictal epileptiform discharges across the cortico-striatal-thalamo-cortical loop. The depth probe insertion site used in this study placed shanks of layer A and layer B in the striatum (Fig. 4.2). Developing an electrical stimulation protocol which could activate the relevant striatal pathways and lead to progressive ictal activity within the thalamus and the cortex could provide an extremely useful acute *in vivo* model for imaging these circuits with depth fnEIT. Therefore, a subset of subcortical stimulation sites for induction of electrographic seizures were aimed at the caudate-putamen (CPu) complex in the striatum.

Selection of stimulation parameters for inducing electrographic seizures

The electrical seizure model in anaesthetised rats was firstly developed using planar electrodes implanted subdurally on one hemisphere (Hannan et al., 2020b). The shape, the surface area, and the spatial distribution of these electrodes are distinct from those of the probe. Geometrical differences determine the capacity to stimulate the regions of interest as well as the injected charge density and distribution, key factors in the safety of the procedure (Britton 2018; Grande et al., 2020). For example, in ESM, charge density and charge per phase, two main derivatives of the stimulation current amplitude, are the gold-standard metrics for setting the safe current limit (McCreery et al., 1990). The calculation is based on the Shannon equation which estimates the charge density threshold for neural damage during electrical stimulation with respect to the dimensions of the stimulating electrodes (Shannon, 1992). Therefore, the electrical stimulation parameters employed for seizure induction need to be adjusted for the current depth array to achieve a desired outcome with minimal unwarranted consequences.

For an epilepsy model to be relevant and viable, electrical stimulation needs to synchronise neighbouring neuronal networks into a state of abnormal repetitive oscillations akin to the rhythmic discharges during the ictal phase of an electroclinical epileptic seizure (Kalamangalam et al., 2014). However, neuronal damage due to injection of high amplitude currents should be avoided to maintain the integrity of the neural networks of interest. This is especially important for serial EIT image acquisition where multiple seizures are sequentially induced in the same brain region until the entire injection protocol is completed. Based on the evidence in the literature, it appears that the synchronisation of epileptogenic networks is conditional to the total charge delivered by the electrical pulses and their frequency as well as the pulse width which vary across subjects and brain regions (Luccarelli et al., 2021; Motamedi et al., 2007). Hence, when optimising the epilepsy model in this chapter, it was important to establish and standardise the stimulation parameters for inducing consistent electrical seizures across the ROIs. The section below describes in further detail the rationale for the selection of each stimulation parameter tested in this method development study.

1) **Pulse amplitude (0.2 – 4 mA) and width (1 ms)**. The amplitude and the duration of the electrical pulses directly dictate the charge per phase as well as the charge density at the contact area (Kuncel & Grill, 2004; McCreery et al., 1990). Whilst the recommended upper limit for the charge density at the surface electrodes is 30 μm/cm^2, the precise stimulation current level is often determined empirically by titrating the amplitude from the arbitrary subthreshold stimulus. Moreover, the existing guidance is tailored mostly to the non-penetrating macroelectrode arrays and might not be applicable to the stimulation with the penetrating microelectrodes. Indeed, studies in cats with chronically implanted cochlear microelectrodes suggest that charge per phase is an exclusive factor in neural tissue injury when considering

small diameter electrodes (McCreery et al., 1992, 1997). It is unclear if such relationship translates to electrical stimulation for the purpose of seizure induction. Therefore, in this study, the starting current level was extrapolated from seizure induction parameters in Hannan et al. (2020a, 2020b). With the optimal stimulation current amplitude ranging 1 – 2 mA for epicortical electrodes, an equivalent charge density could be achieved by injecting ~0.2 – 0.3 mA with depth electrodes. Thus, the starting current level for seizure induction with the depth array was chosen 0.2 mA. The upper limit differed between rats based on the ability to evoke satisfactory ADs as described in 4.1.3.3. Pulse width was kept at 1 ms due to multitude of evidence in favour of millisecond-duration pulses for generation of electrical seizures (Hannan et al., 2020a, 2020b; Modameti et al., 2007).

2) **Stimulation frequency (100 Hz) and duration (1 – 10 s)**. Due to high charge density at the depth electrode surface, it is desirable to keep the stimulation duration short. Consequently, the frequency of the pulses must be kept high so that at least 100 pulses are delivered in total (Mareš et al., 2002). An electrical stimulation study in kindled rats by Lothman and Williamson (1992) showed that the threshold for hippocampal ADs was intricately linked to the specific combinations of stimulation frequency and duration. AD threshold was inversely related to the stimulation duration up to 5 seconds and was at a lower end for stimulation frequencies ≥50 Hz. These findings together with the stimulation frequency and duration in Hannan et el. (2020b) model were used in decision-making for the selection of the precise stimulation frequency and duration. The frequency of 100 Hz was chosen with the aim to maximise the number of stimuli at the shortest stimulus duration (1 second) and to avoid potential neural damage due to repetitive exposure to high charge density. The maximal stimulus duration tested in this study was 10 seconds as per Hannan et al. (2020b) design.

3) **Stimulation mode**. Despite the increasing prevalence of depth arrays in clinical applications for therapeutic DBS and pre-surgical mapping, the biophysical properties of electrical brain stimulation are poorly understood. Most protocols with superficial arrays utilise bipolar as opposed to monopolar stimulation paradigms due to concentrated current delivery and minimal off-target current flows (Kuncel & Grill, 2004; Nathan et al., 1993). The practical difference lies within the electrode configuration used to inject the current. Bipolar stimulation refers to the stimulation between adjacent depth contacts whereas monopolar stimulation uses a distant reference electrode. Unlike in epicortical stimulation, the effects of the stimulation mode are not intuitive with the depth electrodes. Studies show that bipolar stimulation

is sensitive to the orientation of the neuronal tracts next to the stimulating electrodes limiting the current spread in longitudinal tracts (Kombos & Süss, 2009). However, the current spread is less well-controlled in monopolar stimulation which can become counterproductive when inducing focal seizures. Therefore, the electrical seizure model developed in this chapter employed bipolar stimulation.

4.1.3.4 Developing a technique for extracting fast impedance changes from depth recordings

To enable the extraction of fast impedance changes associated with ictal epileptiform ADs on depth electrodes, a reliable method for isolating and averaging reproducible electrographic patterns was paramount. Moreover, it was necessary to predict which SEEG waveforms would correspond to fast impedance drops and which electrographic patterns would be associated with no change in tissue conductivity. This was not intuitive as the recording electrodes in this experimental model were embedded in the vicinity of the activated neural networks as opposed to being arranged at the boundary where the detected signal represents spatially and temporally summated changes. In contrast, stereo-arrays were expected to trace the local recruitment of the epileptogenic circuits during ictal ADs and their evolution between the individual depth electrodes. Thus, only those electrographic patterns which reflected the activation of identical neural pathways could be averaged together to produce a representative footprint of ictal impedance changes in the brain.

The cellular and molecular pathways underlying the most common AD types have been described in the literature and can be used to predict the characteristics of fast depth impedance changes during ictal ADs (McCormick & Contreras, 2001). Based on the results of Hannan et al. (2020b), the most consistent and frequent type of ADs in the current rat model of on-demand electrical seizures was expected to be SWDs. As described in section 4.1.3.2, the coherent discharge of excitatory neurons during the ‘spike’ component and the subsequent neuronal silence attributed to the ‘wave’ part of the SWDs suggested that impedance change was likely to occur during the former (Neckelmann et al., 2000; Timofeev et al., 2002; Timofeev & Steriade, 2004). This hypothesis agreed with the observed activity pattern in Hannan et al. (2020b) model; however, it was unclear whether the temporal mismatch between the local changes on the depth electrodes and the summated changes at the brain surface would affect the representation of fast impedance changes detected by the depth probe. Furthermore, it was important to methodically distinguish between different SWD subtypes when they originate from cortical and/or subcortical structures in order to map the full trajectory of a seizure necessary for effective DBS protocols (Sitnikova & Van Luijtelaar, 2007).

In the previous fnEIT studies using epicortical electrodes, fast impedance changes were isolated and averaged triggering of the peaks of the SWD spikes which were identified and sorted using an automated unsupervised neuronal spike detection and classification algorithm (Hannan et al., 2020a; Hannan et al., 2018b; Quiroga et al., 2004). This algorithm is designed to identify spikes in multiunit recordings (600 – 3000 Hz) and to separate them into clusters based on their wavelet transform (Quiroga et al., 2004). Albeit time-efficient, this method is not optimised for processing of low-frequency signals, such as epileptic spikes (~15 – 20 Hz) and SWDs (1 – 5 Hz) in rats. Hence, the outcome tends to be contaminated with detection errors and, according to Hannan et al. (2018) findings, required manual adjustment which implies that subjective qualitative analysis of the signal was used as the ground truth making the automated spike classification somewhat redundant (Hannan et al., 2020b; Hannan et al., 2018b).

Whilst the current computational neuroscience landscape is vast with the available tools for automated signal processing and detection of ictal and interictal spikes, they typically rely on common discrete spike features, such as the spike amplitude, the prominence, the width, or the principal components (Gardy et al., 2020; Kyle et al., 2023; Mălîia et al., 2016; Stern et al., 2009; Valenti et al., 2006). Despite the integrative designs, these methods are rarely used without complementary visual inspection which has been occasionally reported to outperform the computational methods (Valenti et al., 2006). In light of this evidence, the technique for accurately identifying and clustering depth SWDs for the purpose of this study was developed by combining objective binary thresholding of the spike amplitude (≥ ~1 mV) and prominence (>0.1 mV) and subjective qualitative sorting of reproducible SWDs based on their morphological characteristics. The technique was firstly applied to the epicortical recordings which served as a positive control (Hannan et al., 2018b). To determine whether the surface activity was reflective of the intraparenchymal changes, epicortical and depth recordings of neocortical SWDs induced by electrical stimulation of the sensorimotor cortex were then compared (Hannan, et al., 2018b; Mareš et al., 2002). Since the epileptic spikes represent the hypersynchronous firing across multiple neural networks, alignment of spikes of different epicortical SWD categories was expected across multiple depth channels. The depth electrode which provided the best match to the surface activity and displayed the most prominent spikes was considered a 'leading' depth electrode located closest to the SOZ and was used for manual placement of trigger markers. Once the data analysis method was developed and tested, all other depth recordings were processed using triggers from a leading depth electrode in each recording to maximise the consistency and to ensure that no information was inadvertently lost by triggering off low voltage fluctuations distal to the SOZ. The method was trialled by processing epicortical and depth single-channel impedance recordings during neocortical SWDs induced in the same rat for accurate comparability.

4.1.3.5 Assessing the safety and the physiological impact of depth probe implantation

One of the main aspects which had to be critically assessed in this study to ensure the viability of the model and recording method was the neurophysiological impact of probe insertion. Invasive implantation of neuroprosthetic devices is known to trigger two types of responses in the surrounding tissues (Kozai et al., 2015; Szarowski et al., 2003). An acute response pertains to immediate tissue damage which includes (1) the tearing of the vasculature and neural cells with associated disruption to the BBB; (2) the volumetric displacement of tissue which, in combination with haemorrhaging and vasogenic oedema, causes mechanical strain and increases intracranial pressure. Following an acute response, microglia, the resident immune cells of the CNS, start transitioning from the resting (ramified) to activated (motile) state which enables their migration and aggregation around the implant (Kozai et al., 2012; Stence et al., 2001). Together with astrocytes, microglia ensheath and insulate the device from the surrounding neurons (Turner et al., 1999). The formation of the encapsulating matrix constitutes the second type of, or chronic, response. This response is continuously reinforced by sustained glial activation and the release of proinflammatory cytokines in response to the leakage of the molecules exogenous to the CNS (e.g., erythrocytes, immunoglobulins) through the compromised BBB (Kozai et al., 2010; Kozai et al., 2012; Szarowski et al., 2003; Winslow et al., 2010). Chronic inflammatory reaction is neurotoxic and eventually results in neurodegeneration and cell death (McConnell et al., 2009). All of these changes can adversely impact the functional capacity of the brain and compromise the experimental model under investigation.

Whilst the classification of acute and chronic reactions to neural implants is subjective, the first physiological changes start to occur with minutes of the probe insertion and can last up to several weeks post-implantation. Nonetheless, studies tracking the transition of fluorescently-labelled microglia show minimal changes in their motility for at least the first 6 – 12 hours after the intervention (Kozai et al., 2012; Stence et al., 2001). Since all experimental preparations in this study were non-recovery and lasted for up to 12 hours, acute tissue responses due to haemorrhaging and oedema were more relevant to the stability of the model and the impact on the recording quality. To assess the histological changes imposed by the probe insertion, seven rats were sacrificed for post-mortem processing after the completion of the recordings. The brains were dissected and processed for staining with haematoxylin and eosin (H&E) to visualise changes in cellular morphology around the insertion sites. Immunohistochemical markers were not examined as they were not expected to develop in the time course of the experiments. Depth arrays were always removed from the brain before fixing the tissue in the preservative, so that the probes can be reused. Such experimental protocol enabled the assessment of probe durability from a translational research standpoint.

In addition to informing safety, post-mortem histological analysis served as an independent method for verifying the anatomical location of each shank within the brain for additional evaluation of the insertion accuracy.

The real functional impact of acute brain damage could not be directly inferred from histological analysis due to the well-known degeneracy and redundancy of neural networks. Therefore, three additional control measures were implemented for tracking changes in brain activity post-insertion with respect to its pre-insertion state. ECoG traces on all epicortical channels were monitored during and after the insertion of the probe. Any periods of ECoG suppression or complete electrographic quiescence were considered signs of shock or adverse effects on the brain. ECoG changes informed about the insertion impact in the remote regions of the hemisphere not covered by the depth probe and where recordings of evoked activity were not practicable. To monitor the local impact of the probe which permeated a large portion of S1, epicortical and depth forepaw SEPs were tracked over time. The reason for tracking forepaw SEPs on both arrays were two-fold. Epicortical recordings served as an independent positive control for brain function but reflected summated activity of multiple forepaw S1 subfields recruited upon the activation of the median nerve. In contrast, depth electrodes were expected to detect more localised evoked forepaw activity and potentially reveal functional changes at a smaller scale.

4.2 Materials and Methods

4.2.1 Animal preparation and surgery

Experiments detailed in this chapter were performed in adult Sprague-Dawley rats, 300 – 450 g. Induction of the general anaesthesia as well as the surgical procedures, including cannulation of femoral vessels and craniectomy of the right hemisphere, were performed as described in 2.2.1 and 3.2.1. After the completion of all neurosurgical procedures, general anaesthesia was maintained using a combination of ≤0.6 % isoflurane and 20 µg/kg/hr IV fentanyl with an initial loading dose of 5 – 10 µg/kg. Acute supplemental boluses of fentanyl (5 – 10 µg/kg) were injected if vital signs indicated lightening of anaesthesia. In experiments where seizures were accompanied by profound motor symptoms producing artefacts in ECoG or SEEG data, the rats were paralysed with 1 – 2 mg/kg IV pancuronium bromide administered every ~90 min to maintain neuromuscular blockade for the duration of the recordings. All animal experimental work complied with the Animals (Scientific Procedures) Act 1986 and Home Office regulations.

As in previous chapters, respiratory parameters, ECG, IBP and core body temperature were monitored throughout the duration of each experiment (described in 2.2.1). A flowchart summarising the animal preparation procedures is shown in Fig. 4.5.

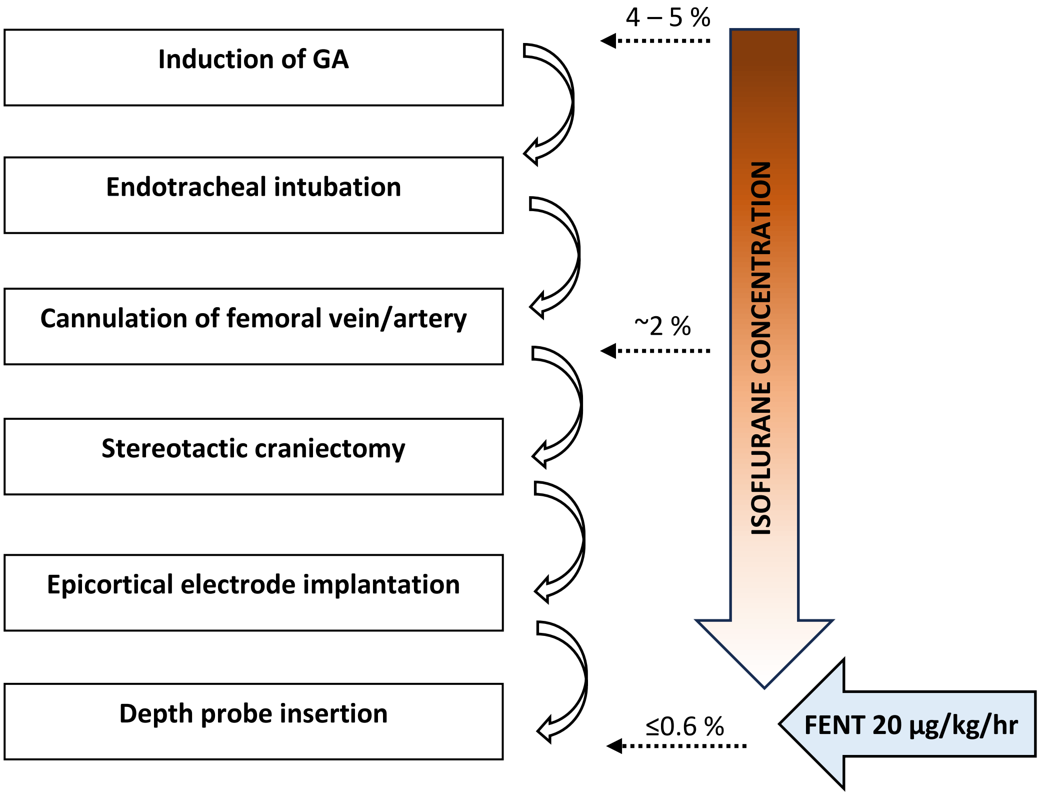

Figure 4.5. A flowchart summarising the animal preparation and surgical procedures. Isoflurane level (ISO) was gradually reduced from 4-5% administered at the induction of anaesthesia to ~2% for maintenance during surgery. After the implantation of the depth array, isoflurane was further reduced to ~0.6% and combined with a constant infusion of fentanyl (FENT) at 20 μg/kg/hr.

A planar epicortical array containing a 4 x 4 mm aperture centred on the forelimb S1 was implanted on the exposed cortex. The depth probe was inserted through the aperture by lowering it at 0.1 mm/s using a micromanipulator (Narishige International Ltd., London, UK) attached to the stereotaxic frame. Both arrays were fixed within custom-made holders. Warm (~38°C) aCSF was regularly applied to the exposed brain surface for maintaining moisture and for rinsing the blood off the insertion site. Depth probe insertion was consistently accompanied by a period of electrographic quiescence. Recordings were not commenced until complete functional recovery of the brain was observed. The reference and ground electrodes were placed through an incision in the nuchal skin before the implantation of the epicortical array.

4.2.2 Physiological impact of probe insertion

4.2.2.1 External bleeding

Any bleeding on the surface of the brain during/immediately after the probe insertion was noted in rats later sacrificed for histological processing (N = 7). Bleeding severity was classified subjectively into the following categories according to bleeding duration and/or visible perforation of a major blood vessel: 1) no visible bleeding; 2) minimal bleeding which stopped spontaneously after the insertion of the probe and did not require repeated applications of aCSF; 3) moderate bleeding which continued several minutes after inserting the probe and required multiple applications of aCSF; 4) severe bleeding which continued longer than a few minutes after probe insertion and where penetration of a major pial vessel(s) was observed.

4.2.2.2 Functional assessments pre- and post-implantation

Changes in brain function were assessed in rats which were sacrificed for histological processing (N = 7 rats). Two types of assessments were carried out. Firstly, changes in ECoG during and after the probe insertion with respect to pre-insertion pattern were assessed qualitatively. Any periods of electrographic quiescence were timed. Secondly, forepaw SEP were periodically recorded with the epicortical and depth electrodes (N = 6 rats). Evoked activity was stimulated by applying square symmetric biphasic charge-balanced pulses, 0.3 ms in duration, at a supramaximal current (2 – 10 mA) and at a frequency of 2 Hz to the contralateral forepaw via subdermal Ag/AgCl needle electrodes. Stimulation was delivered for at least 2 minutes to collect and average a minimum of 120 evoked responses. Recordings were obtained by both depth and epicortical electrodes at a minimum of two different timepoints post-insertion. The obtained recordings were then grouped into the following categories of post-insertion timings: 10 min, 20 min, 30 min, 1 – 2 hours, 2 – 3 hours, 3 – 4 hours, 4 – 5 hours and >5 hours (n = 24 recordings, N = 6 rats). Electrodes detecting the largest SEPs which were visibly distinct from baseline noise in the averaged signal were identified in each recording and their peak-to-peak amplitude was tracked over time in each rat. To account for the variation in the size of the SEPs across rats, the change in the SEP amplitude was expressed as a percent change with respect to the pre-implantation SEP amplitude on the same epicortical electrode or with respect to the first SEP measurement obtained on the same depth electrode. A two-way ANOVA was conducted to determine whether the SEP size was impacted by the visible amount of bleeding and whether the SEP amplitude changed significantly over time after probe implantation (dependent variable: SEP amplitude; independent variables: bleeding severity, time). The post-hoc pairwise comparisons were performed using a Tukey-Kramer test. A significance level $\alpha = 0.05$ was used for all analyses.

4.2.3 Depth probe insertion precision

The depth probe insertion rigor was assessed by localising the maximal forelimb and hindlimb SEPs on the depth electrodes and evaluating their consistency across rats (n = 40 recordings, N = 13 rats). Somatosensory stimulation was sequentially applied to a contralateral forepaw and a contralateral hindpaw in each rat using the same stimulation protocol as described in 4.2.2. The raw signal on each depth electrode was averaged triggering off the repeated stimulus in 500 ms epochs which spanned from 250 ms pre-stimulus to 250 ms post-stimulus. The peak-to-peak amplitude of the resulting SEPs was calculated to determine the top three channels which were deemed to be in the vicinity of the respective S1 divisions.

The probe position consistency describing insertion precision was characterised by a new measure, termed intensity of the forepaw and hindpaw SEPs on depth electrodes across rats. The SEP intensity was a combined measure of the amplitude and the location of the SEPs and described the recurrence of the maximal SEPs on the same depth electrodes across depth probe insertion trials. SEP intensity was derived by scoring the three maximal SEPs on a three-point system. Electrodes were rated by assessing each recording independently and then summing the points. The depth electrode which always detected the largest forepaw SEPs across all 25 recordings of somatosensory forepaw activity was scored 25 x 3 = 75 points (n = 25 recordings, N = 12 rats). Similarly, the electrode which recorded the largest hindpaw SEPs across all 15 recordings of evoked hindpaw activity was awarded 15 x 3 = 45 points (n = 15 recordings, N = 12 rats). Electrodes which never detected one of the top three SEPs received 0 points. The final intensity measure was a normalised intensity score computed by dividing the total points awarded for each electrode by the maximal possible score, that is 75 or 45 for forepaw and hindpaw SEPs, respectively. Depth electrodes which detected the largest SEPs in all recordings received the score of 1.0 while electrodes which never detected SEPs received a score of 0. The final intensity score of ≥0.5 on at least one depth electrode was considered to the indicate consistent anatomical placement the depth array across subjects. The probability of the largest SEPs recurring on the same depth electrode was calculated by dividing the recurrence frequency of the maximal SEPs across all recordings by the total number of recordings and expressing it in percent.

4.2.4 Induction of electrical seizures

Electrical seizures were induced by the stimulation of cortical and subcortical areas (N = 7 rats). Seizure induction sites were grouped by the region (cortical vs. subcortical) and ranked by the distance between stimulating electrodes (1 – 3.77 mm). All epileptiform events were provoked by administering a train of square biphasic symmetric charge-balanced pulses with a duration of 1 ms and oscillating at 100 Hz. Stimulation current intensity and stimulation duration were varied between 0.2 – 4 mA and 2 – 10 seconds, respectively. If the stimulation resulted in abnormal ADs containing stereotypical waveforms, such as rhythmic sharp waves, spikes or polyspikes, and SWDs or polyspike-and-wave discharges (PSWDs) appearing immediately after the cessation of stimulation and lasting for ≥6 seconds, an induction event was deemed successful. In cases where stimulation-induced ADs lasted >30 seconds with concomitant evolution in morphology and frequency as well as motor symptoms, they were classed as prolonged ADs. Stimulations were spaced by a minimum of 10 minutes to minimise kindling and allow sufficient time for post-ictal recovery (Hannan et al., 2020b). To ensure adequate distinction between the background activity and stimulation-induced ADs, baseline and post-ictal SEEG were recorded for up to 1 min prior to the delivery of the stimulus and up to 10 min after the cessation of epileptiform activity.

4.2.5 Single-channel epicortical and depth measurements of fast impedance changes during ictal ADs

Single-channel recordings of epicortical (n = 1) and depth (n = 3) fast impedance changes during neocortical ictal ADs were obtained in one rat (N = 1). Seizures were induced using the optimised induction protocol by delivering the stimulation via a neocortical pair of depth electrodes which yielded the prolonged ADs during the optimisation of the model. To capture epicortical fast impedance changes, AC of 1.725 kHz and 50 µA was injected via a pair of epicortical electrodes proximal to the epicortical contact detecting the largest SWDs. Fast impedance changes on the depth electrodes were subsequently recorded in the same rat during the same type of seizure whilst injecting 1.725 kHz, 50 µA EIT current via the seizure-stimulating electrodes.

4.2.6 Selection of trigger markers for averaging ictal ADs

For extracting ictal fast impedance changes, trigger markers were placed manually at the peaks of the spikes from reproducible epicortical SWDs. An absolute peak-to-peak amplitude threshold of 1 mV and a minimal spike prominence threshold of 0.1 mV was used to identify the leading channels. The selected SWDs were grouped by subjective evaluation of their electrographic feature similarity. Triggers corresponding to identical SWDs were used to average epicortical ictal fast impedance changes and verified against the literature (Hannan et al., 2018b). This served as a positive control confirming the physiological integrity of the epileptogenic tissue generating fast neural changes during seizures.

Next, epicortical trigger markers were aligned with the SWDs detected by all depth electrodes during the same neocortically-induced seizure. A ‘leading’ depth electrode was determined by the largest spike prominence of the recorded depth SWDs and by their near-precise alignment with the epicortical trigger markers from each cluster. These findings were used to guide the identification of the ‘leading’ depth electrode in subsequent single-channel recordings in the same rat (n = 3 seizures, N = 1 rat). Thresholding in later recordings was streamlined using an intrinsic MATLAB function (The MathWorks, Inc., Natick, MA, USA) which isolated the local maxima with a pre-specified prominence and was followed by manual clustering as described above.

4.2.7 Histological processing and analysis

Seven rats (N = 7) were sacrificed for histological processing and analysis. Once the recordings were completed, rats were euthanised by an overdose of IV pentobarbital (200 mg/kg). Immediately following the confirmation of death, the depth probe and the epicortical array were carefully explanted trying to minimise additional inadvertent damage to the exposed hemisphere. The skull was removed from the contralateral hemisphere by drilling a mirrored craniotomy. The brain was swiftly excised using a pair of miscroscissors and removed from the skull using a rongeur. A 10 % neutral-buffered formalin solution was used to preserve the brain tissue for a minimum of 2 months. Further processing was conducted in an automated tissue processor Leica ASP300 (Leica Microsystems Ltd, Sheffield, UK). The fixed brains were exposed to a sequence of reagents, namely, 70 % ethanol, 90 % ethanol, xylene, and infiltrated with paraffin. The processed brain tissue was then embedded in paraffin wax on Leica EG1150H Embedding station ASP300 (Leica Microsystems Ltd, Sheffield, UK). Once set, the embedded tissue was sectioned coronally with a vibrating microtome Leica RM2235 ASP300 (Leica Microsystems Ltd, Sheffield, UK) every 100 µm in the first sample (rat 5 in Table 4.1) and every 50 µm in the remaining three samples (n = 305 slices, N = 7 rats). The thickness of the microtomy was 5 µm. Each section was stained with the H&E stain in the Autostainer Leica ST5020 (Leica Microsystems Ltd, Sheffield, UK) and then scanned with a Hamamatsu NanoZoomer S360 scanner (Hamamatsu Photonics K. K., Hamamatsu City, Japan) for visualisation. Histological analysis was performed qualitatively by comparing the histopathological markers between the hemispheres for within-subjects control and across the rats for between-subject control. Each slice was matched with the AP coordinates in the Paxinos and Watson (2013) rat brain atlas and examined for signs of brain damage. Brain damage, or injury, was defined by the presence of extravascular erythrocytes and lymphocytes, neural tissue rarefaction caused by oedema, cytoplasmic vacuolation, pyknosis, and mechanical tearing. Slices were examined using NDP viewer software (Hamamatsu Photonics K. K., Hamamatsu City, Japan). Probe insertion accuracy was measured by quantifying the difference in the expected and the real probe distance from bregma and from the midline. The most anterior slice with visible probe damage was labelled as layer A and used as a reference point for determining the real insertion site. The remaining insertion points were identified either in reference to layer A, or by localising specific shank-related injury based on the recorded locations of external bleeding. The position of the probe in ML axis was determined by manually estimating the average distance between the middle shank in layer A and the midline over all slices with a clearly visible insertion site for this shank. All abnormal histological findings were compared between different external bleeding categories and correlated with other physiological assessments to determine potential functional implications. The brain area occupied by the largest lesion (defined by the evidence of brain damage as above) in each rat was quantified using ImageJ2 (Schindelin et al., 2012).

4.2.8 Electrical testing of the depth arrays

There were eight probes available for this project, and each of those probes were electrically tested at least once to ensure their suitability for recording seizures and/or associated fast/slow neural changes with EIT. Depth electrode impedance was measured by two methods. Initial characterisation was performed via the electrochemical impedance spectroscopy (EIS) using the Palmsens 4 potentiostat (PalmSens BV, Houten, The Netherlands) recording electrode impedance in a frequency range of 1 – 2 kHz. If, according to EIS measurements, >50 % electrodes in the array had an impedance of >5 kΩ, the probe was considered unusable. Based on these metrics, one out of eight available arrays was immediately discarded. Further testing was performed in a saline tank where electrode impedance was measured using a two-electrode technique. An AC with an amplitude of 100 µA and frequency of 1.725 kHz was passed sequentially between each depth electrode and a large circular Ag-AgCl reference electrode submerged in the tank. Voltage measurements were obtained by the same injecting electrodes. According to Ohm's law, the resulting standing voltage on the injecting channels was proportional to the transfer impedance which, in this case, was a combined product of the impedance of saline and the impedance of both injecting electrodes. As the measurements were taken with respect to one of the injecting electrodes (reference electrode) and given the negligible impedance of saline at room temperature, the transfer impedance with each injection pair could be approximated by the impedance of the injecting depth electrode. The depth electrode impedances were therefore estimated as follows:

$$Injecting\ electrode\ impedance\ Z\ (k\Omega) = \frac{Standing\ voltage\ V\ (mV)}{Injection\ current\ I\ (\mu A)}$$

Each array was re-used until one of the following: 1) the number of electrodes with acceptable impedance dropped below the 50 % threshold; 2) subjective qualitative increase in background noise was observed in depth electrode recordings; 3) mechanical damage to the probe occurred during implantation/removal of the probe from the brain.

4.2.9 Recording hardware

Both somatosensory stimulation and seizure induction was driven by the Keithley 6221 current sources (Keithley Instruments Ltd, Solon, OH, USA) with parameters of injected current manually controlled via the custom MATLAB code (The MathWorks, Inc., Natick, MA, USA).

Epicortical and depth recordings were made with respect to a large circular (~7 mm in diameter) Ag-AgCl reference electrode placed under the rat's nuchal skin before the implantation of the epicortical array. ECoG and LFP data was collected from all available epicortical and depth electrodes which yielded a maximum of 37 and 36 recordings, respectively. Data was sampled at 25 kHz using all 128 channels in the actiCHamp EEG amplifier (Brain Products GmbH, Gilching, Germany; see Appendix A for detailed specifications). Data collection and real-time display was controlled by the BrainVision Recorder software (Brain Vision LLC, Morrisville, NC, USA).

4.2.10 Data processing and analysis

4.2.10.1 Recordings of electrical seizures

Recordings from each depth and epicortical electrode were filtered with a 1 Hz high-pass filter (1st order, Butterworth) followed by a 100 Hz low-pass filter (5th order, Butterworth). Mains noise was removed by an application of a 50-Hz notch filter (2nd order, IIR). Ictal ADs, which fit the definition provided in section 4.1.3.3, were identified by visual qualitative inspection of the filtered recordings and comparison to the baseline SEEG/ECoG. The peak-to-peak amplitude and the duration of the train of ADs was quantified for identifying the optimal electrical stimulation parameters yielding the most consistent and the longest seizures.

4.2.10.2 Single-channel fast impedance recordings of ictal activity

Recordings from each depth and epicortical electrode were firstly filtered with a 500 Hz bandpass filter, ±250 Hz around the carrier frequency (5th order, Butterworth). This provided a temporal resolution of 4 ms. Demodulation was then performed using the Hilbert transform. Demodulated data was segmented into 150 ms epochs (-50 ms to 100 ms) around the trigger markers isolated as described in section 4.2.5. The timepoint of 0 ms marked the peak of the spike component. Before segmentation, a 10 Hz high-pass filter (4th order, Butterworth) was applied to eliminate any potential cardiac (~5 Hz) and respiratory (~1 – 2 Hz) modulations in the recorded data which could create artefactual impedance changes. All epochs were averaged together to yield a fast impedance change which was expected within 60 ms around the peak of the spike (-30 ms to +30 ms) and identified by visual assessment. Epochs which contained data points greater than the upper quartile plus five times the interquartile range or less than the lower quartile minus five times the interquartile range were considered outliers and were removed before averaging. Timepoints corresponding to statistically significant impedance changes with respect to baseline in the averaged signal were determined by running a one-way t-test for each time point across all epochs with a significance level $\alpha = 0.05$. Resulting p-values were adjusted using Bonferroni correction method with the same significance level.

4.3 Results

4.3.1 Electrical quality testing of depth arrays

Electrical testing showed that seven out of eight probes available for the method development had >70 % of electrodes with acceptable impedance before their first use (Fig. 4.5). Only one out of eight available probes had <50 % of electrodes with impedance of ≤5 kΩ. Repeated impedance measurements showed that the number of ‘good’ electrodes in all probes decreased with use (Fig. 4.6). However, none of the re-tested probes (probe 1, 3, 4, 6, 7) approached the threshold of unacceptable impedance after the first use (Fig. 4.6). The probes which were re-tested three times displayed the same trend after two uses (probes 1 and 7; Fig. 4.6). Probe 7 showed an unusual increase in the number of ‘good’ electrodes in the second test but then declined similarly to other probes.

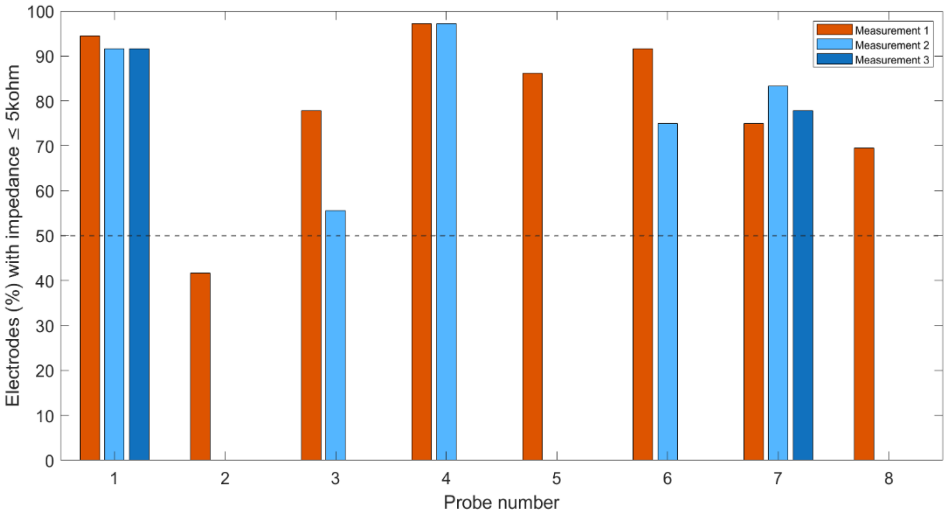

Figure 4.6. Proportion of depth electrodes with acceptable contact impedance across all probes designed for the purpose of the project. All probes were coated with PEDOT:PSS to achieve contact impedance low enough for neural EIT recordings. One out of eight available probes (probe no. 2) did not meet the criteria and was immediately discarded. The probes were used one at a time and replaced when/if electrode impedance exceeded the threshold, recordings displayed increased background noise or probe incurred mechanical damage. The dashed line signifies the probe quality threshold.

4.3.2 Depth probe insertion site reproducibility across animals

Evoked somatosensory forepaw and hindpaw activity detected by the depth electrodes was a functional marker for probe insertion precision. Overall, the intensity scores for both the forelimb and the hindlimb SEPs suggested precise and accurate depth probe insertion site across tested subjects (Fig. 4.7).

The depth electrodes which detected maximal forepaw SEPs in ≥50 % of the recordings were A4, A8, B4, and B8 with SEP intensity scores of 0.4, 0.39, 0.51 and 0.37, respectively (n = 25 recordings, N = 12 rats; Fig. 4.7). The intensity values for the remaining electrodes which detected one of the three maximal SEP across all sweeps ranged between 0.03 – 0.08 with 4 – 16 % detection frequency. The depth electrodes which reproducibly recorded maximal hindpaw SEPs in ≥50 % of recordings were B12 and C12 with intensity scores of 0.56 and 0.62, respectively (n = 15 recordings, N = 12 rats; Fig. 4.7). The intensity values for the remaining electrodes which recorded maximal SEPs in at least one recording ranged between 0.02 – 0.20 with the detection frequency of 6.7 – 33.3 %.

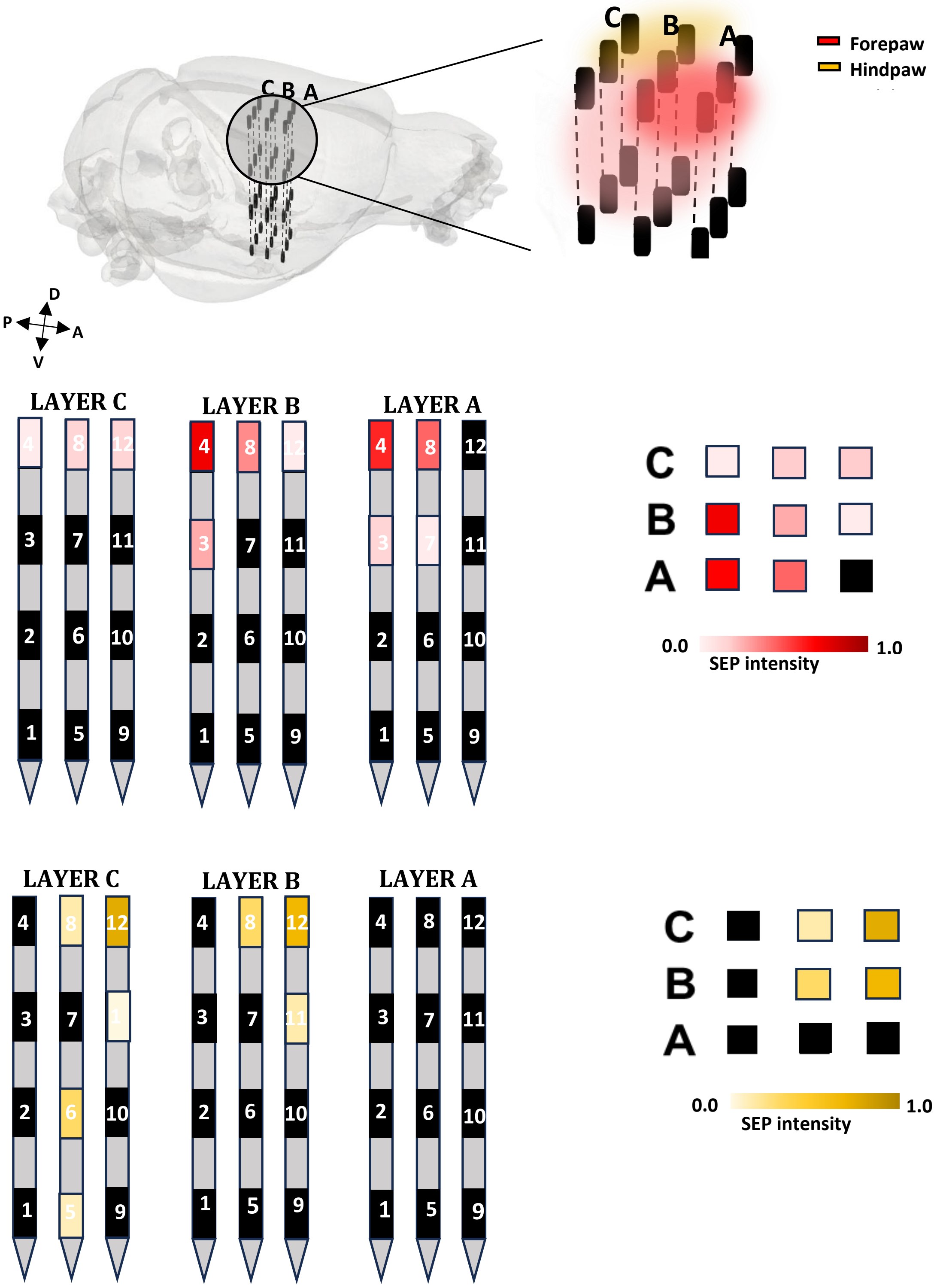

Figure 4.7. Reproducibility of the location of forepaw (red) and hindpaw (yellow) SEPs on depth electrodes across rats served as a marker of probe insertion accuracy and precision. Probe insertion accuracy and precision was assessed by recording evoked forepaw and hindpaw activity using the depth electrodes (n = 40 recordings, N = 13 rats). SEP intensity was derived by scoring the electrodes based on the amplitude and the frequency of forepaw and hindpaw SEPs. Forepaw SEPs were reproducibly detected on the electrodes in the antero-lateral portion of the array (maximal intensity 0.52) whereas hindpaw SEPs were mostly located on the electrodes in the posteromedial portion of the array (maximal intensity 0.6). The location of the maximal SEPs agreed with the predicted insertion site shown in Figure 4.2 and the intensity of these SEPs indicated high insertion precision.

4.3.3 Optimal seizure induction parameters and stimulation sites

There was a total of 94 seizure induction trials in seven rats (n = 94, N = 7) at 13 different stimulation sites in selected cortical and subcortical structures. The distance between the stimulating electrodes ranged 1.00 – 3.77 mm. Overall, when the stimulation was delivered for <2 seconds, acceptable ADs could be evoked in only one out of 14 trials across all selected regions and irrespective of the current amplitude (n = 14 inductions, N = 3 rats). Additionally, only 41% of stimulations with ≤0.5 mA led to successful ADs in both cortical and subcortical stimulations (n = 64 induction attempts, N = 3 rats). Moreover, over 50 % of successful stimulations at low current levels (≤0.5 mA) were delivered for ≥5 seconds. The seizures lasting up to 1.5 minutes were observed when electrical stimulation was administered at a minimum intensity of 2 mA for at least 5 seconds (n = 9 inductions, N = 2 rats).

4.3.3.1 Cortical stimulations

Induction of consistent neocortical ADs was attempted at eight stimulation sites (n = 44 inductions, N = 7 rats). Successful stimulations (n = 28) induced ADs lasting 7.2 – 89.7 seconds (median 17.2 seconds). Prolonged ADs were evoked in 43 % of the trials (n = 12 inductions) with the majority (36 %) induced with stimulating electrodes flanking the boundary between hindlimb primary somatosensory and motor cortices (S1/M1HL) and whisker S1 (S1BF) with an interelectrode distance of 3.77 mm (n = 10 inductions). In all cases, the observed ictal activity comprised primarily 1 – 4 Hz SWDs with an amplitude of up to 4 mV and were occasionally interspersed with fast (8 – 10 Hz) runs of rhythmic sharp waves which then tapered off to slow (≤1 Hz) PSWDs at the end of the seizure (Fig. 4.8). The largest SWDs were typically detected by the electrodes with the peak forepaw activity, namely electrodes A4, A8, B4, and B8 (Fig. 4.6 and 4.7). SWDs were morphologically homogeneous between seizures and temporally aligned across electrodes within each seizure (Fig. 4.8). On the contrary, PSWDs were always smaller and more inconsistent in their presentation than SWDs. Seizures were frequently accompanied by motor symptoms including forelimb clonus and/or whole-body tonic response with the contraction towards the non-stimulated side.

4.3.3.2 Subcortical stimulations

Induction of consistent subcortical ictal ADs was trialled at five stimulation sites located in the thalamus and the striatum (n = 50 inductions, N = 5 rats). Successful stimulations (n = 29) produced trains of ADs lasting 7.6 – 33.3 seconds (median 17.8 seconds). Prolonged ADs were observed in 7 % of the trials where the stimulation was directed at CPu complex (electrode separation distance 2.87 mm). The most prominent ADs with an average amplitude of 2 mV were observed on the same contacts as those featured in neocortical seizures. The morphology of the ADs evoked by subcortical stimulation was akin to neocortical and comprised positive- or negative-facing SWDs (1 – 4 Hz) and mostly negative-facing PSWDs (≤1 Hz) (Fig. 4.9).

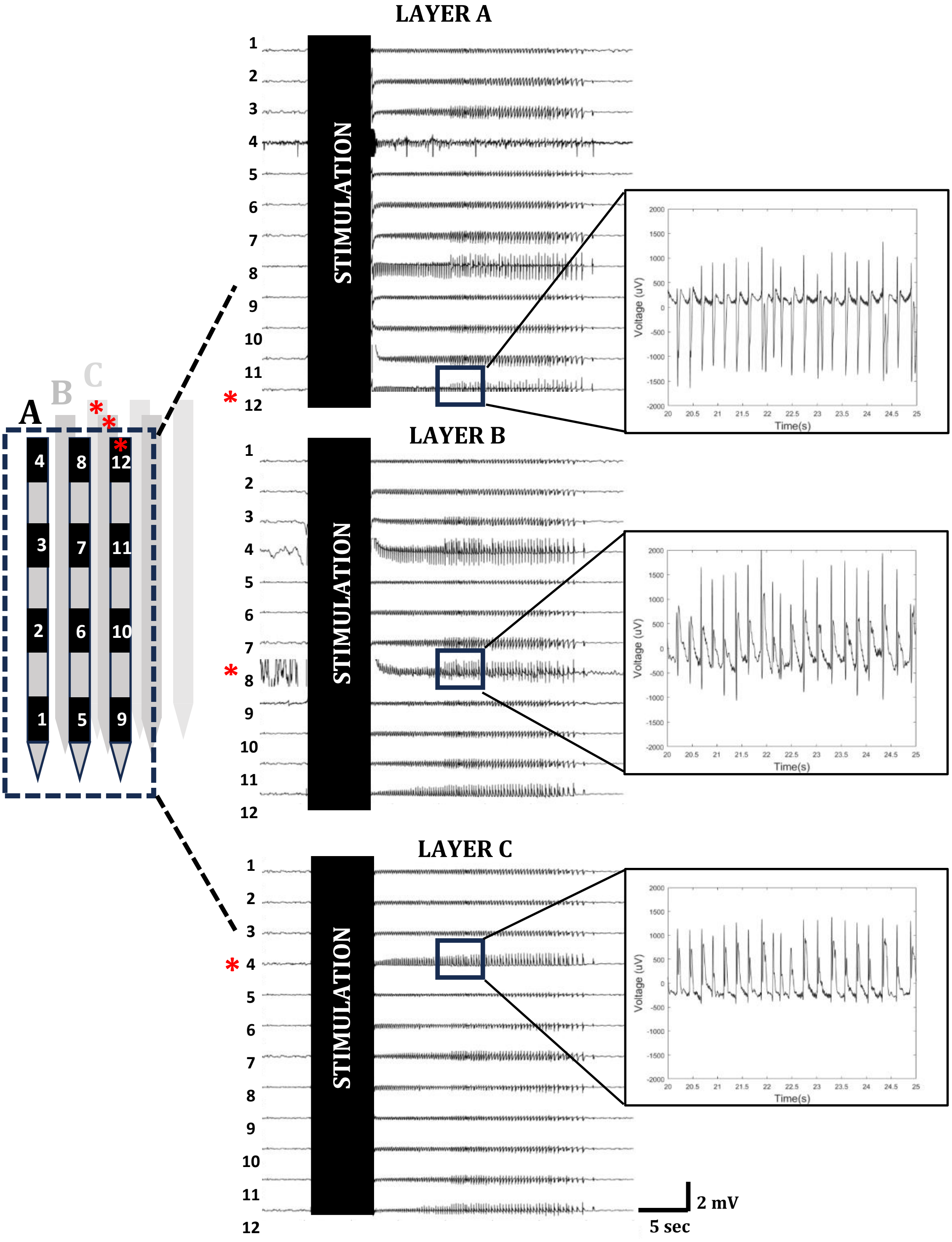

Figure 4.8. A representative example of depth electrode recordings during a neocortically-induced seizure. Electrical stimulation of S1 region delivered across all six cortical layers reliably produced a burst of ADs which predominantly comprised 1 – 4 Hz SWDs with an amplitude of up to 4 mV. Largest ADs were detected on the most superficial contacts as shown in the figure.

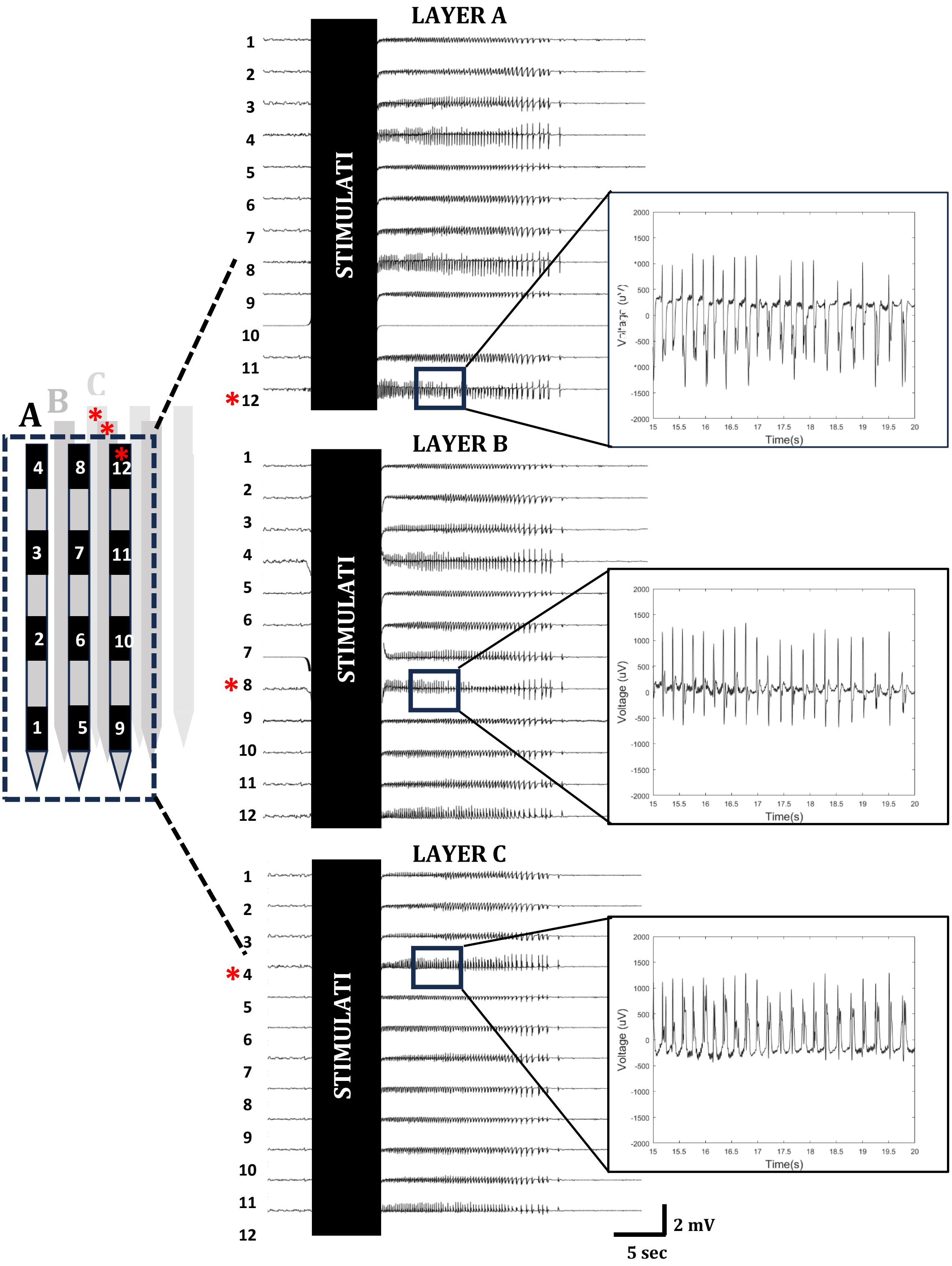

Figure 4.9. A representative example of depth electrode recordings during a subcortically-induced seizure. Electrical stimulation of subcortical structures provoked a burst of ADs which contained mostly SWDs and PSWDs at variable frequencies and with an amplitude of 1 – 4 mV. The figure shows an example of a run of ADs resulting from the stimulation of the dorsal striatum, an important functional component of basal ganglia.

4.3.4 The trigger selection method for extracting fast ictal impedance changes on depth electrodes

Neocortical seizures were induced by delivering the stimulation using a pair of depth electrodes which yielded the longest ADs established in the previous method development section (4.3.3). Single-channel epicortical fast impedance changes were simultaneously recorded by injecting current through a proximal pair of epicortical electrodes (n = 1 recording, N = 1 rat). The electrical seizure lasted for approximately 50.2 seconds and could be divided into two distinct phases (Fig. 4.10). The first part of the seizure was composed of 1 – 4 Hz SWDs interleaved with occasional isolated spikes and slower (≤1 – 4 Hz) sharp waves which gradually tapered off into low-amplitude PSWDs in the second part of the seizure (Fig. 4.10). The morphology of PSWDs was mixed and, therefore, they could not be averaged. In the first phase of the seizure, two electrodes were identified as consecutively 'leading' based on the stereotypic appearance of reproducible SWDs, their overall amplitude and spike prominence (electrode 4 and 9, Fig. 4.10). SWDs were then grouped into clusters and triggers were placed at the peaks of the spikes of each SWD within the respective cluster.

This arbitrary trigger selection was verified by using them to average epicortical fast impedance changes associated with ictal SWDs. The first cluster of SWDs yielded maximal impedance changes of -0.04 % on two electrodes (Fig. 4.12A, $p < 0.05$, one-way t-test with Bonferroni correction). The second cluster yielded maximal impedance changes of -0.03 – -0.07 % on four epicortical electrodes (Fig. 4.12B, $p < 0.05$, one-way t-test with Bonferroni correction).

Next, the epicortical trigger markers were aligned with the extracellular voltage changes recorded by the depth electrodes during the same seizure (Fig. 4.11). Each cluster of epicortical trigger markers aligned with a different set of 'leading' depth electrodes. The first set of epicortical triggers corresponded to the peaks of distinct spikes (prominence of >0.1 mV) detected by the depth electrodes in the top cortical layers (Fig. 4.2 and 4.11). In comparison to the first cluster, the second set of epicortical trigger markers did not match as many of the depth SWDs (Fig. 4.11, grey lines in the bottom plots are in misalignment). Overall, SWDs detected by the depth electrodes at the boundary between the bottom cortical layers and the subcortical structures matched most precisely with the second set of trigger markers (Fig. 4.2 and 4.11).

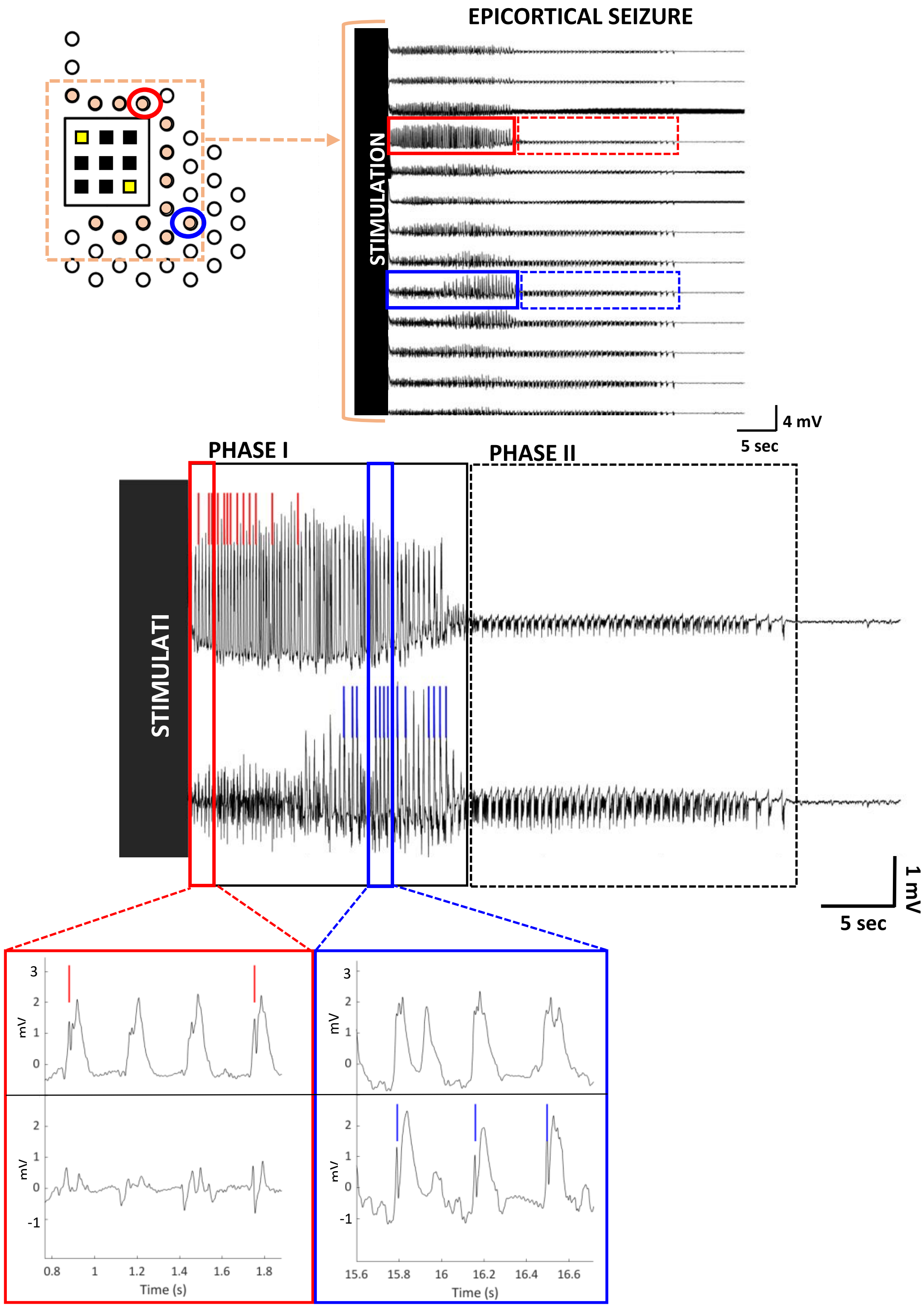

Figure 4.10. Epicortical triggers were placed manually by identifying different SWD types. Neocortical seizure was evoked by electrical stimulation of sensorimotor cortex using the depth probe. Epicortical recordings showed two distinct phases of the induced seizure based on the types of ADs. Phase I commenced immediately after the stimulation and comprised predominantly 1 – 4 Hz SWDs as well as sharp waves, and occasional isolated spikes. Phase II consisted predominantly of slow (≤1 Hz) PSWDs with largely variable morphology. Two leading epicortical electrodes were identified based on the amplitude, the prominence and the morphological similarities of the comprising SWDs. This resulted into two distinct clusters of epicortical SWDs. Red and blue colours signify two different SWD clusters isolated from two different leading electrodes in the epicortical array.

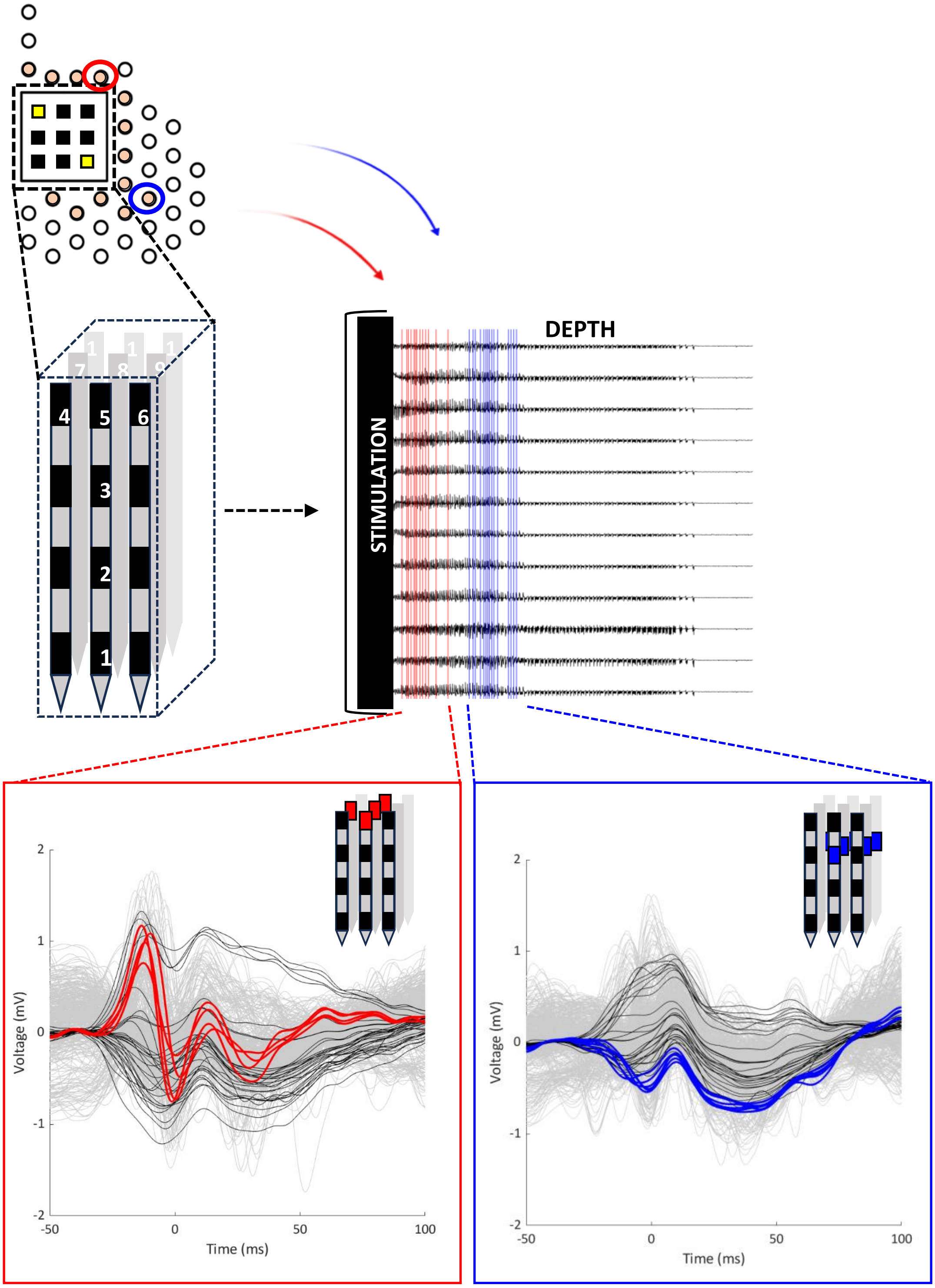

Figure 4.11. Epicortical trigger markers from different SWD categories aligned with depth SWDs from different cortical layers. Triggers isolated from each SWD cluster were aligned with the depth recordings to establish the leading depth electrodes considered proximal to the epicentre of epileptiform activity in each timepoint. Both groups of triggers aligned with a discrete subset of depth electrodes detecting the most prominent spikes. The first subset of trigger markers near-perfectly aligned with the spikes detected by the depth electrodes in the most superficial cortical layers. The second subset of epicortical triggers aligned best with the depth SWDs in the bottom cortical layers indicating the spread of the seizure over time. Red and blue colours signify trigger markers from two different leading epicortical electrodes with two distinct SWD clusters. The corresponding leading depth channels are shown in the same colours. Bottom panel: grey lines represent individual SWDs from each depth electrode while black lines represent the averaged SWDs from those channels.

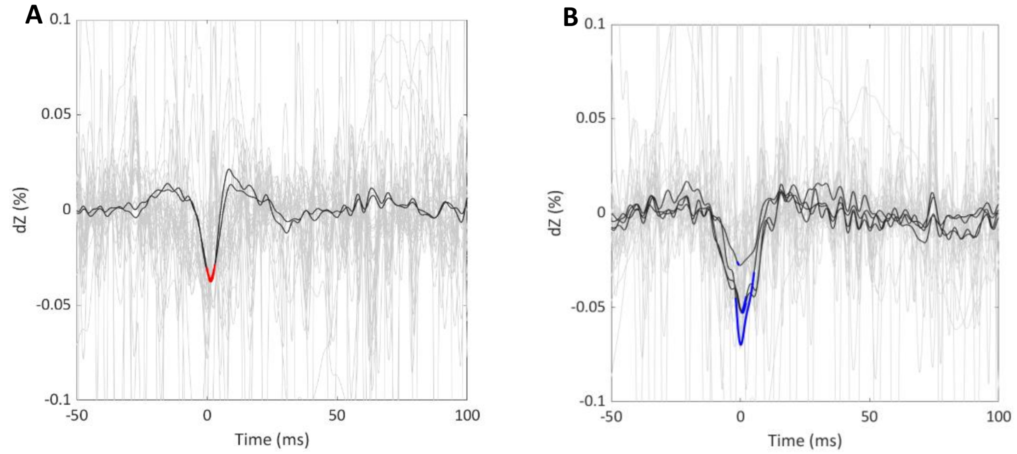

Figure 4.12. Manual trigger identification reliably isolated epicortical fast impedance changes associated with different SWD types. Epicortical single-channel impedance recordings were segmented and averaged using trigger markers from two SWD clusters isolated by manual detection. Significant fast impedance changes of -0.04 % were detected on two electrodes based on the triggers from the first cluster (significant timepoints in red; p < 0.05, one-way t-test with Bonferroni correction). Significant fast impedance changes of -0.03 – -0.07 % were detected on four epicortical electrodes based on the triggers from the second cluster (significant timepoints in blue; p < 0.05, one-way t-test with Bonferroni correction). Black lines represent significant epicortical fast impedance changes on individual electrodes while grey lines represent average impedance traces on the remaining electrodes.

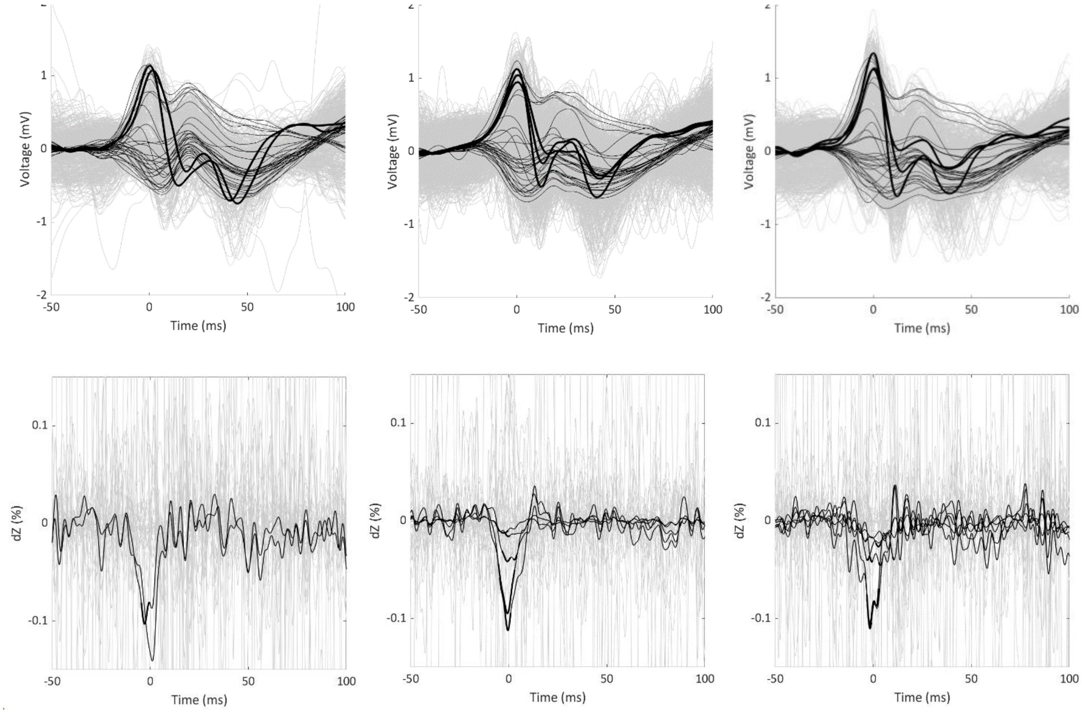

Figure 4.13. Depth electrodes with the most prominent spikes were used for accurate positioning of the trigger markers and subsequent averaging of ictal fast impedance changes associated with depth SWDs. The most prominent neocortical SWDs were consistently detected by the same depth electrodes and displayed qualitatively identical characteristics. The isolated depth SWDs yielded significant impedance changes with the amplitude of -0.01 – -0.11 % (n = 3 recordings, N = 1 rat). Significant timepoints are marked with bold lines (p < 0.05, one-way t-test with Bonferroni correction). Top panel: grey lines represent individual SWDs isolated from all depth electrodes, black lines are averaged SWDs on each depth electrode, the lines in bold are the averaged SWDs from the leading electrodes. Bottom panel: black lines represent significant negative impedance changes from individual depth electrodes; grey lines represent impedance changes detected by the remaining depth electrodes.

Based on the above findings, the accuracy of subjective trigger isolation method was tested in the same rat by recording single-channel fast impedance changes during ictal neocortical SWDs on the depth electrodes (n = 3 recordings, N = 1 rat). In each recording, the most prominent spikes were consistently detected by electrodes 4 and 7 labelled according to the numbering system in Fig. 4.11 (Fig. 4.13). Filtered SEEG data from these electrodes was used to isolate the trigger markers for averaging identical ictal SWDs. There were 21 – 45 reproducible SWDs within each seizure (mean = 34 triggers). Averaging impedance traces corresponding to these SWDs yielded significant negative fast impedance changes of -0.01 – -0.11 % with a mean change of -0.06 ± 0.01 % (mean ± S.E., n = 3 recordings, N = 1 rat; $p < 0.05$, one-way t-test with Bonferroni correction) associated with the ictal SWDs on 12 depth electrodes across three seizures in this rat (Fig. 4.13; significant changes shown in black). Due to current deflection, three statistically significant positive impedance changes with an amplitude of 0.04 – 0.17 % were detected by three different electrodes in two recordings; however, they were not considered physiologically significant (Fig. 4.13; $p < 0.05$, one-way t-test with Bonferroni correction).

4.3.5 Assessment of probe implantation accuracy and safety

4.3.5.1 Physiological and functional impact of probe implantation

The summary of all physiological and functional assessments is presented in table 4.1. Visible bleeding severity upon probe insertion ranged from none to severe in seven rats (N = 7). There were no signs of haemorrhaging in two rats, bleeding was minimal in one rat, moderate in two rats and severe in the remaining two rats.

ECoG changes post-insertion were recorded in six of those seven rats (changes in one rat were not recorded in error). A notable decrease in ECoG amplitude was seen in all rats for up to 30 min following the insertion of the probe. Complete electrographic quiescence was observed for 2 – 10 min in four rats (Table 4.1).

Epicortical and depth forepaw SEPs were monitored pre- and post-insertion in six out of seven rats since reliable SEPs could not be evoked at any point during the experiment in one of seven rats. The results are shown in figure 4.14. Both bleeding severity and time after insertion correlated significantly with the change in the epicortical forepaw SEP relative to the pre-insertion amplitude (n = 24 SEP sweeps, N = 6 rats; $p < 0.05$, two-way ANOVA; Fig. 4.13 A). Overall, epicortical SEPs showed a tendency to increase with time (Fig. 4.14). There was an initial statistically insignificant drop of -42.5 ± 24.0 % (mean ± S.E.) in epicortical SEP size within the first 10 min post-insertion followed by a statistically significant increase of 237.4 ±

75.1 % by 3 – 4 hours post-insertion with respect to baseline and 10 min measurements ($p < 0.05$, Tukey-Kramer post-hoc test).

In contrast to epicortical SEPs, the amplitude of depth SEPs was only impacted by the time of the recording but not by the bleeding severity (n = 18 SEP sweeps, N = 6 rats; respective p-values of <0.01 and >0.1, two-way ANOVA; Fig. 4.14B). Depth SEPs were significantly larger at 30 min, 1 – 2 hours, 3 – 4 hours, and 4 – 5 hours when compared to their initial amplitude but not with respect to each other (corresponding p-values of $p < 0.001$ and $p > 0.1$, Tukey-Kramer post-hoc test). The amplitude intermittently returned to baseline level between 1 – 2 hours post-insertion and dropped below baseline at >5 hours post-insertion ($p < 0.01$ in both cases, Tukey-Kramer post-hoc test).

4.3.5.3 Histological findings

Probe insertion accuracy

Based on the earliest signs of histological damage in coronal slices, probe insertion location could have deviated from the expected site towards the anterior of the brain by 0.7 – 1.7 mm, with a median deviation of 1.7 mm (n = 16 slices, N = 7 rats). The probe was located more laterally than expected by 0.6 – 1.9 mm with a median shift of 1.7 mm towards the lateral edge of the hemisphere (n = 16 slices, N = 7 rats). Examples of brain slices with the markers of insertion sites at each probe layer from two rats are shown in Figure 4.15.

Brain damage

Histological processing revealed that all shanks across all probes and all rats left visible brain lesions (n = 305 slices, N = 7 rats; Fig. 4.16). The likely insertion sites were localised by the following markers. There was vertical tearing of neural tissue along the DV axis with and without extravascular accumulation of blood. In cases where mechanical lesions were not visible, neural tissue appeared rarefied and oedemic. Affected brain regions in all rats also displayed signs of hydropic degeneration and pyknosis. Representative examples of various types of histological damage surrounding probe insertion points identified in brain slices are shown in Figure 4.16.

The cross-sectional area of the largest insertion-related lesion in each rat ranged between 0.29 – 6.10 mm^2 (Table 4.1). The most pronounced damage was observed in rats with severe external bleeding and occupied 4.45 mm^2 and 6.10 mm^2 of the coronal brain slices at -0.40 mm and +1.2 mm AP, respectively (Fig. 4.15). These slices corresponded to insertion sites for probe layers B and A, respectively. Conversely, the shanks which have caused the most damage across all sacrificed animals were mostly in layer C (4/7 rats, Table 4.1).

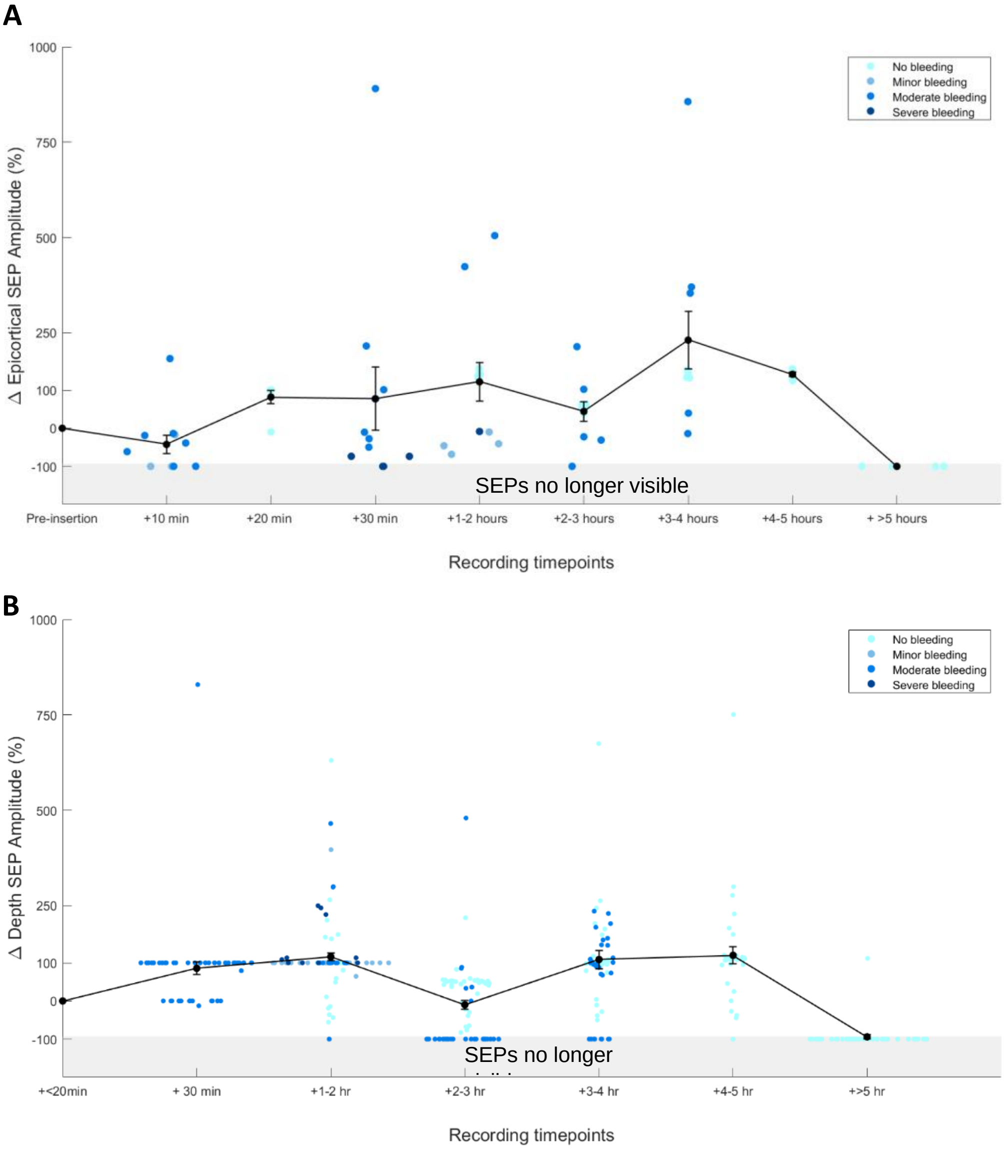

Figure 4.14. Changes in the amplitude of epicortical (A) and depth (B) forepaw SEPs post-insertion. Epicortical and depth recordings of evoked forepaw activity were used as markers for acute physiological and functional impact of probe insertion. Recordings were grouped by the severity of visible bleeding (none, minor, moderate and severe) and assigned different colours. Each dot in the plot represents a percent change in the amplitude of the maximal forepaw SEPs on individual electrodes with respect to pre-insertion amplitude (epicortical) or the first post-insertion measurement (depth). A change of -100 % was assigned to the recordings were no SEPs larger than background noise could be identified after averaging. The mean change ± S. E. at each timepoint is shown in black. Time elapsed post-insertion had a significant, albeit positive, impact on the amplitude of both the epicortical and depth SEPs (respective p-values of < 0.01 and < 0.001, two-way ANOVA). Bleeding severity was a significant factor in the size of epicortical but not depth SEPs (respective p-values of $p < 0.01$ and $p > 0.1$, two-way ANOVA). (A) The amplitude of epicortical SEPs stayed relatively constant until 3 – 4 hours after insertion when they increased significantly with respect to the pre-insertion and +10 min measuremets ($n = 24$ recordings, $N = 6$ rats; $p < 0.05$, Tukey-Kramer test). The amplitude dropped significantly at the end of the experiments when compared to the peak at 3 – 4 hours ($p < 0.05$, Tukey-Kramer post-hoc test). (B) Depth SEPs were significantly larger at 30 min, 1-2 hours, 3-4 hours and 4-5 hours post-insertion when compared to the initial measurement ($n = 18$ recordings, $N = 6$ rats; $p < 0.001$, Tukey-Kramer post-hoc test). The mean amplitude at +2-3 hours was not different from baseline ($p > 0.1$, Tukey-Kramer post-hoc test) but significantly differed from all other timepoints in both directions ($p < 0.01$, Tukey-Kramer post-hoc test). Depth SEPs were also significantly smaller after >5 hrs versus immediately post-insertion ($p < 0.001$, Tukey-Kramer post-hoc test).

Figure 4.15. Representative damage produced by insertion of each probe layer in rats which suffered severe externally visible bleeding. Black triangles (Δ) point to histological markings of shank insertion points. The dashed lines (--) mark the boundaries of the largest continuous lesions around the insertion sites identified and quantified in each rat. In Rat 6, brain sections corresponding to all three probe layers displayed pronounced cellular vacuolation and tissue rarefaction due to cytoplasmic swelling; shanks in layer B additionally caused small haemorrhages whereas shanks in layer C mechanically tore neural tissue. In Rat 6, the largest area of injury, or lesion, was marked by cellular vacuolation and tissue tearing (measuring 6.10 mm^2). In contrast, in Rat 7, all three probe layers produced significant intraparenchymal haemorrhaging with the largest lesion (measuring 4.45 mm^2) at the suspected level of layer B.

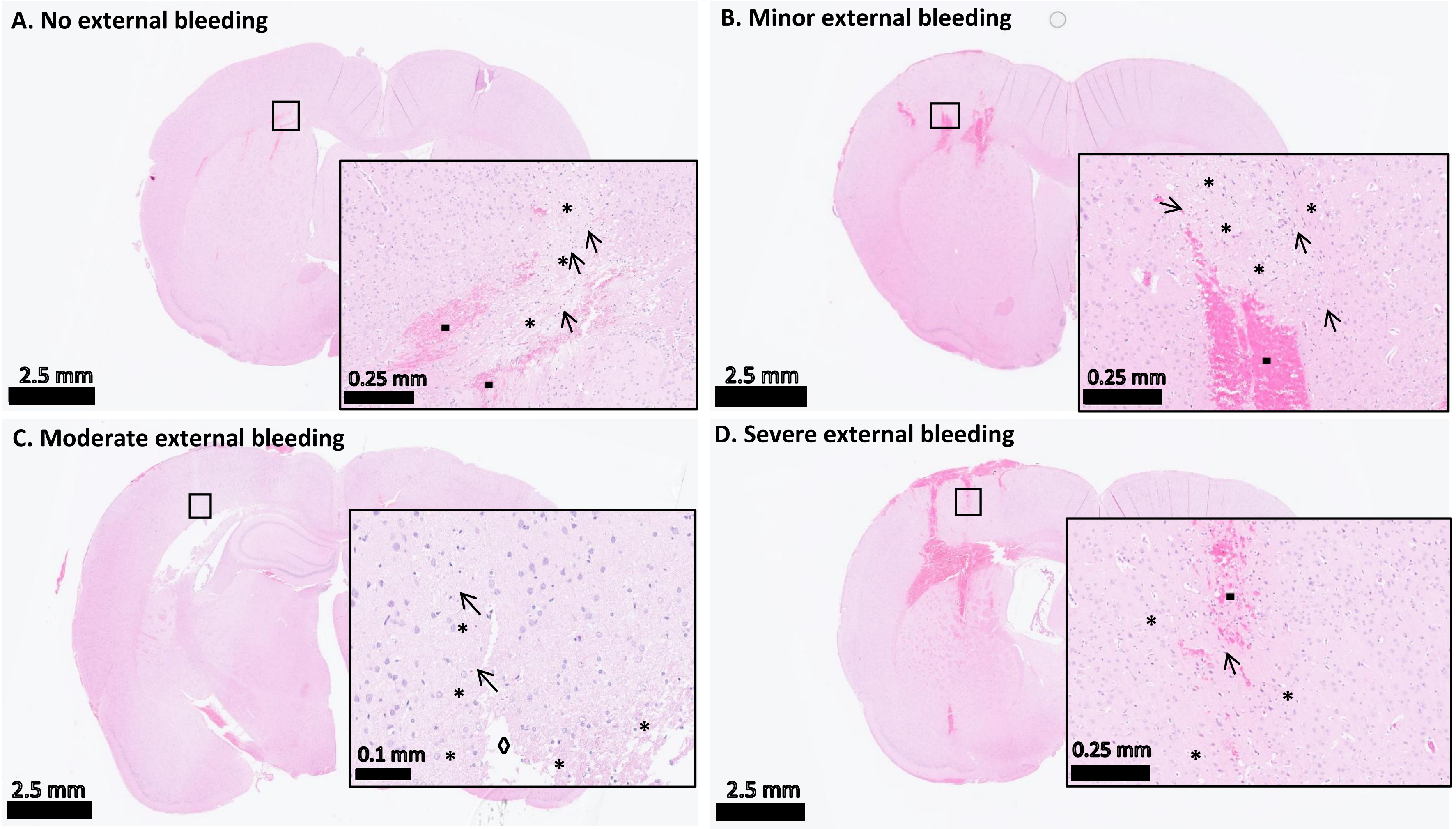

Figure 4.16. Representative examples of histopathological changes in the rat brain following the probe insertion in different rats classified by the severity of visible bleeding. Different types of tissue injury are marked by the following symbols: * - vacuolation/oedema; ↓ - pyknosis; □ – extravascular blood; ◊ - mechanical tearing. External signs of bleeding were weakly correlated with the severity of histopathological damage which manifested in a similar manner in all bleeding categories.

Table 4.1. Summary of the physiological biomarkers of brain injury and post-mortem findings in sacrificed rats. Downward arrow (↓) denotes decreases in the listed measures. P.I. – post-insertion period; Mech. lesion – mechanical lesion; Haem. lesion(s) – haemorrhagic lesion(s).

		Rat 1	Rat 2	Rat 3	Rat 4	Rat 5	Rat 6	Rat 7
Bleeding severity		No bleeding	No bleeding	Minimal	Moderate	Moderate	Severe	Severe
Bleeding location		N/A	N/A	Posterior shanks	Not recorded	Anterior shanks	Posteromedial shank pierced a pial vessel	Mid-lateral shank pierced a pial vessel
ECoG	Silence?	Not recorded	No	Yes, ~3 min	Yes, ~3 min	No	Yes, ~10 min	Yes, ~2 min
	Changes	Not recorded	Transient amplitude ↓	Amplitude ↓ for 11 min P.I.	Amplitude ↓ for 30 min P.I.	Amplitude and frequency ↓ for 12 min P.I.	Amplitude ↓	Amplitude ↓ for 10 min P.I.
SEP	Epi	0.1 – 0.7 mV	0.4 – 0.5 mV	0.1 – 0.4 mV	0.1 – 0.4 mV	0.1 – 2.1 mV	None	0.1 – 0.3 mV
	Depth	0.1 – 1.1 mV	0.2 mV	0.1 – 0.6 mV	0.1 – 0.3 mV	0.1 – 1.0 mV	None	0.1 – 0.5 mV
Histological findings	Layer A	Haem. lesions +1.0 – +1.2 mm AP	Haem. lesions +0.2 mm AP	Haem. lesions +0.7 – +1.2 mm AP	Haem. lesions +0.48 – +0.7 mm AP	Haem. lesions +0.7 – +1.2 mm AP	Neural tissue rarefaction and vacuolation, haem./ mech. lesions +1.2 mm AP	Large haem. lesion(s) +0.5 – +1.0 mm AP
	Layer B	Neural tissue vacuolation, pyknosis, haem./ mech. L. +0.2 mm AP	Neural tissue rarefaction and vacuolation, haem. lesions -0.3 – -0.4 mm AP	Neural tissue vacuolation, haem. lesions +0.2 mm AP	Neural tissue vacuolation, pyknosis, haem. lesions -0.2 – -0.4 mm AP	Neural tissue rarefaction, haem./ mech. lesions -0.26 – +0.2 mm AP	Neural tissue vacuolation, haem./ mech. lesions +0.2 mm AP	Neural tissue vacuolation, haem./ mech. lesions -0.4 mm AP
	Layer C	Mech. lesions -0.4 mm AP	Vacuolation, pyknosis, haem. lesions -1.3 – -1.4 mm AP	Haem./mech. lesions -0.4 mm AP	Vacuolation, pyknosis, haem. lesions -1.3 – -1.6 mm AP	Haem./mech. lesions -1.6 mm AP	Neural tissue rarefaction and vacuolation, mech. lesions -0.4 – -1.4 mm AP	Vacuolation, haem. lesions -1.3 – -1.4 mm AP
	Largest lesion	Layer C 1.85 mm^2	Layer C 1.30 mm^2	Layer A 1.38 mm^2	Layer C 0.29 mm^2	Layer C 2.95 mm^2	Layer A 6.10 mm^2	Layer B 4.45 mm2

4.4 Discussion

4.4.1 Summary of the optimised model and imaging method with the custom stereo-arrays

The purpose of this study was to develop a reliable experimental model for recording neural impedance changes during cortical and subcortical ictal epileptiform discharges in the rat brain using EIT and custom stereo-electrode arrays. This chapter covered a range of methodological assessments and optimisation procedures for the electronics and for the selected animal model of epileptic activity. In summary, the electrochemical tests showed that EIT depth arrays were consistent across production batches and were suitable for prolonged (up to 12 hours) repeated recordings without significant impact on their quality and durability (Fig. 4.6). Using an apertured electrode array for guiding the probe insertion proved to result in anatomically precise implantation of the depth array (Fig. 4.7). The insertion accuracy appeared to deviate marginally from the target across the trials (Table 4.1).

Assessments of the neurophysiological impact of depth probe insertion provided conflicting but generally positive outcomes. The extent of visible bleeding upon penetration of brain surface correlated weakly with changes in brain activity (Table 4.1). Moreover, the functional capacity of the brain did not appear to be negatively affected by probe implantation for at least up to 5 hours after insertion despite visible histopathological changes in post-mortem samples (Fig. 4.14, 4.15 and 4.16).

The optimisation of the electrical epilepsy model yielded universal parameters for induction of reproducible seizures in cortical and subcortical structures. Delivery of square bipolar charge-balanced pulses of 1 ms and 2 mA in amplitude at 100 Hz for 5 seconds via cortically and subcortically located depth electrodes consistently induced ictal ADs with or without the propensity to develop into prolonged seizures lasting up to 1.5 min (Fig. 4.8 and 4.9). ADs comprised predominantly SWDs as well as sharp waves and PSWDs. As expected, SWDs displayed the most reproducible morphology across all seizures and were therefore used for averaging associated fast impedance changes. The most prominent depth SWDs aligned with the epicortical leading channels and therefore provided a reference for identifying trigger markers (Fig. 4.11). Significant fast neural impedance changes recorded on depth contacts to verify the new trigger isolation technique had a mean amplitude of ~-0.1 % and displayed similar electrographic characteristics to epicortical ictal impedance changes (Hannan et al., 2020b).

4.4.2 Technical considerations and limitations

There are several important technical challenges and limitations of the developed model which should be considered before its implementation and the assessment of broader applications for intracranial fast and slow neural EIT with the custom depth arrays.

4.4.2.1 Technical challenges: equipment and experimental set-up

Despite the overall high quality of the custom-made probes, their inconsistency posed a challenge in comparing the results from different experimental preparations (Fig. 4.6). Whilst two out of seven usable probes maintained impeccable impedance characteristics with continued use (probe 1 and 4), the remaining five arrays deteriorated at variable rates and, therefore, required robust testing prior to each experiment to ensure optimal electrical performance. Although electrode delamination was expected due to mechanical friction, the reason for variable inter-electrode and inter-probe coating stability was unclear. It was possible that the electropolymerisation method used for coating depth electrodes in this study determined not only the conductivity properties but also the long-term stability of PEDOT films (Castagnola et al., 2014). Electrodes in all seven probes were coated individually using the galvanostatic method of electrochemical polymerization. The amplitude of the applied current was varied between electrodes and probes based on the visual inspection of the coated surface. This may have resulted in variable thickness of polymer films and their surface morphology which could have directly impacted the impedance of the electrodes (Castagnola et al., 2014). Non-uniform requirements for applied current were likely caused by manufacturing irregularities and wire bond failures offering scope for improvement in probe production process. Nonetheless, electrode attrition rate never exceeded 20 % which indicated high overall coating stability and enabled probe recycling between experiments (Fig. 4.6). Successful re-use of all seven depth probes also confirmed that the custom EIT depth arrays were able to withstand repeated injection of high amplitude currents (mA’s) for induction of electrical seizures as well as prolonged injections of low-amplitude EIT currents (µA’s). These findings agreed with the literature showing minimal changes in impedance of chronically implanted stimulated electrodes over a period of weeks with transient improvement in the first two days due to bleeding and CSF accumulation (Evers et al., 2022).

Another technical challenge in this experimental preparation was a wide-angle craniectomy and implantation of a subdural array to guide the correct insertion site for the depth probe. The complexity of the procedure increased the risk for mechanical trauma and introduced room for error. The analysis of histological changes attributable to probe insertion, mainly stab wounds, suggested that depth array was likely to have been consistently inserted up to 1.7 mm off the expected insertion site (Table 4.1). Considering the dimensions of individual shanks and their spacing, this discrepancy would have shifted the shanks anteriorly by an entire probe layer.

This conclusion is speculative as histological pre-processing can cause shrinkage of the brain and therefore lead to inaccurate localisation of insertion sites. Nonetheless, any deviations from intended insertion site are directly related to the placement of epicortical array which could be avoided by restricting the cranial window to the size of the depth array. However, the necessity for measuring brain activity independently of the probe was considered to, at present, outweigh the risks imposed by the additional procedures and was therefore a preferred method for depth probe positioning in this experimental model.

4.4.2.2 Limitations of electrical epilepsy model

The epilepsy model chosen for this experimental preparation also has its limitations. Electrical induction method produces controlled stereotyped ADs and focal seizure-like patterns which typically engage overlapping neural circuits (Hannan et al., 2020b; Kandratavicius et al., 2014). This is useful for the purpose of serial fnEIT; however, it fails to mimic the unprovoked and unpredictable nature of electroclinical seizures seen in epileptic syndromes (Cook et al., 2013; Kudlacek et al., 2021). This drawback of electrical induction method can be addressed by using chemical or genetic epilepsy models which are characterised by spontaneous seizures of variable presentation. Whereas slow neural changes during spontaneous seizures can be recorded using parallel EIT system, intracerebral fast neural impedance changes with sufficient SNR can only be extrapolated by averaging the signal to a repeated trigger due to technological constraints and background noise in brain imaging data (Hannan et al., 2020a; Hannan, et al., 2018b; Witkowska-Wrobel et al., 2021). This requires repeatable induction of on-demand electrophysiological changes involving identical neural pathways in the brain. For imaging pathological activity with EIT, these criteria can be met by recording electrical ADs which can develop into clinical seizures with analogous semiology to the habitual ones (Aungaroon et al., 2017; Blume et al., 2004; Gollwitzer et al., 2018; Kämpfer et al., 2020). Hence, for proof-of-concept depth EIT studies of fast and slow neuropathological changes, electrically-induced epileptiform ADs and electrographic seizures are justified as an adequate approximation of spontaneous seizures occurring in epilepsies and epilepsy syndromes.

4.4.2.3 Safety assessments

Safety of any diagnostic or therapeutic implantable device is crucial when considering its translation from an investigational technique to a clinically relevant diagnostic and therapeutic tool. Hence, to ensure the validity and long-term success of intracranial EIT with the optimised 3D depth arrays, it was paramount to examine the physiological impact of the probe insertion. Several safety tests were designed to control for key physiological variables, namely, real-time external signs of pervasive injury, changes in brain vital signs, and acute histopathological markers. However, each test was constrained due to the availability of equipment. Therefore, the following limitations of the safety assessments should be carefully considered before extrapolating their results to the general safety of the experimental model.

Firstly, the assessment of external bleeding severity was largely subjective. Even though the classification of the bleeding severity was anchored to objective measures, such as the time until stoppage or visible penetration of pial vessels, the precise quantification was impossible and may have skewed the results. Interestingly, some research suggests that the extent of neurovascular insult might be benchmarked against the size of the damaged blood vessel (Kozai et al., 2010). Two-photon microscopy images of cerebral vasculature in mice with a penetrating microelectrode have shown reduction in both external and internal haemorrhaging when major cerebral vessels (>5 µm in diameter) were avoided (Kozai et al., 2010). The observed trend was not statistically significant for the surface bleeding ($p = 0.22$) and was at the border of significance for sub-surface vessels ($p = 0.049$) indicating that additional adequately powered studies might be necessary to discriminate the differences between the groups, if any (Kozai et al., 2010)

Functional brain performance effects after the probe insertion were based on acute changes in ECoG as well as hourly fluctuations in forepaw SEP amplitude (Fig. 4.14; Table 4.1). Whilst providing quantitative measures of potential insertion impact, the results of these assessments were strongly confounded by changes in anaesthetic state due to introduction of fentanyl whilst weaning the isoflurane. Isoflurane is known to affect the amplitude of the SEPs measured in rats and humans due to its strong CNS-suppressant properties (Kortelainen et al., 2014; Porkkala et al., 1994; Rojas et al., 2006). Based on the literature, the increase in the amplitude of the epicortical forepaw SEPs over hours in this study can be explained by gradual metabolism and clearance of isoflurane whilst its minimal alveolar concentration is reduced by administration of fentanyl (Hannan et al., 2020b; Lang et al., 1996). Albeit confounded, the observation is still valuable as it suggests that any collateral tissue damage exerted by the probe was not significant enough to cause deterioration in functionality and overcome the reversal of CNS depression due to lowered isoflurane. Further studies could be performed under stable anaesthetic which would permit both surgical intervention and monitoring of brain activity with minimal suppression to confirm this hypothesis.

The last safety assessment was histological analysis of post-mortem brain tissue. Histopathological markers were used for localising the anatomical insertion points of each shank and comparing to the opposite hemisphere. Unfortunately, the processing of brain tissue imposes limitations to the information that can be extracted from the histological samples. Thus, histological findings need to be interpreted with caution when drawing conclusions about the safety and viability of the model. Exposure to a series of dehydrating reagents causes tissue shrinkage which distorts the dimensions (Hillman, 2000). This makes accurate localisation of shank insertion sites impracticable even with anatomical landmarks. Data interpretation is further complicated by the spacing and thickness of the histological sections which are chosen arbitrarily. In this study, brain samples were sectioned into 5 µm-thick coronal slices every 100 µm in the first rat brain submitted for processing (rat 5 in Table 4.1) and in 50 µm intervals in the remaining ones as suggested by the lead histopathologist. Since shanks in this depth array measure ~100 µm along the AP axis, such sectioning pattern was expected to capture the signs for all insertion points. However, even marginal shank misalignment could have placed some of the insertion sites outside of the sectioning plane.

Furthermore, probes were always extracted prior to tissue fixation and immediately after euthanasia but before rigor mortis. The mere removal of the implant before fixing the brain in a preservative is a confounding but necessary step if re-usability of the probes is the goal. Whilst some form of histological damage, including but not limited to, the stab wounds was successfully identified and attributed to all shanks across rats, superficial insertion points were not always visible (Fig. 4.15, 4.16). Soft tissue movement upon probe removal could have disguised tissue penetration points and rendered inaccurate localisation of the probe insertion coordinates. This is also supported by the evidence in the literature showing secondary neurovascular damage due to tissue compression extending into the distal brain regions (Bjornsson et al., 2006). More importantly, probe removal might have caused additional injury due to rupture of blood clots which form upon initial tearing of large arterioles and arteries (Rosidi et al., 2011). This was however expected only in a subset of animals if the insertion coordinates in fact deviated between rats (Table 4.1). Insertion differences as minimal as 50 µm had theoretical preventative impact from causing major neurovascular damage due to the divergence of penetrating cortical vessels from their surface origin point (Kozai et al., 2010).

Lastly, brain slices in this study were only stained with an H&E stain which visualises the microscopic architecture of the tissue but gives little to no insight into the activation of specific immune cells and, thus, deleterious pathways in response to injury. The latter can be examined by using targeted immunostaining with fluorescently labelled antibodies against proteins found in activated glial cells. For example, multiple studies have utilised elevated expression of glial fibrillary acidic protein (GFAP) to track the development of immune response to external insult in the CNS (Biran et al., 2005; Gallego et al., 2012; Kozai et al., 2012; Szarowski et al., 2003). Amongst other popular antigens are lysosomal glycoproteins (CD68), complement receptor 3 (CR3), B4 isolectin (IB_4) which have also been broadly employed in immunohistological analyses of brain tissue (Biran et al., 2005; Htain et al., 1994; Stence et al., 2001). However, most of these preparations look at long-lasting immune responses on timescales exceeding those of depth EIT recordings in terminal experimental preparations. Therefore, whilst acute reaction to neural implant commences within minutes and immediately triggers a progressive inflammatory cascade, reactive gliosis is unlikely to be significant in this model. If so, H&E staining is sufficient to visualise the structural changes in the tissue without the need for immunohistology.

Nevertheless, considering the broader goal of developing a clinical depth EIT system, additional studies could be conducted to investigate the immunoreactivity and neurodegeneration after insertion of the probe. Similarly to studies described in the literature, two-photon microscopy could be used to image acute and chronic probe damage *in vivo* whereas confocal microscopy could be used to examine immunohistological changes in brain samples preserved with the probe *in situ*. It would be of interest to know if the probe geometry and the insertion technique adopted in this experimental preparation are the source of any additional damage which can be easily circumvented (Andrei et al., 2012; Andrei et al., 2011; Edell et al., 1992; Sharafkhani et al., 2022; Welkenhuysen et al., 2011). These tests would instruct mechanical modifications which could improve the safety of the probes for successful long-term imaging of epileptiform activity with intracranial depth EIT.

4.4.3 Feasibility of neural EIT with the developed experimental model

This study addressed an array of feasibility measures for successful high-resolution imaging of pathophysiological neural circuits in the rat brain with a new custom stereo-electrode array and EIT. The results of each method development stage consequently yielded collective but non-exclusive criteria for proof-of-concept rodent studies. It is apparent that all facets of the model should be optimally functioning to maximise the feasibility of accurate fnEIT image acquisition and physiological consistency across subjects to ensure scientific rigor. Therefore, this section describes the key parameters of the experimental model optimised in this chapter and how their values should guide the exclusion and inclusion of future experimental preparations as respectively invalid or scientifically sound. The discussion is laid out in order of the questions raised in the purpose of this chapter. The summary is provided in Table 4.2.

4.4.3.1 Criteria for probe quality and mechanical stability

The threshold for the optimal electrical performance of the probe which was applied at the start of this study should be carried over into imaging studies with a few caveats. The insertion of the probe is likely to produce a variable degree of intracerebral bleeding across rats thereby changing the physicochemical environment of the depth electrodes. In some cases, this might negatively affect the contact impedance and, consequently, the recording quality. Therefore, the standing voltage on the depth channels should always be evaluated after insertion and prior to initiating EIT recordings to avoid saturating the amplifier. In addition to that, the phase angle of the coated electrodes could be measured as a marker for their capacitive properties.

Large phase angle would indicate coating deterioration which would make the electrode unsuitable for reliable recordings of EIT signal (Xiao et al., 2004).

Whilst the above criteria are universal for both fast and slow EIT recordings acquired serially or in parallel, the latter imaging system has additional requirements. Parallel current injection through multiple electrode pairs significantly increases the standing voltage on all depth channels and increases the chances of saturation. Therefore, aside from the electrode impedance, parallel recording system is particularly sensitive to the DC offset. Considering the limits of the actiCHamp EEG amplifier used for EIT recordings, the DC shift of ≥ ±400 mV renders electrode unsuitable for simultaneous injection. Since the electrode surface material and the electrolyte composition directly impact the electrode potential values, the resulting DC shift can be impacted by both delamination and nearby accumulation of blood (Kamp et al., 2005). Therefore, DC bias should be measured on each depth channel upon probe implantation before commencing slow neural EIT using the parallel EIT system.

4.4.3.2 Criteria for a valid experimental model

Arguably, the most crucial criteria are those defining a valid experimental model which can accurately mimic a clinical or pre-clinical scenario of interest.

Induction of representative and clinically relevant seizures

Acute rat model of electrical ADs evoked with the new custom stereo-electrode array proved to yield sufficiently reproducible seizures during both neocortical and subcortical stimulations (Fig. 4.8 and 4.9). Stereotypic SWDs observed during epileptiform activity in the obtained recordings enabled the averaging of fast impedance changes from repeatedly activated neural circuits (Fig. 4.11 and 4.13). Stimulation parameters appeared largely universal across seizures with the frequency (100 Hz), pulse width (1 ms), and stimulation duration (5 seconds) consistent with the previous studies (Hannan et al., 2020b; Motamedi et al., 2007; Shigeto et al., 2013). Stimulation intensity was subjective; however, currents of <1 mA did not consistently yield seizures of sufficient duration defining an empirical threshold for successful ADs. Therefore, whilst keeping the frequency, pulse width and stimulation duration constant, in future studies current amplitude should be adjusted on case-by-case basis according to the real-time seizure characteristics.

Reproducibility of probe position

The reproducibility of this experimental model should be continuously verified. Based on the results of this chapter, recordings of forepaw and hindpaw evoked activity can be reliably used as functional markers of anatomical position of the probe as well as of the functional capacity of the brain at any given moment (Fig. 4.7 and 4.14). However, determining the exact deviation between the expected and the actual insertion site remains a challenge (Table 4.1). It is possible that the mismatch between the modelled and the real location of the electrodes could affect the spatial accuracy of image reconstruction; however, it is unclear whether observed margins would have any significant effect. Therefore, going forward, functional localisation of the probe should be continued prior to EIT recordings to aid the neurophysiological interpretation of the results.

Safety of probe insertion

The last but not the least consideration of a valid experimental model is its safety. Histological analyses combined with the visual and functional assessments reported mixed outcomes with high inter-subject variability (Table 4.1). In the context of the published research, the current histology results suggest that complete damage prevention is practically unattainable but that does not automatically invalidate the experimental preparation due to other factors. Avoiding the penetration of major surface vessels seems to be critical. Otherwise, restricted perfusion of deeper brain regions coupled with mechanical strain from volumetric tissue displacement and vasogenic oedema can create a hypoxic environment and lead to ischemia (Kozai et al., 2012). Whilst neurodegeneration due to immunoreactivity and neurotoxicity of extravasated blood plasma proteins is unlikely within the timeframe of an EIT experiment, reduced tissue oxygenation can distort neural and metabolic changes making EIT images inaccurate (Abdul-Muneer et al., 2015; Agyemang et al., 2021; Ralay Ranaivo & Wainwright, 2010). Aside from large blood vessel injury, other types of visible damage should only be classified as significant if the functional performance of the brain is impaired (Fig. 4.14, 4.15). Hence, future experimental preparations should only be excluded from analysis if the depth probe perforates pial arteries or veins, or in cases where SEPs are undetectable or irreversibly diminish over time.

4.4.3.3 Acceptable recordings and their processing technique

Due to the nature of serial fnEIT and necessity to average independent seizures, the recorded signal needs to meet pre-defined criteria conducive to accurate EIT reconstruction of fast neural ictal impedance changes. This includes the specifications of the epileptiform activity being averaged as well as the noise tolerability in the recording system. Analysis of single-channel impedance recordings from depth electrodes showed that ictal ADs provoked by electrical stimulation morphed over time (Fig. 4.10). Therefore, only a proportion of the recorded seizure comprising reproducible SWDs could be averaged into a representative pattern of fast neural changes occurring over the course of a single seizure. Comparison of different SWD clusters showed that activity immediately following the stimulation was more electrographically cognate than later phases of the seizure (Fig. 4.11). The prominence of the spikes was the primary feature which determined their alignment and trigger selection for extrapolating the associated impedance changes (Fig. 4.13). Therefore, to standardise the analysis of future depth fnEIT recordings, the most prominent SWDs in the context of a given seizure should be considered the principal candidates for averaging. The absolute amplitude of the selected SWDs should always be ≥1 mV (Hannan et al., 2018b). The ‘leading’ depth electrode should be established in reference to the epicortical SWDs and subsequent qualitative sorting as detailed in this chapter. If multiple epicortical electrodes meet the criteria, the ‘leading’ electrode should be selected on the basis of spike prominence. Thresholding could be performed manually or using a MATLAB function as described in 4.2.6.

Fast neural impedance changes recorded by depth electrodes were in a range of -0.01 – -0.11 % (Fig. 4.13). Impedance changes on the depth electrodes were similar in magnitude to those recorded on the epicortical contacts but surprisingly smaller than peak changes reported in the literature using a similar recording setup (Hannan et al., 2018b). The discrepancy could be explained by a choice of suboptimal injection pair in this chapter versus the impedance responses recorded with a full EIT injection protocol in Hannan et al. (2018b) study. This is equally applicable to the depth fast impedance changes which might exceed -0.1 % provided all injection-measurement pairs are explored. Nonetheless, a small signal amplitude makes the system particularly sensitive to fluctuations in baseline noise caused by electrical equipment or unforeseen changes in neurophysiological environment of the probe. This impacts the SNR which is a key factor in feasibility of EIT image reconstruction. As observed in this chapter, seizures can vary in duration which directly determines the number of averages and, in turn, the SNR. Therefore, to ensure that the SNR of the largest changes stays relatively constant and above ~3, a baseline noise <~0.03 % should be maintained in the averaged signal. Since the average number of ADs suitable for averaging in a single neocortical seizure recorded during fast neural impedance measurements was 34 (21 – 45 in single-channel impedance recordings), the noise after demodulation should be no larger than ~0.2 % to ensure consistent SNR across recordings. With the expected standing voltage of 1 – 10 mV on recording depth electrodes, a 0.2% noise level would correspond to 2 – 20 µV of raw baseline noise before averaging. Impedance recordings which contain baseline noise of >20 µV or >0.2% but show >34 reproducible SWDs can be deemed acceptable provided the noise level after averaging is reduced <~0.03 %, as described above. Any recordings with a higher noise level in either unaveraged, or averaged impedance measurements should be rejected. The calculations and the principles used to arrive at the acceptable noise level in fast impedance recordings before and after averaging are described in detail in section 4.1.3.3.

Table 4.2 Summary of inclusion and exclusion criteria for neural EIT recordings with the depth arrays.

Assessment category:	Parameter:	Criteria:
Depth probe quality	Electrode impedance	• ≥50 % electrodes with impedance ≥5 kΩ
Depth probe insertion rigor	Depth forelimb/hindlimb SEPs	• Recurrence of maximal SEPs on depth electrodes with SEP intensity ≥0.5
Depth probe implantation safety	Visible bleeding	• Rats with severe bleeding to be excluded
	Epicortical/ depth forelimb/hindlimb SEPs	• Rats with absent or deteriorating SEPs to be excluded
Acceptable seizures/ADs	Duration	• ≥6 seconds
	Characteristics of SWDs	• Morphologically identical • Absolute amplitude ≥1 mV • SWDs with maximal spike prominence (min. 0.1 mV) within the selected cluster
Acceptable fnEIT data	Baseline noise	• ~<0.03 % in the averaged dZ trace • <0.20 % or <20 µV before averaging

Chapter 5

High-resolution three-dimensional imaging of individual ictal epileptiform discharges in rats using penetrating stereo-electrode arrays and fast neural EIT

5.1 Introduction

At the time of writing this thesis, no common electrophysiological and neuroimaging technique is capable of tracing the precise spatiotemporal recruitment of neural circuits during physiological or pathological brain activity with a mesoscopic resolution. Whilst microscopic and macroscopic imaging modalities are vast, there is a lack of methods for tracking the activity in real time at the scale of neuronal networks. This is particularly relevant for neurological disorders like epilepsy characterised by widespread spontaneous aberrant bursts of synchronised neural activity with largely unpredictable spread into brain regions distal to seizure-generating focus. Rapid expansion in artificial intelligence and machine-learning algorithms has provided tools for predictive modelling of epileptic network dynamics. However, research has been mostly confined to simulations with controlled parameters which frequently fail to account for biological variability and human error in typical experimental and clinical conditions. Therefore, there is an unmet need for a practical tool which would allow us to investigate the epileptogenicity of neuronal networks anywhere in the brain with sufficient spatiotemporal resolution and, thereby, unravel the complexity of seizures in various epilepsies and related neurological conditions. Intracranial depth EIT of fast neural activity holds potential to fulfil these aims. This chapter describes a pilot study which was conducted as a preliminary feasibility assessment of a new method for imaging the three-dimensional propagation of ictal epileptiform activity in an anaesthetised rat model developed in the previous chapter. This method, combining fnEIT with novel penetrating depth electrode arrays, was used to produce dynamic images of averaged ictal epileptiform discharges with a millisecond and submillimetre resolution. The possibility of imaging individual ictal discharges without averaging and with the same temporal resolution was also investigated and compared to the three-dimensional reconstructions of simultaneous SEEG recordings, the gold-standard of the field.

5.1.1 Background

Current guidelines for pre-surgical assessment of epilepsy patients outline a stepwise investigation comprising a series of non-invasive and invasive tests (see Chapter 1 for details). The goal of these evaluations is to refine the presumed epileptogenic area and map the precise boundaries of the resective tissue with localisation of any proximal eloquent brain regions which should be avoided during the procedure. A multimodal approach is typically taken to ensure a favourable benefit-to-risk profile for each patient and to maximise the chances of total post-operative seizure-freedom. However, a sizable proportion of the resective surgeries do not achieve a desired outcome of complete seizure suppression and recurrence is seen in up to 84 % of patients (Téllez-Zenteno et al., 2005; Yoon et al., 2003). A low success rate is generally attributable to localisation errors due to the shortcomings of standard neuroimaging techniques. This issue could theoretically be circumvented by intracranial fnEIT which might offer an unprecedented insight into the three-dimensional functional re-organisation of pathological neural networks with a millisecond and micrometre accuracy.

5.1.1.1 Limitations of the common techniques for imaging and localising seizures

Due to the mechanistic complexity of epileptogenesis and ictogenesis, a comprehensive picture of a seizure onset, propagation and termination can be established only with recording techniques which combine high temporal and spatial resolution as well as sensitivity to distal sources. As discussed in Chapter 1, scalp EEG meets the time-resolution criteria albeit provides no information on the topography of the detected activity. This can be solved by mathematical source localisation methods; however, image reconstruction is limited by the ill-posed nature of the inverse problem. *A priori* assumptions defining parameters like dipole orientation or position are often made in order to arrive at a unified solution (Grech et al., 2008). Using penetrating intracranial electrodes can improve the accuracy due to the source proximity; however, the inverse solution remains non-unique. Moreover, targeted implantation of SEEG electrodes restricts the field of view due to an estimated maximal sampling radius of 5 – 10 mm (Tantawi et al., 2021; von Ellenrieder et al., 2012). Therefore, depth electrodes are usually placed in a putative EZ and along a presumed propagation pathway; otherwise, the SOZ can be misidentified due to volume conduction of electrical currents (Khoo et al., 2020).

The deficits in spatial resolution and coverage could in principle be addressed with tomographic imaging techniques such as fMRI and single-photon emission CT (SPECT). Both techniques are designed to detect localised cerebral perfusion changes and, therefore, provide surrogate measurements of brain activity with a spatial resolution ranging from <1 mm in high field strength fMRI to ~7 millimetres in SPECT (Barisano et al., 2019; Baumgartner et al., 2019; Spencer, 1994). Unfortunately, these modalities are constrained to imaging of interictal activity due to safety and logistical issues. As such, they delineate an irritative rather than epileptogenic zone which is larger and less specific. The above limitations obscure the identification of the real EZ. Consequently, surgical resection based on ambiguous diagnosis can negatively affect the well-being of the patient with no clear improvement to their quality of life.

5.1.1.2 Deficiencies of previous fast neural EIT studies in epilepsy

Attempts have been made to address the gap in epilepsy clinical practice by developments in intracranial fnEIT. Experiments, however, have been restricted to terminally-anaesthetised rodent models of hippocampal and neocortical epileptiform activity induced by electrical stimulation or injection of convulsive agents (Hannan et al., 2020a; Hannan, et al., 2018b; Vongerichten et al., 2016). The results showed fast impedance decreases of up to ~-0.3 % during both ictal and interictal cortical discharges which could be reconstructed into functional images with a resolution of up to 2 ms. Hippocampal discharges corresponded to 10 times smaller changes albeit traceable with a similar temporal resolution (Hannan et al., 2020a). These fnEIT studies were carried out using planar epicortical arrays with 30 – 57 contacts and required a relatively large cranial window (~50 – 100 mm^2) for implantation. The main drawback of the recording technique was inability to discriminate fast activity deeper than the outer third of the brain. Even the largest impedance changes could be extracted only after averaging multiple discharges and seizures together which was crucial for improvement of the SNR (Hannan et al., 2020a; Hannan, et al., 2018b). Fundamentally, the detected fast impedance changes represented a summated activity pattern due to superficial placement of the electrodes. The study outlined in this chapter was designed to explore the feasibility of generating more granular fnEIT images of epileptiform activity occurring anywhere in the rat brain with a millisecond resolution and in real time without the need for averaging. The current study tackled the drawbacks of the previous studies by implementing a novel depth array which was expected to reveal the chronological recruitment of cortical and subcortical networks during repeatable and stereotypic ictal epileptiform discharges occurring within an electrically induced seizure.

5.1.2 Purpose

The purpose of this work was to investigate the feasibility of imaging cortically and subcortically generated ictal epileptiform activity, specifically ictal SWDs, with fast neural EIT and an optimised stereo-electrode array in anaesthetised rats. The main objective of this study was to answer the following questions: (1) Based on the criteria derived during the method development, which experimental preparations/collected data are suitable for fast neural depth EIT? (2) Can depth fnEIT images of averaged ictal SWDs from neocortical and subcortical seizures be reconstructed from a serial EIT protocol? (3) Is it possible to generate fnEIT images of individual ictal discharges in a single shot using this depth array? (4) How do real-time depth fnEIT images compare to the inverse source reconstructions of individual ictal discharges from simultaneously recorded SEEG data?

5.1.3 Experimental Design

Six terminally anesthetised rats were used for collecting imaging data in this study. Recordings were obtained during ictal discharges induced by the stimulation of the sensorimotor cerebral cortex (henceforth termed ‘cortical seizures’; N = 4 rats) and by the stimulation of the striatum (henceforth termed ‘subcortical seizures’; N = 2 rats). These datasets and experimental preparations were firstly evaluated technically and against the inclusion/exclusion criteria established in 4.4.3. This eligibility screening eliminated three datasets collected in three rats from the cortical group and one dataset collected in one rat from the subcortical group. All further data analysis and interpretation presented below was performed in one EIT dataset from each group collected in two rats in total (N = 2).

Seizures were provoked and recorded with an optimised stereo-electrode array implanted through an apertured subdural electrode mat. Such recording set-up enabled the precise implantation of the depth array targeted at the centre of the S1 and penetrating thalamic and striatal nuclei, all implicated in generation of various ictal discharges, particularly spike-and-wave activity (more details in 4.1.3.3; Moeller et al., 2008; Pizzo et al., 2021). The depth array was assembled in a rigid 3 x 3 grid of probes with four rectangular 0.1 x 0.5 mm electrodes on each probe. Such electrode design was tailored specifically to intracranial EIT and optimised for sufficient resolution and coverage in fast neural EIT recordings (more details in 4.1.1.2). A schematic representation of the experimental set-up and method is shown in Fig. 5.1.

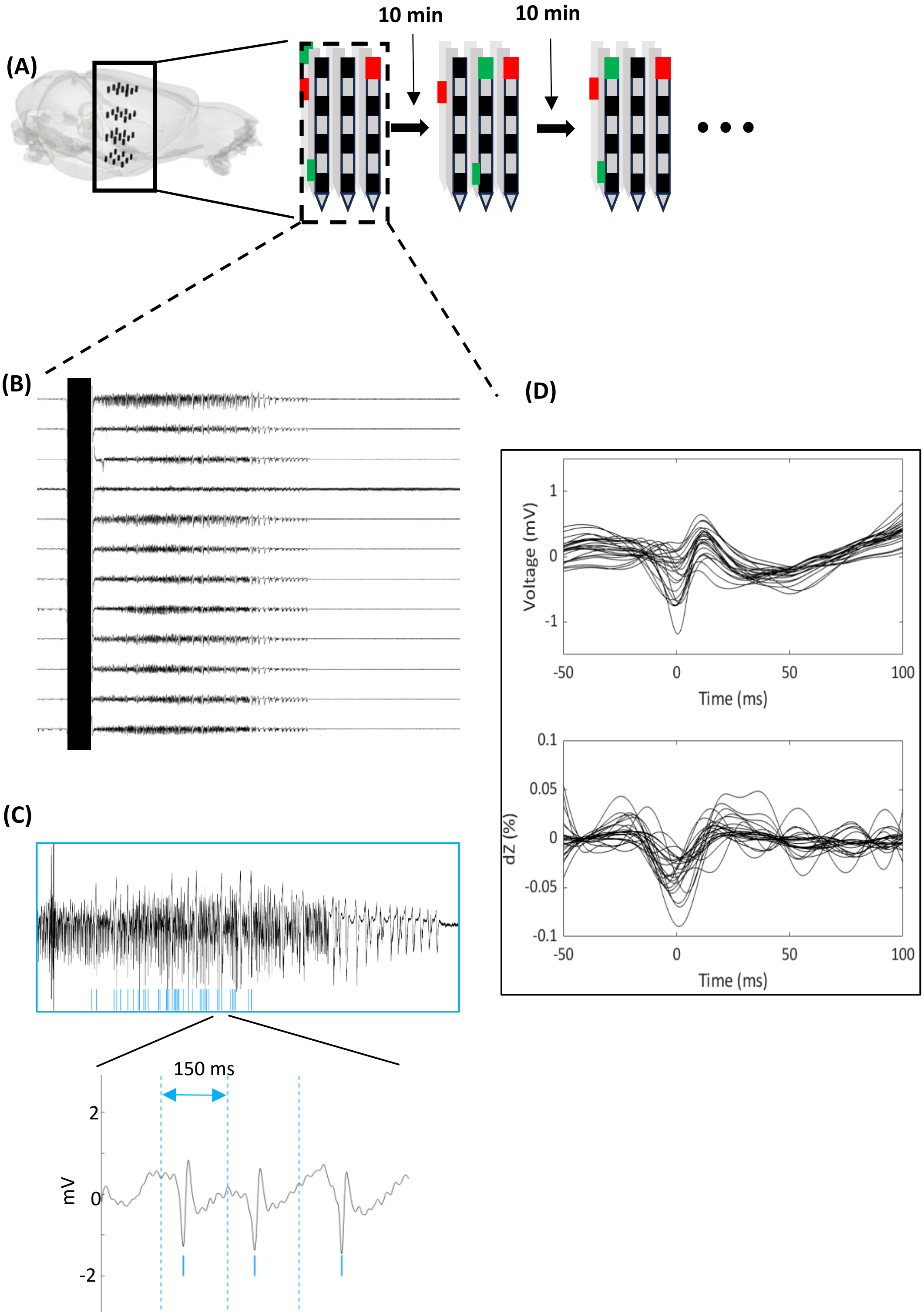

Figure 5.1. Experimental design and method for recording fast neural activity in the rat brain during ictal SWDs using serial EIT and depth electrode arrays. (A) EIT data was collected using a serial current injection protocol. Each seizure was induced by electrical stimulation of either cortical, or subcortical brain regions using two different depth electrode pairs (cortical pair shown in red). EIT current was injected simultaneously via sequential pairs of depth electrodes switched with each seizure (shown in green). Induction of sequential seizures was spaced by at least 10 min to ensure brain recovery. (B) All stimulations resulted in focal electrical seizures comprising SWDs, PSWDs, and sharp waves with SWDs being the most consistent and reproducible form of ADs. (C) A leading depth electrode was then identified by aligning epicortical and depth recordings. Trigger markers were placed at the peaks of the spikes for segmentation and averaging of associated fast impedance changes on all electrodes (D).

An electrical model of on-demand epileptiform ADs developed by Hannan et al. (2020b) and refined for the current experimental preparation and electrode configuration in Chapter 4 was used for this study. A detailed justification for choosing this epilepsy model over others is provided in 4.1.1.1 and 4.1.3.3. In summary, controlled induction of stereotypical ADs with repetitive and reproducible electrographic features tackled two challenges. According to results of the method development, ictal fast impedance decreases were expected on the order of ~-0.1 %. Therefore, the anticipation was that averaging of multiple impedance changes from near-identical epileptiform ADs might be necessary to achieve a sufficient SNR for image reconstruction. Moreover, consistent SWD morphology within and between electrically-induced seizures allowed serial data acquisition. Each seizure corresponded to a new current injection pair which collectively formed an EIT imaging protocol (Fig. 5.1A). Therefore, consecutive seizures were induced in order collect the full EIT dataset of transfer impedance measurements which corresponded to all current injection pairs and which were then used to reconstruct one EIT image. This data acquisition paradigm was required for fnEIT due to the necessary signal bandwidth (up to 1 kHz) for capturing conductivity changes over milliseconds in acutely depolarised neurons.

Impedance measurements from each injection pair were collected during individual seizures using a current amplitude of 50 µA and a carrier frequency of 1725 Hz derived from a previous epilepsy EIT study with a similar experimental design (Fig. 5.1; Hannan et al., 2018b). A new EIT protocol was obtained for each experiment by modelling a set of optimal injection pairs which provided unbiased whole-hemisphere coverage and excluded saturated channels from the protocol (Faulkner et al., 2017). In each case, the number of injection pairs was determined by the proportion of depth electrodes with satisfactory contact impedance (< 5kΩ).

The feasibility and the performance of fnEIT with the optimised stereo-array was explored by imaging cortical and subcortical seizures. These ictal events were provoked by stimulating confined regions within two main brain structures, namely the pre-frontal cortex and the limbic system. The rationale for such experimental design was three-fold. First, it was preferable to start with a known model of epileptiform activity with established evidence in EIT literature. Neocortical SWDs induced by the stimulation of the sensorimotor cortex have been successfully imaged previously with fnEIT and epicortical electrode arrays in anaesthetised rats (Hannan, et al., 2018b). Previous work enabled informed hypotheses and predictions for the characteristics of fast neural impedance changes recorded with the novel 3D array. Moreover, the two recording methods could be compared and contrasted when considering the clinical applicability of fnEIT. Lastly, it was of interest to explore the full spatiotemporal trajectory of neocortical SWDs, a goal which could not be achieved with electrodes on the brain surface (Hannan, et al., 2018b). The involvement, if any, of subcortical structures in the maintenance of neocortical SWDs was expected to be visualised and potentially settle an ongoing debate on the leading role between the thalamus and the neocortex (Timofeev & Steriade, 2004). The neocortical stimulation showed promising results in Chapter 4 by yielding prolonged seizures (>30 seconds) with distinct SWDs which produced significant fast impedance changes on multiple depth electrodes (Fig. 4.12). Therefore, the cortical seizure induction protocol was used as the first epilepsy model in this study.

The subcortical stimulation site was predominantly of an exploratory nature. The primary objective of this study was a proof-of-concept for whole-brain imaging of pathological neural activity with fnEIT and depth probes which has not been achieved to date (Faulkner, 2019; Hannan et al., 2020a). Hence, with an updated recording setup in place, it was important to investigate the potential for imaging fast electrical activity during epileptiform ADs originating in brain structures which resided deeper than the outer third of the brain. Due to a fixed probe implantation site, a limited number of subcortical stimulation targets could be explored for this purpose. The ultimate selection of a caudate-putamen complex in the striatum was based on the emerging role of basal ganglia in controlling the trajectory of various types of seizures as well as on the ability to evoke consistent ADs in this structure as established in Chapter 4 (Vuong & Devergnas, 2018). Again, it was of interest to investigate whether fnEIT could reveal unknown functional connectivity changes in the cortico-striatal-thalamo-cortical loop during electrical SWDs which could enhance our understanding of SWD dynamics.

5.1.3.1 SEEG source reconstruction

To evaluate the translational potential and clinical utility of depth fnEIT, it was crucial to compare the accuracy of fnEIT to the standard-of-care. In a clinical setting, SEEG recordings of propagating ictal activity are frequently considered a sufficient source of the three-dimensional information about the seizure trajectory. However, in surgical cases, each SEEG probe is usually implanted separately to maximise coverage of the putative EZ. Therefore, SEEG electrode spacing is normally large enough for the epileptiform patterns to appear visibly distinct on different SEEG contacts between the SOZ and the regions of spread. In this study, fixed shank and electrode arrangement meant that epileptiform ADs were always detected on all electrodes and the variation between the recording channels was not immediately apparent in all seizures. Thus, objective evaluation of individual SWD sources could only be achieved by reconstructing current density distribution during these ictal discharges using SEEG source imaging (SESI). Since SEEG data was acquired together with fnEIT recordings, the same ictal ADs could be reconstructed with both methods. Therefore, SESI was expected to serve a positive control for the fast neural activity onset and spread over individual SWDs as identified from fnEIT.

As explained above, due to multiple EIT current injection pairs and necessity for within-seizure averaging, tomographic reconstruction of a single SWD required acquisition of repeatable seizures containing identical characteristic SWDs. On the other hand, SESI could be used to reconstruct all individual SWDs within each consecutive seizure. Therefore, the degree of similarity between the SESI reconstructions could be used to test the assumption that SWDs from different epileptiform events were physiologically reproducible. This was control was necessary due to implementation of a new electrode design and epilepsy model, and for accurate interpretation of fnEIT results.

For comprehensive analysis, each SWD isolated from each cortical and subcortical seizure acquired as part of the respective fnEIT protocols would ideally need to be reconstructed with SESI and then cross-referenced. However, since each cortical and subcortical seizure contained between ~30 – 100 near-identical SWDs, this would have yielded >500 SESI reconstructions. This kind of computational work could not be accomplished for this thesis due to time limitations. Therefore, with the constraints in mind, SESI was only used to reconstruct a subset of SWDs which were also imaged in a single shot with fnEIT. The chosen SWDs were from different timepoints of a stereotypic electrical seizure and enabled the comparison of the underlying fast neural activity with the evolution of seizure. The first SWD reconstructed with SESI and with fnEIT was the first reproducible SWD of each cortical seizure. This was considered to represent the neural circuitry engaged at the start of ictal activity. The second SWD was selected within 10 seconds of the first one. This choice was based on the observation that, by this timepoint, the prominence of otherwise qualitatively identical SWDs tended to increase by at least 10 % of the initial value. Therefore, it was of interest to investigate any potential changes in the neural circuits underpinning this subtle evolution in SWD morphology.

5.2 Materials and Methods

5.2.1 Animal preparation and surgery

Experiments were performed in adult Sprague-Dawley rats, 300 – 450 g. Induction of general anaesthesia, surgical procedures and the implantation of epicortical and depth arrays were performed as described in 4.2.1. and Fig. 4.5. Anatomical location of the depth array was confirmed by verifying that the maximal forepaw and hindpaw SEPs were detected by the most sensitive contacts. Details of the technique can be found in 4.2.2, 4.2.3, and 4.3.2.

5.2.2 Induction of cortical and subcortical seizures

Ictal epileptiform ADs were induced by electrical stimulation of cortical (n = 95 seizures, N = 4 rats) and subcortical (n = 37 seizures, N = 2 rats) structures using the Keithley 6221 as the current source (Keithley Instruments Ltd, Solon, OH, USA) and a stereo-electrode array described in 4.1.1.2. Neocortical stimulation was delivered across all six cortical layers via a pair of depth electrodes located at the boundary between the S1/M1HL and the S1BF (inter-electrode distance 3.77 mm). Subcortical stimulation was delivered to the CPu via the depth electrodes separated by 2.87 mm. All epileptiform events were elicited by injecting a 5 s-train of 100 Hz square biphasic symmetric charge-balanced pulses. Each pulse lasted 1 ms and had an amplitude of 1 – 4 mA. The current intensity was titrated for each rat and adjusted for each consecutive stimulation according to the appearance and the duration of ADs in the preceding ictal event to ensure their duration remained >6 s.

5.2.3 Electrodes and other hardware

Recordings corresponding to each injection pair in the imaging protocol were acquired serially using the ScouseTom EIT system (Avery et al., 2017) with the actiCHamp EEG amplifier (Brain Products GmbH, Gilching, Germany; see Appendix A for detailed specifications) and the Keithley 6221 current source (Keithley Instruments Ltd, Solon, OH, USA). The depth electrode array contained nine shanks with four rectangular 0.1 x 0.5 mm electrodes (36 contacts in total) spaced by 1 mm and 2 mm in ML/AP and in DV axes, respectively. The probes were implanted through the centre of forelimb S1 region using the apertured epicortical array which contained 37 circular planar contacts (0.6 mm in diameter) arranged around the insertion site. Further details on both arrays are provided in 4.1.1.2. Depth electrodes were tested after coating and in advance of the experiments as described in 4.2.8 to ensure that >50 % of the recording contacts had acceptable contact impedance (≤5 kΩ).

5.2.4 Data collection

SEEG/ECoG and transfer impedance recordings were collected simultaneously on all channels connected to the epicortical and depth electrodes in reference to a circular Ag-AgCl electrode, ~7 mm in diameter, tucked under the nuchal skin. Data was sampled at 25 kHz. In all EIT recordings, current (1.725 kHz, 20 – 50 µA) was injected sequentially through 14 – 33 pairs of electrodes comprising a full EIT protocol in each instance. A specific set of electrode injection pairs comprising the imaging protocol were derived for each experiment by modelling the optimal current injection pattern which yielded uniform sensitivity to impedance changes throughout the hemisphere of interest (Faulkner et al., 2017). The precise number of injection pairs was dictated by the number of the depth electrodes with acceptable contact impedance in each depth array. Transfer voltage measurements were collected at the same time by all 36 depth electrodes. Each recording contained a baseline activity period of up to 90 seconds, electrical stimulation (5 s) and the resulting seizure (~ 30 – 100 s) with a post-ictal period of up to 5 min ensuring return of normal resting-state activity.

5.2.5 Data processing and analysis

The raw data from channels connected to the epicortical electrodes contained only the ECoG. The raw signal from the channels connected to the depth electrodes contained both the SEEG and the transfer impedance measurements. Each type of signal was extracted by applying different digital filters.

Each impedance recording within each of the EIT datasets comprised 36 impedance measurements obtained by all available depth electrodes. As in 3.2.4, these impedance measurements were considered independent and with equal variance. Therefore, in the context of discussing fast impedance changes, the lowercase ‘n’ is used to represent the number of individual impedance measurements acquired within the respective EIT recording from one injection pair. In the context of EIT images, a lowercase ‘n’ represents the number of seizures recorded serially as part of the EIT protocol. The number of rats is signified by an uppercase ‘N’.

5.2.5.1 SEEG data

First, SEEG and ECoG were visualised by filtering the data from depth and epicortical electrodes with a 1 Hz high-pass filter (1st order, Butterworth) followed by a 100 Hz low-pass filter (5th order, Butterworth). Mains noise was eliminated by applying a 50 Hz notch filter (2nd order, IIR). This permitted the visualisation of ictal epileptiform ADs which were then inspected for manual classification and sorting (Fig. 5.1B). The rationale and detailed justification for this method can be found in sections 4.1.3.4, 4.2.6 and 4.3.4. In summary, an epicortical electrode detecting the largest (≥ 1 mV) and the most prominent (0.1 mV threshold) SWDs was identified first as it was considered to represent the origin of these ADs (Fig. 4.10). Trigger markers were placed manually at the peaks of the spikes of those SWDs which appeared morphologically alike (Fig. 5.1C). The selection of SWDs as opposed to other types of ADs for averaging and reconstruction of associated fast impedance changes was based on their stereotypic appearance from seizure to seizure. Based on the previous research, epileptiform events with consistent characteristics, including but not limited to the shape, amplitude and prominence, were assumed to reflect analogous neural circuit activity and could therefore be averaged together into a representative ictal electrographic signature (Hannan, 2019). Morphologically identical epicortical SWDs were clustered and aligned with the SWDs detected by the depth contacts. This enabled the identification of a 'leading' depth electrode(s). The SWD type/cluster which recurred between seizures was chosen for averaging and tomographic reconstruction of underlying impedance changes (Fig. 5.1D). The 'leading' depth electrodes were consistent between the impedance recordings within each rat. Where necessary, adjustment of trigger markers was performed based on the SWDs from the 'leading' depth channels. The final set of trigger markers was used to isolate individual SWDs into 150 ms epochs with a 50 ms pre-spike interval and 100 ms post-spike period which included the wave component (Fig. 5.1C, D). Only SWDs which contained spikes with the largest prominence relative to the other SWDs within the same seizure were used for processing the associated impedance changes.

In neocortical seizures, two SWDs from each seizure were isolated for real-time fnEIT image reconstructions and for SESI. The first SWD was selected from the onset of each seizure. The second SWD was one that occurred within the next 10 s and that displayed increased spike prominence (> 1 mV) with respect to the first SWD. For the purpose of SESI, recordings of these SWDs were filtered with a 40 Hz high-pass filter (1st order, Butterworth) to eliminate any low frequency trends in the data. Depth electrodes were re-referenced with the common averaged reference method widely used for spatial filtering of EEG, ECoG, SEEG and other neural recordings (Bertrand et al., 1985; Kubánek et al., 2009; Ludwig et al., 2009; Satzer et al., 2022). This method entailed the subtraction of the mean value of all electrodes from each recording channel processed for image reconstruction.

5.2.5.2 EIT data

Fast impedance changes were isolated by filtering the raw voltage measurements with a 500 Hz band-pass filter, ±250 Hz around the carrier frequency of 1.725 kHz. Demodulation of the filtered signal was then performed using the Hilbert transform. Demodulated data was filtered with a 10 Hz high-pass filter (4th order, Butterworth) to eliminate any potential artefacts due to unwanted cardiac (~5 Hz) or respiratory (~0.5 – 1 Hz) modulations of the recorded signal. As in previous chapters, changes in the transfer voltage measurements were considered to represent transfer impedance changes. Due to the frequency of the injected current, the modulus of the complex impedance correctly reflected the resistive component and was therefore used for reconstructing EIT images (Faulkner et al., 2018a). The demodulated and filtered data was segmented into 150 ms epochs where 0 ms corresponded to the peak of the spike with a 50 ms pre- and 100 ms-post trigger intervals (-50 ms to +100 ms). Saturated and noisy channels, defined by criteria in 4.4.3.3, were discarded from further analysis. Injecting channels were removed from the cortical but not subcortical seizure imaging dataset because of the lower injection current amplitude used in the latter recordings (50 and 20 µA for cortical and subcortical seizures, respectively).

For reconstruction of a mean SWD-related fast impedance change, epochs from individual depth electrodes during any one seizure – and, therefore, current injection pair – were averaged together. This yielded a mean transfer impedance measurement per recording channel. Outlying epochs were removed prior to averaging using the same criteria as in Chapter 3. Averaged impedance changes were thresholded based on the noise level in two inactivity periods which were (1) the first 20 ms of the epoch (-50 to -30 ms) and (2) the last 20 ms of the epoch (130 to 150 ms). Traces containing noise larger than double the mean noise value for each of these intervals across all measurement pairs were eliminated. The amplitude of any significant impedance changes in the remaining traces was computed with respect to baseline.

For reconstruction of single-shot EIT images, unaveraged epochs corresponding to two SWDs selected in 5.2.5.1 were isolated into separate datasets. In each case, outlying epochs which contained datapoints greater/lower than the 75th percentile plus/minus five times the interquartile range were removed. This elimination process did not exclude epochs where outlying datapoints were in periods (1) and (2) due to filtering artefacts.

Due to small sample size of acceptable EIT imaging datasets in cortical and subcortical groups, the amplitude of significant dVs/dZs in each case was presented as a range of significant dV/dZ values corresponding to all individual injection-measurement pairs used for generating a single EIT image.

In all cases, an impedance change with respect to baseline was reconstructed every millisecond of the epoch. The subsampled voltage traces were filtered with the 50 Hz low-pass filter (5th order, Butterworth) to ensure smoothness of the signal and produced a minimal temporal resolution of 20 ms.

5.2.6 Eligibility screening of EIT data

Validity of the collected data was assessed pre- and post-acquisition by addressing the eligibility criteria detailed in 4.4.3.

Insertion site accuracy and precision was verified by checking which depth electrodes detected the largest forelimb and hindlimb SEPs across all rats to ensure high SEP intensity values (details in 4.3.2).

As far as the impact of the probe insertion was concerned, severe bleeding or damage to pial blood vessels was considered a sign of compromised brain health and, thereby, was deemed to invalidate the experimental preparation. Similarly, where monitored, SEPs which completely ceased over the course of the experiment were deemed to represent adverse post-implantation effects on brain physiology rendering subjects unsuitable for serial fnEIT data collection.

The third set of criteria triaged rats based on the electrographic characteristics of electrical seizures. Subject which displayed ictal SWDs with inconsistent morphology between seizures (assessed by qualitative inspection) or those which failed to reach the acceptable amplitude threshold (1 mV) were discarded.

Criteria for acceptable noise were applied post-processing and before averaging to ensure that the final SNR of the transfer impedance measurements is suitable for image reconstruction. Impedance recordings which contained excessive noise in the baseline (>0.2 % or >20 µV) or displayed artefactual modulations from a known source were discarded from further analysis.

Lastly, any other technical issues which compromised the reliability of the recorded data, including but not limited to faulty equipment or electronics, were also considered to render the data unsuitable for processing.

5.2.7 Image reconstruction

5.2.7.1 EIT images

The forward solution of the boundary voltages which result from the injection and recording electrode combinations defined in the protocol was computed in 120 – 360 min with EIDORS software (Adler & Lionheart, 2006) on an anatomically realistic FEM rat brain mesh composed of 3 million tetrahedral elements. Computations were done using a research workstation (Dell Precision, Dell Inc., UK, 256GB RAM, 16 Intel Xeon CPU cores). Each boundary voltage measurement was obtained in reference to a 9 mm-diameter electrode positioned over the cerebellar cortex. The tetrahedral FEM mesh comprised three conductivity layers, namely the grey matter, white matter, and the CSF, with conductivity values of 0.3 S/m, 0.15 S/m and 1.79 S/m, respectively (Horesh, 2006). The inverse problem was solved by calculating and inverting the Jacobian matrix. The reconstruction was then performed on a coarser mesh composed of ~300,000 hexahedral elements, 200 µm in size, using zeroth-order Tikhonov regularisation. Noise-based correction was performed upon selection of a fixed regularisation parameter derived via the generalized cross-validation (Mason et al., 2024). The reconstructed impedance changes were visually represented by the significance Z-score ($Z_{\delta\sigma}$) calculated by dividing the reconstructed conductivity values by the standard deviation of the conductivity changes predicted to result from the random uncorrelated Gaussian noise.

5.2.7.2 SEEG inverse source localisation

The forward solution was computed using the FEM method in EIDORS software (Adler & Lionheart, 2006). Current density distribution in the brain was simulated for a given dipole oriented along x, y and z axes in each voxel of the tetrahedral FEM mesh (Adler & Lionheart, 2006). The inverse problem was solved by consequently generating a three-dimensional lead field matrix and inverting it. The SEEG source reconstruction was performed on a hexahedral mesh with ~300,000 elements, 200 µm in size, using zeroth-order Tikhonov regularisation with generalised cross-validation. Nose-based correction was performed with random Gaussian noise. The reconstructed electrical activity was visualised using a normalised current density measure (J) calculated for each voxel at each time point.

5.2.8 Image analysis

Each EIT recording and SESI reconstruction were analysed independently.

5.2.8.1 EIT images

Active voxels were defined as those with $Z_{\delta\sigma} \geq 3$ (Aristovich et al., 2014).

Based on analysis of raw impedance data and on findings of previous similarly designed EIT studies of epileptic ADs, conductivity changes during an averaged neocortical SWD reconstructed within 40 ms of the peak of the spike component (-20 to +20 ms) were regarded as significant (Hannan et al., 2018b). These significant changes were visualised by applying a 40 % threshold to the maximal reconstructed conductivity Z-score value (Hannan, 2019).

For subcortical seizures, the temporal window of significant conductivity changes during an averaged SWD was extended to +35 ms based on the analysis of raw impedance data. EIT images of subcortical SWDs were initially visualised with the same 40 % threshold. However, with this Z-score limit, no significant activity was visible between +/-10 ms of the spike peak where the largest decreases in the transfer voltage were observed in the raw dV traces (Fig. 5.3). Qualitative visual analysis of EIT images with different conductivity thresholds suggested that the ictal trajectory could be deciphered by selecting the voxels with a Z-score in a range of 10 – 20 % of maximal reconstructed $Z_{\delta\sigma}$ value.

In single-shot EIT images of individual unaveraged neocortical SWDs, only activity reconstructed between +/-10 ms of the spike peak was deemed significant based on raw dVs. A similar $Z_{\delta\sigma}$ thresholding principle as that used for visualising subcortical seizures was applied to images of individual neocortical SWDs reconstructed from unaveraged EIT recordings. Physiologically relevant activity could only be seen when selecting the voxels with the Z-score of 40 – 60 % the maximal reconstructed $Z_{\delta\sigma}$ value. Values outside of this range introduced significant noise into the image obscuring the physiologically relevant activity pattern.

5.2.8.2 SEEG source images

Significant changes in the current density distribution reconstructed from SEEG data were isolated by applying a standard threshold of 50 % the maximal J value (full width at half maximum, FWHM). To enable anatomical localisation of significant active voxels, EIT and SESI images were overlayed with the 3D image of the expected coordinates of the depth electrodes.

5.2.9 Statistical analysis

Significant fast impedance changes were identified using the same method as described in 3.2.8.2. Timepoints corresponding to significant impedance responses in each averaged impedance trace were identified by performing a one-way t-test ($\alpha = 0.05$) for each timepoint across all epochs isolated from a corresponding impedance measurement. Measurements obtained by individual depth electrodes were evaluated separately. Significant impedance changes during individual neocortical SWDs were assessed across all injection-measurement pairs simultaneously ($\alpha = 0.01$). The resulting p-values were adjusted with Bonferroni correction in both cases. Differences in the amplitude and the SNR of impedance changes associated with individual SWDs from different timepoints of a neocortical seizure were assessed with a two-sample t-test ($\alpha = 0.05$).

Within- and between-seizure similarity was quantified by creating a binary mask for each SESI reconstruction of individual SWDs. Mask pixel values of 1 were assigned to elements of the mesh which contained a normalised J value above the threshold (FWHM). Mask pixel values of 0 were assigned to the remaining elements which were considered to display background activity. Binary masks corresponding to each SESI reconstruction of the first SWD from 14 neocortical seizures and to each reconstruction of the subsequent SWD from the same seizures were then independently summed together to obtain two significance maps where the elements contained values ranging from 0 to 14. Significant activity was evaluated by computing the p-values for each voxel in the sum of 14 binary masks using the same method as in 3.2.8.4. Voxels with $p < 0.05$ were considered to display significant activity.

5.3 Results

5.3.1 EIT data screening

Six EIT datasets were acquired for the purpose of this study, one full dataset per rat (N = 6 rats). Four rats were used to collect impedance recordings during cortical seizures (N = 4) whereas the remaining two rats were used for collecting recordings of subcortical seizures (N = 2).

Eligibility screening rendered three out of four datasets in the cortical group unsuitable for analysis. Two of these datasets were dismissed due to technical issues with the recording equipment which compromised data quality. The third dataset was discarded because of visible damage to a major pial vessel during the implantation of the depth probe. One out of two EIT datasets from the subcortical group was discarded due to lack of acceptable seizures across the induction attempts (see 4.4.3 for detailed criteria).

The remaining results therefore refer only to data from one rat in cortical and one rat in subcortical seizure induction groups.

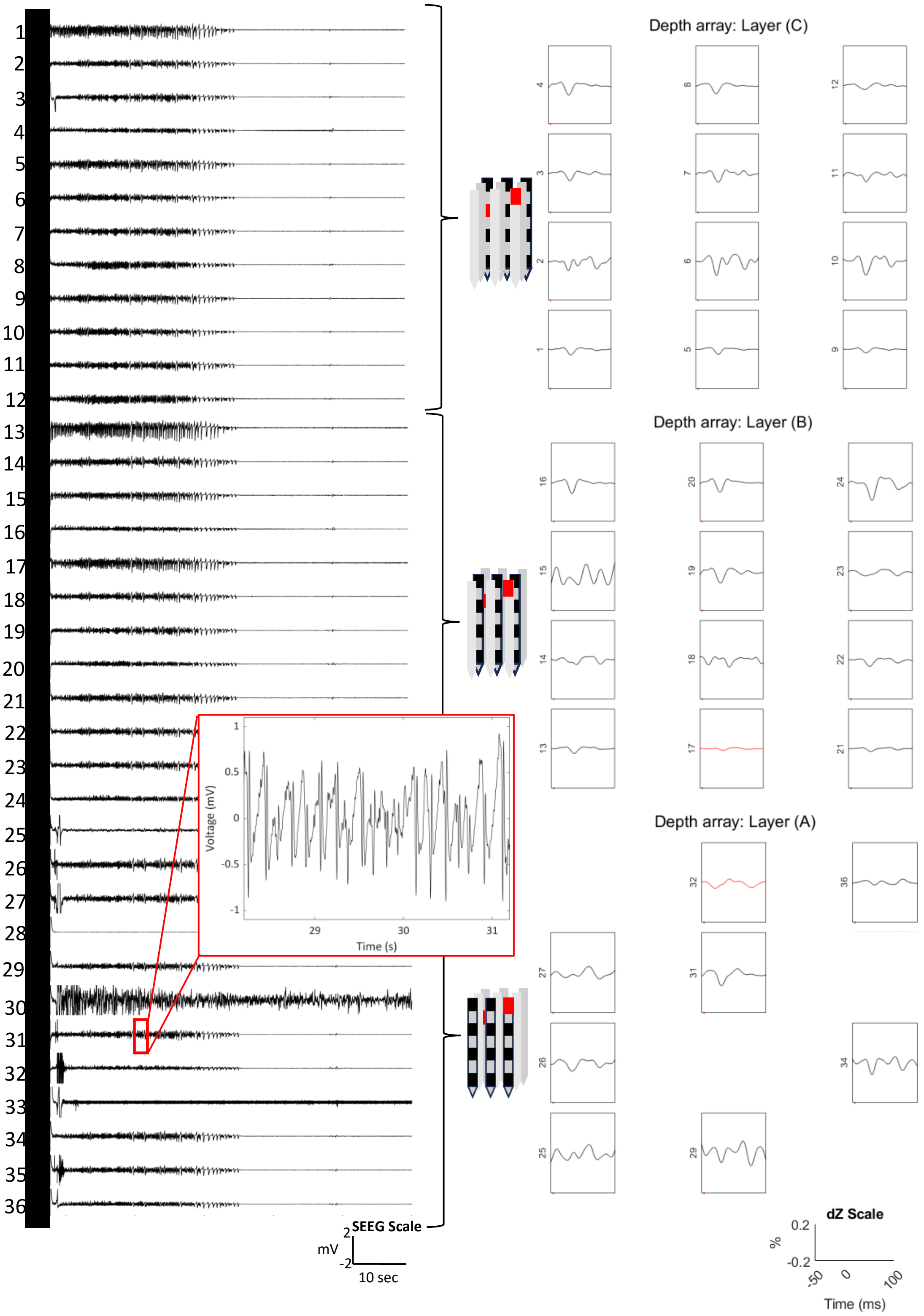

Figure 5.2. A representative example of cortically induced electrical seizures with a burst of stereotypic SWDs and a topographical distribution of the corresponding fast impedance changes during the average of these isolated SWDs. Translaminar stimulation of the sensorimotor cortex yielded focal electrical seizures lasting 60.5 ± 22.8 s (n = 14 seizures, N = 1 rat). The relative positions of the depth contacts which administered the stimulation current are marked in red on the 3D representations of the array. Layers A, B, and C represent the shank triplets comprising the depth probe in antero-posterior direction. SWDs were the dominant and the most consistent form of ictal activity. Spikes within these SWDs were associated with significant negative fast dZs occurring within ±20 ms of the peak of the spike component ($p < 0.05$). Impedance traces are shown on the right. Impedance changes recorded by electrodes injecting EIT current are shown in red. Excessively noisy impedance recordings are not displayed.

5.3.2 Electrographic characteristics of electrical seizures imaged with fast neural depth EIT

5.3.2.1 Cortical stimulation

Electrical seizures induced by stimulating the sensorimotor cortex presented consistently with a stereotypic pattern of rhythmic focal 1 – 5 Hz SWDs which tended to evolve into bursts of low-frequency PSWDs and sharp waves (Fig. 5.2). Some seizures contained brief periods (~20 s) of high-frequency (~8 Hz) sequential spikes returning to slow oscillations towards the end of the seizure. Across recording contacts and seizures, SWDs displayed the most consistent morphology of all ADs with the largest amplitude (up to 4 mV) and spike prominence (≥~1 mV) detected on contact 31 (Fig. 5.2). The duration of neocortical seizures ranged 23.9 – 100.9 s with an average duration of 60.5 ± 22.8 s (mean ± S.D; median = 62.4 s; n = 14 seizures, N = 1 rat). Each seizure contained 22 – 81 near-identical SWDs used for averaging the associated fast impedance responses (Fig. 5.2).

5.3.2.2 Subcortical stimulation

Stimulation of the CPu yielded seizures with similar ictal electrographic pattern to the neocortical ones and contained predominantly SWDs interspersed with sharp waves (Fig. 5.3). The amplitude and the prominence of the spikes within the detected SWDs were comparably smaller with values up to 2.5 mV and <1 mV, respectively, detected consistently on contact 12 (Fig. 5.3). Epileptiform activity induced subcortically was also shorter in comparison to ictal ADs in the neocortex. The duration of subcortically provoked seizures ranged 13.4 – 53.9 s with a mean duration of 27.8 ± 11.6 s (mean ± S.D.; median = 23.5 s; N = 22 seizures, n = 1 rat). Each seizure contained 16 – 106 reproducible SWDs used for averaging the resulting fast impedance responses (Fig. 5.3).

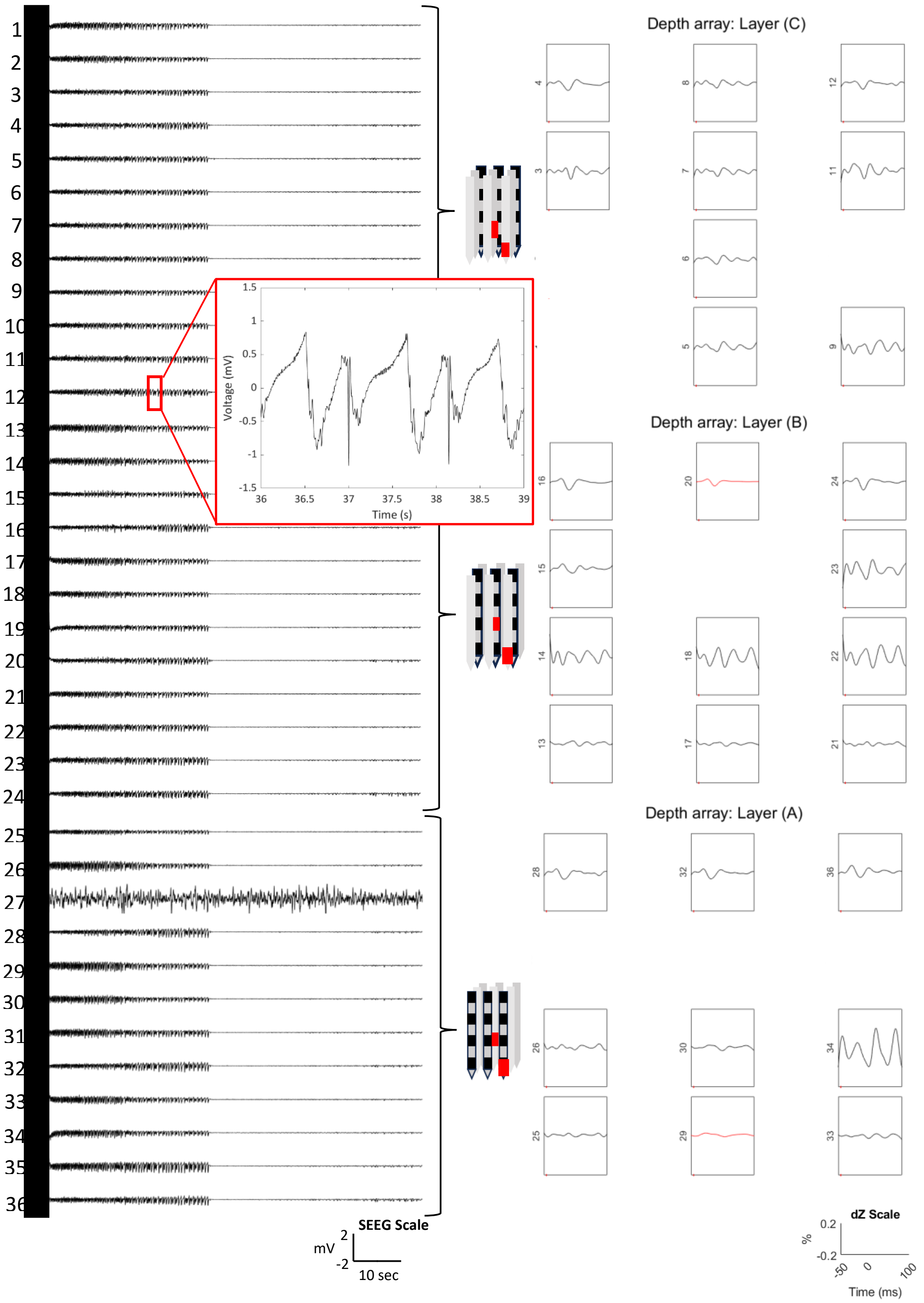

Figure 5.3. A representative example of subcortically triggered electrical seizures containing a burst of repetitive SWDs and a topographical distribution of the corresponding fast impedance changes during the average of the spikes within these SWDs. Electrical stimulation of the subcortical caudate-putamen nuclei yielded focal electrical seizures lasting was 27.8 ± 11.6 s (mean ± S.D.; n = 22 seizures, N = 1 rat). The relative positions of the depth contacts which administered the stimulation current are marked in red on the 3D representations of the array. Layers A, B and C represent the shank triplets comprising the depth probe along AP axis. SWDs were the most consistent form of ictal activity and were associated with significant negative fast dZs within -20 ms to +35 ms around the peak of the spike component centred at 0 ms ($p < 0.05$). Impedance changes recorded on electrodes injecting EIT current are shown in red. Excessively noisy impedance recordings are not displayed.

5.3.3 Fast impedance changes during ictal SWDs recorded with EIT and depth electrodes

5.3.3.1 Cortical seizure induction

Neocortical SWDs were associated with significant fast impedance decreases in phase with a spike component in 61 % of impedance measurements across all seizures and current injection pairs ($p < 0.05$ with Bonferroni correction; n = 319 measurements from 14 seizures, N = 1 rat). The detected impedance decreases were between -0.30 – -14.0 µV (-0.020– -0.22 %, median = 0.035 %; n = 319 measurements from 14 seizures, N = 1 rat). Significant changes were confined to +/- ~20 ms around the peak of the spike and occasionally accompanied by an impedance overshoot of variable amplitude (Fig. 5.4). The SNR ranged between 1.80 – 150.0 (median = 11.0). A representative topographical distribution of fast impedance responses recorded during one seizure is shown in Fig. 5.2.

Visual inspection of the demodulated data confirmed that fast impedance changes during individual neocortically induced SWDs were visible by naked eye before averaging (Fig. 5.5). This suggested that the SNR of the impedance signal was sufficient for a single-shot fnEIT. To investigate this hypothesis, two sequential impedance responses during individual ictal SWDs separated by up to 10 s were isolated from neocortical seizures for real-time imaging. SWDs isolated from the beginning of the neocortical seizures (SWD1) produced significant negative impedance changes in 95 % of impedance measurements ($p < 0.01$ with Bonferroni correction; n = 303 measurements from 14 seizures, N = 1 rat; Fig. 5.5, top panel). The amplitude of impedance decreases on recording electrodes ranged between -0.020 - -19.0 µV (-0.0003 - -0.70 %; median = -0.065 %; n = 303, N = 1).

Similarly, fast impedance decreases associated with spikes from the SWD occurring up to 10 s later (SWD2+) were significant in 97 % of impedance measurements ($p < 0.01$ with Bonferroni correction; n = 308 measurements from 14 seizures, N = 1 rat; Fig. 5.5, bottom panel). The amplitude of these changes was -0.055 – -21.0 µV (-0.0012 – -0.41%; median = -0.055 %; n = 308, N = 1). Statistically significant change in transfer impedance occurred between 10 ms preceding and 10 ms following the peak of the spike component (-10 to +10 ms) during either SWD.

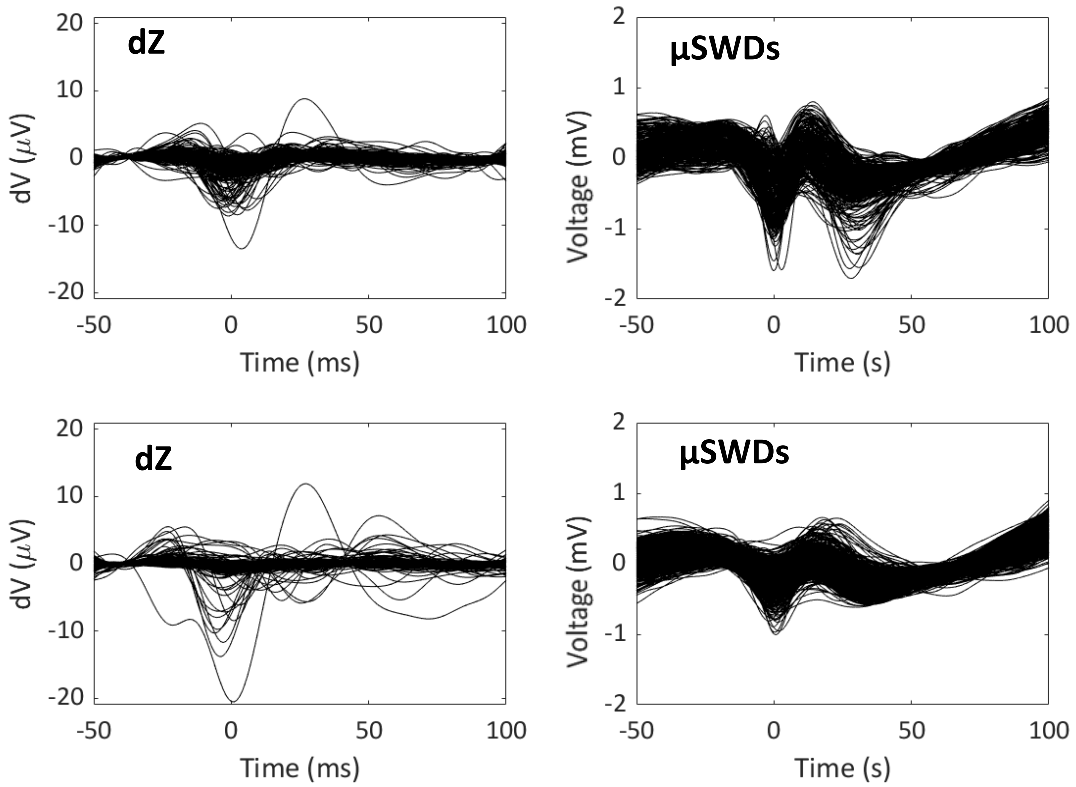

Figure 5.4. Averaged fast impedance responses with corresponding ictal SWDs acquired from the full EIT protocol during seizures induced by cortical (top panel) and by subcortical (bottom panel) stimulation. The top panel represents all fast impedance changes (dZ) during the averaged neocortical SWDs from all seizures and all recording channels (µSWDs). The bottom panel represents the fast impedance changes in response to subcortically triggered and averaged SWDs. Significant changes in impedance ranging -0.30 − -14.0 µV were detected within -/+20 ms of the spike during neocortical SWDs and -0.070 − -14.0 µV within -20 to +35 ms of the spike during subcortical SWDs ($p < 0.05$ with Bonferroni correction).

There was no difference in the amplitude of both raw (dV, µV) and proportional (dZ, %) fast impedance changes associated with individual SWDs ($p > 0.05$, two-sample t-test; Fig. 5.5). In contrast, the SNR of the impedance changes occurring during the first SWD of the seizure was significantly higher than the SNR of the impedance response to the SWD in next 10 seconds ($p < 0.001$, two-sample t-test; Fig. 5.5). The corresponding SNRs ranged 0.040 – 60.0 (median = 4.1) and 0.040 – 29.0 (median = 3.1) for SWD1 and SWD2+.

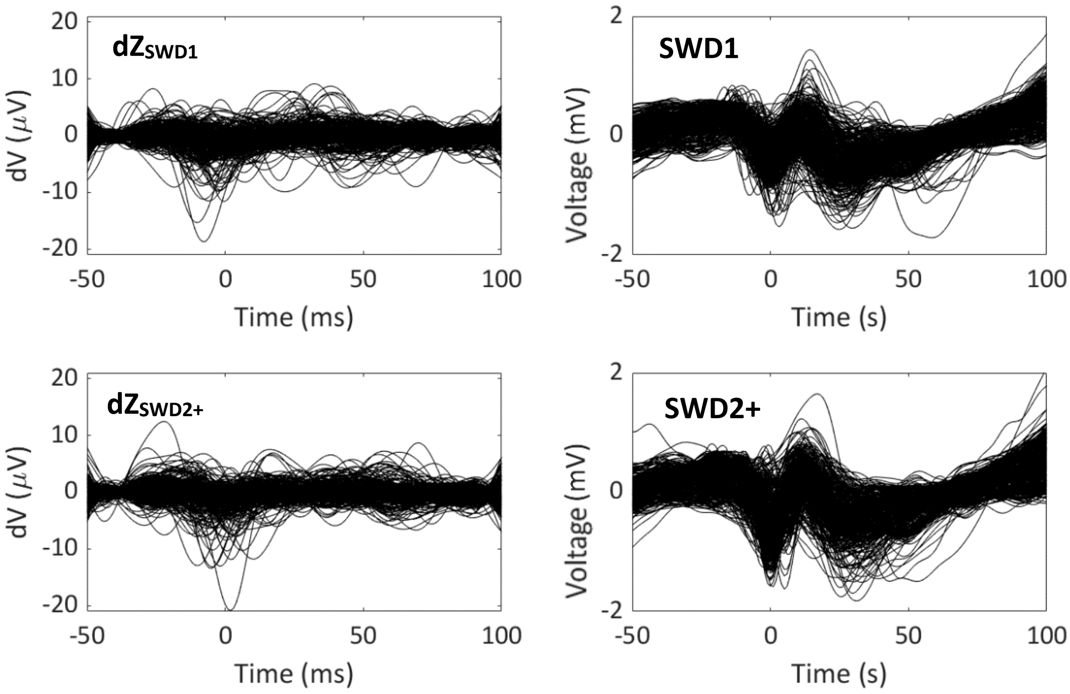

Figure 5.5. Fast impedance decreases during individual SWDs evoked by neocortical stimulation were visible in demodulated data before averaging. The top panel represents fast impedance changes (dZ) corresponding to the first SWD (SWD1) isolated from SEEG recordings obtained during each of 14 seizures by all depth electrodes. The bottom panel represents fast impedance changes in response to individual SWDs occurring after ~10 seconds into the seizure and displaying increased spike prominence relative to the initial SWDs (SWD2+). Significant change in impedance with respect to baseline occurred within 20 ms of the peak of the spike (-10 to +10 ms) in both sets of unaveraged epochs ($p < 0.01$ with Bonferroni correction). There was no difference in the amplitude of impedance changes associated with SWDs from different timepoints of a neocortical seizure ($p < 0.05$, two-sample t-test). However, the SNR of ictal fast impedance changes was significantly greater at the start of the seizure ($p < 0.001$, two-sample t-test).

5.3.3.2 Subcortical seizure induction

Ictal SWDs produced by subcortical stimulation yielded significant fast impedance changes in 13 % of impedance measurements across all seizures and injection pairs ($p < 0.05$ % with Bonferroni correction; n = 507 measurements from 22 seizures, N = 1 rat). The amplitude of the detected changes was -0.070 − -14.0 µV (-0.010 − -0.11 %; median = -0.031 %; n = 507, N = 1 rat) with their SNR ranging between 2.70 – 53.0 (median = 8.50). Significant changes commenced and peaked between -20 to +35 ms of the peak of the spike (0 ms). The data is shown in the bottom row of Fig. 5.4.

5.3.4 Intracranial depth EIT images of ictal SWDs in the rat brain

5.3.4.1 Fast neural EIT of averaged ictal SWDs: neocortical and subcortical seizures

Dynamic images of averaged ictal SWDs from neocortical and subcortical seizures were reconstructed from two EIT datasets, one in each group.

Ictal fast neural changes during an averaged SWD from neocortical seizures appeared firstly around the bottom depth electrodes in shanks B and C located between the central amygdaloid nucleus and lateral globus pallidus (Fig. 5.6; see Fig. 4.2 for anatomical reference points). These conductivity changes expanded in the caudal (-6 ms) and dorsal (-4 ms) directions; however, they were considered physiologically irrelevant in this seizure model. Between -4 ms and 0 ms, conductivity changes appeared in the CPu and in the cortex which were considered physiologically plausible and relevant. Activity in the cortex originated in bottom layers of the whisker division of the S1 (S1BF) at -4 ms. This was followed by lateral propagation between the S1BF and the S1FL/HL (-2 to 0 ms) and looping back to S1BF (+1 to +4 ms). The activity started to cease gradually 4 ms after the spike peak.

Images of a subcortically induced SWD were considerably noisier than images of a neocortically induced SWD (Fig. 5.7). A marked proportion of reconstructed changes localised to the ventral and caudal regions of the brain (-12 to +6 ms) which were considered physiologically irrelevant in this scenario. Nonetheless, simultaneously, significant conductivity evolved in the S1. Fast neural changes started in the bottom layers of S1BF at -20 to -18 ms (Fig. 5.7). The activity then shifted briefly to the top cortical layers around the border between S1HL and S1FL (-16 to -15 ms; not shown) before looping back to the S1BF, albeit anterior to the initial focus (-12 ms; Fig. 5.7). Activity subsequently spread in the posterior and dorsoventral directions (-12 to -6 ms). This involved the propagation between the depth electrodes in the shanks A located in the bottom cortical layer of the facial S1 to the depth electrodes in the shanks C located in the superficial cortical layers of the facial S1 (Fig. 5.7). Epileptiform activity continued to spread horizontally encompassing an enlarging cortical region with simultaneous engagement of the CPu (up to 0 ms). After peaking, ictal activity translocated to the secondary somatosensory cortex (S2) and gradually diminished (+18 ms).

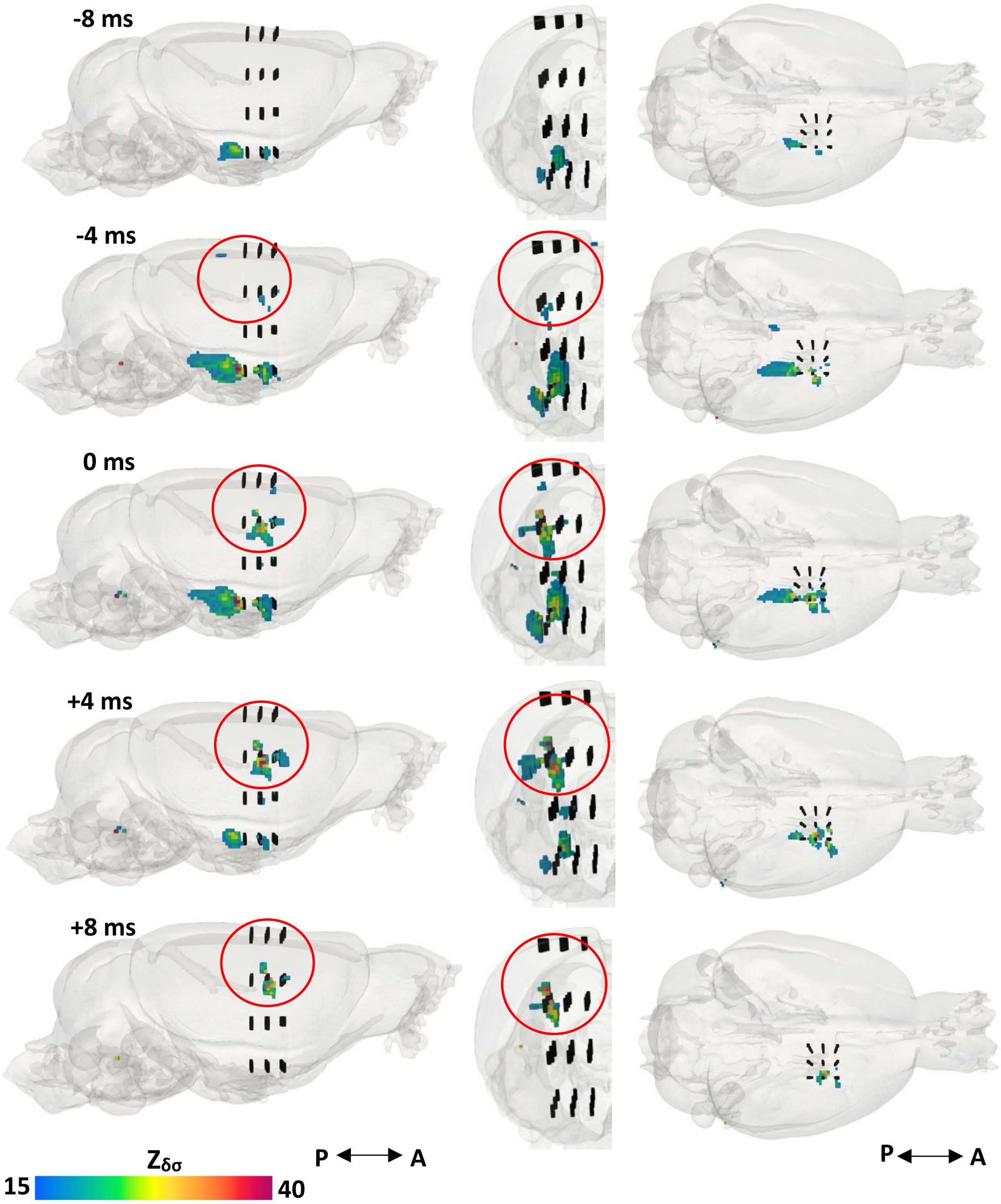

Figure 5.6. The spatiotemporal trajectory of fast impedance changes during an averaged ictal SWD provoked by cortical stimulation. The figures represent the propagation of the averaged fast neural activity during an ictal SWD at five timepoints from – 8 ms to +8 ms with respect to the peak of the spike component (0 ms). The left column depicts the SWD trajectory in the sagittal plane, the middle column in the coronal plane, and the right column in the transverse plane. Physiologically significant fast neural activity (encircled in red) originated in the bottom cortical layers of S1BF (-4 to 0 ms). Further expansion was seen in lateral direction (0 to +4 ms) and peak activity was reached at +4 ms. The decline was observed afterwards (+8 ms) with complete cessation by +10 ms (not shown). The black markings define the expected 3D positions of the depth electrodes. The Z-score of conductivity changes is denoted by $Z_{\delta\sigma}$.

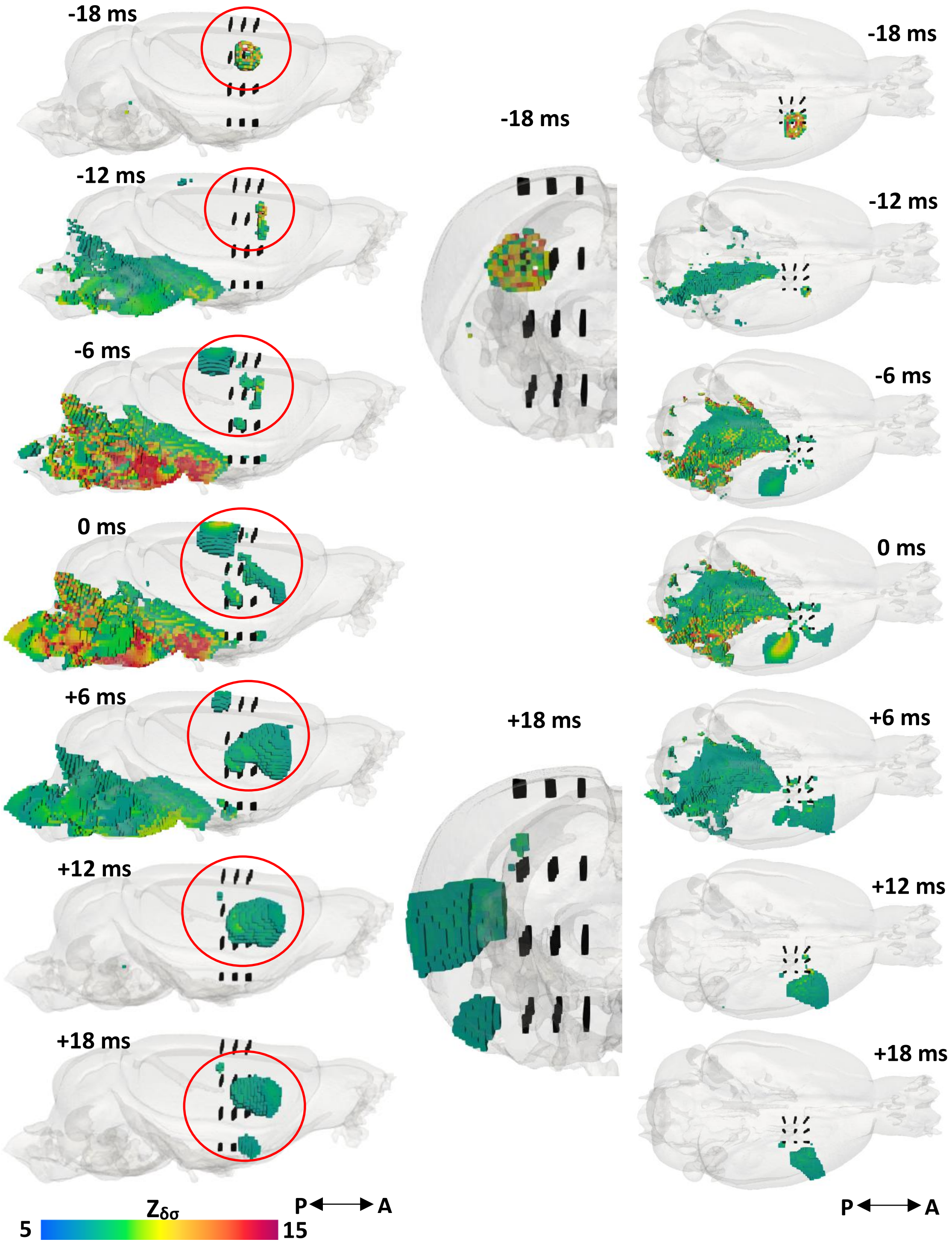

Figure 5.7. The spatiotemporal trajectory of fast impedance changes during an averaged ictal SWD provoked by subcortical stimulation. The figures represent the propagation of the averaged fast neural activity during an averaged ictal SWD at seven timepoints from – 18 ms to +18 ms with respect to the peak of the spike component (0 ms). The left column depicts the SWD trajectory in the sagittal plane, the middle column in the coronal plane, and the right column in the transverse plane. Physiologically significant ictal activity (encircled in red) originated in the bottom layers of S1BF and propagated between different divisions of the S1. The black markings define the expected 3D positions of the depth electrodes. The Z-score of conductivity changes is denoted by $Z_{\delta\sigma}$.

5.3.4.2 Single-shot EIT images of individual neocortical SWDs

Fast neural activity during individual ictal SWDs (SWD1 and SWD2+) isolated from different timepoints of a reproducible electrical seizure showed distinct patterns of intracerebral conductivity changes reconstructed every 2 ms within ±10 ms of the peak of the spike component (Fig. 5.8). The propagation trajectories of these SWDs overlapped partially (red circles in Fig. 5.8).

Significant fast changes in brain impedance during the first SWD (SWD1) started at -10 ms in three distinct cortical regions (Fig. 5.8, left column). Ictal activity commenced in the superficial layers of the primary and secondary motor cortices (M1/2) anterior to the depth array with a simultaneous conductivity increase in the deeper layers of the S1BF and S1HL. Activity propagated both tangentially and orthogonally to the cortical layers with an enlargement of the initial foci seen along the DV and AP axes. Maximal change was observed between -6 and -4 ms after which ictal changes started to cease before terminating at +6 ms near the border of the M1 and the S1HL regions (Fig. 5.8, bottom left). In addition to the cortical regions, conductivity changes were also reconstructed in the ventrolateral (VL) and ventromedial (VM) nuclei of the thalamus (-8 to 0 ms) where activity was detected for ~8 ms before the spike reached its peak in SEEG data (0 ms).

Images of fast neural changes during a later SWD (SWD2+) were considerably noisier with a large proportion of conductivity changes reconstructing in the ventral and rostral brain regions (Fig. 5.8, right column). Due to their location, these conductivity changes were not considered physiologically relevant. Significant and physiologically relevant ictal activity during SWD2+ originated in the trunk representation within the S1 (S1Tr) with concurrent activation of the basal ganglia observed around the bottom of the anterior shanks (-10 ms; Fig. 5.8, right column). A rapid recruitment of multiple cortical regions was observed within the following 2 ms, including the S1HL and S1FL. Ictal activity subsequently propagated to the M1/2 two milliseconds before the spike reached its peak (-2 ms). Activity pattern seen between 0 to +6 ms followed a similar trajectory to the ictal activity during SWD1 between -8 and -2 ms (Fig. 5.8, red circles).

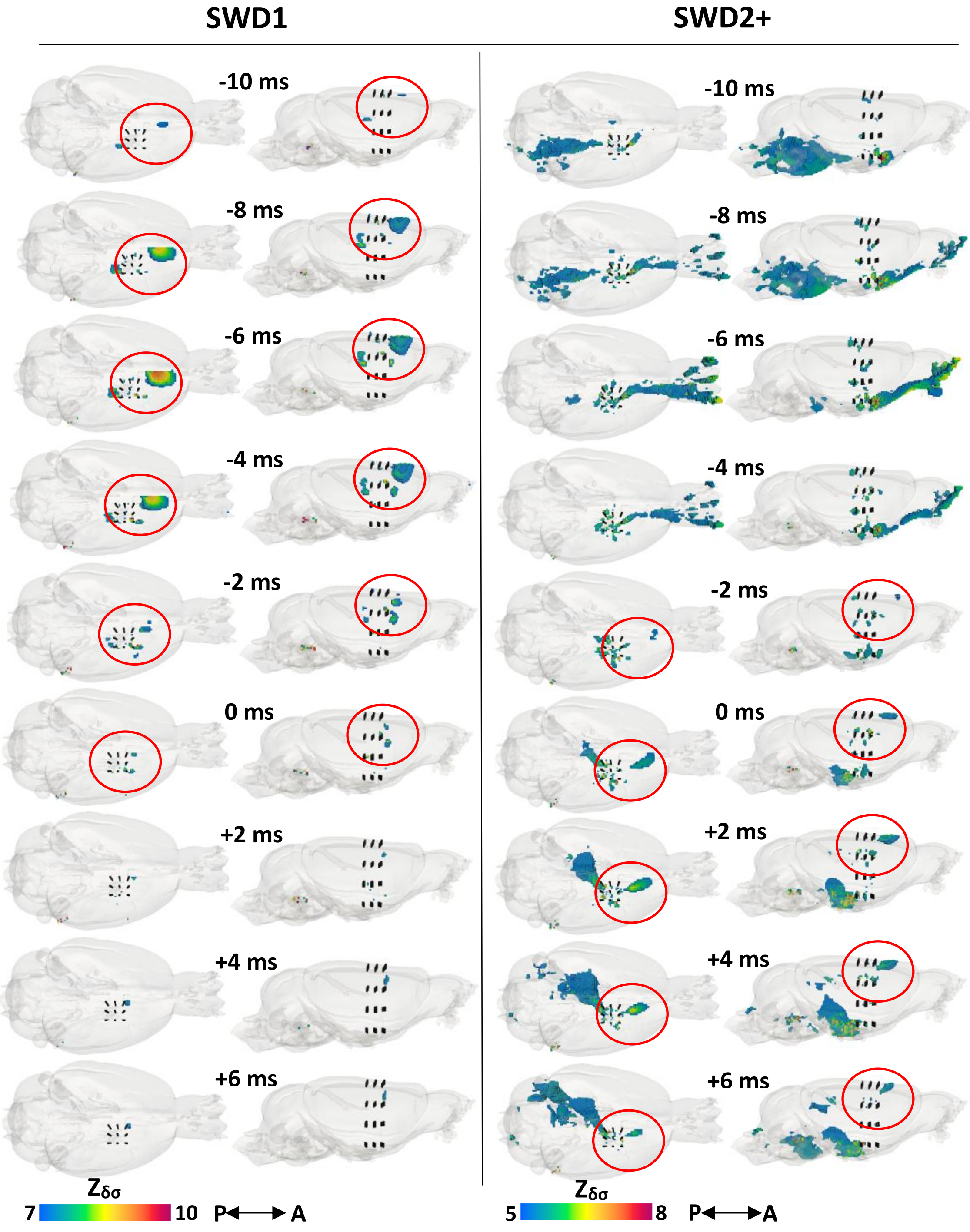

Figure 5.8. Comparison of single-shot EIT images of two sequential ictal SWDs isolated from neocortical seizures. Left hand column represents reconstruction of spike-related conductivity changes during the first SWD (SWD1) isolated from a reproducible cortical seizure (n = 14 seizures, N = 1 rat). Right hand column depicts the same timepoints reconstructed using impedance data recorded during the ictal SWD which occurred within the next 10 s (SWD2+). The ictal trajectories of individual SWDs reconstructed from different timepoints of the same seizure overlapped marginally with overlapping neural circuits engaged at different timepoints of reconstructed discharges (overlapping activity encircled). Black markings denote the 3D positions of the depth electrodes; $Z_{\delta\sigma}$ represents the Z-score of the reconstructed conductivity change.

5.3.5 Significant ictal activity reconstructed from SEEG data: within and between seizure overlap

Current density changes during the spike portion of individual ictal SWDs used for single-shot EIT (section 5.3.4) were reconstructed using simultaneously recorded SEEG data ($n = 14$ seizures, $N = 1$ rat). Statistical analysis of SESI reconstructions produced from the first SWD of every neocortical seizure showed significant common active voxels between -6 to -4 ms leading up to the spike peak ($p < 0.05$; $n = 14$ seizures, $N = 1$ rat; Fig. 5.9). On the other hand, significant overlap between the ictal SWDs within the following 10 seconds of these seizures was observed only at -1 ms and +1 to +2 ms of the spike peak ($p < 0.05$; $n = 14$ seizures, $N = 1$ rat; Fig. 5.9).

Detailed qualitative analysis of individual SESI reconstructions enabled a more intricate comparison of the differences in SWD dynamics within and between seizures. Visual inspection of the current density changes during significant timepoints revealed that the SWD onset zone shifted with each induction and depended on the time of the day when the recording was obtained (red transparent voxels, Fig. 5.9). Stimulations at the start of experiments ('Early seizure', Fig. 5.9) produced SWDs which tended to originate in the sensorimotor cortices (S/M 1/2) located anterior to the array and moved into deeper and more posterior cortical regions. With repeated inductions ('Late seizure'), the primary ictal focus gradually migrated to the superficial cortical layers posterior to the depth probe and continued to propagate ventrally and anteriorly towards the bottom of the S1BF as the seizure evolved (Fig. 5.9, right column). Overall, there were more common active voxels between the SWD1's than the SWD2+'s suggesting the divergence of epileptogenic circuits with progression of seizures. Schematics of the entire epileptogenic network constructed from the combined results of fnEIT and SESI is provided in Fig. 5.10.

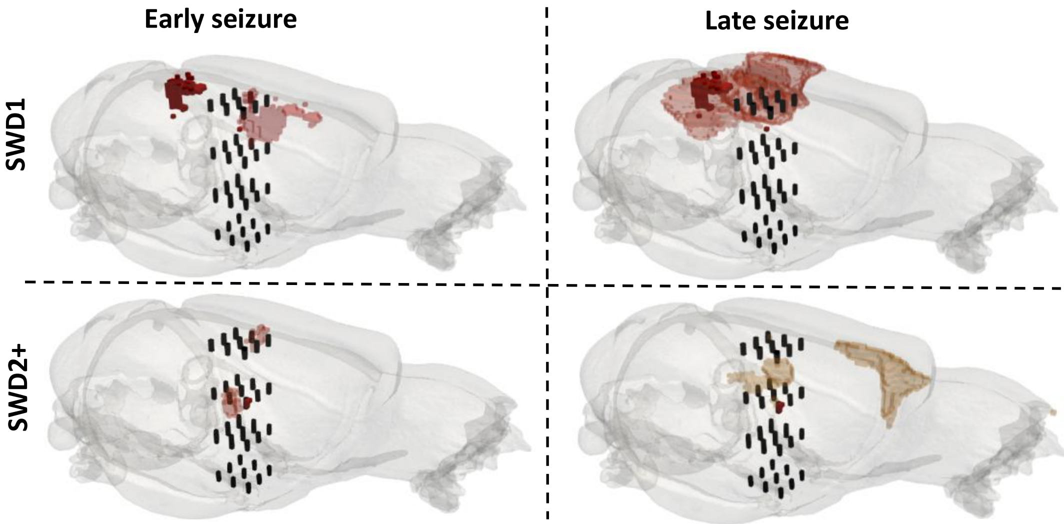

Figure 5.9. Common neural activity within and between seizures extrapolated from SEEG source images of neocortical ictal SWDs. Common active voxels (dark red) were determined by the application of binary masks across all SESI reconstructions thresholded at FWHM (n = 14 seizures, N = 1 rat). The figure shows the timepoints with maximal significant common activity during the first SWD of each seizure (SWD1) and the subsequent SWD occurring within the next < 10 seconds (SWD2+). Transparent voxels represent an example of individual SWD source reconstructions from two seizures provoked at different times of the day. For visualisation purpose, only activity corresponding to ≥75 % of the maximal reconstructed current source density value (J) is displayed here. The black markings signify the expected 3D positions of the depth electrodes.

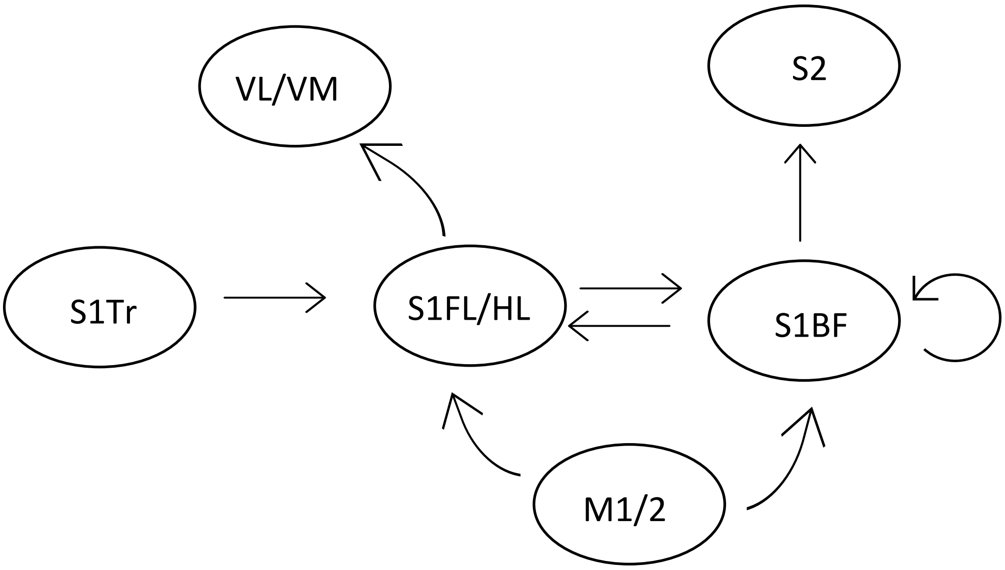

Figure 5.10. The proposed epileptogenic network underlying the spike portion of the ictal SWDs during electrical seizures in rats. Fast neural activity depicted by EIT images both averaged and unaveraged SWDs appeared to converge in the forelimb, hindlimb and whisker barrel portions of the S1. This suggested that these regions may have comprised an epileptogenic zone and were necessary for the maintenance of the electrical seizures. M1 – primary motor cortex; M2 – secondary motor cortex; S1BF - primary somatosensory cortex, whisker barrel field; S1FL - primary somatosensory cortex, forelimb region; S1HL - primary somatosensory cortex, hindlimb region; S1Tr - primary somatosensory cortex, trunk region; S2 – secondary somatosensory cortex; VL - ventrolateral thalamic nucleus; VM - ventromedial thalamic nucleus.

5.4 Discussion

5.4.1 Summary of results

This study investigated the feasibility of enhanced-resolution imaging of pathologic neural activity during ictal epileptiform discharges in murine brain with intracranial fast neural EIT and stereo-electrode arrays. The aim was to determine whether the 3D trajectories of ictal SWDs evoked by stimulation of various brain regions could be deciphered with high spatiotemporal precision using this new imaging method. To achieve this, preliminary fnEIT recordings with acceptable noise characteristics were collected in two rats during cortically and subcortically induced reproducible electrical seizures containing consistent and repeatable SWDs (Fig. 5.2 and 5.3). The results from each imaging dataset showed significant impedance decreases associated with the spike portion of the averaged ictal SWDs (Fig. 5.4). The amplitude of the averaged changes was relatively similar between groups and ranged between ~ -0.01 to -0.2 %. However, the SNR of impedance changes resulting from neocortically triggered SWDs was higher than those produced by subcortical stimulation (median SNR values of 11.0 and 3.1, respectively). Therefore, impedance changes associated only with individual neocortical spikes were visible by naked eye before averaging and suggested that, for the first time, real-time imaging of fast electrical activity without within-seizure averaging was potentially feasible with fnEIT and intracranial electrodes (Fig. 5.5).

As a proof-of-concept, EIT images of fast impedance changes during both averaged and unaveraged ictal SWDs were reconstructed in this study (Fig. 5.6, 5.7, 5.8). In line with the raw EIT data, images of subcortically triggered averaged SWDs were considerably noisier than the neocortical ones and contaminated with a significant proportion of active voxels in the distal brain regions which were not considered physiologically relevant in this epilepsy model (Fig. 5.7). However, activity in physiologically relevant brain regions overlapped between stimulation paradigms (Fig. 5.6, 5.7). The ictal propagation trajectory depicted in reconstructions of averaged cortical and subcortical SWDs involved common epileptogenic areas, including the facial, forelimb and hindlimb subfields of the S1. Real-time images of individual neocortical SWDs depicted the same S1 areas with additional activity observed in the motor cortices and the thalamus (Fig. 5.8). Surprisingly, the order of neural circuit recruitment between individual SWDs appeared temporally misaligned and did not follow the neural activity pattern observed in the images of the averaged SWDs. This suggested that the precise propagation trajectories of individual SWDs were distinct which was supported by few overlapping voxels between the SEEG source images of individual SWDs (Fig. 5.9). However, this was an isolated finding in one rat and could not be at present generalised. Nevertheless, the main ictal foci remained preserved across both imaging modalities and epileptiform events and may have indicated the boundaries of the putative EZ in this epilepsy model (Fig. 5.10).

Since the above findings represented data from only two rats, the reproducibility of the results could not be demonstrated and, therefore, physiological significance of the findings may be limited and should be interpreted with caution. Nevertheless, this pilot study demonstrated that the new imaging method combining fnEIT with a novel penetrating depth array can produce images of neural impedance changes occurring over milliseconds in the rat brain during ictal SWDs. It was also shown that real-time imaging of ictal discharges without within-seizure averaging might be feasible with EIT if sufficient SNR was achieved, albeit further studies are necessary to confirm this. According to SESI and fnEIT images, neural circuits underlying individual SWDs displayed unexpected spatiotemporal heterogeneity. SWD circuits varied within and between electrical seizures (Fig. 5.8 and 5.9). This finding contradicted previous assumptions about the controlled and reproducible nature of electrical ADs (Fig. 5.8, 5.9; Hannan, 2019). Due to low sample size used in this study, no firm conclusions can be drawn from this result. The observed variation might simply reflect inherent biological variability within the species. To ensure that an accurate representation of neural circuit behaviour on a population level is obtained, a larger sample size would need to be used. If follow-up studies with statistical analyses were to confirm that neural circuits vary randomly between the same type of seizures, it would impact our current understanding of epileptogenic mechanisms which are considered to overlap between similar ictal discharges. As such, the utility of an acute electrical rat epilepsy model for serial EIT data acquisition which relies on overlap in brain activity between repetitive bouts of neural activity might need to be re-assessed (Hannan, 2019).

5.4.2 Technical considerations

Even though a total of six rats were used to collect the data for this study, four of these datasets did not meet the eligibility criteria established in Chapter 4. Such a high recording attrition rate suggested that the complexity of the experimental set-up and/or protocol made acquisition of good quality data challenging and has put the reproducibility of the observed results in question. On the other hand, habitual electroclinical seizures are inherently non-homogenous which was also supported by the results of this study (Fig. 5.8). Therefore, validation of depth fnEIT for epilepsy can only be objectively achieved by concurrent bimodal imaging. Such an approach was taken in this study by simultaneously recording and reconstructing SEEG data. SESI provided some, albeit limited, insight into the consistency of three-dimensional trajectories assumed by individual ictal discharges as well as the accuracy of the EIT images. Nonetheless, future cross-functional imaging studies involving additional techniques should be undertaken using the same rat model of electrical afterdischarges in multiple animals to verify the putative EZ reconstructed in this study.

The pilot data acquired in this study demonstrated that single-shot fnEIT of ictal spikes was possible provided an acceptable noise level was achieved. Considering that genetic and chemical rodent epilepsy models mimic the habitual seizures more accurately, depth fnEIT could theoretically be attempted for imaging spontaneous seizures. Appropriate hardware enabling a wide injection frequency spectrum would need to be designed for this purpose to permit parallel acquisition of fast neural impedance changes, equipment unavailable at the time of conducting this study.

5.4.3 Significance of the findings

Several interesting, albeit preliminary, findings were made in this chapter. It was demonstrated that the maximal local intracerebral fast impedance changes associated with the averaged ictal SWDs might be of a similar magnitude (up to ~ -0.2 %) to the impedance measurements from the surface of the cerebral cortex (Hannan et al., 2018b). This observation was surprising as the signal was expected to be closer to 1% due to the vicinity of the active brain tissue to the recording electrodes (Liston et al., 2012). In fact, impedance decreases during individual SWDs reached higher values, namely ~-0.7 % during the first SWD and ~-0.4 % during the subsequent SWDs (Fig. 5.5). This suggested that averaging lowered the amplitude of the detected changes with some spikes yielding markedly smaller impedance decreases than others. This pattern was consistent with significant decrease in the SNR observed between fast impedance changes underlying individual SWDs (section 5.3.3.1; Fig. 5.5).

The biophysical mechanism of fast neural impedance changes could partially explain the above finding. It is known that larger extracellular voltage fluctuations during the spike portion of the SWD result in bigger impedance drops due to activation of a larger brain volume. The amplitude of SWDs between seizures varied up to 400 % in this study whereas the prominence of the spike component was relatively stable within each seizure with a marginal increase with its progression (examples in Fig. 5.2 and 5.3). The latter spike property was considered dominant in defining the consistency of the selected SWDs as it described their morphology more thoroughly and was expected to better reflect the associated fast impedance changes. The relatively uniform appearance of the isolated SWDs and consistent spike prominence was expected to represent reproducible neural circuit activity with consistent extracellular field potential changes and subsequently equivalent impedance characteristics (Hannan, 2019). However, the amplitude difference could have had a more significant impact than predicted. It is also possible that the fast change in neural tissue impedance decreased with repeated ictal discharges due to anoxic depolarisation and disruption of existing ionic gradients which affect the transmembrane voltage (Olsson et al., 2006; Ullah et al., 2015). However, in that case, spikes would be expected to have gradually diminished which was not seen until the end of the seizures. Therefore, it is more likely that the SWD clusters used for averaging associated impedance responses inadvertently included mixed SWD types reflecting distinct neural pathways (van Luijtelaar & Coenen, 1986). A more granular classification of ADs based on intricate electrographic features could potentially resolve the issue. Unfortunately, as discussed in the previous chapter, current tools for computerised spike sorting are subpar in their performance to the subjective manual grouping. Previous fnEIT studies of epileptic seizures in rats used a semi-supervised neuronal spike classification algorithm designed for analysing multiunit recordings (Hannan et al., 2020a; Hannan et al., 2018). This technique was deemed unsuitable for the purpose of this study due to detection errors (see 4.1.3.4 for details). Thus, a designated algorithm could be developed for processing ictal SEEG in future fnEIT studies and incorporate an extended electrographic profile for distinguishing different ictal patterns. This might improve the consistency and reliability of the ictal fnEIT images.

The hypothesis of different neural patterns underlying individual ictal SWDs was supported by the images reconstructed from single-shot fnEIT recordings (Fig. 5.8). Albeit preliminary and only in one rat, this was a major achievement of this study as it showed that fast impedance changes during epileptiform activity recorded with intracranial fnEIT in anaesthetised rats can be reconstructed into physiologically plausible real-time images. EIT depicted the propagation of ictal activity between similar regions of the sensorimotor cortex within 20 ms of the peak of the spike during two isolated ictal SWDs separated by ~<10 seconds (Fig. 5.5). The first SWD engaged circuits across all six cortical layers in the facial S1 region replicating the findings of Hannan et al. (2018b) who used a similar experimental paradigm. Additional foci were also observed in the motor cortices and S1HL, regions targeted with electrical stimulation for inducing ictal ADs. Surprisingly, the pattern of neural activity reconstructed from the SWD within the next 10 seconds was spatially and temporally shifted with respect to the seizure initiation as well as significantly noisier (Fig. 5.8). Ictal activity originated in the S1Tr as opposed to S1BF but spread quickly (within 2 ms) to the surrounding S1 territories. The spike trajectory seen at the beginning of the seizure (SWD1) was engaged albeit with ~10 ms delay when compared to the earlier SWD (Fig. 5.8). This suggested that epileptogenic network expanded with the evolution of the seizure as ictal activity looped through functionally inter-related sensorimotor regions of the cerebral cortex. This conclusion was also supported by the EIT images of averaged SWDs which highlighted the convergence points between the individual ictal discharges, namely the S1BF/HL/FL (Fig. 5.6, 5.7, 5.8).

The main purpose of using the depth electrode array for fnEIT was the prospect of enhanced spatial specificity and depth resolution. As such, the prediction was that fnEIT with the stereo-arrays would permit the discrimination of the full cortico-thalamic-cortical loop underpinning

SWDs, a goal unachievable using electrodes on the cortical surface (Hannan, et al., 2018b; Steriade & Contreras, 1998). Interestingly, the fast activity in the thalamus was only detected in single-shot fnEIT images of the SWDs within seconds of seizure initiation (SWD1; Fig. 5.7). Neither the images of the later ictal discharges (SWD2+), nor the average of all SWDs induced by either stimulation paradigm detected thalamic activity (Fig. 5.6, 5.7, 5.8). Thalamic fast impedance changes commenced in the ventrolateral and ventromedial nuclei 8 ms prior to the peak of the SEEG spike and lasted for ~8 ms (Fig. 5.8). The immediate emergence of the thalamic activity during cortically provoked seizures reinforced the findings of many *in silico* and *in vivo* studies which demonstrated that the reticular nucleus of the thalamus (RT) was both necessary and sufficient for the generation of the pathologic spike-wave oscillations (Fan et al., 2017; Meeren et al., 2009). On the other hand, cortical fast neural activity was seen predominantly without thalamic involvement which supported the idea that neocortical regions were capable of sustaining SWDs without a subcortical pacemaker and might be a leading structure in the initiation of SWDs (Meeren et al., 2005; Meeren et al., 2002; Timofeev & Steriade, 2004). Since the thalamic activity was not discernible in the EIT images of the averaged SWDs, thalamic nuclei may not have been activated for the entire duration of the seizure. In fact, recordings of electrical seizures in chemical feline epilepsy model showed a time delay between the paroxysmal spikes in the cortex and the multi-unit activity associated with thalamic spindles, an oscillatory phenomenon mechanistically analogous to SWDs (Steriade & Contreras, 1998). Nonetheless, further studies would be necessary to demonstrate the reproducibility of these preliminary findings in other rats.

It is noteworthy that thalamic activity in this study was detected in VL and VM nuclei which have been shown to participate in spontaneous SWDs detected in inbred rat strains genetically prone to epileptic seizures (Vergnes et al., 1987). Furthermore, these thalamic structures reside in immediate proximity to the RT whose profound role in the bilateral SWDs during non-convulsive seizures was discussed in Chapter 4 (Cho & Paz, 2022). It is possible that even marginal lateral deviation of the probe insertion site as seen in histological analysis in Chapter 4 could have placed the same depth electrodes in the centre of the RT instead of VL/VM. Therefore, independent *in situ* verification of the insertion site would be necessary in future experiments to ensure that the location of the reconstructed activity is based on accurate placement of depth electrodes.

Interestingly, EIT images showed that the recruitment of the thalamus (-8 to -4 ms) was accompanied by rapid activation (-2 to 0 ms) of the basal ganglia implicated in higher-order seizure control (Fig. 5.8; Vuong & Devergnas, 2018). It is possible that this was a reconstruction artefact. However, it is also feasible that this activity was physiologically relevant. Research suggests that elaborate functional connectivity with both excitatory and inhibitory inputs between the striatum and the thalamocortical network enables the bidirectional tuning of the ictal activity which is relevant for both the maintenance and the suppression of seizures (Chen et al., 2014; Hu et al., 2022; Joel & Weiner, 1994). The evidence comes predominantly from studies of the absence seizures due to their characteristic expression of bilateral ~3 – 4 Hz SWDs (Paz et al., 2005; Slaght et al., 2004). Whereas animal studies have mainly focused on the nigral governance of SWD progression, clinical observations have repeatedly highlighted increased activity in caudate-putamen nucleus, a pattern also observed in all four fnEIT reconstructions in this study (Depauls et al., 1990; Deransart et al., 1996; Colin Deransart & Depaulis, 2002; Luo et al., 2012; Pizzo et al., 2021).

Stimulation of both the neocortex and the CPu induced SWDs with similar trajectories involving a concurrent activation of the S1 and the lateral portion of the CPu (Fig. 5.6 and 5.7). Since the striatal activity in EIT recordings was detected more consistently than the thalamic one seen in a singular reconstruction of an isolated SWD, it raises questions about the hierarchy of the subcortical networks in the epileptic seizure dynamics. This would be important in designing effective neuromodulation strategies which are currently biased towards the thalamic stimulation due to its role as a global rhythm generator (Du et al., 2021; Fan et al., 2017; Gouveia et al., 2024). Combining fast and slow neural EIT in further studies with additional imaging modalities could help to establish the precise role of the striatal and thalamic nuclei in the origin, progression and termination of ictal SWDs.

5.4.4 Future work

A crucial step in the future work would be to replicate the preliminary findings presented in this study in other rats. Another important direction for future studies would be to validate these findings by employing real-time slow neural EIT of electrical seizures induced with the same cortical and striatal electrical stimulation paradigms. Secondary changes in neural tissue impedance due to localised cell swelling imaged during repeatedly induced seizures could inform the reproducibility of the ictal trajectories between individual bouts of ADs. Furthermore, additional experiments could be performed to further explore the feasibility of a single-shot fnEIT during spontaneous focal seizures induced by administration of penicillin, pentylenetetrazole or bicuculline, all well-established chemical models of epileptic seizures (Aygun & Ayyildiz, 2021; Stankiewicz et al., 1995; Steriade & Contreras, 1998). Similarly to this study, care should be taken to avoid generalisation of seizures ensuring that fast impedance changes remained localised and distinct from the background neural activity.

Chapter 6

Imaging the full trajectory of electrical seizures in rats with stereo-electrode arrays and slow neural EIT

6.1 Introduction

Preliminary findings of a proof-of-concept intracranial fast neural depth EIT study detailed in Chapter 5 suggested that ictal epileptiform discharges with virtually identical electrographic characteristics might assume spatially stochastic propagation trajectories. Real-time EIT images of fast impedance changes during individual ictal SWDs, the most consistent and reproducible form of epileptiform ADs observed in this epilepsy model, provided insight into the potential neural circuit recruitment pattern over tens of milliseconds. However, a comprehensive picture of the fast neural circuit dynamics during an entire electrical seizure could not be delineated due to insufficient intra- and inter-seizure similarity across the remaining AD types. The available technology did not permit parallel acquisition of fnEIT data which would have been necessary to achieve this purpose. Therefore, to support the results of fast neural depth EIT and to further investigate the spatiotemporal differences between individual seizures induced by the same stimulation paradigm, imaging of pathological slow neural changes was conducted using a parallel EIT and an intracranial stereo-electrode array and an analogous experimental set-up to Chapter 5. The aim of this study was to delineate the full pathway of individual neocortical seizures and to capture their three-dimensional footprint over seconds following an ictal onset. Slow EIT images corresponding to periods of consistent spike-wave activity could then be compared to fast neural EIT data from the previous chapter in order to verify the results and strengthen the conclusions.

6.1.1 Background

Imaging of peri-ictal cerebral oedema in animal models has been successfully attempted before using various EIT systems. The initial study which recorded and reconstructed slow impedance changes associated with seizures was performed in anaesthetised rabbits using the original Sheffield Mark 1 EIT system and a ring of 16 intracranial electrodes (Rao, 2000). Impedance increases of ~7 % were observed upon electrical stimulation of the cortex which induced focal electrographic seizures. Slow changes in cerebral tissue impedance commenced with a delay from the onset of the seizure and surpassed its duration by several minutes (Rao, 2000). A similar pattern, albeit at a smaller scale, was observed in a later EIT study performed in rats undergoing spontaneous seizures induced by injection of chemoconvulsants (Vongerichten et al., 2016). Impedance increases reached a peak amplitude of ~2 % within several seconds of the start of the seizure (20 s in duration) and dissipated with its cessation. Due to inter-seizure variability, EIT images of slow epileptic activity were produced from one injection pair which was the main drawback of this study. This also reinforced the need for a parallel data acquisition system for imaging neural activity of variable presentation.

The first multi-frequency parallel EIT system designed by Dowrick et al. (2015) was employed for imaging spontaneous seizures in a swine epilepsy model (Dowrick et al., 2015; Witkowska-Wrobel et al., 2021). Slow impedance increases of up to 10 % were recorded during cyclic epileptic activity induced by intracranial injection of benzylpenicillin in anaesthetised pigs. In the case of focal seizures, impedance measurements could be reconstructed into tomographic real-time images of slow neural activity occurring over several seconds following its initiation. The onset and the spread of slow impedance changes were corroborated by SEEG\ECoG data with remarkable accuracy suggesting that parallel EIT was a useful complementary imaging modality for perioperative epilepsy monitoring (Witkowska-Wrobel et al., 2021).

Nonetheless, despite the promising results, Witkowska-Wrobel et al. (2021) study was limited in its design. First, it utilised both subdural electrode mats and depth probes which are typically mutually exclusive in surgical epilepsy patients. Whilst the type of array is dictated by the suspected EZ, the current safety profile favours the penetrating electrodes (Khoo et al., 2020; Sacino et al., 2019; Schmidt et al., 2016). The standard clinical SEEG arrays typically comprise individually inserted probes with large and sparse contacts which are suboptimal for EIT where a fixed and denser geometry is necessary. Moreover, the frequency spectrum used for slow EIT in the porcine brain was likely sub-optimal for recording slow neural activity as show in the frequency-sweep experiments by Hannan et al. (2018a) and in Chapter 3 of this thesis. Therefore, an updated EIT study was necessary to combat all these limitations with hardware and recording arrangement tailored to its purpose. This study was designed to address this by collecting real-time images of electrical seizures using a new parallel EIT system and a stereo-electrode array created specifically for intracranial EIT measurements. Whilst the previous parallel slow neural EIT (snEIT) data was gathered in a chemical epilepsy model, the current experimental design used an electrical rat epilepsy model for continuity and result comparability in this thesis.

The only study which comprehensively explored slow neural activity in the rat brain during electrical seizures was conducted using repurposed serial fnEIT data (Hannan et al., 2021). Each EIT injection pair in the imaging protocol was administered during individual seizures whilst relying on the assumption that repeated electrical stimulation of a sensitive brain region produced epileptiform changes with a predictable and consistent neural activity pattern (Hannan, 2019). As such, reconstructed images were considered to represent the evolution of a stereotypic ictal event with slow impedance changes depicting underlying neuronal oedema. However, there were several pitfalls in this assumption. Whilst the author demonstrated that electrical stimulation of the neocortex or the hippocampus reliably resulted in a burst of SWDs with characteristic morphology and frequency, seizures occasionally contained other AD types, such as sharp waves or polyspike complexes (Hannan et al., 2021; Hannan et al., 2020a; Hannan et al., 2018b). Fundamentally, the full scope of epileptogenic activity varied from seizure to seizure making comparison between the injection pairs inaccurate. Moreover, the findings of the previous chapter of this thesis indicated that even individual ictal SWDs might assume distinct propagation trajectories whilst preserving a common cortical focus which could be distilled from the averaged data. Therefore, realistic images of peri-ictal cell swelling over the course of the seizure could only be generated by collecting the entire imaging dataset in a single recording, an arrangement feasible exclusively with a parallel data acquisition system.

6.1.2 Purpose

The purpose of this work was to image the slow neural changes in the rat brain during electrical seizures using a parallel EIT system and an optimised penetrating stereo-electrode array. The study was designed to answer the following questions: 1) Does slow neural activity pattern during individual electrical seizures provoked with the same stimulation paradigm differ between and within subjects? 2) How do slow neural EIT images of ictal epileptiform activity compare to single-shot fast neural EIT of ictal SWDs isolated from the same seizure type? 3) What are the implications of the findings?

6.1.3 Experimental Design

Data from three anaesthetised rats were used for this study. Slow neural EIT was collected in two rats using a parallel EIT system and a penetrating stereo-electrode array with a 3 x 3 stacked probe design (Fig. 6.1). Fast neural EIT recordings from one rat presented in Chapter 5 were re-used in this study for comparing the results. Depth electrodes were implanted through an apertured subdural mat which guided the desired insertion site fixed at the centre of the forelimb S1 to ensure comparability of imaging results between Chapters 5 and 6. Electrical seizures were induced by the translaminar stimulation of the sensorimotor cortex using the same depth electrode pair as used for inducing neocortical seizures in Chapter 5.

These depth electrodes were located in the M1/S1HL and the S1BF. Neocortical stimulation site was chosen based on the results of Chapter 5. Stimulation of the sensorimotor cortex in this specific location appeared to consistently yield longer seizures with larger ictal discharges than the stimulation of the subcortical sites. Therefore, the resulting slow neural activity pattern was expected to be more elaborate and include both cortical and subcortical structures making this cortical seizure induction site more suitable for this study (see Chapters 4 and 5 for further details and Fig. 6.1 for a representative example). Moreover, the single-shot fnEIT images were reconstructed only using neocortical seizure data and could therefore be compared to snEIT data in this study.

The current study was designed to address the shortcomings of the previous research and to complement the fast neural depth EIT recordings presented in the previous chapter. Slow EIT was performed with the same custom parallel system as the one implemented for recording physiologically evoked slow neural activity in Chapter 3 at an optimal frequency range (4 – 6 kHz). Using depth electrodes for snEIT was expected to improve the SNR of the slow impedance changes occurring due to cell swelling at a finer scale and enable the visualisation of the full epileptogenic pathway from the induction to the cessation of seizure in a single shot. Despite having access to both epicortical and depth electrodes, imaging data was collected using only the depth contacts to mimic the clinical situation. The epicortical array served purely as a landmark for accurate probe implantation and as an independent tool for monitoring brain physiology, both of which were important whilst implementing a novel recording design (refer to 4.1.3.5 and 4.2.3.2 for details). An apertured epicortical array is expected to become redundant with further technical improvements and when the result consistency can be demonstrated in multiple rats.

Slow neural changes in the epileptogenic brain tissue were expected to differ between electrical seizures within and across animals according to the specific ictal SEEG pattern. Periods of repetitive and stereotypic ictal SWDs were predicted to cause cell swelling-related impedance changes in the forelimb, the hindlimb and the facial sub-fields of the primary somatosensory cortex where fast impedance changes predominated in the fnEIT reconstructions. It was of interest to determine the latency of slow changes, if any, in the thalamic nuclei due to the discrepancy observed between the fnEIT reconstructions of individual SWDs and their average in the previous chapter.

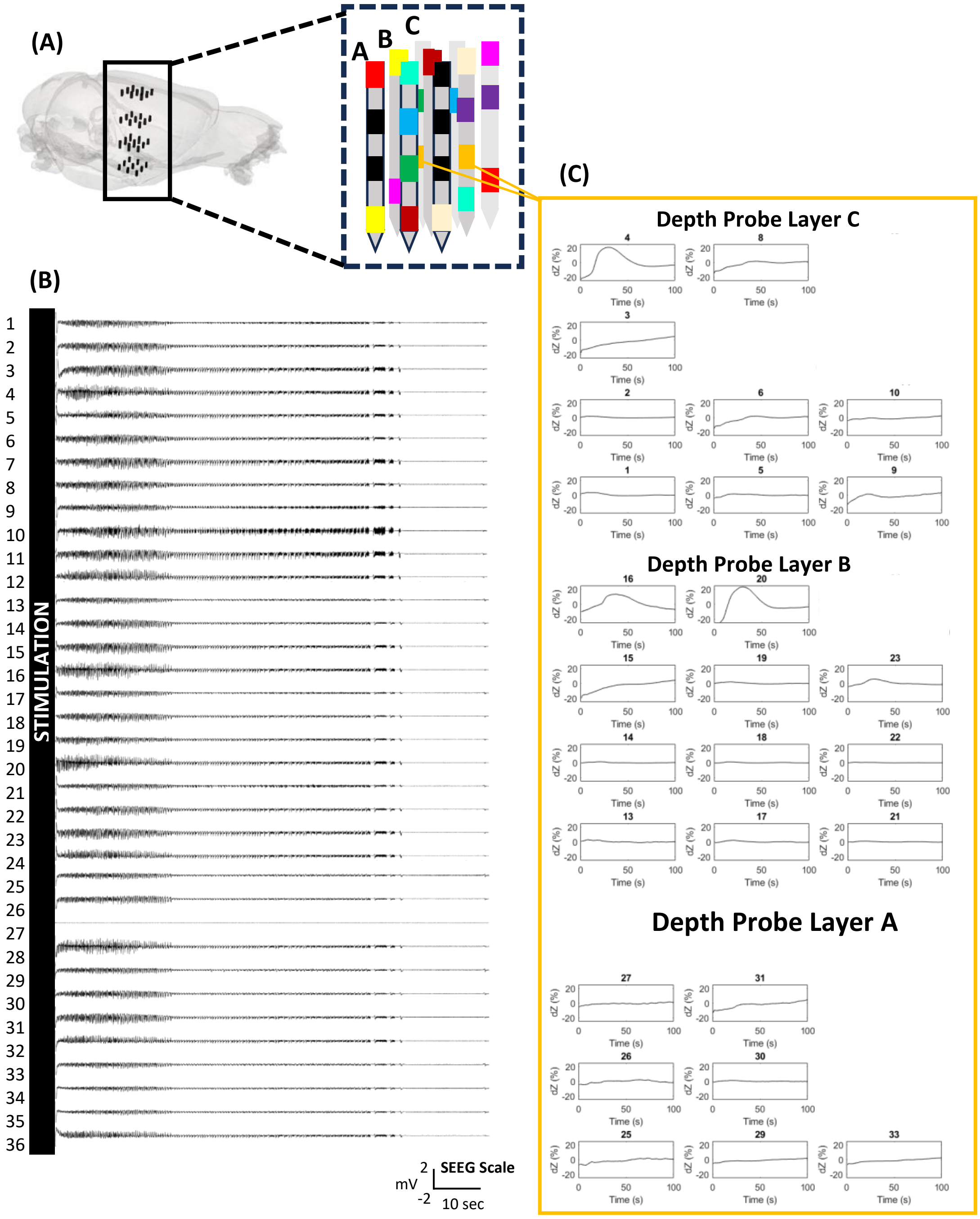

Figure 6.1. Imaging slow neural activity in the rat brain during an electrical seizure with the parallel EIT system and a stereo-electrode array. Section (A) represents a parallel current injection paradigm for imaging a single seizure in real time. Different colours correspond to simultaneous EIT injection pairs which comprised an imaging protocol. Specific pairs were selected for each rat by modelling. Up to 12 constant ACs, 4 – 6 kHz, were injected simultaneously whilst measuring the resulting transfer voltage changes on all depth electrodes. Section (B) displays a representative SEEG recording on each of 36 depth electrodes during an electrical seizure induced by the cortical stimulation. The resulting proportional slow impedance changes (%) recorded during this seizure using one of the injection pairs from the protocol (marked in colour ●) are shown in (C). Layers A, B and C represent shank triplets as arranged in the probe with layer A located the most anteriorly. Timepoint 0 marks the first impedance measurement following the stimulation. Channels with a post-stimulation DC shift of >+/-25 % are not displayed.

6.2 Materials and Methods

6.2.1 Animal preparation and surgery

Adult Sprague-Dawley rats weighing 300 – 450 g were used for this study. The anaesthetic regime was analogous to that of Chapter 4 and 5. A full description of the physiological preparation and surgical procedures can be found in 4.2.1. The depth probe was implanted through an apertured epicortical array on the left hemisphere in the same anatomical location as before which was verified by the location of the forepaw and hindpaw SEPs on the same depth contacts (see 4.2.2, 4.2.3, and 4.3.2 for details). As per criteria in 4.4.3, neither rat experienced severe bleeding from the brain, nor there was any visible injury to the superficial major blood vessels.

6.2.2 Seizure induction protocol

The technique for inducing electrical seizures is detailed in sections 4.2.4 and 5.2.2. The depth electrodes used for delivering the stimulation to provoke epileptiform afterdischarges were in the same cortical regions and at the same depth as the pair used for inducing neocortical SWDs in Chapter 5. Briefly, a 5 s train of 1 ms-long square bipolar charge-balanced pulses (2 mA, 100 Hz) were delivered across all six layers of the sensorimotor cortex between the hindlimb S1/M1 border and the whisker S1. Stimulation was administered using the Keithley 6221 current source (Keithley Instruments Ltd, Solon, OH, USA). All seizures provoked by this method met the minimal amplitude and duration criteria as described in 4.4.3.

6.2.3 Data collection and hardware

Recordings corresponding to each injection pair in the imaging protocol were acquired simultaneously using frequency-division multiplexing and a modified ScouseTom EIT system described in section 3.2.2. The system comprised the actiCHamp EEG amplifier (Brain Products GmbH, Gilching, Germany; see Appendix A for detailed specifications) and a custom-made rack of five parallel current sources enabling injection of up to 30 separate currents at ~4 – 6 kHz. All current injection pairs were separated by ~50 Hz and had an amplitude of 25 µA. Each rat was implanted with a new stereo-electrode array (described in 4.1.1.2). Both depth arrays contained >50 % of electrodes with impedance of ≤5 kΩ as per criteria in 4.4.3.

SEEG and transfer impedance recordings were collected from all channels connected to the depth electrodes and digitized at a sampling frequency of 25 kHz. All data was recorded in reference to a large Ag-AgCl electrode (~7 mm in diameter) placed under the nuchal skin as in the previous studies. A full EIT protocol comprised 10 – 12 parallel injection pairs optimised to record intracerebral impedance changes anywhere in the hemisphere of interest (Faulkner et al., 2017). Each recording was up to 5 min in duration and contained electrical stimulation with the resulting seizure and a sufficiently long post-ictal period to ensure the return of normal resting state which was considered the baseline activity.

6.2.4 Data processing and analysis

Raw voltage recordings contained both SEEG and impedance data which were extracted by application of different digital filters.

Hereafter, the number of individual seizures imaged in separate EIT recordings are denoted by a lowercase ‘n’. The number of rats used to collect those EIT recordings is denoted by an uppercase ‘N’.

6.2.4.1 SEEG recordings

To visualise SEEG of each seizure, raw data from all depth electrodes was filtered with a 1 Hz high-pass filter (1st order, Butterworth) and a 100 Hz low-pass filter (5th order, Butterworth). Mains noise was eliminated with a 50 Hz notch filter (2nd order, IIR).

Each seizure was analysed by visual qualitative inspection of SEEG recordings on all depth electrodes to determine the onset and the spread of ictal activity. First, recordings of epileptiform activity were assessed against the criteria for acceptable seizures defined in section 4.4.3 and Table 4.2. Then, the ictal activity pattern across all depth electrodes was examined in order to locate its focal origin. Due to close spacing of depth contacts and probes, all electrodes could detect the full evolution of each seizure. Therefore, seizure onset and spread was considered to be predominantly defined by the amplitude of the ictal ADs and by the immediate presence of polyspikes and PSWDs (Gollwitzer et al., 2018; Witkowska-Wrobel et al., 2021). The seizure was considered focal if the largest epileptiform ADs were limited to <25% of the contacts and if clear distinction with respect to the remaining SEEG recordings was observed. The duration of each seizure was calculated from the end of electrical stimulation to the last ictal discharge recorded in the SEEG data.

6.2.4.2 EIT recordings

Voltage recordings from all depth electrodes were filtered ±10 Hz around each carrier frequency in the injection protocol (4th order, Butterworth). Demodulation of each voltage trace was then performed with the Hilbert transform. The modulus of the complex impedance change was used to reconstruct EIT images as it was considered representative of the resistive component of complex impedance due to injection frequencies of <10 kHz (Faulkner et al., 2018a). The filtered and demodulated traces were downsampled 250 times and normalised to the last 10 seconds of each recording as this period reliably reflected post-ictal return to baseline. A slow change in impedance with respect to baseline was calculated at each second of the recording. An additional 0.5 Hz low-pass filter (3rd order, Butterworth) was applied prior to image reconstruction to maximise the SNR and provide a minimal temporal resolution of 2 s. The frequency cut-off was chosen after evaluation of the initial results which suggested that slow impedance changes consistently lasted ~30 seconds in all seizures. Measurements from saturated channels and injecting channels were discarded from the datasets acquired at the corresponding carrier frequency. The remaining voltage traces were thresholded such that impedance measurements with a noise level of ≥5 µV in the post-ictal period were excluded (Witkowska-Wrobel et al., 2021). Significant impedance changes were identified by comparing the dZ values +/- 5 seconds around the peak with the baseline using a paired t-test ($p = 0.01$). The maximum impedance change was defined as the peak voltage change across all significant channels recorded during each seizure. The average maximum impedance change across seizures within each rat was then calculated and shown as mean dV (mV) ± S.D. across three recordings in each rat. For representing the topographical distribution of slow dZs, voltage changes were normalised to the amplitude of the standing voltage on that channel and expressed in percent (dZ, %).

6.2.5 Image reconstruction

The forward solution was computed with EIDORS software (Adler & Lionheart, 2006) on an anatomically realistic tetrahedral FEM rat brain mesh with 3 million elements using a research workstation (Dell Precision, Dell Inc., UK, 256GB RAM, 16 Intel Xeon CPU cores). It took 120 – 360 min for the forward calculation. Each boundary voltage measurement was taken in reference to a separate electrode positioned over the cerebellar cortex. As previously, tetrahedral FEM mesh comprised three conductivity layers, namely the grey matter, white matter, and the CSF (Horesh, 2006). The inverse problem was solved by calculating and inverting the Jacobian matrix. The image reconstruction was performed on a hexahedral mesh composed of ~300,000 hexahedral elements, 200 µm in size, using zeroth-order Tikhonov regularisation with noise-based correction (Aristovich et al., 2014; Mason et al., 2024). It took up to 10 min to calculate an inverse solution per seizure. To ensure consistency between studies, a fixed regularisation parameter was chosen for each EIT recording as described in 5.2.6.1. The reconstructed impedance changes were visually represented by the significance Z-score ($Z_{\delta\sigma}$) calculated by dividing the reconstructed conductivity values by the standard deviation of the conductivity changes predicted to result from random uncorrelated Gaussian noise.

6.2.6 Image analysis

Each snEIT recording was analysed independently (n = 6 recordings, N = 2 rats). Significant slow impedance changes associated with cell swelling were visualised by applying a threshold to the negative Z-score values representing the negative conductivity changes. Voxels with $Z_{\delta\sigma} \leq -3$ and lower than 30 % of the most negative Z-score value were considered significant. After the thresholding, the reconstructed activity pattern was examined by visual analysis in reference to the expected anatomical probe insertion site (see Chapter 4, Fig. 4.2). SnEIT timepoints corresponding to bursts of stereotypic SWDs were compared qualitatively with the single-shot and averaged fnEIT images from Chapter 5.

6.3 Results

6.3.1 SEEG recordings of electrical seizures

Stimulation of the sensorimotor cortex reliably produced electrical seizures in both rats (n = 6 seizures, N = 2 rats; Fig. 6.1). Stimulation was followed by an immediate DC shift and subsequent ictal epileptiform ADs comprising SWDs, PSWDs and sharp waves. SWDs exhibited the most consistent features across all seizures in both rats.

6.3.1.1 Rat 1

SEEG recordings showed that all three seizures in the first rat originated near the top middle contact of depth probe layer B (Fig. 6.2). The seizures first spread laterally along the superficial cortical layers and then involved subcortical structures which included thalamic nuclei penetrated by the most medial shank in probe layer C (see Fig. 4.2 for the anatomical structures surrounding each probe layer). The duration of seizures ranged between 17.8 s – 77.2 s.

6.3.1.2 Rat 2

SEEG recordings in rat 2 showed that all three seizures may have been generalised. Based on the amplitude of the ictal ADs, epileptiform activity may have originated around the bottom contacts in the middle and lateral shanks of probe layers B and C, respectively, located in the basal forebrain (Fig. 6.3). However, a clear focal onset could not be distinguished in any of the seizures suggesting rapid secondary generalisation. The duration of ictal activity in rat 2 was between 14.7 s – 18.1 s.

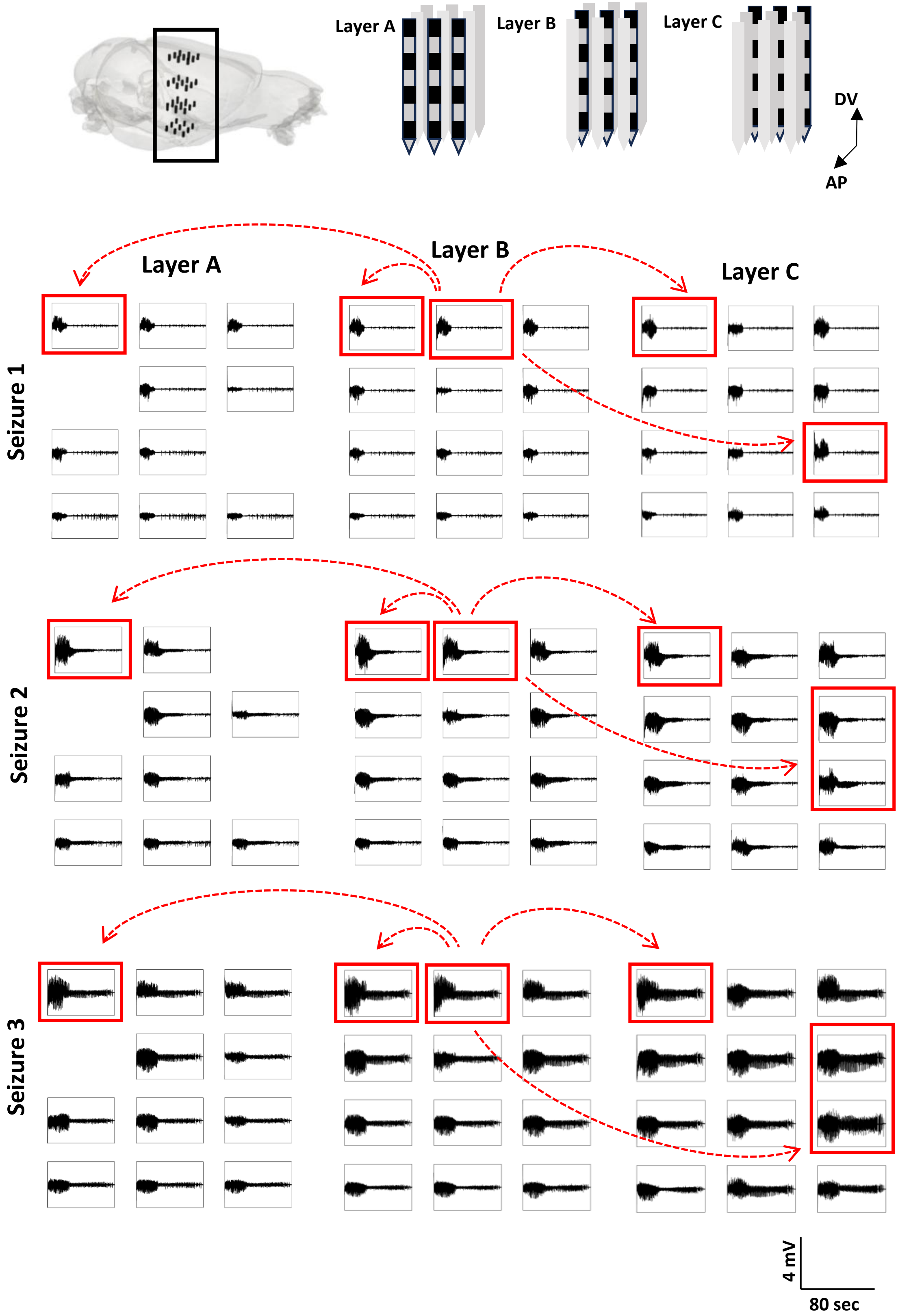

Figure 6.2. SEEG recordings of electrical seizures obtained by all depth electrodes in rat 1. Based on the amplitude of ictal ADs, seizure onset was consistently identified around the superficial contacts in depth probe layer B. Seizures tended to spread laterally along the cortex and ventrally into the basal hippocampus and ventrolateral/ventromedial thalamic nuclei. The movement of seizure focus is marked by arrows. Electrodes detecting the largest ADs at any point of the seizure are highlighted by red squares. Saturated or excessively noisy channels are not shown in this figure. AP – anteroposterior axis; DV – dorsoventral axis.

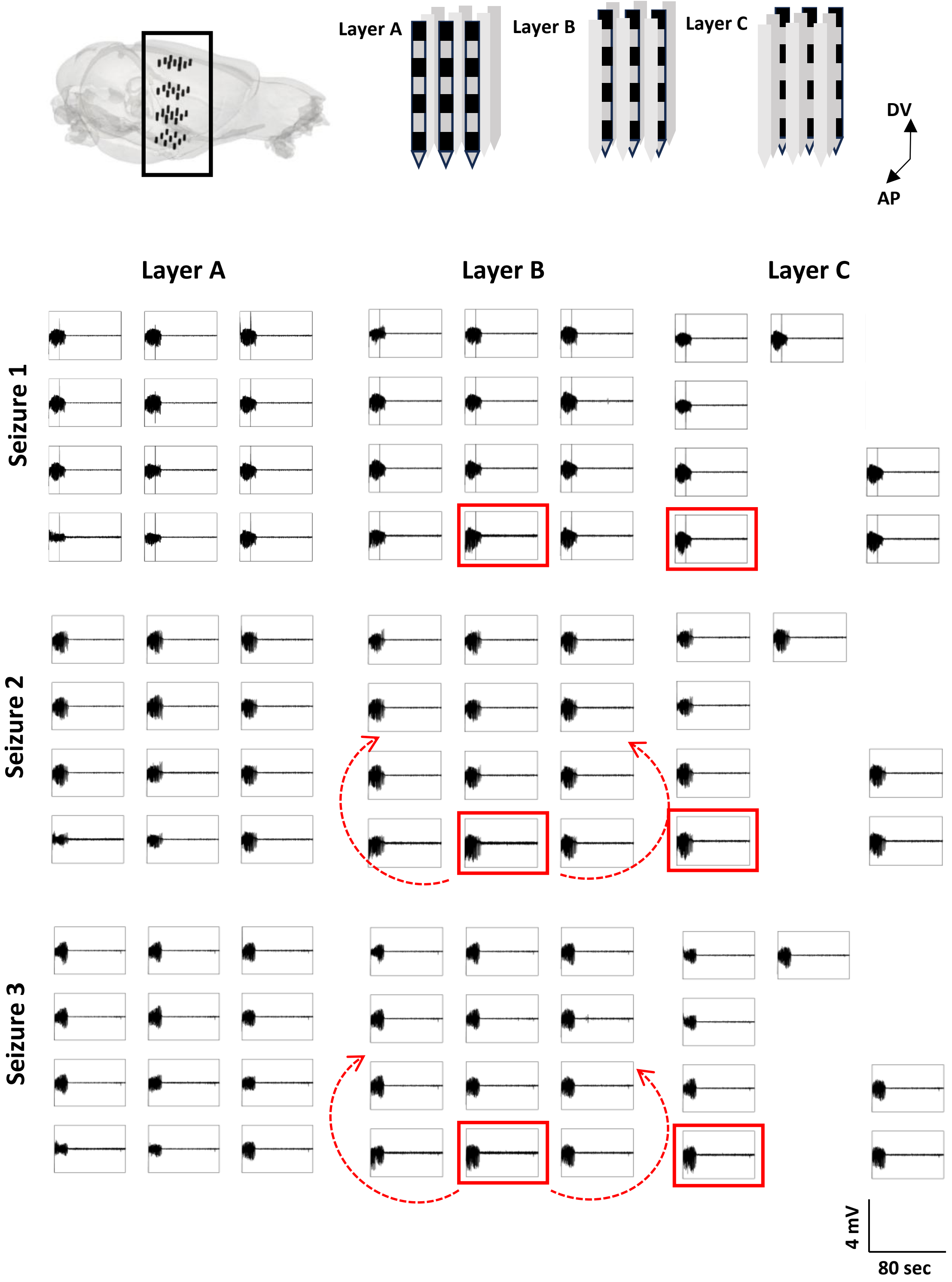

Figure 6.3. SEEG of electrical seizures captured by all depth electrodes implanted in rat 2. Based on the amplitude of epileptiform ADs, seizures may have originated around the bottom contacts in depth probe layers B and C which were expected to be in the basal forebrain structures, namely the hypothalamus and the basal ganglia. However, a clearly defined focus could not be established, indicating that seizures rapidly generalised (likely direction of propagation is marked by arrows). Electrodes detecting the largest ADs are highlighted by red squares. Saturated or excessively noisy channels are not shown in this figure. AP – anteroposterior axis; DV – dorsoventral axis.

6.3.2 Slow impedance changes during electrically evoked seizures

Each electrical seizure was associated with slow impedance responses commencing with the end of electrical stimulation (Fig. 6.4). Significant positive impedance changes comprised >50 % of transfer impedance measurements in each rat ($p < 0.01$, two-sample t-test; n = 6 seizures, N = 2 rats). The mean amplitude of the peak positive changes detected across all seizures and injection-measurement pairs was 0.56 ± 0.07 mV in rat 1 (12.0 ± 0.02 %; range 10.0 – 14.0 %; n = 3, N = 1) and 0.44 ± 0.10 mV in rat 2 (20.0 ± 0.2 %; range 6.3 – 44.0 %; n = 3, N = 1). Significant negative changes were less frequent than positive ones ($p < 0.01$, two-sample t-test; n = 6 seizures, N = 3 rats). The maximal amplitude reached of -0.30 ± 0.01 mV in rat 1 (-6.4 ± 0.2 %; range -6.2 – -6.6 %; n = 3, N = 1) and -0.15 ± 0.02 mV (-16.0 ± 4.2 %; range -11.0 – -21.0 %; n = 3, N = 1). An example of the topographical distribution of proportional slow impedance responses extracted from one of the injection pairs is shown in Fig. 6.1.

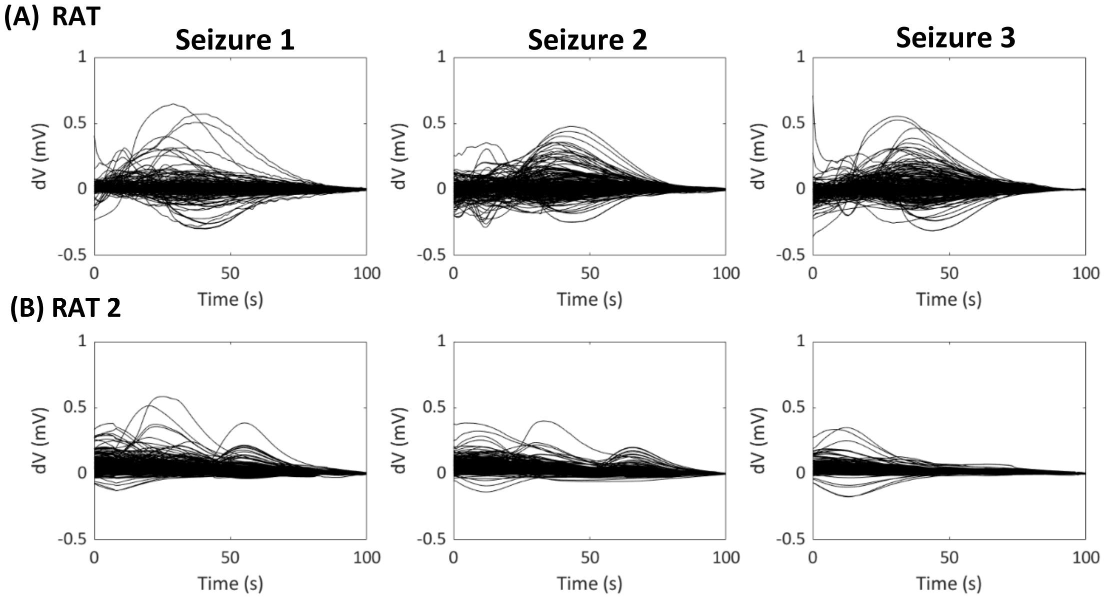

Figure 6.4. Slow impedance changes during individual electrical seizures recorded in two rats. Each graph shows the raw impedance changes (mV) detected by all injection-measurement electrode combinations during each seizure in rat 1 (A) and rat 2 (B). Timepoint 0 corresponds to the first datapoint recorded after the end of electrical stimulation administered for seizure induction (stimulation period not shown).

6.3.3 Three-dimensional reconstructions of the full seizure dynamics

Qualitative evaluation of parallel EIT images confirmed that the slow neural activity pattern following ictal epileptiform activity induced by repeated electrical stimulation of sensorimotor cortex was similar within but not between animals (Fig. 6.5 and 6.6).

6.3.3.1 Slow neural changes during individual seizures in rat 1

In all seizures, cerebral tissue impedance increased first in the cortex with the active voxels appearing within 10 seconds of seizure initiation (Fig. 6.5). Even though two out of three seizures started in the hindlimb S1 region, peak activity was concentrated in the facial and whisker representations of the S1 in all three seizures. A spread of peri-ictal oedema was visible in S1BF for up to 30 seconds post-stimulation. After that, impedance started to increase in the subcortical structures. Activity was observed in the ventrolateral and ventromedial thalamic nuclei (depth probe layer C) at ~35 – 45 s following electrical stimulation. Clear changes in basal ganglia, specifically in the caudate-putamen complex, were only observed at the start of the first seizure. Slow neural changes completely ceased within 70 seconds during all seizures regardless of their duration.

(A) RAT 1: SEIZURE 1

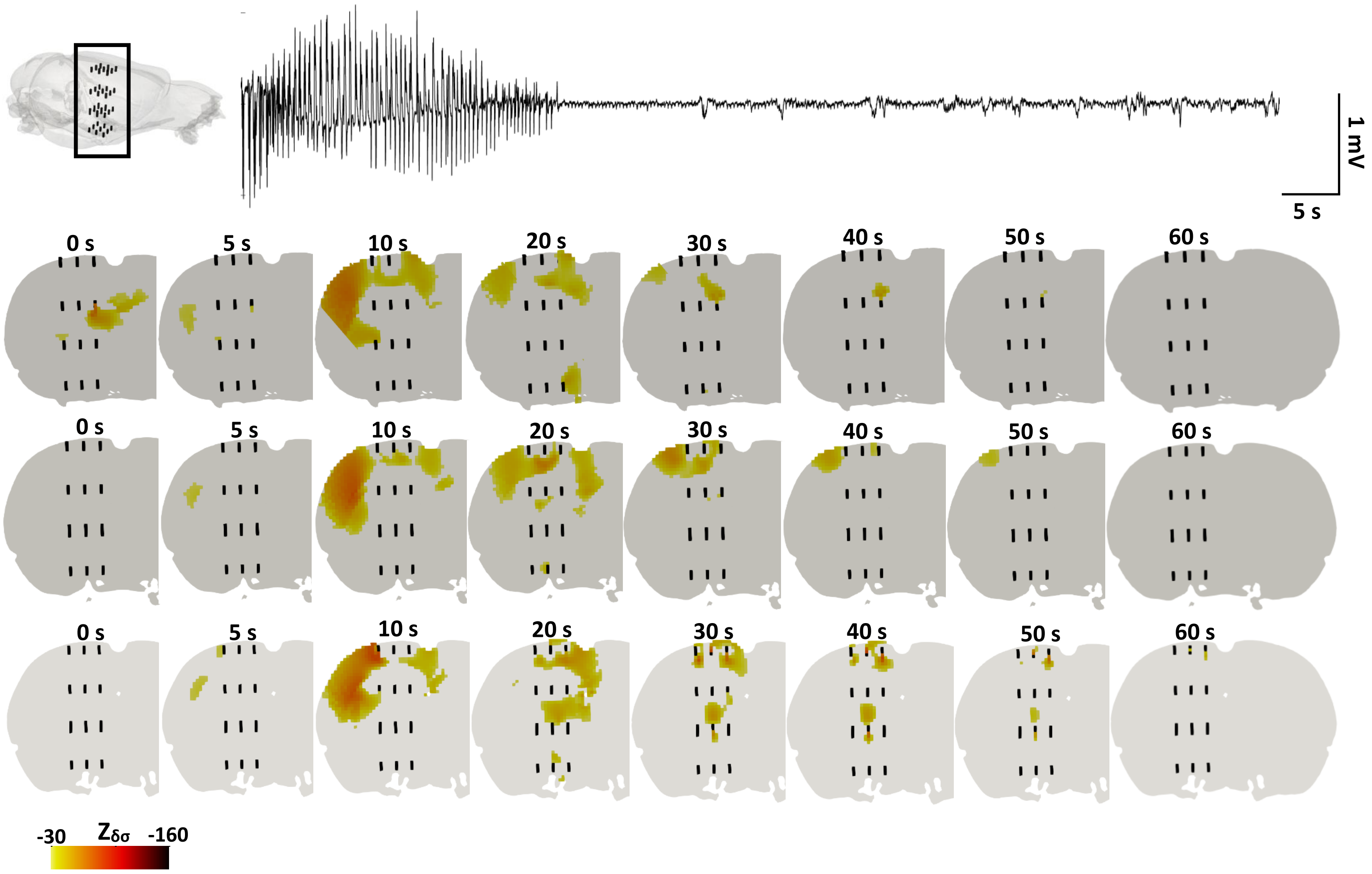

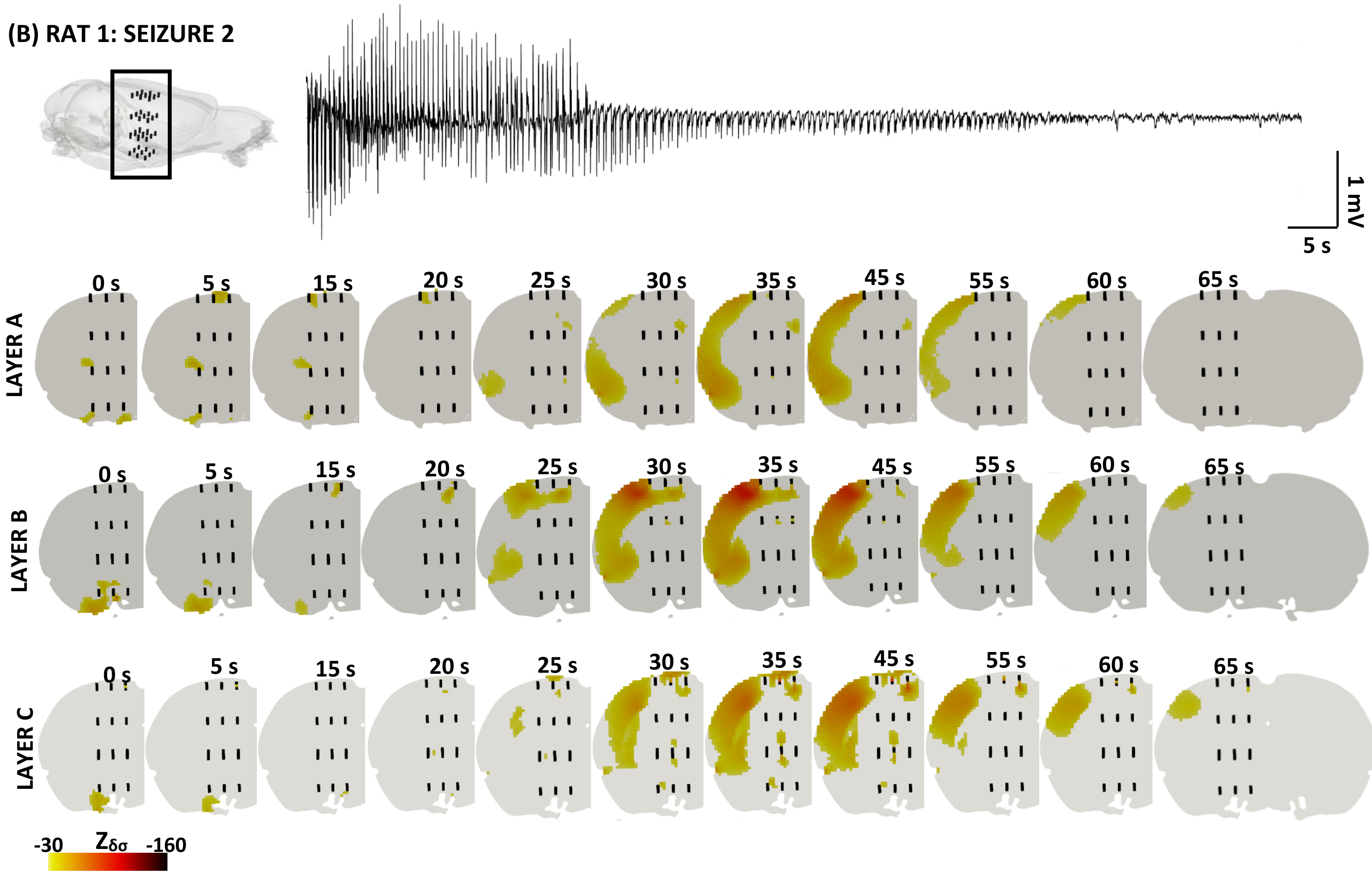
(B) RAT 1: SEIZURE 2
1 mV
5 s
0 s
5 s
15 s
20 s
25 s
30 s
35 s
45 s
55 s
60 s
65 s
LAYER A
LAYER B
LAYER C
-30
$Z_{\delta\sigma}$
-160

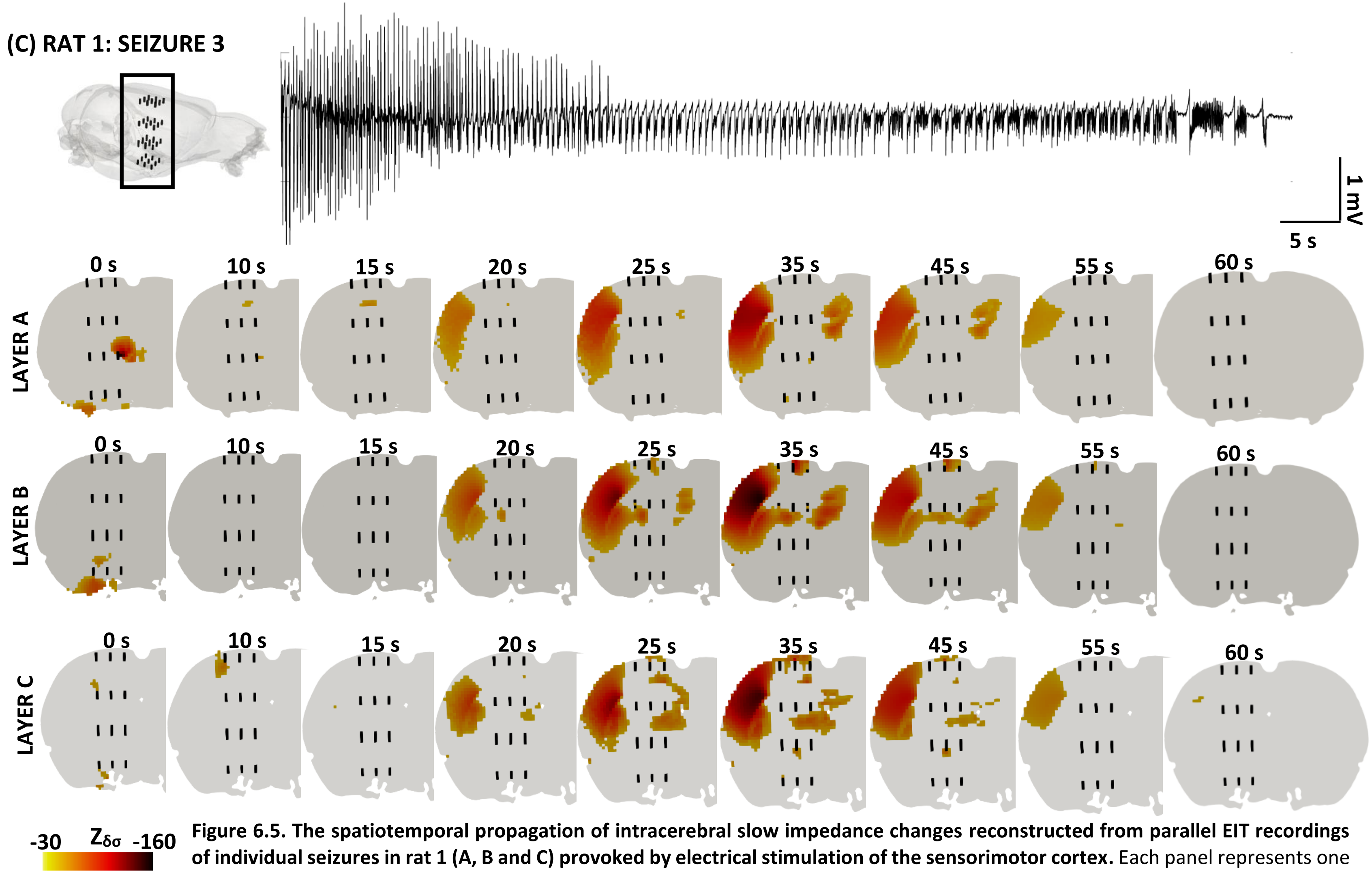

Figure 6.5. The spatiotemporal propagation of intracerebral slow impedance changes reconstructed from parallel EIT recordings of individual seizures in rat 1 (A, B and C) provoked by electrical stimulation of the sensorimotor cortex. Each panel represents one seizure with the corresponding SEEG recording from the depth electrode closest to the putative SOZ. All three seizures commenced in the cortex and propagated laterally within the first 20 seconds. Activity in subcortical structures, namely the basal hippocampus and the thalamus, were observed after the 30 second mark when the peak activity was reconstructed in the EIT images. The Z-score of the reconstructed conductivity changes is expressed by $Z_{\delta\sigma}$.

6.3.3.1 Slow neural changes individual electrical seizures in rat 2

Slow neural activity during all three seizures in the second rat was maximal at the outset of the seizure and decreased with time (Fig. 6.6). Despite overall generalised appearance, a well-defined focus of activity marked by the most significant $Z_{\delta\sigma}$ values between the second and third row of electrodes in layers B and C was visible in the internal capsule, a white matter structure located in the inferomedial part of the hemisphere. Additionally, bilateral slow changes were observed in the nerve fibres within the corpus callosum (layers A, B, C; Fig. 6.6). Besides the white matter tracts, a distinct focus could be seen in the facial S1 region and in the VPM/VPL thalamic nuclei (layer C) at the start of each seizure and for at least the next 30 seconds. Cell swelling-related impedance changes ceased within 70 seconds following the first seizure, within 80 seconds following the second seizure, and within 50 seconds of the last seizure (Fig. 6.6).

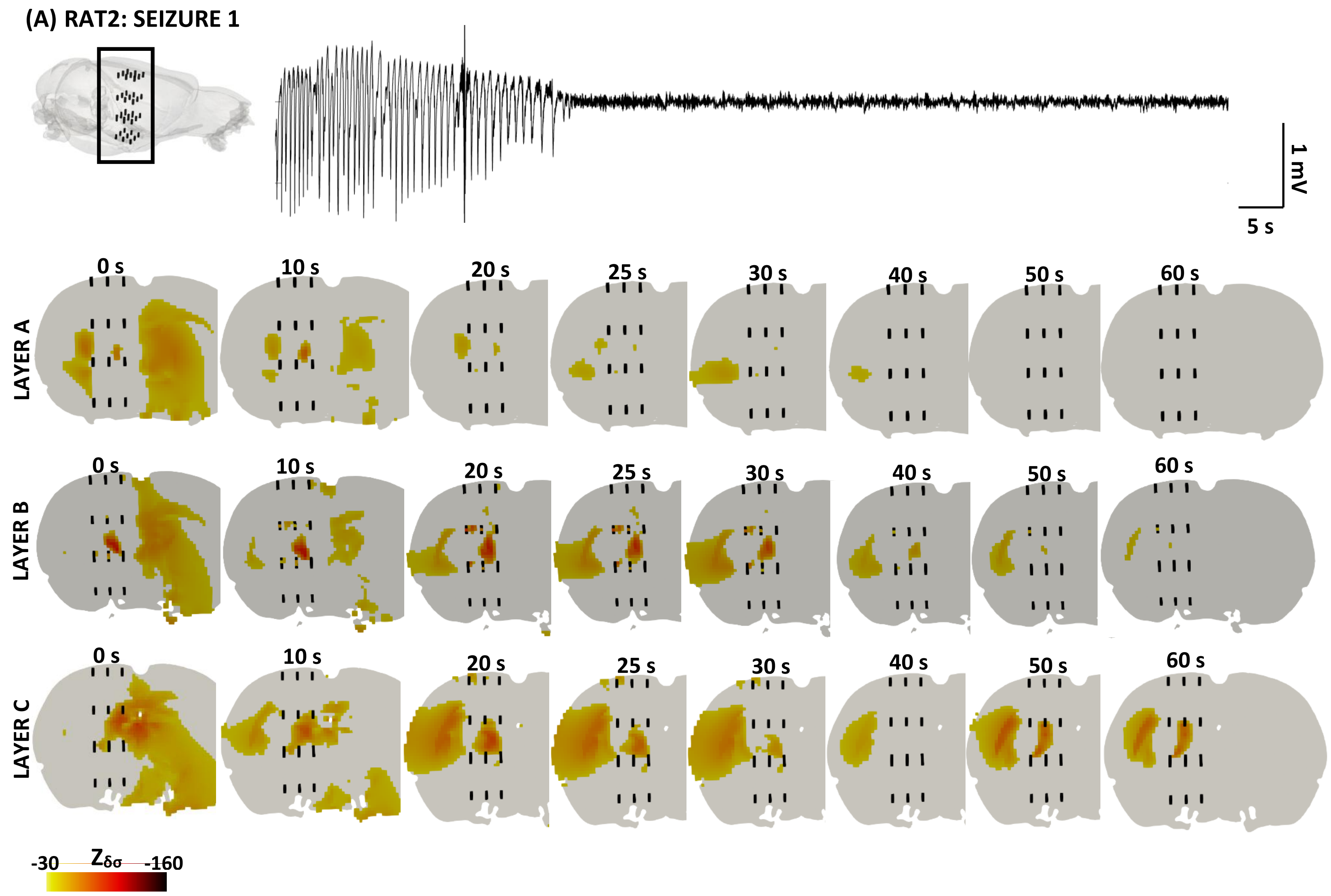
(A) RAT2: SEIZURE 1
1 mV
5 s
LAYER A
LAYER B
LAYER C
0 s
10 s
20 s
25 s
30 s
40 s
50 s
60 s
-30
Zδσ
-160

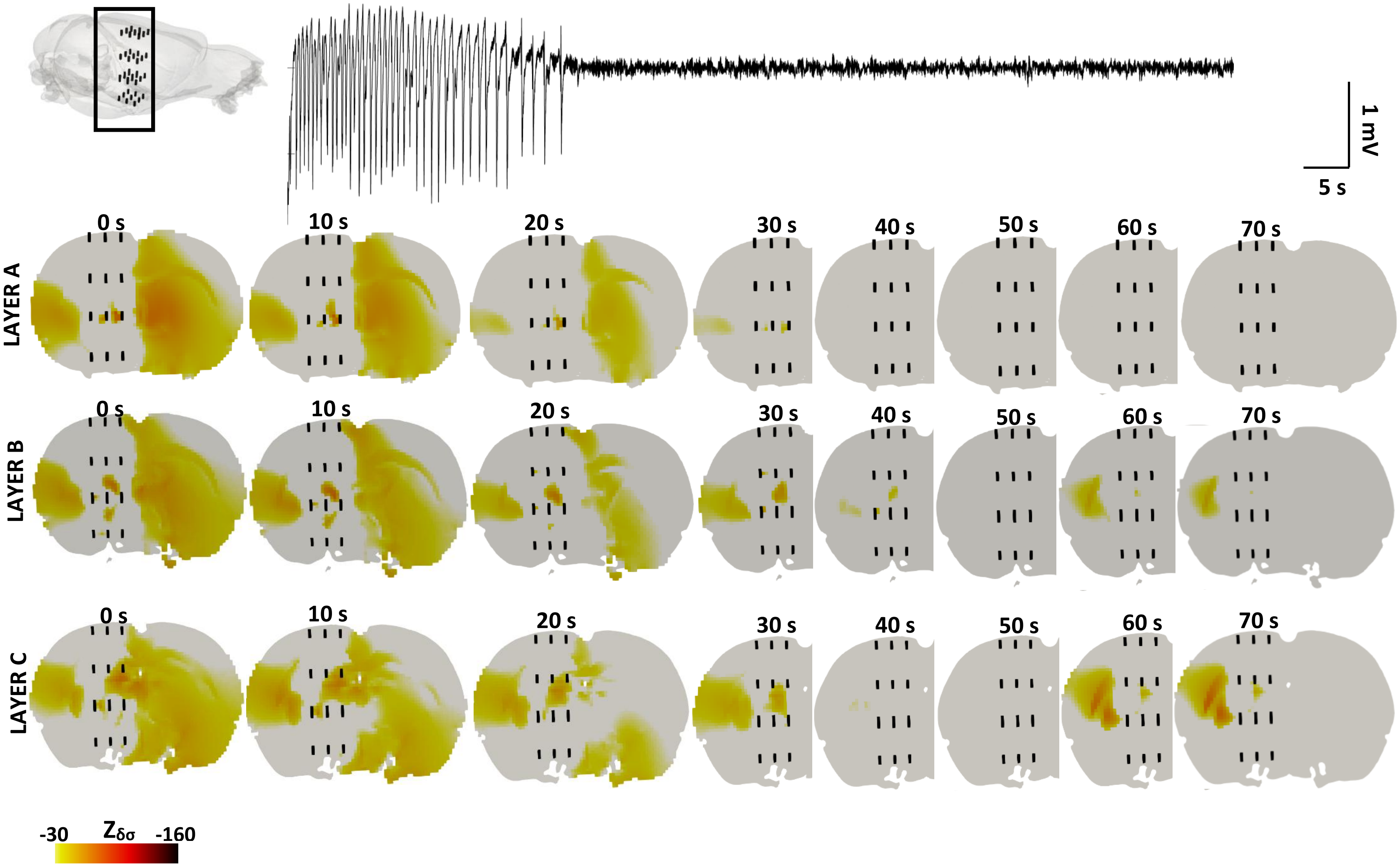

(B) RAT 2: SEIZURE 2

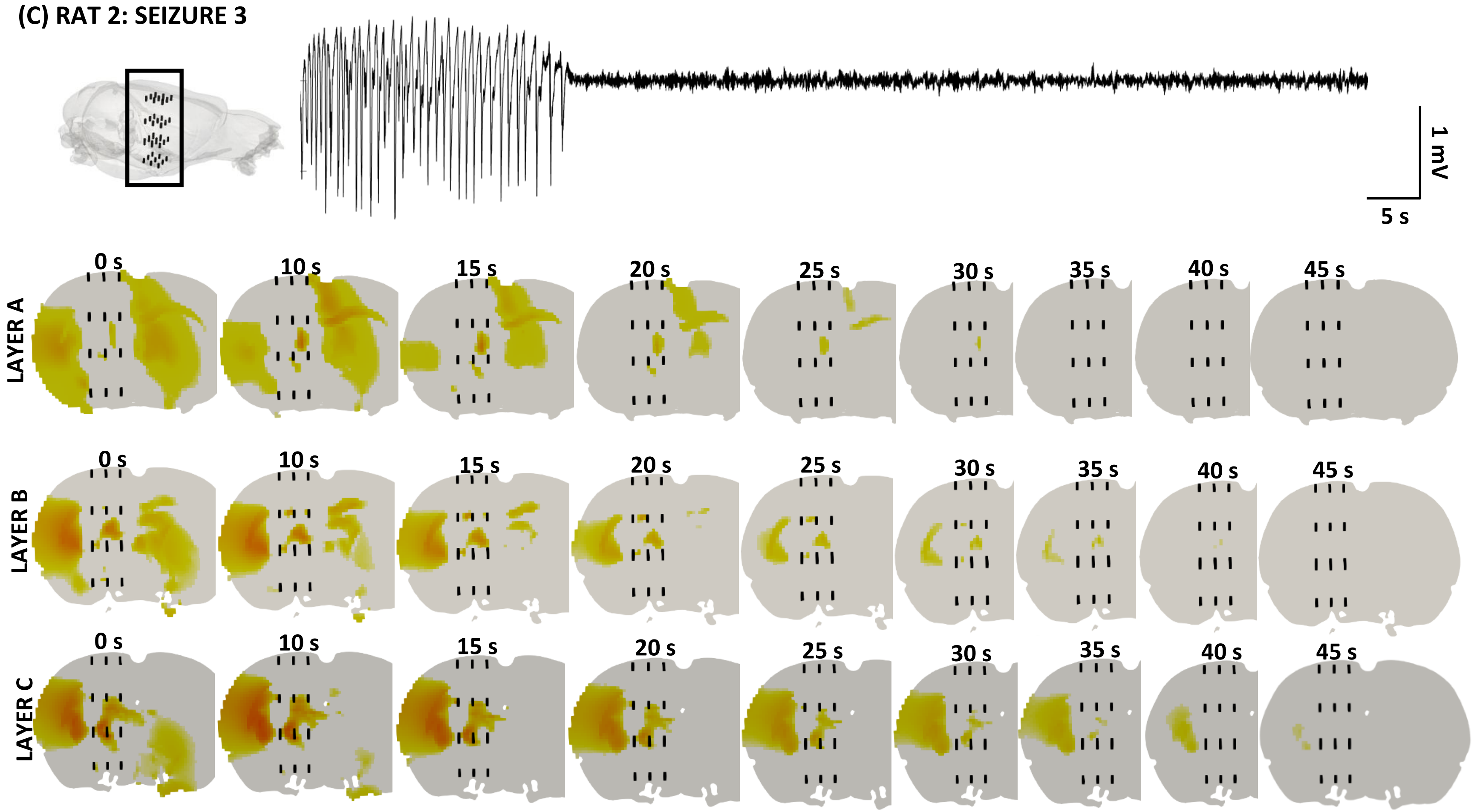

Figure 6.6. The spatiotemporal propagation of intracerebral slow impedance changes reconstructed from parallel EIT recordings of individual seizures in rat 2 (A, B and C) provoked by electrical stimulation of the sensorimotor cortex. Each panel represents one seizure with the corresponding SEEG recording from the depth electrode closest to the putative SOZ. All three seizures commenced appeared to commence in the basal forebrain and generalise by propagating through the corpus callosum, the white matter arc visible from the first timepoint after the stimulation. The Z-score of the conductivity changes is expressed by $Z_{\delta\sigma}$.

6.3.4 Fast versus slow neural changes during electrical seizures

6.3.4.1 Rat 1

All three seizures provoked in rat 1 contained a rhythmic run of stereotypic ictal SWDs at 3 – 5 Hz (Fig. 6.7). The most prominent SWDs were always detected by the depth electrode located in the middle shank of layer A. The anatomical location of this contact was expected between the bottom layer of the S1HL/FL area and the dorsal portion of the caudate-putamen (see Fig. 4.2 for anatomical reference points). SWDs were detected as early as 4 s after the end of stimulation and lasted for 10 – 30 seconds, after which they morphed into PSWDs until the seizure completely terminated.

Slow EIT images reconstructed during the period when ictal SWDs were observed in SEEG recordings (5 – 30 s) showed activity which resided predominantly in the cortex (Fig. 6.5). Slow changes emerged at 5 – 15 seconds post-stimulation and propagated in the vicinity of the layer A electrode with the most distinct SWDs (Fig. 6.7). In comparison to these observations, peak fast neural impedance changes reconstructed from individual ictal SWDs in the previous study localised predominantly to the M1 anterior to the array whereas peak fast neural activity reconstructed from the average of all isolated SWDs localised to the facial S1 which was where most slow neural changes occurred (Fig. 6.8).

6.3.4.1 Rat 2

Results of SEEG recording analysis and slow neural EIT images indicated that seizures in rat 2 were likely of a generalised nature. This suggested that ictal SWDs detected in this rat were of different type than the focal SWDs evoked in other rats. This invalidated the comparison between the previously acquired fast neural EIT images and slow neural EIT images in this rat.

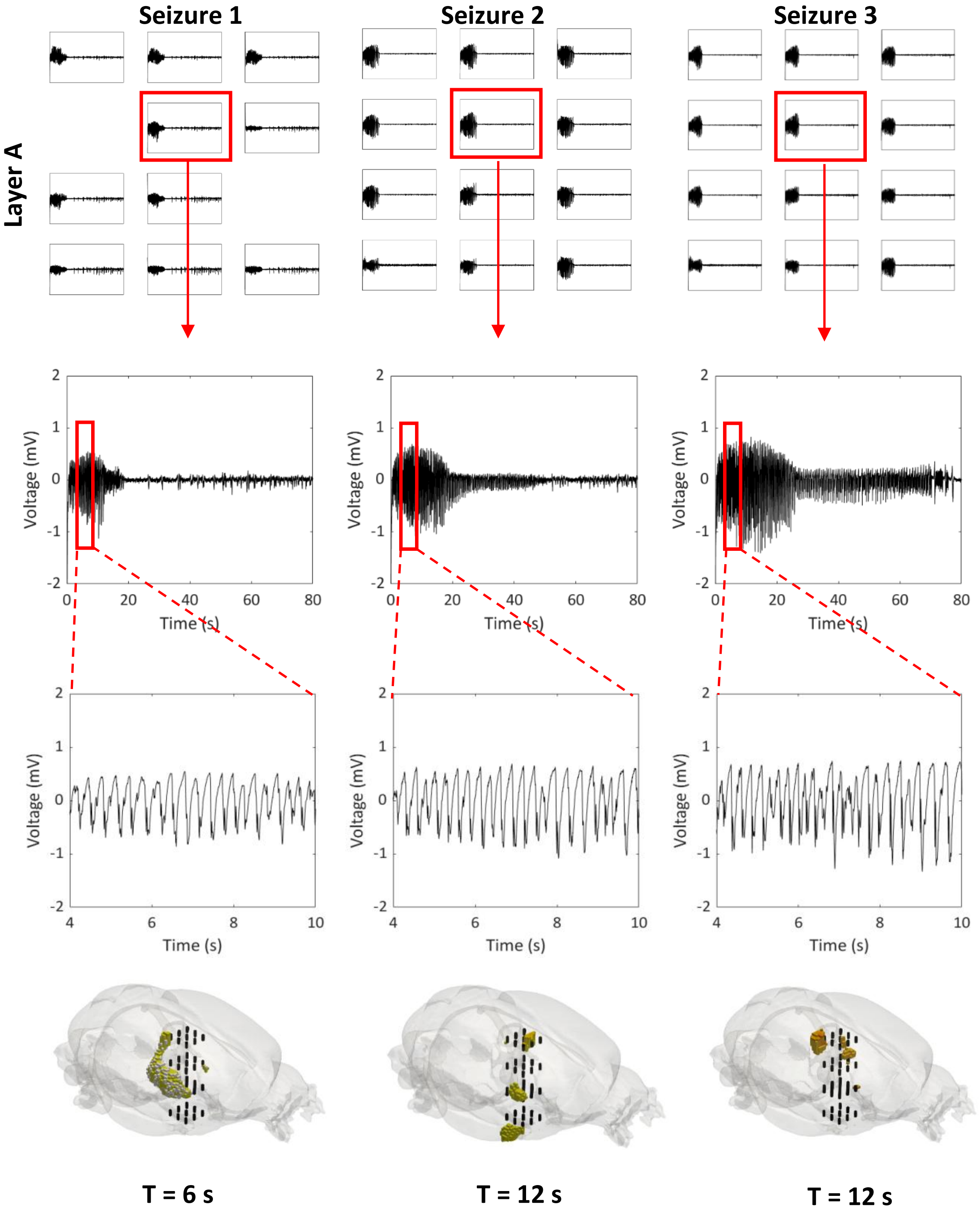

Figure 6.7. All focal seizures contained a period of repetitive and reproducible SWDs at the onset of ictal activity which corresponded to slow cortical impedance changes. SWDs were most prominent on the middle electrode in depth probe layer A. The graphs show the position of the electrode detecting a burst of SWDs during each of the focal electrical seizures in rat one. The enlarged version of the start of the SWD train is shown below. A snapshot of slow neural activity (signified by a timepoint 'T') upon the onset of ictal SWDs is at the bottom of the figure.

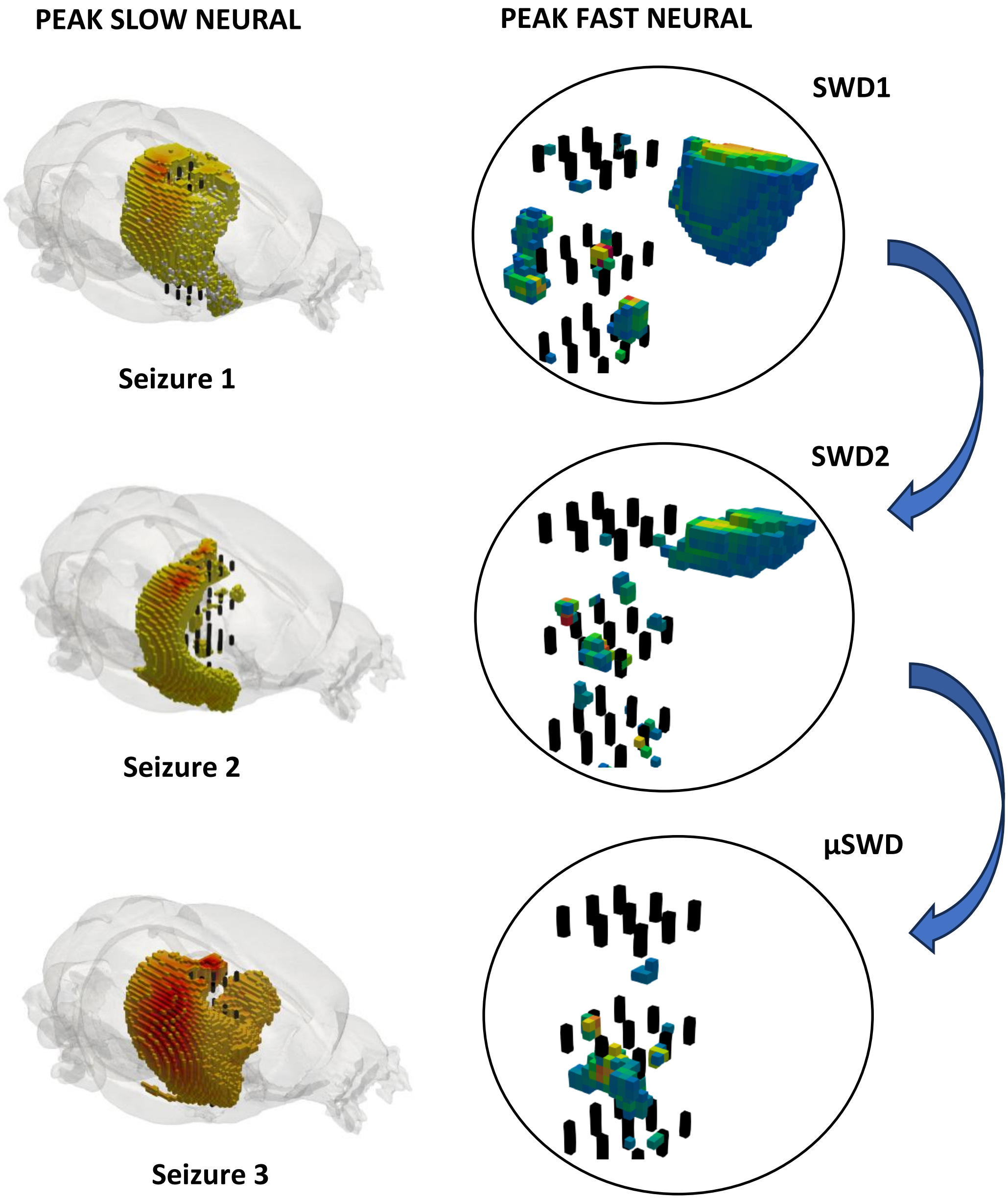

Figure 6.8. Comparison of the spatial distribution of peak intracerebral impedance changes during fast and slow neural activity associated with ictal epileptiform activity in the rat brain. Images on the left demonstrate the maximal extent of slow neural impedance increase detected during/after electrically induced seizures. Images on the right show the peak fast neural impedance changes associated with the spike portion of SWDs extracted from electrical seizures induced with the same stimulation paradigm in a different rat. Top to bottom: fnEIT images on the right represent transient (<50 ms) impedance decreases during the ictal spikes from individual SWDs (SWD1 and SWD2+) and from the average of all SWDs (µSWD) within each stereotypic electrical seizure. At its maximum, slow neural activity shown on the left occupied most of the S1BF as well as other cortical and subcortical regions with established functional connectivity. This agreed with the images of the peak fast neural activity during the spike portion of the averaged SWDs (µSWD) showing a clear ictal focus in the bottom cortical layers of S1BF. On the other hand, peak fast changes during individual ictal spikes were mostly detectable in the M1 with some activity in the S1BF and in the thalamus.

6.4 Discussion

6.4.1 Summary of results

The aim of this study was to acquire dynamic real-time 3D EIT images of the full scope of ictal epileptiform activity induced by electrical stimulation of the rat sensorimotor cortex. The goal of the experiments was to support the findings of the previous chapter and provide complementary information on the secondary neural changes during the same type of seizures. Parallel EIT recordings showed that slow intracerebral impedance increases during all electrical seizures were reliably detected by multiple depth electrodes without the need for averaging and were clearly visible after demodulation of the signal (Fig. 6.1 and 6.4). The reconstructed activity pattern was similar within but not between rats (n = 6, N = 2; Fig. 6.5 and 6.6). Whilst positive impedance changes with an average amplitude of 12 % and clear focal onset in the somatosensory cortex could be seen during all three seizures in the first rat, ictal activity in the second rat appeared generalised and the average value of the associated proportional slow impedance changes were nearly double the size (20.0 %; Fig. 6.4, 6.6).

Comparison to fnEIT data acquired in the previous chapter revealed that slow activity associated with each of the focal seizures propagated between the same cortical areas as the fast impedance changes lasting <50 ms and associated with the hypersynchronous neuronal firing during the ictal spikes. Qualitative inspection and comparison of fn/snEIT images suggested that slow EIT images better represented the trajectory of the averaged rather than the individual ictal spikes isolated from identical SWDs occurring within each electrical seizure. These preliminary findings reinforced the conclusion that sequential ictal discharges within a stereotypic electrical seizure may stochastically recruit overlapping neural circuits which ultimately converge forming an epileptogenic network with a common focal point. However, disparity between the EIT images from different rats necessitate further experiments to ensure result reproducibility.

6.4.2 Technical limitations and considerations

There are several important technicalities which should be accounted for when interpreting the results of this study. First, the sample size used for collecting snEIT data was too small for performing statistical analyses. Therefore, images were inspected only qualitatively which could have introduced bias into the interpretation of the findings. Moreover, whilst six seizures were imaged altogether, only three appeared purely focal and further restricted the inference of the results. Nonetheless, EIT images within each rat appeared reproducible suggesting that reconstructed activity represented the true evolution of ictal epileptiform activity in each instance. SEEG recordings additionally supported the EIT data showing a similar activity propagation pattern.

Whilst fnEIT images of ictal SWDs depicted similar brain areas as snEIT images, these datasets were acquired in separate experiments introducing another confounding factor into the picture. Due to narrow spacing of parallel injection frequencies (Δfreq = 50 ± 25 Hz), simultaneous fast and slow neural EIT recordings were not feasible in this study. Comparison between two experimental preparations relied on the control of key parameters such as seizure induction site and stereotypic appearance of ictal ADs. Nonetheless, experimental errors, such as mispositioning of the probe, could have resulted in stimulation of different cortical networks and resulted in distinct propagation trajectories of ictal discharges. This would explain the generalised appearance of seizures in the second rat whose depth array may have been implanted off-target with stimulating electrodes penetrating the corpus callosum or internal capsule which would have enabled bilateral seizure spread. As post-mortem histological analyses were not performed in these rats, this hypothesis is speculative. However, considering the results, future studies could revisit the prospect of histology on the brain samples fixed with the probe *in situ*. This would ensure that the shank insertion coordinates were established as accurately as possible and permit the verification of the anatomical probe location at the time of EIT recordings.

Inability to verify the probe insertion site was an important limitation of this study. Based on the results of the method development (Chapter 4), localisation of maximal forepaw and hindpaw SEPs on depth electrodes was used as a proxy for electrode implantation accuracy. However, this method only ensured that the most superficial contacts penetrated the right cortical regions. This strategy did not account for potential bending of the shanks due to surface tension and sheer force. Kinked probes would have placed deeper electrodes at an angle to the expected insertion plane. Aside from post-mortem analysis, a potential solution to this problem in future studies would be to use a complementary imaging tool, such as ultrasound, purely for navigating the insertion of depth electrodes (Simfukwe et al., 2022). Alongside intraoperative MRI and CT, ultrasound is frequently utilised in resective neurosurgeries due to low cost and ease of use. Its ability to distinguish between grey and white matter as well as parenchymal blood vessels would help to guide the implantation of the depth array with increased accuracy and precision. Additional benefit of avoiding penetrating arteries and veins would be improved safety and physiological stability of the procedure.

The next limitation was associated with the seizure induction method. Since ictal activity was induced by injection of a high-amplitude current, the onset of slow neural impedance changes was hidden by the stimulation artefact. This was also apparent from the shape of slow impedance responses, some of which peaked immediately after the cessation of seizure-provoking stimulus (Fig. 6.4). Even though most impedance recordings peaked within 30 seconds after the stimulation, stimulation artefact may have hidden the true onset of slow neural activity. This would mean that the SOZ could have been mislocalised in some of the reconstructions. The only solution to this problem would be to use chemical or genetic epilepsy models. However, these epilepsy models could not be used for imaging fast neural activity with EIT due to multiple serial current injection pairs. Therefore, to ensure a valid comparison between fnEIT and snEIT images, the same electrical seizure induction method was chosen for both studies.

Another important factor which may have affected the results of this study was the geometry of the depth electrode array. Fixed shank arrangement with narrow interstices but relatively sparse contacts was designed specifically for optimal recording of fast neural impedance changes. Depolarisation-related impedance drops are significantly more confined and smaller than slow neural impedance changes caused by cell swelling. It is therefore possible that the full extent of slow neural activity could not be captured with this kind of electrode array. However, since seizures were expected to have a focal origin, limited coverage should have been sufficient for imaging the local evolution of the seizure.

In addition to that, slow EIT images could have been impacted by the choice of the reconstruction method. A similar depth EIT study conducted by Faulkner (2019) using two penetrating intracranial probes for imaging evoked thalamic fast neural activity in one hemisphere of the rat brain showed that first-order Tikhonov regularisation tended to produce more accurate images than zeroth-order Tikhonov regularisation which was used in the current study. However, due to unpredictable seizure behaviour, it was important not to bias the reconstructions towards any particular outcome which was a risk posed by introducing stronger priors with the first-order Tikhonov regularisation (Tikhonov et al., 1995). Moreover, zeroth-order regularisation with noise-based correction has previously been shown to produce sufficiently accurate images of epileptic activity in pigs implanted with penetrating intracranial electrode arrays (Witkowska-Wrobel et al., 2021). Yet, the specific geometry of the depth electrodes used in this study has never been applied for collecting snEIT data before. Thus, the optimal reconstruction method has not been investigated. Even the type of noise incorporated in the reconstruction algorithm for the noise-based correction could have affected the accuracy of the images (Mason et al., 2024). Mason et al. (2024) recently showed that EIT image quality is superior when using uncorrelated, or background noise, versus correlated, or current-source noise. Whilst the study in this chapter used artificial uncorrelated Gaussian noise for noise-based correction, the precise noise figure was chosen on the basis of the average baseline noise retrieved post-processing from snEIT obtained across all recording channels. This might be important when considering the electrode distribution in this depth array as the background noise might be amplified due to the proximity of recording electrodes and multiple simultaneous current injections. Future studies could tackle this issue by testing a series of image reconstruction methods in attempt to devise a seizure-specific reconstruction technique.

6.4.3 Implications of the findings

As hypothesised, the three-dimensional trajectory of seizures reconstructed from slow EIT recordings differed markedly between rats but were relatively similar from one ictal event to the other within each animal. Whilst consistent focal seizures developed in the first rat, ictal epileptiform activity unexpectedly generalised in the second rat despite a consistent electrical stimulation protocol (Fig. 6.5 and 6.6). These findings provide important insights into the results of the previous chapter. All seizures recorded in both studies contained bursts of reproducible SWDs which were initially assumed to represent activation of identical unilateral neural circuits due a fixed stimulation site. Furthermore, lateralisation was monitored by an ictal SEEG pattern across the depth electrodes. Bilateral spread was considered unlikely due to the location of stimulating electrodes. However, the proximity between the shanks meant the ictal ADs were detected in SEEG recordings of all depth contacts making the distinction between the generalised and the focal seizures tricky. Even though an epicortical array was used together with the depth array in these experiments, subdural recordings provided limited insight into seizure onset and spread due to the aperture in the middle of the array. Hence, the current experimental design was not sufficiently stringent to guarantee seizure consistency and to prevent their generalisation which could have impacted the type of SWDs observed during the seizures.

Studies in a genetic rat model of absence epilepsy have shown that two types of SWDs, namely local and generalised, can be distinguished during spontaneous absence seizures (Midzianovskaia et al., 2001). Unlike Type I SWDs, which can be detected across all components of thalamo-cortical circuit, Type II SWDs are exclusive to the cortex and assume distinct frequency and morphology to Type I SWDs (Sitnikova & Van Luijtelaar, 2007). This suggests that lateralisation of seizures can dictate the specific neural circuits recruited during the propagation of individual ictal SWDs. Together with snEIT data, this evidence provides one potential explanation for the disparity between the fnEIT images of individual SWDs reconstructed in the previous chapter. Since SWD selection and clustering was performed using visual identification of the ‘leading’ electrodes in the cerebral cortex, bilateral spread of ictal activity would have not been immediately apparent. Transition from type II to type I SWDs would mean that a reproducible pattern of fast neural impedance changes was associated with a limited number of ictal ADs at the start of each seizure and that averaging of SWDs isolated from the entire ictal discharge may have been based on false assumptions. In that case, single-shot EIT recordings, whether fast or slow, were more likely to yield a truthful representation of neural circuit activity during each electrical seizure than images produced from the averaged signal. Nevertheless, additional studies are needed to support this hypothesis.

6.4.3.1 Slow neural activity during focal seizures

Despite the variable electrographic pattern, slow neural changes during all focal seizures in the first rat were concentrated in virtually the same cortical and subcortical regions (Fig. 6.5). This consistency may be attributed to repeatable presence of the following epileptiform abnormalities: stereotypic SWDs, sharp waves and rhythmic PSWDs. Even though each type of ictal discharge is known to reflect distinct oscillations in TC pathways, neocortical seizure induction may have biased the ictal trajectory to cortico-cortical propagation (McCormick & Contreras, 2001; Timofeev & Steriade, 2004). Extracellular recordings in the neocortex and the thalamus of anaesthetised cats previously demonstrated that intracortical, but not thalamic, injection of a convulsive agent bicuculline produced reliable SW/PSW seizures which persisted after thalamectomy but ceased upon corticectomy (Steriade & Contreras, 1998). This conclusion is also supported by reproducible but delayed emergence of thalamic activity in snEIT images of all three seizures ~20 – 30 s after their onset (Fig. 6.5). It is possible that this activity pattern represented thalamic entrainment from the cortical focus which has been suggested in previous studies (Avoli et al., 1983; Meeren et al., 2002). As such, in the context of an ongoing debate between the cortex and the thalamus as the leading structure in neocortical seizures, snEIT images might provide valuable information on the order of recruitment within this epileptogenic network.

Both real-time and averaged fast neural EIT images from the previous chapter featured activity in the caudate-putamen complex. Therefore, it was surprising that reproducible slow neural impedance changes were not detected in any of the striatal structures. It is possible that the active voxels representing significant fast conductivity changes during ictal spikes in the basal ganglia were a reconstruction artefact. However, it is also plausible that distinct cellular composition of the CPu in comparison to the cortex and the thalamus rendered different susceptibility to cell volume changes in these brain structures. For example, using two-photon laser scanning microscopy and whole-cell patch recordings in rodent brain slices, Brisson & Andrew (2012) showed that neocortical pyramidal neurons were significantly more sensitive to anoxic depolarisation, a pathophysiological phenomenon analogous to seizures, than magnocellular endocrine cells in the hypothalamus which were weakly depolarised and therefore resistant to swelling. In fact, the same group demonstrated a distinct boundary between the lower- and higher-order brain structures in terms of their vulnerability to ischemic insult (Brisson et al., 2013). Light transmittance imaging showed pronounced irreversible cytotoxic oedema in the neocortex, the thalamus and the striatum, all of which experienced a markedly stronger wave of anoxic depolarisation than the hypothalamus. Similar recordings were obtained from the striatal neurons in brain slices exposed to hypoxic conditions (Calabresi et al., 1995; Pisani et al., 1997). However, albeit epileptic seizures and anoxic depolarisation are characterised by common molecular and cellular changes, they fall on a continuum of integrated responses in cell volume, ionic concentrations and oxygen supply (Ullah et al., 2015). Therefore, without direct evidence of striatal neuron behaviour during seizures and, more specifically, during hypersynchronous firing of cortical excitatory neurons it is unclear whether the absence of detectable slow impedance changes in this region has any physiological significance. Nonetheless, it would be of interest to investigate this possibility further, especially because clinical studies of paediatric and adult absence epilepsy cases have shown volumetric and diffusion changes in some subcortical nuclei, including but not limited to, CPu (Luo et al., 2011; MacEachern et al., 2020).

With respect to the previous studies of slow intracerebral impedance changes during focal seizures in animal models, this chapter presented comparable results. Impedance increases ranging from ~2 to ~10 % have been reported during chemically and electrically induced seizures in rats, cats, rabbits and pigs (Elazar et al., 1966; Hannan et al., 2021; Van Harreveld & Schadé, 1962; Vongerichten et al., 2016; Witkowska-Wrobel et al., 2021). Such a broad range of values may be attributed to species-specific responses or to reflect variability in recording equipment and experimental conditions. This speculation is supported by the current preliminary findings showing that impedance of epileptogenic tissue could locally increase by up to 10 % during focal neocortical electrical seizures in anaesthetised rats. This value is more than double that recorded in rats by Hannan et al. (2021) who used a similar experimental paradigm with serial fnEIT and epicortical electrodes. The change is, however, of a similar magnitude to slow impedance responses detected in the porcine brain during spontaneous epileptic activity (Witkowska-Wrobel et al., 2021). The similarity between this study and the current experimental design is the use of penetrating depth electrodes instead of planar epicortical arrays for recording snEIT. Proximity to the epileptogenic source is likely to influence not only the amplitude of the recorded activity but also the distribution and the topography of the responses. This might also explain why, in contrast to Hannan et al. (2021)

who demonstrated synchronised slow impedance changes on different measurement electrodes during the same type of seizures, this study showed variability in response times across recording channels as the seizure progressed (Fig. 6.4). However, considering that images were acquired only in one animal, the results might reflect an isolated instance of exceptionally large impedance changes falling at the far end of the bell curve.

Slow EIT images of three focal neocortical seizures induced in the first rat agreed with the fnEIT data only in part. Unexpectedly, slow neural activity was less similar to the single-shot images of individual ictal spikes than to the images of fast neural activity during an averaged SWD (Fig. 6.8). An obvious reason for this discrepancy is the varied electrographic composition of the recorded seizures which contained more than one type of ictal discharges. FnEIT images showed impedance changes occurring only during similar ictal SWDs which represented a small proportion of the seizure. However, as the 'spike' portion of these SWDs was assumed to reflect unified firing of multiple neuronal populations and the 'wave' component to signify neuronal silence, images of repeatable SWDs were expected to illustrate a somewhat stereotypic depolarisation/depression pattern across the entire epileptogenic network (McCormick & Contreras, 2001). Therefore, it is surprising that the M1 which was strongly implicated in single-shot fnEIT reconstructions is not the focus of ictal activity in snEIT images (Fig. 6.8). Nonetheless, snEIT images of the peak ictal activity detected within the facial S1 align with Hannan et al. (2021) results, albeit displaying greater extent of focal slow neural changes. Epidural recordings of spontaneous ictal SWDs in WAG/Rij rats, a genetic model of absence epilepsy, has also shown a consistent cortical focus in the peri-oral region of the S1, comprising the subfields of the nose, the upper lip and the vibrissae, during non-motor seizures (Meeren et al., 2002). The same study additionally demonstrated that the other S1 areas consistently lagged with respect to the facial S1 but were reproducibly ahead of the thalamic nuclei. These findings match the activity pattern observed in the snEIT recordings of the focal seizures in this study. The proclivity of the facial S1 region to initiate SWDs has been attributed to increased expression of voltage-gated sodium channel subunits $Na_v1.1$ and $Na_v1.6$ (Klein et al., 2004). Together with increased expression of these sodium channel subtypes, changes in somatosensory neuron morphology has been hypothesised to render them hyperexcitable and lead to the development of absence seizures with cyclic SWDs (Karpova et al., 2005).

The concordance of snEIT images with the location of the fast neural impedance changes during the averaged SWDs might suggest one of the following. The propagation trajectory of individual ictal discharges may have varied due to changes in the epileptogenic network, including but not limited to synaptic and ephaptic interactions as well as fluctuations in electrical fields (Zhang et al., 2014). However, all epileptiform oscillations may have propagated through a common region of the greatest sensitivity which, according to data, was the S1BF. In fact, analysis of seizure-onset patterns together with the lesional MRI data from pharmacorefractory epilepsy patients has demonstrated that electrographic epileptiform abnormalities are frequently shared between the SOZ and the regions of spread (Perucca et al., 2014). This suggests that the reliance on the trajectory of individual ictal discharges expressed by real-time fnEIT may not represent the true anatomical SOZ. Therefore, based on these preliminary findings, a complete picture of the full-scale seizure dynamics may only be achieved with a combination of single-shot snEIT and fnEIT of the ictal spikes across the imaged seizure.

6.4.3.2 Slow neural activity during focal-to-bilateral seizures

Bihemispheric slow impedance changes with clear implication of the white matter tracts revealed that focally induced neocortical seizures generalised almost immediately following the cortical stimulation in the second rat (Fig. 6.6). This was supported by the size of the proportional impedance changes which reached 20 % during these seizures albeit the absolute transfer voltage measurements remained within the similar range to the first rat (Fig. 6.4). Significantly larger proportional changes suggested that the standing voltage on recording electrodes was lower in this experimental preparation than during recordings of generalised seizures. Since a different probe was utilised in each rat, changes in the standing field were most likely due to variation in electrode impedance which could have been influenced by the coating quality or the physiological environment of the electrodes.

The size of the normalised impedance changes recorded in this rat was akin to the rise in brain impedance during spreading depression or even cerebral ischemia seen in the same species (Holder, 1992a, 1992b, 1992c). Since these phenomena share cellular mechanisms with epileptic seizures, it is not inconceivable that local measurements with the depth probe would be better equipped to reflect the extent of neural changes during global seizures. However, it is questionable that the amplitude of these changes was even larger than what was recorded during generalised seizures in pigs (Witkowska-Wrobel et al., 2021). As no electrical and technical issues were detected during these experiments and the depth electrode impedances were in line with the requirements established in 4.4.3, the unusual measurement values were unlikely to have been due to faulty equipment. Nonetheless, additional studies with the same imaging method and protocol would be necessary to reproduce the findings. If impedance of the brain tissue during focal-to-generalised seizures in rats can in fact rise by 20 %, non-invasive EIT imaging could theoretically be considered for these types of ictal events.

Activity in the facial S1 region as well as the ventroposterior thalamic nuclei suggests that seizures in rat 2 may have originated in the same SOZ as those in rat 1. The thalamus is known to mediate bilateral cortical synchronisation during both absence and motor seizures

(Brodovskaya et al., 2022; Dabrowska et al., 2019; Meeren et al., 2009). However, seizure spread was an unexpected finding, since the induction paradigm was consistent between rats and exhibited reproducible focal seizures with consistent semiology (i.e., contralateral forelimb clonus) throughout the method development and in the previous studies using similar techniques (Hannan et al., 2020b). Rapid generalisation is consistent with the interhemispheric transfer via the corpus callosum, a white matter bundle which exhibited significant increase in impedance during all three seizures in this rat (Fig. 6.6). Recordings of frontal lobe focal-to-bilateral seizures induced by the implantation of a cobalt wire in the mouse pre-motor cortex has previously shown that ictal spread to the contralateral cortex facilitated by the corpus callosum precedes activity in the contralateral thalamus (Brodovskaya et al., 2022). However, it is likely that amplification of ictal discharges occur in the ipsilateral TC circuits before the seizure spreads into the other hemisphere (Kusske & Rush, 1978). This evidence aligns with the spatial pattern of slow neural activity in EIT images but does not match the temporal sequence. Since the LFP recordings have demonstrated that callosal seizure spread occurs within tens of milliseconds, it is likely that electrical stimulation which was administered for 5 seconds in this study masked the focal seizure onset and ipsilateral propagation before it translocated into the contralateral hemisphere (Brodovskaya et al., 2022).

It is also likely that slow cerebral impedance changes initiated upon the onset of ictal epileptiform activity lagged with respect to the depolarisation of neurons. This has been demonstrated by delayed peaking of slow impedance increases in the grey matter of epileptogenic brain tissue during seizures (Hannan et al., 2021; Holder, 2021a). However, to date, direct measurements of impedance changes caused by the water movement into the nerve fibres comprising the white matter have not been undertaken. Indirect evidence of this phenomenon has nonetheless been obtained by other imaging techniques (Iwasa et al., 1980). The most recent study which imaged spontaneous focal, secondarily generalised seizures in a swine epilepsy model using a parallel EIT system could not distinguish slow impedance changes in grey and white matter (Witkowska-Wrobel et al., 2021). This was due to the composition of the reconstruction mesh which did not incorporate differences in conductivity between the grey and the white matter. The rat brain meshes used in this study were segmented into three conductivity layers, namely the grey matter, the white matter, and the CSF; therefore, distinction between the slow neural activity in the neuronal cell bodies and dendrites, and in their axons was possible. Even though the spatial resolution was defined by the voxel size in the hexahedral mesh, the spatial specificity was restricted by the resolution of the MRI images used for the segmentation of the conductivity layers. With rapid developments in MRI technology, including diffusion-tensor imaging and quantitative susceptibility mapping, future EIT reconstruction meshes could be partitioned into finer cerebral structures (<100 µm resolution) enabling an even more granular visualisation of activity flow between different neuronal compartments (Wang et al., 2020; Wei et al., 2016).

6.4.4 Future work

Considering the inter-animal variability in seizure expression when induced by the electrical stimulation method, future studies should shift to using snEIT for imaging spontaneous seizures in genetic or chemical rodent epilepsy models. Additionally, a complementary imaging tool should be implemented for verifying the probe insertion site *in situ*, to ensure accurate positioning of depth electrodes with respect to key brain structures (e.g., corpus callosum) and to ascertain that the reconstructed images represent the real manifestation of the seizure. Issues with ictal SEEG analysis due to depth electrode proximity and challenges with EIT image reconstruction also questions the optimal depth probe geometry. Therefore, parallel studies investigating alternative electrode designs and appropriate image reconstruction techniques could take place additionally. All in all, this study has shown preliminary data suggesting that parallel slow neural EIT of epileptiform activity might serve as a useful tool for imaging abnormal neural circuit activity in the rat brain. At its present state, single-shot EIT of slow neural changes following the initiation of a seizure event may be a more accurate imaging modality than fast neural EIT of the same type of activity because of the ability to cover the full scope of an entire ictal event. Hence, the development of this technique should be continued with a goal of clinical translatability in the near future.

Chapter 7

Conclusions

7.1 Summary of studies

With reflection to the overarching purpose of this thesis (section 1.3), the work presented in the experimental chapters can be summarised as follows. The first two studies were performed using a canonical rat model of evoked brain activity to image slow neural impedance changes using EIT and surface electrodes. The results showed that EIT of functional neurovascular changes in the rat brain are currently unattainable with a non-invasive recording set-up (Chapter 2). On the other hand, if electrodes are placed on the surface of the cerebral cortex, slow neural activity can be discriminated over seconds in the superficial neocortical layers using the parallel EIT and frequency-division multiplexing (Chapter 3). Surprisingly, neural tissue impedance was shown to significantly increase, rather than drop, in response to a physiological stimulus. Therefore, the results suggested that slow cerebral haemodynamic changes following neuronal activation might have been overwhelmed by transient cell swelling, another well-established epiphenomenon occurring upon brief and intense depolarisation of neurons due to disruption of physiological transmembrane ionic gradients. Unfortunately, prolonged averaging (>~30 min) was necessary for satisfactory SNR which suggested that the technique was impracticable at its current state. In the context of the previous research in our group, the outcome of the first part of this thesis indicated that, with the present recording equipment, slow EIT of functional brain activity could not achieve the desired three-dimensional real-time brain coverage when using non-penetrating extra- or intracranial electrodes.

Having considered the above findings, the project continued with intracranial depth electrode arrays. The novelty of this work was the use of a highly optimised stereo-electrode grid which was designed to enhance the spatial resolution and the field of view of neural EIT in the rat brain. The focus of the project moved towards imaging neuropathological brain activity, specifically epileptic seizures, since this application of EIT was considered to carry the greatest and the most useful translational potential. The initial body of work (Chapter 4) involved the optimisation of the experimental method and the epilepsy model for investigative proof-of-concept depth EIT studies. A rat model of on-demand ictal epileptiform discharges originally developed for epicortical EIT recordings was chosen and adapted for these studies (Hannan et al., 2020b). Controlled induction of stereotypic electrical seizures which consistently contained reproducible spike-wave discharges enabled acquisition of both fast and slow neural EIT recordings. The preliminary results in one rat showed that, for the first time since the conception of an EIT technique, imaging of fast impedance changes associated with acute hypersynchronous depolarisation of epileptic nervous tissue during an ictal spike was potentially feasible in a single shot without within-seizure averaging (Chapter 5). This study not only demonstrated that real-time fast neural EIT could, in principle, be developed into a viable imaging method but also provided valuable neuroscientific insight into the potential neural circuit dynamics underlying spike-wave activity. Provisional images reconstructed from fast neural EIT recordings of ictal spikes isolated from individual SWDs demonstrated stochastic patterns of propagation which involved sensorimotor cortical areas and ventroposterior thalamic nuclei with established functional connectivity. All reconstructed trajectories converged on a single cortical area, namely the facial somatosensory cortex, reinforcing its epileptogenicity and ability to sustain SWDs without the thalamic input as seen in rodents genetically pre-disposed to absence seizures (Meeren et al., 2002). Collectively, these preliminary findings are important for both animal and clinical research due to the implication of SWDs in a range of different *in vivo* epilepsy models and types of electroclinical seizures, including but not limited, to absence epilepsy (Blumenfeld, 2005)

The work in the last experimental chapter was completed to extend and support the results of Chapter 5. Due to the technical limitations, fast impedance changes covering an entire electrical seizure could not be recorded using multifrequency EIT. On the contrary, the time course of the slow increase in the epileptogenic tissue impedance due to peri-ictal neuronal oedema was conducive to parallel slow EIT. The same rat epilepsy model of acute stereotypic electrical afterdischarges was used for this study enabling side-by-side comparison of fast and slow ictal intracerebral impedance changes. Slow EIT images showed a relatively stable pattern of secondary neural activity within but not between subjects following induction of sequential focal seizures with or without secondary generalisation. SOZ depicted by slow EIT recordings largely agreed with the fnEIT data which identified facial S1 as the key area.

Taken together, the findings of this thesis suggested that intracranial EIT with depth electrodes could be a useful and informative technique for visualising neuropathologic brain circuit activity in rats over different imaging time scales provided the above results could be reliably reproduced. Albeit preliminary, the above outcomes carry potential translational impact and suggest future clinical applications of intracranial EIT in medically refractory epilepsy cases. With further development, real-time fast neural EIT measurements in patients with pre-implanted depth electrodes could be used to precisely disassemble the neural propagation pathways of individual ictal discharges. Having this data would not only greatly advance our understanding of epileptic neural networks but also aid the construction of closed-loop DBS protocols for alternative treatment approaches. If successful, intracranial depth EIT could ultimately become a widely-used clinical neuroimaging technique and lead to a global reduction in epilepsy burden.

7.2 Future research directions

Based on the findings of this thesis, there are several lines of research which could be pursued to further progress EIT as a functional brain imaging technique.

Following unsuccessful attempts to image intracerebral slow impedance changes with scalp electrodes in Chapter 2, a fruitful research avenue would be to investigate the exact contribution of each intra- and extracranial layer to the suppression of the amplitude of neural impedance changes recorded with EIT upon regional brain activation. The study in this thesis suggested that both empirical and modelling-based estimates failed to accurately predict the real-life scenario. An ‘elimination’ study where impedance recordings during the same type of brain activity would be recorded using the scalp, subgaleal, epidural, subdural and intraparenchymal electrodes, implanted in this order, could instruct the attenuation of the signal caused by each type of tissue and, thereby, might enable more precise simulations which could potentially help to identify the detectability limits for brain EIT.

The pursuit of slow neural EIT with a multifrequency system and epicortical electrodes as a replacement imaging strategy for rodent fMRI would be enhanced by technical improvements to reduce the measurement noise. This is not a unique issue and has been identified during the previous projects in our group (Hannan, 2019). To date, mathematical developments of EIT image reconstruction techniques have incorporated noise as a ‘weighting factor’ which significantly improved the image quality, especially for brain and nerve EIT (Aristovich et al., 2014; Mason et al., 2024). However, practical adjustments have been limited since the principal source of noise is still debatable and the estimated signal amplitude is remarkably small. Nonetheless, continued updates in the available hardware, including the current sources and the electrodes, are promising (Chapman et al., 2019; Ravagli et al., 2022). If significant reduction in noise could be achieved and a method for chronic epicortical electrode implantation compatible with EIT recordings could be designed, single-shot chronic imaging of slow neural impedance changes in awake or anaesthetised rats could theoretically be achieved with non-penetrating intracranial electrodes. Such development would potentially make EIT a preferred functional imaging tool in rodent research due to its versatility and a relatively low cost. Additionally, improvements in epicortical EIT with a parallel system would enable further investigation of the physiological basis for the positive intracerebral impedance changes occurring over several seconds upon sensory brain stimulation. Reproducible multimodal imaging of these secondary neural changes would broaden our understanding of the interplay between different cellular and molecular processes during functional activity in the brain, and instruct how their disruption might impact the performance of neural networks in health and disease (Iadecola, 2017).

The major focus of future research should be further development of intracranial depth EIT for real-time imaging of fast and slow neural changes in the brain upon both physiological stimuli and during seizures. The first step would be to reproduce the preliminary findings presented in Chapters 5 and 6. However, arguably, future experiments would be more beneficial if *in vivo* fast and slow neural EIT data was gathered with stereo-arrays of different geometries. These studies would need to be accompanied by detailed histological analyses of the implantation effects to ensure minimal brain injury. Even though the degree of cerebral tissue damage resulting from the insertion of the depth array did not correlate with the deterioration in the functional performance of the rat brain in this study (Chapter 4), sparing major blood vessels is likely an important caveat (Kozai et al., 2010). It would be, therefore, informative to compare the physiological impact of targeted insertion of individual probes to an intracranial depth array with a fixed base since the former has previously proven an acceptable method for collecting EIT recordings in pigs (Witkowska-Wrobel, 2020). However, independent insertion of depth electrodes would significantly complicate the experimental set-up and require additional imaging of precise electrode locations in each animal. Therefore, the cost-to-benefit ratio should be carefully assessed before undertaking such developments.

From purely neuroscientific perspective, accurate fast and slow neural EIT recordings of real time ictal changes in the rat brain would be of tremendous value. Therefore, continued progression in this area would be a worthwhile line of research. Since pilot data for single shot imaging of individual SWDs have been demonstrated in this thesis, exploring impedance changes due to electrical activity during other types of ADs would be of interest. However, due to variability in their manifestation, unbiased and stringent classification of ictal waveforms would be crucial. This would require a trustworthy signal processing algorithm created specifically for this purpose and should be the first point of improvement when working towards a precise real-time fast neural EIT of epileptiform activity. Such development could potentially permit the imaging of an entire electrical seizure with fast neural EIT, albeit this undertaking would require not only significant computational resources but also a functional parallel system with a suitable bandwidth spanning tens of kilohertz. Nonetheless, with rapid growth and advance in technology across scientific disciplines, this may be possible in the near future.

Once the above improvements were made, intracranial depth EIT could be slowly introduced into the pre-clinical and clinical research as an ancillary or even an independent imaging tool. The proposed applications would involve purely investigational measurements with scientific and exploratory objectives as well as diagnostic and even therapeutic realms. For instance, ictal and interictal neural EIT data could be used to generate personalised epileptogenic network models for simulating patient-specific effects of selected therapeutic interventions (Jirsa et al., 2023). As such, fast and slow neural impedance measurements could become a default component of dynamic network modelling systems and be used for predicting changes in the critical parameters facilitating the onset of seizures (Dallmer-Zerbe et al., 2023). In fact, a novel mathematical model, called the Epileptor, devised by Jirsa et al. (2014), attempted to describe seizure dynamics based on three groups of five state variables which closely resemble the temporal profile of fast and slow intracerebral impedance changes associated with ictal and interictal epileptiform events. The first two groups of four variables explain the nature of rapid ictal discharges and spike-wave oscillations and correspond to unique patterns of fast impedance changes during neuronal depolarisation. The fifth, permittivity, variable is akin to slow biophysical changes in the epileptogenic network shown to recurrently drive the system towards the seizure threshold (Jirsa et al., 2014). Interestingly, experimental evidence gathered in parallel by the same research group showed a tight correlation between the permittivity variable and the fluctuations in extracellular K^+ (Jirsa et al., 2014). Since potassium concentration is known to play a pivotal role in the shrinkage of extracellular space during seizures, the permittivity variable could be equated to slow impedance changes following ictal discharges (Olsson et al., 2006).

All in all, these examples illustrate that, given sufficient further development, intracranial depth EIT could not only be integrated into the state-of-the-art computational neuroscience techniques but also provide a practicable neuroimaging modality for detailed examination of physiologic and pathologic neural network activity in a healthy and epileptic brain at an unmatched spatiotemporal resolution.

References

Abdul-Muneer, P. M., Chandra, N., & Haorah, J. (2015). Interactions of Oxidative Stress and Neurovascular Inflammation in the Pathogenesis of Traumatic Brain Injury. *Molecular Neurobiology*, *51*(3), 966–979. https://doi.org/10.1007/s12035-014-8752-3

Adey, W. R., Kado, R. T., & Didio, J. (1962). Impedance measurements in brain tissue of animals using microvolt signals. *Experimental Neurology*, *5*(1), 47–66. https://doi.org/10.1016/0014-4886(62)90069-9

Adler, A. (2004). Accounting for erroneous electrode data in electrical impedance tomography. *Physiological Measurement*, *25*(1), 227–238. https://doi.org/10.1088/0967-3334/25/1/028

Adler, A. (2021a). Electrical Impedance Tomography. In A. Adler & D. Holder (Eds.), *Electrical Impedance Tomography: Methods, History and Applications* (Second, pp. 3–11). CRC Press.

Adler, A. (2021b). The EIT Forward Problem. In A. Adler & D. Holder (Eds.), *Electrical Impedance Tomography: Methods, History and Applications* (Second, pp. 79–107). CRC Pr.

Adler, A., & Lionheart, W. R. B. (2006). Uses and abuses of EIDORS: An extensible software base for EIT. *Physiological Measurement*, *27*(5). https://doi.org/10.1088/0967-3334/27/5/S03

Agyemang, A. A., Kvist, S. V., Brinkman, N., Gentinetta, T., Illa, M., Ortenlöf, N., Holmqvist, B., Ley, D., & Gram, M. (2021). Cell-free oxidized hemoglobin drives reactive oxygen species production and pro-inflammation in an immature primary rat mixed glial cell culture. *Journal of Neuroinflammation*, *18*(1), 1–13. https://doi.org/10.1186/s12974-020-02052-4

Ahlfors, S. P., Han, J., Lin, F. H., Witzel, T., Belliveau, J. W., Hämäläinen, M. S., & Halgren, E. (2010). Cancellation of EEG and MEG signals generated by extended and distributed sources. *Human Brain Mapping*, *31*(1), 140–149. https://doi.org/10.1002/hbm.20851

Alf, M. F., Wyss, M. T., Buck, A., Weber, B., Schibli, R., & Krämer, S. D. (2013). Quantification of brain glucose metabolism by18F-FDG PET with real-time arterial and image-derived input function in mice. *Journal of Nuclear Medicine*, *54*(1), 132–138. https://doi.org/10.2967/jnumed.112.107474

Algotsson, L., Messeter, K., Rosén, I., & Holmin, T. (1992). Effects of nitrous oxide on cerebral haemodynamics and metabolism during isoflurane anaesthesia in man. *Acta Anaesthesiologica Scandinavica*, *36*(1), 46–52. https://doi.org/10.1111/j.1399-6576.1992.tb03420.x

Amend, M., Ionescu, T. M., Di, X., Pichler, B. J., Biswal, B. B., & Wehrl, H. F. (2019). Functional resting-state brain connectivity is accompanied by dynamic correlations of application-dependent [18 F]FDG PET-tracer fluctuations. *NeuroImage*, *196*(November 2018), 161–172. https://doi.org/10.1016/j.neuroimage.2019.04.034

Andrei, A., Welkenhuysen, M., Nuttin, B., & Eberle, W. (2012). A response surface model predicting the in vivo insertion behavior of micromachined neural implants. *Journal of Neural Engineering*, *9*(1). https://doi.org/10.1088/1741-2560/9/1/016005

Andrei, Alexandru, Welkenhuysen, M., Ameye, L., Nuttin, B., & Eberle, W. (2011). Chronic behavior evaluation of a micro-machined neural implant with optimized design based on an experimentally derived model. *Proceedings of the Annual International Conference of the IEEE Engineering in Medicine and Biology Society, EMBS*, 2292–2295. https://doi.org/10.1109/IEMBS.2011.6090577

Aristovich, K. Y., Dos Santos, G. S., & Holder, D. S. (2015). Investigation of potential artefactual changes in measurements of impedance changes during evoked activity: Implications to electrical impedance tomography of brain function. *Physiological Measurement*, *36*(6), 1245–1259. https://doi.org/10.1088/0967-3334/36/6/1245

Aristovich, K. Y., Packham, B. C., Koo, H., Santos, G. S. dos, McEvoy, A., & Holder, D. S. (2016). Imaging fast electrical activity in the brain with electrical impedance tomography. *NeuroImage*, *124*, 204–213. https://doi.org/10.1016/j.neuroimage.2015.08.071

Aristovich, K. Y., Santos, G. S. Dos, Packham, B. C., & Holder, D. S. (2014). A method for reconstructing tomographic images of evoked neural activity with electrical impedance tomography using intracranial planar arrays. *Physiological Measurement*, *35*(6), 1095–1109. https://doi.org/10.1088/0967-3334/35/6/1095

Atkinson, D., D'Souza, T., Rajput, J. S., Tasnim, N., Muthuswamy, J., Marvi, H., & Pancrazio, J. J. (2022). Advances in Implantable Microelectrode Array Insertion and Positioning. *Neuromodulation*, *25*(6), 789–795. https://doi.org/10.1111/ner.13355

Aungaroon, G., Zea Vera, A., Horn, P. S., Byars, A. W., Greiner, H. M., Tenney, J. R., Arthur, T. M., Crone, N. E., Holland, K. D., Mangano, F. T., & Arya, R. (2017). After-discharges and seizures during pediatric extra-operative electrical cortical stimulation functional brain mapping: Incidence, thresholds, and determinants. *Clinical Neurophysiology*, *128*(10), 2078–2086. https://doi.org/10.1016/j.clinph.2017.06.259

Avery, J., Dowrick, T., Faulkner, M., Goren, N., & Holder, D. (2017). A versatile and reproducible multi-frequency electrical impedance tomography system. *Sensors (Switzerland)*, *17*(2). https://doi.org/10.3390/s17020280

Avoli, M., Gloor, P., Kostopoulos, G., & Gotman, J. (1983). An analysis of penicillin-induced generalized spike and wave discharges using simultaneous recordings of cortical and thalamic single neurons. *Journal of Neurophysiology*, *50*(4), 819–837. https://doi.org/10.1152/jn.1983.50.4.819

Avoli, Massimo, & Gloor, P. (1982a). Interaction of cortex and thalamus in spike and wave discharges of feline generalized penicillin epilepsy. *Experimental Neurology*, *76*(1), 196–217. https://doi.org/10.1016/0014-4886(82)90112-1

Avoli, Massimo, & Gloor, P. (1982b). Role of the thalamus in generalized penicillin epilepsy: Observations on decorticated cats. *Experimental Neurology*, *77*(2), 386–402. https://doi.org/10.1016/0014-4886(82)90252-7

Aydin, Ü., Vorwerk, J., Dümpelmann, M., Küpper, P., Kugel, H., Heers, M., Wellmer, J., Kellinghaus, C., Haueisen, J., Rampp, S., Stefan, H., & Wolters, C. H. (2015). Combined EEG/MEG can outperform single modality EEG or MEG source reconstruction in presurgical epilepsy diagnosis. *PLoS ONE*, *10*(3). https://doi.org/10.1371/journal.pone.0118753

Aygun, H., & Ayyildiz, M. (2021). Vortioxetine increases absence-like seizures in WAG/Rij rats but decreases penicillin- and pentylenetetrazole-induced seizures in Wistar rats. *Epilepsy and Behavior*, *116*, 107797. https://doi.org/10.1016/j.yebeh.2021.107797

Bandettini, P. A., & Cox, R. W. (2000). Event-related fMRI contrast when using constant interstimulus interval: Theory and experiment. *Magnetic Resonance in Medicine*, *43*(4), 540–548. https://doi.org/10.1002/(SICI)1522-2594(200004)43:4<540::AID-MRM8>3.0.CO;2-R

Barber, Brown, & Avis. (1992). Image Reconstruction in Electrical Impedance Tomography Using Filtered Back Projection. *14th Annual International Conference of the IEEE Engineering in Medicine and Biology Society*, *5*, 1691–1692. https://doi.org/10.1109/iembs.1992.590088

Barber, C. C., & Brown, B. H. (1983). Imaging spatial distributions of resistivity using applied potential tomography. *Electronic Letter*, *19*(22), 933–935. https://doi.org/10.1049/el:19830637

Barisano, G., Sepehrband, F., Ma, S., Jann, K., Cabeen, R., Wang, D. J., Toga, A. W., & Law, M. (2019). Clinical 7 t MRi: Are we there yet? A review about magnetic resonance imaging at ultra-high field. *British Journal of Radiology*, *92*(1094). https://doi.org/10.1259/bjr.20180492

Barkley, G. L., & Baumgartner, C. (2003). MEG and EEG in epilepsy. *Journal of Clinical Neurophysiology*, *20*(3), 163–178. https://doi.org/10.1097/00004691-200305000-00002

Barth, D. S., Sutherling, W., Broffman, J., & Beatty, J. (1986). Magnetic localization of a dipolar current source implanted in a sphere and a human cranium. *Electroencephalography and Clinical Neurophysiology*, *63*(3), 260–273. https://doi.org/10.1016/0013-4694(86)90094-5

Baumann, S. B., Wozny, D. R., Kelly, S. K., & Meno, F. M. (1997). The electrical conductivity of human cerebrospinal fluid at body temperature. *IEEE Transactions on Biomedical Engineering*, *44*(3), 220–223. https://doi.org/10.1109/10.554770

Baumgartner, C., Koren, J. P., Britto-Arias, M., Zoche, L., & Pirker, S. (2019). Presurgical epilepsy evaluation and epilepsy surgery [version 1; peer review: 2 approved]. *F1000Research*, *8*. https://doi.org/10.12688/f1000research.17714.1

Benardo, L. S. (1994). Separate activation of fast and slow inhibitory postsynaptic potentials in rat neocortex in vitro. *The Journal of Physiology*, *476*(2), 203–215. https://doi.org/10.1113/jphysiol.1994.sp020124

Berg, A. T., Berkovic, S. F., Brodie, M. J., Buchhalter, J., Cross, J. H., Van Emde Boas, W., Engel, J., French, J., Glauser, T. A., Mathern, G. W., Moshé, S. L., Nordli, D., Plouin, P., & Scheffer, I. E. (2010). Revised terminology and concepts for organization of seizures and epilepsies: Report of the ILAE Commission on Classification and Terminology, 2005-2009. *Epilepsia*, *51*(4), 676–685. https://doi.org/10.1111/j.1528-1167.2010.02522.x

Bernier, G. P., Richer, F., Giard, N., Bouvier, G., Merrier, M., Turmel, A., & Saint-Hilaire, J. -M. (1990). Electrical Stimulation of the Human Brain in Epilepsy. *Epilepsia*, *31*(5), 513–520. https://doi.org/10.1111/j.1528-1157.1990.tb06099.x

Bertrand, O., Perrin, F., & Pernier, J. (1985). *A theoretical justification of the average reference in topographic evoked potential studiesJustification théorique de la référence moyenne dans les études topographiques de potentiels évoqués*. *62*, 462–464.

Bevan, J. A., & Hwa, J. J. (1985). Myogenic tone and cerebral vascular autoregulation: The role of a stretch-dependent mechanism. *Annals of Biomedical Engineering*, *13*(3–4), 281–286. https://doi.org/10.1007/BF02584245

Bezanilla, F. (2007). Voltage-Gated Ion Channels Biological Membrane. In S.-H. Chung, O. S. Andersen, & V. Krishnamurthy (Eds.), *Biological Membrane Ion Channels: Dynamics, Structure, and Applications* (pp. 81–118). Springer New York. https://doi.org/10.1007/0-387-68919-2_3

Biran, R., Martin, D. C., & Tresco, P. A. (2005). Neuronal cell loss accompanies the brain tissue response to chronically implanted silicon microelectrode arrays. *Experimental Neurology*, *195*(1), 115–126. https://doi.org/10.1016/j.expneurol.2005.04.020

Birn, R. M., & Bandettini, P. A. (2005). The effect of stimulus duty cycle and “off” duration on BOLD response linearity. *NeuroImage*, *27*(1), 70–82. https://doi.org/10.1016/j.neuroimage.2005.03.040

Birzis, L., & Tachibana, S. (1964). Local cerebral impedance and blood flow during sleep and arousal. *Experimental Neurology*, *9*(4), 269–285. https://doi.org/10.1016/0014-4886(64)90024-X

Bjornsson, C. S., Oh, S. J., Al-Kofahi, Y. A., Lim, Y. J., Smith, K. L., Turner, J. N., De, S., Roysam, B., Shain, W., & Kim, S. J. (2006). Effects of insertion conditions on tissue strain and vascular damage during neuroprosthetic device insertion. *Journal of Neural Engineering*, *3*(3), 196–207. https://doi.org/10.1088/1741-2560/3/3/002

Blad, B., Bertenstam, L., Rehncrona, S., Bjartmarz, H., & Törnqvist, A. L. (2005). Measurement of contact impedance of electrodes used for deep brain stimulation. *Itbm-Rbm*, *26*(5–6), 344–346. https://doi.org/10.1016/j.rbmret.2005.07.003

Blamire, A. M., Ogawa, S., Ugurbil, K., Rothman, D., McCarthy, G., Ellermann, J. M., Hyder, F., Rattner, Z., & Shulman, R. G. (1992). Dynamic mapping of the human visual cortex by high-speed magnetic resonance imaging. *Proceedings of the National Academy of Sciences of the United States of America*, *89*(22), 11069–11073. https://doi.org/10.1073/pnas.89.22.11069

Blume, W. T., Jones, D. C., & Pathak, P. (2004). Properties of after-discharges from cortical electrical stimulation in focal epilepsies. *Clinical Neurophysiology*, *115*(4), 982–989. https://doi.org/10.1016/j.clinph.2003.11.023

Blumenfeld, H. (2005). Cellular and network mechanisms of spike-wave seizures. *Epilepsia*, *46*(9), 21–33. https://doi.org/10.1016/j.ddmod.2008.07.005

Bolomey, L. (1985). Rapid production of positron emitting labeled compounds for use in cardiology PET studies. *Nuclear Inst. and Methods in Physics Research, B*, *10–11*(PART 2), 969–971. https://doi.org/10.1016/0168-583X(85)90151-X

Boone, K. G., & Holder, D. S. (1996). Effect of skin impedance on image quality and variability in electrical impedance tomography: A model study. *Medical and Biological Engineering and Computing*, *34*(5), 351–354. https://doi.org/10.1007/BF02520003

Boone, K., Lewis, A. M., & Holder, D. S. (1994). Imaging of cortical spreading depression by EIT: Implications for localization of epileptic foci. *Physiological Measurement*, *15*(2A). https://doi.org/10.1088/0967-3334/15/2A/024

Boone, Kevin Graham. (1995). *The possible use of applied potential tomography for imaging action potentials in the brain*. *August*, 194.

Boto, E., Holmes, N., Leggett, J., Roberts, G., Shah, V., Meyer, S. S., Muñoz, L. D., Mullinger, K. J., Tierney, T. M., Bestmann, S., Barnes, G. R., Bowtell, R., & Brookes, M. J. (2018). Moving magnetoencephalography towards real-world applications with a wearable system. *Nature*, *555*(7698), 657–661. https://doi.org/10.1038/nature26147

Brain Products GmbH. (2016). ActiCHamp User Manual. In *ActiCHamp Operating Instructions Product Revision 04*. https://www.brainproducts.com/solutions/actichamp/

Brienza, M., & Mecarelli, O. (2019). Neurophysiological Basis of EEG. In O. Mecarelli (Ed.), *Clinical Electroencephalography* (pp. 9–21). Springer.

Brisson, C. D., Lukewich, M. K., & Andrew, R. D. (2013). A Distinct Boundary between the Higher Brain ' s Susceptibility to Ischemia and the Lower Brain ' s Resistance. *PLoS ONE*, *8*(11), 1–14. https://doi.org/10.1371/journal.pone.0079589

Brisson, D. C., & Andrew, D. R. (2012). A neuronal population in hypothalamus that dramatically resists acute ischemic injury compared to neocortex. *Journal of Neurophysiology*, *108*(2), 419–430. https://doi.org/10.1152/jn.00090.2012

Brodovskaya, A., Batabyal, T., Shiono, S., Sun, H., & Kapur, J. (2022). Distinct Roles of Rodent Thalamus and Corpus Callosum in Seizure Generalization. *Annals of Neurology*, *91*(5), 682–696. https://doi.org/10.1002/ana.26338

Brown, B. H. H., & Seagar, A. D. D. (1987). The Sheffield data collection system. *Clin. Phys. Physiol. Meas*, *8*(4A), 91. https://iopscience.iop.org/article/10.1088/0143-0815/8/4A/012%0Ahttps://iopscience.iop.org/article/10.1088/0143-0815/8/4A/012/meta

Buxton, R. B. (2013). The physics of functional magnetic resonance imaging (fMRI). *Reports on Progress in Physics*, *76*(9). https://doi.org/10.1088/0034-4885/76/9/096601

Byrne, J. H. (2014). Postsynaptic Potentials and Synaptic Integration. In *From Molecules to Networks: An Introduction to Cellular and Molecular Neuroscience: Third Edition* (Third Edit). Elsevier Inc. https://doi.org/10.1016/B978-0-12-397179-1.00016-6

Calabresi, P., Pisani, A., Mercuri, N. B., & Bernardi, G. (1995). On the mechanisms underlying hypoxia-induced membrane depolarization in striatal neurons. *Brain*, *118*, 1027–1038.

Cao, L., Li, H., Fu, D., Liu, X., Ma, H., Xu, C., Dong, X., Yang, B., & Fu, F. (2020). Real-time imaging of infarction deterioration after ischemic stroke in rats using electrical impedance tomography. *Physiological Measurement*, *41*(1). https://doi.org/10.1088/1361-6579/ab69ba

Cardu, R., Leong, P. H. W., Jin, C. T., & McEwan, A. (2012). Electrode contact impedance sensitivity to variations in geometry. *Physiological Measurement*, *33*(5), 817–830. https://doi.org/10.1088/0967-3334/33/5/817

Castagnola, V., Bayon, C., Descamps, E., & Bergaud, C. (2014). Morphology and conductivity of PEDOT layers produced by different electrochemical routes. *Synthetic Metals*, *189*, 7–16. https://doi.org/10.1016/j.synthmet.2013.12.013

Chang, P. C., Procissi, D., Bao, Q., Centeno, M. V., Baria, A., & Apkarian, A. V. (2016). Novel method for functional brain imaging in awake minimally restrained rats. *Journal of Neurophysiology*, *116*(1), 61–80. https://doi.org/10.1152/jn.01078.2015

Chapman, C. A. R., Aristovich, K., Donega, M., Fjordbakk, C. T., Stathopoulou, T. R., Viscasillas, J., Avery, J., Perkins, J. D., & Holder, D. (2019). Electrode fabrication and interface optimization for imaging of evoked peripheral nervous system activity with electrical impedance tomography (EIT). *Journal of Neural Engineering*, *16*(1). https://doi.org/10.1088/1741-2552/aae868

Charles, A. C., & Baca, S. M. (2013). Cortical spreading depression and migraine. *Nature Reviews Neurology*, *9*(11), 637–644. https://doi.org/10.1038/nrneurol.2013.192

Chaudhary, U. J., Carmichael, D. W., Rodionov, R., Thornton, R. C., Bartlett, P., Vulliemoz, S., Micallef, C., McEvoy, A. W., Diehl, B., Walker, M. C., Duncan, J. S., & Lemieux, L. (2012). Mapping preictal and ictal haemodynamic networks using video-electroencephalography and functional imaging. *Brain*, *135*(12), 3645–3663. https://doi.org/10.1093/brain/aws302

Chen, B. R., Bouchard, M. B., McCaslin, A. F. H., Burgess, S. A., & Hillman, E. M. C. (2011). High-speed vascular dynamics of the hemodynamic response. *NeuroImage*, *54*(2), 1021–1030. https://doi.org/10.1016/j.neuroimage.2010.09.036.High-speed

Chen, M., Guo, D., Wang, T., Jing, W., Xia, Y., Xu, P., Luo, C., Valdes-Sosa, P. A., & Yao, D. (2014). Bidirectional Control of Absence Seizures by the Basal Ganglia: A Computational Evidence. *PLoS Computational Biology*, *10*(3). https://doi.org/10.1371/journal.pcbi.1003495

Chiaravalloti, A., Micarelli, A., Ricci, M., Pagani, M., Ciccariello, G., Bruno, E., Alessandrini, M., & Schillaci, O. (2019). Evaluation of Task-Related Brain Activity: Is There a Role for 18F FDG-PET Imaging? *BioMed Research International*, *2019*. https://doi.org/10.1155/2019/4762404

Cho, F. S., & Paz, J. T. (2022). Thalamocortical organization and function: new insights and implications. In *Neurobiology of the Epilepsies: From Epilepsy: A Comprehensive Textbook*.

Cohen, D. (1968). Magnetoencephalography: evidence of magnetic fields produced by alpha-rhythm currents. *Science*, *161*(3842), 784–786.

Cohen, D. (1972). Magnetoencephalography: Detection of the brain's electrical activity with a superconducting magnetometer. *Science*, *175*(4022), 664–666. https://doi.org/10.1126/science.175.4022.664

Colbourn, R., Hrabe, J., Nicholson, C., Perkins, M., Goodman, J. H., & Hrabetova, S. (2021). Rapid volume pulsation of the extracellular space coincides with epileptiform activity in mice and depends on the NBCe1 transporter. *Journal of Physiology*, *599*(12), 3195–3220. https://doi.org/10.1113/JP281544

Cole, K. S., & Curtis, H. J. (1939). Electric impedance of the squid giant axon during activity. *Journal of General Physiology*, *22*(5), 649–670. https://doi.org/10.1085/jgp.22.5.649

Cook, M. J., O'Brien, T. J., Berkovic, S. F., Murphy, M., Morokoff, A., Fabinyi, G., D'Souza, W., Yerra, R., Archer, J., Litewka, L., Hosking, S., Lightfoot, P., Ruedebusch, V., Sheffield, W. D., Snyder, D., Leyde, K., & Himes, D. (2013). Prediction of seizure likelihood with a long-term, implanted seizure advisory system in patients with drug-resistant epilepsy: A first-in-man study. *The Lancet Neurology*, *12*(6), 563–571. https://doi.org/10.1016/S1474-4422(13)70075-9

Cooper, G. M. (2000). *The Cell: A Molecular Approach* (G. M. Cooper (ed.); Fourth Edi). Sinauer Associates.

Cuello Oderiz, C., Von Ellenrieder, N., Dubeau, F., Eisenberg, A., Gotman, J., Hall, J., Hincapié, A. S., Hoffmann, D., Job, A. S., Khoo, H. M., Minotti, L., Olivier, A., Kahane, P., & Frauscher, B. (2019). Association of Cortical Stimulation-Induced Seizure with Surgical Outcome in Patients with Focal Drug-Resistant Epilepsy. *JAMA Neurology*, *76*(9), 1070–1078. https://doi.org/10.1001/jamaneurol.2019.1464

Czajkowski, R., Jayaprakash, B., Wiltgen, B., Rogerson, T., Guzman-Karlsson, M. C., Barth, A. L., Trachtenberg, J. T., & Silva, A. J. (2014). Encoding and storage of spatial information in the retrosplenial cortex. *Proceedings of the National Academy of Sciences of the United States of America*, *111*(23), 8661–8666. https://doi.org/10.1073/pnas.1313222111

Dabrowska, N., Joshi, S., Williamson, J., Lewczuk, E., Lu, Y., Oberoi, S., Brodovskaya, A., & Kapur, J. (2019). Parallel pathways of seizure generalization. *Brain*, *142*(8), 2336–2351. https://doi.org/10.1093/brain/awz170

Dai, M., Wang, L., Xu, C., Li, L., Gao, G., & Dong, X. (2010). Real-time imaging of subarachnoid hemorrhage in piglets with electrical impedance tomography. *Physiological Measurement*, *31*(9), 1229–1239. https://doi.org/10.1088/0967-3334/31/9/012

Dallmer-Zerbe, I., Jiruska, P., & Hlinka, J. (2023). Personalized dynamic network models of the human brain as a future tool for planning and optimizing epilepsy therapy. In *Epilepsia* (Vol. 64, Issue 9, pp. 2221–2238). https://doi.org/10.1111/epi.17690

Danober, L., Deransart, C., Depaulis, A., Vergnes, M., & Marescaux, C. (1998). Pathophysiological Mechanisms of Genetic Absence Epilepsy in the Rat. *Progress in Neurobiology*, *55*(97), 27–57.

Darquié, A., Poline, J. B., Poupon, C., Saint-Jalmes, H., & Le Bihan, D. (2001). Transient decrease in water diffusion observed in human occipital cortex during visual stimulation. *Proceedings of the National Academy of Sciences of the United States of America*, *98*(16), 9391–9395. https://doi.org/10.1073/pnas.151125698

Dawson, D. R., & Killackey, H. P. (1987). The organization and mutability of the forepaw and hindpaw representations in the somatosensory cortex of the neonatal rat. *Journal of Comparative Neurology*, *256*(2), 246–256. https://doi.org/10.1002/cne.902560205

De Zwart, J. A., Silva, A. C., Van Gelderen, P., Kellman, P., Fukunaga, M., Chu, R., Koretsky, A. P., Frank, J. A., & Duyn, J. H. (2005). Temporal dynamics of the BOLD fMRI impulse response. *NeuroImage*, *24*(3), 667–677. https://doi.org/10.1016/j.neuroimage.2004.09.013

de Zwart, J. A., van Gelderen, P., Jansma, J. M., Fukunaga, M., Bianciardi, M., & Duyn, J. H. (2009). Hemodynamic nonlinearities affect BOLD fMRI response timing and amplitude. *NeuroImage*, *47*(4), 1649–1658. https://doi.org/10.1016/j.neuroimage.2009.06.001

Depauls, A., Vergnes, M., Liu, Z., Kempf, E., & Marescaux, C. (1990). Involvement of the nigral output pathways in the inhibitory control of the substantia nigra over generalized non-convulsive seizures in the rat. *Neuroscience*, *39*(2), 339–349. https://doi.org/10.1016/0306-4522(90)90272-6

Deransart, C., Marescaux, C., & Depaulis, A. (1996). Involvement of nigral glutamatergic inputs in the control of seizures in a genetic model of absence epilepsy in the rat. *Neuroscience*, *71*(3), 721–728. https://doi.org/10.1016/0306-4522(95)00471-8

Deransart, Colin, & Depaulis, A. (2002). The control of seizures by the basal ganglia? A review of experimental data. *Epileptic Disorders*, *4*(SUPPL. 3). https://doi.org/10.1684/j.1950-6945.2002.tb00547.x

Destexhe, A., McCormick, D. A., & Sejnowski, T. J. (1999). Thalamic and thalamocortical mechanisms underlying 3 Hz spike-and-wave discharges. *Progress in Brain Research*, *121*, 289–307. https://doi.org/10.1016/s0079-6123(08)63080-0

Devor, A., Sakadžić, S., Srinivasan, V. J., Yaseen, M. A., Nizar, K., Saisan, P. A., Tian, P., Dale, A. M., Vinogradov, S. A., Franceschini, M. A., & Boas, D. A. (2012). Frontiers in optical imaging of cerebral blood flow and metabolism. *Journal of Cerebral Blood Flow and Metabolism*, *32*(7), 1259–1276. https://doi.org/10.1038/jcbfm.2011.195

Dichter, M. A., Herman, C. J., & Selzer, M. (1972). Silent Cells During Interictal Discharges And Seizures. *Brain Research*, *48*, 173–183.

Dietzel, I., & Heinemann, U. (1986). Dynamic Variations of the Brain Cell Microenvironment in Relation to Neuronal Hyperactivity. *Annals of the New York Academy of Sciences*, *481*(1), 72–84. https://doi.org/10.1111/j.1749-6632.1986.tb27140.x

Digimeter Ltd. (2001). *NeuroLogTM User Manual*.

Dijk, G., Pas, J., Markovic, K., Scancar, J., & O'Connor, R. P. (2023). PEDOT:PSS-coated platinum electrodes for neural stimulation. *APL Bioengineering*, *7*(4). https://doi.org/10.1063/5.0153094

Dimakopoulos, V., Neidert, M. C., & Sarnthein, J. (2023). Low impedance electrodes improve detection of high frequency oscillations in the intracranial EEG. *Clinical Neurophysiology*, *153*, 133–140. https://doi.org/10.1016/j.clinph.2023.07.002

Ding, L., & Yuan, H. (2013). Simultaneous EEG and MEG source reconstruction in sparse electromagnetic source imaging. *Human Brain Mapping*, *34*(4), 775–795. https://doi.org/10.1002/hbm.21473

Dogan, M. F., Yildiz, O., Arslan, S. O., & Ulusoy, K. G. (2019). Potassium channels in vascular smooth muscle: a pathophysiological and pharmacological perspective. *Fundamental and Clinical Pharmacology*, *33*(5), 504–523. https://doi.org/10.1111/fcp.12461

Dowrick, T., Sato Dos Santos, G., Vongerichten, A., & Holder, D. (2015). Parallel, multi frequency EIT measurement, suitable for recording impedance changes during epilepsy. *Journal of Electrical Bioimpedance*, *6*(1), 37–43. https://doi.org/10.5617/jeb.2573

Du, M., Li, J., Wang, R., & Wu, Y. (2016). The influence of potassium concentration on epileptic seizures in a coupled neuronal model in the hippocampus. *Cognitive Neurodynamics*, *10*(5), 405–414. https://doi.org/10.1007/s11571-016-9390-4

Du, T., Chen, Y., Shi, L., Liu, D., Liu, Y., Yuan, T., Zhang, X., Zhu, G., & Zhang, J. (2021). Deep brain stimulation of the anterior nuclei of the thalamus relieves basal ganglia dysfunction in monkeys with temporal lobe epilepsy. *CNS Neuroscience and Therapeutics*, *27*(3), 341–351. https://doi.org/10.1111/cns.13462

Dufour, S., Dufour, P., Chever, O., Vallée, R., & Amzica, F. (2011). In vivo simultaneous intra- and extracellular potassium recordings using a micro-optrode. *Journal of Neuroscience Methods*, *194*(2), 206–217. https://doi.org/10.1016/j.jneumeth.2010.10.004

Durduran, T., Burnett, M. G., Yu, G., Zhou, C., Furuya, D., Yodh, A. G., Detre, J. A., & Greenberg, J. H. (2004). Spatiotemporal Quantification of Cerebral Blood Flow during Functional Activation in Rat Somatosensory Cortex Using Laser-Speckle Flowmetry. *Journal of Cerebral Blood Flow and Metabolism*, *24*(5), 518–525. https://doi.org/10.1097/00004647-200405000-00005

Dzhala, V., Ben-Ari, Y., & Khazipov, R. (2000). Seizure accelerate anoxia-induced neuronal death in the neonatal rat hippocampus. *Annals of Neurology*, *48*(4), 632–640. https://doi.org/10.1002/1531-8249(200010)48:4<632::AID-ANA10>3.0.CO;2-3

Ebersole, J. S. (2003). EEG Voltage Topography and Dipole Source Modeling of Epileptiform Potentials. In J. S. Ebersole & T. A. Pedley (Eds.), *Current practice of clinical electroencephalography* (pp. 732–752). Lippincott Williams and Wilkins.

Edell, D. J., Toi, V. Van, McNeil, V. M., & Clark, L. D. (1992). Factors Influencing the Biocompatibility of Insertable Silicon Microshafts. *IEEE Transactions on Biomedical Engineering*, *39*(6), 1–17.

Eggebrecht, A. T., Ferradal, S. L., Robichaux-Viehoever, A., Hassanpour, M. S., Dehghani, H., Snyder, A. Z., Hershey, T., & Culver, J. P. (2014). Mapping distributed brain function and networks with diffuse optical tomography. *Nature Photonics*, *8*(6), 448–454. https://doi.org/10.1038/nphoton.2014.107

Eichele, T., Specht, K., Moosmann, M., Jongsma, M. L. A., Quiroga, R. Q., Nordby, H., & Hugdahl, K. (2005). Assessing the spatiotemporal evolution of neuronal activation with single-trial event-related potentials and functional MRI. *Proceedings of the National Academy of Sciences of the United States of America*, *102*(49), 17798–17803. https://doi.org/10.1073/pnas.0505508102

El Hady, A., Takahashi, D., Sun, R., Akinwale, O., Boyd-Meredith, T., Zhang, Y., Charles, A. S., & Brody, C. D. (2024). Chronic brain functional ultrasound imaging in freely moving rodents performing cognitive tasks. *Journal of Neuroscience Methods*, *403*(November 2023), 110033. https://doi.org/10.1016/j.jneumeth.2023.110033

Elazar, Z., Kado, R. T., & Adey, W. R. (1966). Impedance Changes during Epileptic Seizures. *Elpilepsia*, *7*(4), 291–307.

Evers, J., Sridhar, K., Liegey, J., Brady, J., Jahns, H., & Lowery, M. (2022). Stimulation-induced changes at the electrode-tissue interface and their influence on deep brain stimulation. *Journal of Neural Engineering*, *19*(4). https://doi.org/10.1088/1741-2552/ac7ad6

Fabri, M., & Burton, H. (1991). Topography of connections between primary somatosensory cortex and posterior complex in rat: a multiple fluorescent tracer study. *Brain Research*, *538*(2), 351–357. https://doi.org/10.1016/0006-8993(91)90455-5

Fabrizi, L., Sparkes, M., Horesh, L., Perez-Juste Abascal, J. F., McEwan, A., Bayford, R. H., Elwes, R., Binnie, C. D., & Holder, D. S. (2006). Factors limiting the application of electrical impedance tomography for identification of regional conductivity changes using scalp electrodes during epileptic seizures in humans. *Physiological Measurement*, *27*(5). https://doi.org/10.1088/0967-3334/27/5/S14

Falco-walter, J. (2020). *Epilepsy — De fi nition , Classi fi cation , Pathophysiology , and Epidemiology*. 617–623.

Fan, D., Liao, F., & Wang, Q. (2017). The pacemaker role of thalamic reticular nucleus in controlling spike-wave discharges and spindles. *Chaos*, *27*(7). https://doi.org/10.1063/1.4991869

Faraci, F. M., Breese, K. R., & Heistad, D. D. (1993). Nitric oxide contributes to dilatation of cerebral arterioles during seizures. *American Journal of Physiology - Heart and Circulatory Physiology*, *265*(6 34-6). https://doi.org/10.1152/ajpheart.1993.265.6.h2209

Faria, P., Hallett, M., & Miranda, P. C. (2011). A finite element analysis of the effect of electrode area and inter-electrode distance on the spatial distribution of the current density in tDCS. *Journal of Neural Engineering*, *8*(6). https://doi.org/10.1088/1741-2560/8/6/066017

Faulkner, A. C. M. (2019). *Imaging of evoked neural activity in the rat brain using Electrical Impedance Tomography* (Issue Dr. Thesis). University College London.

Faulkner, M., Hannan, S., Aristovich, K., Avery, J., & Holder, D. (2018a). Characterising the frequency response of impedance changes during evoked physiological activity in the rat brain. *Physiological Measurement*, *39*(3). https://doi.org/10.1088/1361-6579/aab01f

Faulkner, M., Hannan, S., Aristovich, K., Avery, J., & Holder, D. (2018b). Feasibility of imaging evoked activity throughout the rat brain using electrical impedance tomography. *NeuroImage*, *178*(May), 1–10. https://doi.org/10.1016/j.neuroimage.2018.05.022

Faulkner, M., Jehl, M., Aristovich, K., Avery, J., Witkowska-Wrobel, A., & Holder, D. (2017). Optimisation of current injection protocol based on a region of interest. *Physiological Measurement*, *38*(6), 1158–1175. https://doi.org/10.1088/1361-6579/aa69d7

Fayuk, D., Aitken, P. G., Somjen, G. G., & Turner, D. A. (2002). Two different mechanisms underlie reversible, intrinsic optical signals in rat hippocampal slices. *Journal of Neurophysiology*, *87*(4), 1924–1937. https://doi.org/10.1152/jn.00231.2001

Federico, P., Borg, S. G., Šalkauskus, A. G., & MacVicar, B. A. (1994). Mapping patterns of neuronal activity and seizure propagation by imaging intrinsic optical signals in the isolated whole brain of the guinea-pig. *Neuroscience*, *58*(3), 461–480. https://doi.org/10.1016/0306-4522(94)90073-6

Ferradal, S. L., Liao, S. M., Eggebrecht, A. T., Shimony, J. S., Inder, T. E., Culver, J. P., & Smyser, C. D. (2016). Functional Imaging of the Developing Brain at the Bedside Using Diffuse Optical Tomography. *Cerebral Cortex*, *26*(4), 1558–1568.

https://doi.org/10.1093/cercor/bhu320

Ferrari, M. (2007). Progress of near-infrared spectroscopy and topography for brain and muscle clinical applications. *Journal of Biomedical Optics*, *12*(6), 062104. https://doi.org/10.1117/1.2804899

Fertziger, A. P., & Ranck, J. B. (1970). Potassium accumulation in interstitial space during epileptiform seizures. *Experimental Neurology*, *26*(3), 571–585. https://doi.org/10.1016/0014-4886(70)90150-0

Fisher, R. S., Acevedo, C., Arzimanoglou, A., Bogacz, A., Cross, J. H., Elger, C. E., Engel, J., Forsgren, L., French, J. A., Glynn, M., Hesdorffer, D. C., Lee, B. I., Mathern, G. W., Moshé, S. L., Perucca, E., Scheffer, I. E., Tomson, T., Watanabe, M., & Wiebe, S. (2014). ILAE Official Report: A practical clinical definition of epilepsy. *Epilepsia*, *55*(4), 475–482. https://doi.org/10.1111/epi.12550

Fisher, R. S., Van Emde Boas, W., Blume, W., Elger, C., Genton, P., Lee, P., & Engel, J. (2005). Response: Definitions proposed by the International League Against Epilepsy (ILAE) and the International Bureau for Epilepsy (IBE) [4]. *Epilepsia*, *46*(10), 1701–1702. https://doi.org/10.1111/j.1528-1167.2005.00273_4.x

Fitchett, A., Fabbri, J. D., Hu, Y., Cange, J., Kozeniauskaite, K., Shepard, K., Holder, D. S., & Aristovich, K. (2023). Imaging Circuit Activity in the Rat Brain with Fast Neural EIT and Depth Arrays. *International IEEE/EMBS Conference on Neural Engineering, NER*, *2023-April*, 1–4. https://doi.org/10.1109/NER52421.2023.10123878

Fitchett, A., Hewchaiyaphum, A., Holder, D. S., & Aristovich, K. (2022). Geometrical Optimisation of Depth Arrays for Fast Neural EIT. *International Journal of Bioelectromagnetism*, *24*.

Fox, P. T., Mintum, M. A., Raichle, M. E., & Herscovitch, P. (1984). A noninvasive approach to quantitative functional brain mapping with H215O and positron emission tomography. *Journal of Cerebral Blood Flow and Metabolism*, *4*(3), 329–333. https://doi.org/10.1038/jcbfm.1984.49

Fox, P. T., & Raichle, M. E. (1984). Stimulus rate dependence of regional cerebral blood flow in human striate cortex, demonstrated by positron emission tomography. *Journal of Neurophysiology*, *51*(5), 1109–1120. https://doi.org/10.1152/jn.1984.51.5.1109

Fox, P. T., Raichle, M. E., & Thach, W. T. (1985). Functional mapping of the human cerebellum with positron emission tomography. *Proceedings of the National Academy of Sciences of the United States of America*, *82*(21), 7462–7466. https://doi.org/10.1073/pnas.82.21.7462

Franceschetti, S., Sancini, G., Panzica, F., Radici, C., & Avanzini, G. (1998). Postnatal differentiation of firing properties and morphological characteristics in layer V pyramidal neurons of the sensorimotor cortex. *Neuroscience*, *83*(4), 1013–1024. https://doi.org/10.1016/S0306-4522(97)00463-6

Frostig, R. D., & Chen-Bee, C. H. (2012). Intrinsic signal optical imaging. In R. Brette & A. Destexhe (Eds.), *Handbook of Neural Activity Measurement* (pp. 287–326). Cambridge University Press. https://doi.org/10.1017/cbo9780511979958.008

Gabriel, C., Peyman, A., & Grant, E. H. (2009). Electrical conductivity of tissue at frequencies below 1 MHz. *Physics in Medicine and Biology*, *54*(16), 4863–4878. https://doi.org/10.1088/0031-9155/54/16/002

Gabriel, S., Lau, R. W., & Gabriel, C. (1996). The dielectric properties of biological tissues: II. Measurements in the frequency range 10 Hz to 20 GHz. *Physics in Medicine and Biology*, *41*(11), 2251–2269. https://doi.org/10.1088/0031-9155/41/11/002

Gallego, B. I., Salazar, J. J., de Hoz, R., Rojas, B., Ramírez, A. I., Salinas-Navarro, M., Ortín-Martínez, A., Valiente-Soriano, F. J., Avilés-Trigueros, M., Villegas-Perez, M. P., Vidal-Sanz, M., Triviño, A., & Ramírez, J. M. (2012). IOP induces upregulation of GFAP and MHC-II and microglia reactivity in mice retina contralateral to experimental glaucoma. *Journal of Neuroinflammation*, *9*, 1–18. https://doi.org/10.1186/1742-2094-9-92

Gamache, F. W., Dold, G. M., & Myers, R. E. (1975). Changes in cortical impedance and EEG activity induced by profound hypotension. *American Journal of Physiology*, *228*(6), 1914–1920. https://doi.org/10.1152/ajplegacy.1975.228.6.1914

Gardy, L., Barbeau, E. J., & Hurter, C. (2020). Automatic detection of epileptic spikes in intracerebral EEG with convolutional kernel density estimation. *VISIGRAPP 2020 - Proceedings of the 15th International Joint Conference on Computer Vision, Imaging and Computer Graphics Theory and Applications*, *2*, 101–109. https://doi.org/10.5220/0008877601010109

Ghane-Motlagh, B., & Sawan, M. (2013). Design and Implementation Challenges of Microelectrode Arrays: A Review. *Materials Sciences and Applications*, *04*(08), 483–495. https://doi.org/10.4236/msa.2013.48059

Gilad, O., & Holder, D. S. (2009). *Impedance changes recorded with scalp electrodes during visual evoked responses: implications for Electrical Impedance Tomography of fast neural activity*. https://doi.org/10.1016/j.neuroimage.2009.04.085

Gilad, O., Horesh, L., & Holder, D. S. (2007). Design of electrodes and current limits for low frequency electrical impedance tomography of the brain. *Medical and Biological Engineering and Computing*, *45*(7), 621–633. https://doi.org/10.1007/s11517-007-0209-7

Gilad, O., Horesh, L., & Holder, D. S. (2009). A modelling study to inform specification and optimal electrode placement for imaging of neuronal depolarization during visual evoked responses by electrical and magnetic detection impedance tomography. *Physiological Measurement*, *30*(6). https://doi.org/10.1088/0967-3334/30/6/S14

Goldman, D. E. (1943). POTENTIAL, IMPEDANCE, AND RECTIFICATION IN MEMBRANES. *The Journal of General Physiology*, *27*(1), 37–60.

Gollwitzer, S., Hopfengärtner, R., Rössler, K., Müller, T., Olmes, D. G., Lang, J., Köhn, J., Onugoren, M. D., Heyne, J., Schwab, S., & Hamer, H. M. (2018). Afterdischarges elicited by cortical electric stimulation in humans: When do they occur and what do they mean? *Epilepsy and Behavior*, *87*, 173–179. https://doi.org/10.1016/j.yebeh.2018.09.007

Goloshevsky, A. G., Silva, A. C., Dodd, S. J., & Koretsky, A. P. (2008). BOLD fMRI and somatosensory evoked potentials are well correlated over a broad range of frequency content of somatosensory stimulation of the rat forepaw. *Brain Research*, *1195*, 67–76. https://doi.org/10.1016/j.brainres.2007.11.036

Gouveia, F. V., Warsi, N. M., Suresh, H., Matin, R., & Ibrahim, G. M. (2024). Neurostimulation treatments for epilepsy: Deep brain stimulation, responsive neurostimulation and vagus nerve stimulation. *Neurotherapeutics*, *21*(3). https://doi.org/10.1016/j.neurot.2023.e00308

Gratton, G., Corballis, P. M., Cho, E., Fabiani, M., & Hood, D. C. (1995). Shades of gray matter: Noninvasive optical images of human brain responses during visual stimulation. *Psychophysiology*, *32*, 505–509.

Graybiel, A. M. (2000). The Basal Ganglia. *Current Biology*, *10*(14), 219–225. https://linkinghub.elsevier.com/retrieve/pii/B978012802381500018X

Grech, R., Cassar, T., Muscat, J., Camilleri, K. P., Fabri, S. G., Zervakis, M., Xanthopoulos, P., Sakkalis, V., & Vanrumste, B. (2008). Review on solving the inverse problem in EEG source analysis. *Journal of NeuroEngineering and Rehabilitation*, *5*, 1–33. https://doi.org/10.1186/1743-0003-5-25

Grubb, S., Cai, C., Hald, B. O., Khennouf, L., Murmu, R. P., Jensen, A. G. K., Fordsmann, J., Zambach, S., & Lauritzen, M. (2020). Precapillary sphincters maintain perfusion in the cerebral cortex. *Nature Communications*, *11*(1). https://doi.org/10.1038/s41467-020-14330-z

Gu, H., Hu, Y., Chen, X., He, Y., & Yang, Y. (2019). Regional excitation-inhibition balance predicts default-mode network deactivation via functional connectivity. *NeuroImage*, *185*(October 2018), 388–397. https://doi.org/10.1016/j.neuroimage.2018.10.055

Guo, K., Wang, J., Cui, B., Wang, Y., Hou, Y., Zhao, G., & Lu, J. (2022). [18F]FDG PET/MRI and magnetoencephalography may improve presurgical localization of temporal lobe epilepsy. *European Radiology*, *32*(5), 3024–3034. https://doi.org/10.1007/s00330-021-08336-4

Gyengesi, E., Calabrese, E., Sherrier, M. C., Johnson, G. A., Paxinos, G., & Watson, C. (2014). Semi-automated 3D segmentation of major tracts in the rat brain: Comparing DTI with standard histological methods. *Brain Structure and Function*, *219*(2), 539–550. https://doi.org/10.1007/s00429-013-0516-8

Haier, R. J., Siegel, B. V, MacLachlan, A., Soderling, E., Lottenberg, S., & Buchsbaum, M. S. (1992). Regional Glucose Metabolic Changes After Learning a Complex Visuospatial/Motor Task: a PET Study. *Brain Research*, *570*(1–2), 134–143.

Halford, J. J., & Edwards, J. C. (2020). Seizure freedom as an outcome in epilepsy treatment clinical trials. *Acta Neurologica Scandinavica*, *142*(2), 91–107. https://doi.org/10.1111/ane.13257

Hall, C. N., Reynell, C., Gesslein, B., Hamilton, N. B., Mishra, A., Sutherland, B. A., Oâ Farrell, F. M., Buchan, A. M., Lauritzen, M., & Attwell, D. (2014). Capillary pericytes regulate cerebral blood flow in health and disease. *Nature*, *508*(1), 55–60. https://doi.org/10.1038/nature13165

Han, S. H., Son, J. P., Cho, H. J., Park, J. Y., & Kim, S. G. (2019). Gradient-echo and spin-echo blood oxygenation level–dependent functional MRI at ultrahigh fields of 9.4 and 15.2 Tesla. *Magnetic Resonance in Medicine*, *81*(2), 1237–1246. https://doi.org/10.1002/mrm.27457

Hanada, T. (2020). Ionotropic glutamate receptors in epilepsy: A review focusing on ampa and nmda receptors. *Biomolecules*, *10*(3). https://doi.org/10.3390/biom10030464

Hannan, S. (2019). *Imaging fast neural activity in the brain during epilepsy with electrical impedance tomography*. *March*.

Hannan, S., Aristovich, K., Faulkner, M., Avery, J., Walker, M. C., & Holder, D. S. (2021). Imaging slow brain activity during neocortical and hippocampal epileptiform events with electrical impedance tomography. *Physiological Measurement*, *42*(1). https://doi.org/10.1088/1361-6579/abd67a

Hannan, S., Faulkner, M., Aristovich, K., Avery, J., & Holder, D. (2018a). Frequency dependent characterisation of impedance changes during epileptiform activity in a rat model of epilepsy. *Physiological Measurement*, *39*(8), 085003. https://doi.org/10.1088/1361-6579/aad5f4

Hannan, S., Faulkner, M., Aristovich, K., Avery, J., & Holder, D. (2019). Investigating the safety of fast neural electrical impedance tomography in the rat brain. *Physiological Measurement*, *40*(3). https://doi.org/10.1088/1361-6579/ab0d53

Hannan, S., Faulkner, M., Aristovich, K., Avery, J., Walker, M. C., & Holder, D. S. (2020a).

In vivo imaging of deep neural activity from the cortical surface during hippocampal epileptiform events in the rat brain using electrical impedance tomography. *NeuroImage*, *209*(January), 116525. https://doi.org/10.1016/j.neuroimage.2020.116525

Hannan, S., Faulkner, M., Aristovich, K., Avery, J., Walker, M. C., & Holder, D. S. (2020b). Optimised induction of on-demand focal hippocampal and neocortical seizures by electrical stimulation. *Journal of Neuroscience Methods*, *346*(July), 108911. https://doi.org/10.1016/j.jneumeth.2020.108911

Hannan, S., Faulkner, M., Aristovich, K., Avery, J., Walker, M., & Holder, D. (2018b). Imaging fast electrical activity in the brain during ictal epileptiform discharges with electrical impedance tomography. *NeuroImage: Clinical*, *20*, 674–684. https://doi.org/10.1016/j.nicl.2018.09.004

Hansen, A. J., & Olsen, C. E. (1980). Brain extracellular space during spreading depression and ischemia. *Acta Physiologica Scandinavica*, *108*(4), 355–365. https://doi.org/10.1111/j.1748-1716.1980.tb06544.x

Hansen, A. J., & Zeuthen, T. (1981). Extracellular ion concentrations during spreading depression and ischemia in the rat brain cortex. *Acta Physiologica Scandinavica*, *113*(4), 437–445. https://doi.org/10.1111/j.1748-1716.1981.tb06920.x

Harder, D. R., Narayanan, J., & Gebremedhin, D. (2011). Pressure-induced myogenic tone and role of 20-HETE in mediating autoregulation of cerebral blood flow. *American Journal of Physiology - Heart and Circulatory Physiology*, *300*(5), 1557–1565. https://doi.org/10.1152/ajpheart.01097.2010

Harel, N., Lee, S. P., Nagaoka, T., Kim, D. S., & Kim, S. G. (2002). Origin of negative blood oxygenation level-dependent fMRI signals. *Journal of Cerebral Blood Flow and Metabolism*, *22*(8), 908–917. https://doi.org/10.1097/00004647-200208000-00002

Hartzell, H. C. (1981). Mechanisms of slow postsynaptic potentials. *Nature*, *291*(5816), 539–544. https://doi.org/10.1038/291539a0

Haueisen, J., Funke, M., Güllmar, D., & Eichardt, R. (2012). Tangential and radial epileptic spike activity: Different sensitivity in EEG and MEG. *Journal of Clinical Neurophysiology*, *29*(4), 327–332. https://doi.org/10.1097/WNP.0b013e3182624491

Hedrich, T., Pellegrino, G., Kobayashi, E., Lina, J. M., & Grova, C. (2017). Comparison of the spatial resolution of source imaging techniques in high-density EEG and MEG. *NeuroImage*, *157*(December 2016), 531–544. https://doi.org/10.1016/j.neuroimage.2017.06.022

Heiss, W. D., Pawlik, G., Herholz, K., Wagner, R., Göldner, H., & Wienhard, K. (1984). Regional kinetic constants and cerebral metabolic rate for glucose in normal human volunteers determined by dynamic positron emission tomography of [18F]-2-fluoro-2-deoxy-D-glucose. *Journal of Cerebral Blood Flow and Metabolism*, *4*(2), 212–223. https://doi.org/10.1038/jcbfm.1984.30

Herrero-Mendez, A., Almeida, A., Fernández, E., Maestre, C., Moncada, S., & Bolaños, J. P. (2009). The bioenergetic and antioxidant status of neurons is controlled by continuous degradation of a key glycolytic enzyme by APC/C-Cdh1. *Nature Cell Biology*, *11*(6), 747–752. https://doi.org/10.1038/ncb1881

Hill, R. M., Devasagayam, J., Holmes, N., Boto, E., Shah, V., Osborne, J., Safar, K., Worcester, F., Mariani, C., Dawson, E., Woolger, D., Bowtell, R., Taylor, M. J., & Brookes, M. J. (2022). Using OPM-MEG in contrasting magnetic environments. *NeuroImage*, *253*(January), 119084. https://doi.org/10.1016/j.neuroimage.2022.119084

Hillman, E. M. C., Devor, A., Bouchard, M. B., Dunn, A. K., Krauss, G. W., Skoch, J., Bacskai, B. J., Dale, A. M., & Boas, D. A. (2007). Depth-resolved Optical Imaging and

Microscopy of Vascular Compartment Dynamics During Somatosensory Stimulation. *NeuroImage*, *35*(1), 89–104.

Hillman, H. (2000). Limitations of clinical and biological histology. *Medical Hypotheses*, *54*(4), 553–564. https://doi.org/10.1054/mehy.1999.0894

Hirano, Y., Stefanovic, B., & Silva, A. C. (2011). Spatiotemporal evolution of the functional magnetic resonance imaging response to ultrashort stimuli. *Journal of Neuroscience*, *31*(4), 1440–1447. https://doi.org/10.1523/JNEUROSCI.3986-10.2011

Hochman, D. W., Baraban, S. C., Owens, J. W. M., & Schwartzkroin, P. A. (1995). Dissociation of synchronization and excitability in furosemide blockade of epileptiform activity. *Science*, *270*(5233), 99–102. https://doi.org/10.1126/science.270.5233.99

Hodgkin, A. L., & Huxley, A. F. (1952). A QUANTITATIVE DESCRIPTION OF MEMBRANE CURRENT AND ITS APPLICATION TO CONDUCTION AND EXCITATION IN NERVE. *J. Physiol.*, *117*, 500–544.

Hoffman, C. J., Clark, F. J., & Ochs, S. (1973). Intracortical impedance changes during spreading depression. *Journal of Neurobiology*, *4*(5), 471–486. https://doi.org/10.1002/neu.480040508

Holdefer, R. N., Sadleir, R., & Russell, M. J. (2006). Predicted current densities in the brain during transcrania electrical stimulation. *Clinical Neurophysiology*, *117*(6), 1388–1397. https://www.ncbi.nlm.nih.gov/pmc/articles/PMC3624763/pdf/nihms412728.pdf

Holder, D. (2021a). EIT Imaging of Brain and Nerves. In A. Adler & D. Holder (Eds.), *Electrical Impedance Tomography: Methods, History and Applications* (Second, pp. 231–260). CRC Press.

Holder, D. (2021b). Introduction to EIT concepts and technology. In A. Adler & D. Holder (Eds.), *Electrical Impedance Tomography: Methods, History and Applications* (Second, pp. 13–30). CRC Press. https://doi.org/10.1201/9780429399886-2

Holder, D. S. (1987). Feasibility of developing a method of imaging neuronal activity in the human brain: a theoretical review. *Medical & Biological Engineering & Computing*, *25*(1), 2–11. https://doi.org/10.1007/BF02442813

Holder, D. S. (1989). Impedance changes during evoked nervous activity in human subjects: Implications for the application of applied potential tomography (APT) to imaging neuronal discharge. *Clinical Physics and Physiological Measurement*, *10*(3), 267–274. https://doi.org/10.1088/0143-0815/10/3/007

Holder, D. S. (1992a). Detection of cortical spreading depression in the anaesthetised rat by impedance measurement with scalp electrodes: Implications for non-invasive imaging of the brain with electrical impedance tomography. *Clinical Physics and Physiological Measurement*, *13*(1), 77–86. https://doi.org/10.1088/0143-0815/13/1/007

Holder, D. S. (1992b). Electrical impedance tomography with cortical or scalp electrodes during global cerebral ischaemia in the anaesthetised rat. *Clinical Physics and Physiological Measurement*, *13*(1), 87–98. https://doi.org/10.1088/0143-0815/13/1/008

Holder, D. S. (1992c). Detection of cerebral ischaemia in the anaesthetised rat by impedance measurement with scalp electrodes: Implications for non-invasive imaging of stroke by electrical impedance tomography. *Clinical Physics and Physiological Measurement*, *13*(1), 63–75. https://doi.org/10.1088/0143-0815/13/1/006

Holder, D. S., Rao, A., & Hanquan, Y. (1996). Imaging of physiologically evoked responses by electrical impedance tomography with cortical electrodes in the anaesthetized rabbit. *Physiological Measurement*, *17*(4 SUPPL. A), 22–24. https://doi.org/10.1088/0967-3334/17/4A/022

Holthoff, K., & Witte, O. W. (1996). Intrinsic optical signals in rat neocortical slices measured with near-infrared dark-field microscopy reveal changes in extracellular space. *Journal of Neuroscience*, *16*(8), 2740–2749. https://doi.org/10.1523/jneurosci.16-08-02740.1996

Horesh, L. (2006). *Some novel approaches in modelling and image reconstruction for multi-frequency electrical impedance tomography of the human brain*. University College London.

Horitsugi, G., Watabe, T., Kanai, Y., Ikeda, H., Kato, H., Naka, S., Ishibashi, M., Matsunaga, K., Isohashi, K., Shimosegawa, E., & Hatazawa, J. (2017). Oxygen-15 labeled CO2, O2, and CO PET in small animals: evaluation using a 3D-mode microPET scanner and impact of reconstruction algorithms. *EJNMMI Research*, *7*. https://doi.org/10.1186/s13550-017-0335-7

Hosking, P. G. (2003). Surgery for frontal lobe epilepsy. *Seizure*, *12*, 160–166. https://doi.org/10.1016/S1059

Hossmann, K. A. (1971). Cortical Changes Steady During Potential , and After Impedance Total and Excitability of Cat. *Experimental Neurology*, *32*(2), 163–175.

Hotson, J. R., Sypert, G. W., & Ward, A. A. (1973). Extracellular potassium concentration changes during propagated seizures in neocortex. *Experimental Neurology*, *38*(1), 20–26. https://doi.org/10.1016/0014-4886(73)90004-6

Htain, W. -W, Leong, S. -K, & Ling, E. -A. (1994). A comparative Mac-1 immunocytochemical and lectin histochemical study of microglial cells in the normal and athymic mice. *Glia*, *12*(1), 44–51. https://doi.org/10.1002/glia.440120106

Hu, B., Wang, Z., Xu, M., Zhang, D., & Wang, D. (2022). The adjustment mechanism of the spike and wave discharges in thalamic neurons: a simulation analysis. *Cognitive Neurodynamics*, *16*(6), 1449–1460. https://doi.org/10.1007/s11571-022-09788-0

Hu, D., & Huang, L. (2015). Negative hemodynamic response in the cortex: Evidence opposing neuronal deactivation revealed via optical imaging and electrophysiological recording. *Journal of Neurophysiology*, *114*(4), 2152–2161. https://doi.org/10.1152/jn.00246.2015

Huber, L., Uludağ, K., & Möller, H. E. (2019). Non-BOLD contrast for laminar fMRI in humans: CBF, CBV, and CMRO2. In *NeuroImage* (Vol. 197, Issue July 2017, pp. 742–760). https://doi.org/10.1016/j.neuroimage.2017.07.041

Hulvershorn, J., Bloy, L., Gualtieri, E. E., Leigh, J. S., & Elliott, M. A. (2005). Spatial sensitivity and temporal response of spin echo and gradient echo bold contrast at 3 T using peak hemodynamic activation time. *NeuroImage*, *24*(1), 216–223. https://doi.org/10.1016/j.neuroimage.2004.09.033

Huttunen, J. K., Gröhn, O., & Penttonen, M. (2008). Coupling between simultaneously recorded BOLD response and neuronal activity in the rat somatosensory cortex. *NeuroImage*, *39*(2), 775–785. https://doi.org/10.1016/j.neuroimage.2007.06.042

Iadecola, C. (2017). The Neurovascular Unit Coming of Age: A Journey through Neurovascular Coupling in Health and Disease. *Neuron*, *96*(1), 17–42. https://doi.org/10.1016/j.neuron.2017.07.030

Iida, H., Ohata, H., Iida, M., Watanabe, Y., & Dohi, S. (1998). Isoflurane and sevoflurane induce vasodilation of cerebral vessels via ATP-sensitive K+ channel activation. *The Journal of the American Society of Anesthesiologists*, *89*(4), 954–960.

Iivanainen, J., Stenroos, M., & Parkkonen, L. (2017). Measuring MEG closer to the brain: Performance of on-scalp sensor arrays. *NeuroImage*, *147*, 542–553. https://doi.org/10.1016/j.neuroimage.2016.12.048

Iivanainen, J., Zetter, R., Grön, M., Hakkarainen, K., & Parkkonen, L. (2019). On-scalp MEG system utilizing an actively shielded array of optically-pumped magnetometers. *NeuroImage*, *194*(November 2018), 244–258. https://doi.org/10.1016/j.neuroimage.2019.03.022

Iwasa, K., Tasaki, I., & Gibbons, R. C. (1980). Swelling of nerve fibers associated with action potentials. *Science*, *210*(4467), 338–339.

Jamadar, S. D., Ward, P. G. D., Liang, E. X., Orchard, E. R., Chen, Z., & Egan, G. F. (2021). Metabolic and Hemodynamic Resting-State Connectivity of the Human Brain: A High-Temporal Resolution Simultaneous BOLD-fMRI and FDG-fPET Multimodality Study. *Cerebral Cortex (New York, N.Y. : 1991)*, *31*(6), 2855–2867. https://doi.org/10.1093/cercor/bhaa393

Jamadar, S. D., Ward, P. G., Li, S., Sforazzini, F., Baran, J., Chen, Z., & Egan, G. F. (2019). Simultaneous task-based BOLD-fMRI and [18-F] FDG functional PET for measurement of neuronal metabolism in the human visual cortex. *NeuroImage*, *189*(January), 258–266. https://doi.org/10.1016/j.neuroimage.2019.01.003

Jehl, M., Dedner, A., Betcke, T., Aristovich, K., Klofkorn, R., & Holder, D. (2015). A fast parallel solver for the forward problem in electrical impedance tomography. *IEEE Transactions on Biomedical Engineering*, *62*(1), 126–137. https://doi.org/10.1109/TBME.2014.2342280

Jensen, F. E., & Wang, C. (1996). Hypoxia-induced hyperexcitability in vivo and in vitro the immature hippocampus. *Epilepsy Research*, *26*(1), 131–140. https://doi.org/10.1016/S0920-1211(96)00049-6

Jiang, J., Truong, D. Q., Esmaeilpour, Z., Huang, Y., Badran, B. W., & Bikson, M. (2020). Enhanced tES and tDCS computational models by meninges emulation. *Journal of Neural Engineering*, *17*(1). https://doi.org/10.1088/1741-2552/ab549d

Jing, J., Aitken, P. G., & Somjen, G. G. (1994). Interstitial volume changes during spreading depression (SD) and SD-like hypoxic depolarization in hippocampal tissue slices. *Journal of Neurophysiology*, *71*(6), 2548–2551. https://doi.org/10.1152/jn.1994.71.6.2548

Jirsa, V. K., Stacey, W. C., Quilichini, P. P., Ivanov, A. I., & Bernard, C. (2014). On the nature of seizure dynamics. *Brain*, *137*, 2210–2230. https://doi.org/10.1093/brain/awu133

Jirsa, V., Wang, H., Triebkorn, P., Hashemi, M., Jha, J., Gonzalez-Martinez, J., Guye, M., Makhalova, J., & Bartolomei, F. (2023). Personalised virtual brain models in epilepsy. *The Lancet Neurology*, *22*(5), 443–454. https://doi.org/10.1016/S1474-4422(23)00008-X

Jobsis-vander Vliet, F. F. (1999). Discovery of the Near-Infrared Window into the Body and the Early Development of Near-Infrared Spectroscopy. *Journal of Biomedical Optics*, *4*(4), 392–396.

Joel, D., & Weiner, I. (1994). The organization of the basal ganglia-thalamocortical circuits: Open interconnected rather than closed segregated. *Neuroscience*, *63*(2), 363–379. https://doi.org/10.1016/0306-4522(94)90536-3

Jung, W. B., Im, G. H., Jiang, H., & Kim, S. G. (2021). Early fMRI responses to somatosensory and optogenetic stimulation reflect neural information flow. *Proceedings of the National Academy of Sciences of the United States of America*, *118*(11). https://doi.org/10.1073/pnas.2023265118

Kager, H., Wadman, W. J., & Somjen, G. G. (2000). Simulated seizures and spreading depression in a neuron model incorporating interstitial space and ion concentrations.

Journal of Neurophysiology, *84*(1), 495–512. https://doi.org/10.1152/jn.2000.84.1.495

Kaiboriboon, K., Lüders, H. O., Hamaneh, M., Turnbull, J., & Lhatoo, S. D. (2012). EEG source imaging in epilepsyĝ€"practicalities and pitfalls. *Nature Reviews Neurology*, *8*(9), 498–507. https://doi.org/10.1038/nrneurol.2012.150

Kalamangalam, G. P., Tandon, N., & Slater, J. D. (2014). Dynamic mechanisms underlying afterdischarge: A human subdural recording study. *Clinical Neurophysiology*, *125*(7), 1324–1338. https://doi.org/10.1016/j.clinph.2013.11.027

Kameyama, Y. (1994). Effect of isoflurane and sevoflurane on evoked potentials and EEG. *Japanese Journal of Anesthesiology*, *43*(5), 657–664.

Kamp, A., Pfurtscheller, G., Edlinger, G., & Lopes da Silva, F. H. (2005). Technological Basis of EEG Recording. In *Electroencephalography: Basic Principles, Clinical Applications, and Related Fields* (Vol. 1, pp. 127–138). http://books.google.com/books?id=tndqYGPHQdEC&pgis=1

Kämpfer, C., Racz, A., Quesada, C. M., Elger, C. E., & Surges, R. (2020). Predictive value of electrically induced seizures for postsurgical seizure outcome. *Clinical Neurophysiology*, *131*(9), 2289–2297. https://doi.org/10.1016/j.clinph.2020.06.013

Kandel, A., & Buzséki, G. (1997). Cellular-synaptic generation of sleep spindles, spike-and-wave discharges, and evoked thalamocortical responses in the neocortex of the rat. *Journal of Neuroscience*, *17*(17), 6783–6797. https://doi.org/10.1523/jneurosci.17-17-06783.1997

Kandratavicius, L., Alves Balista, P., Lopes-Aguiar, C., Ruggiero, R. N., Umeoka, E. H., Garcia-Cairasco, N., Soares Bueno-Junior, L., & Leite, J. P. (2014). Animal models of epilepsy: use and limitations. *Neuropsychiatric Disease and Treatment*, *10*, 1693–1705.

Kannurpatti, S. S., & Biswal, B. B. (2004). Negative functional response to sensory stimulation and its origins. *Journal of Cerebral Blood Flow and Metabolism*, *24*(6), 703–712. https://doi.org/10.1097/01.WCB.0000121232.04853.46

Karpova, A. V., Bikbaev, A. F., Coenen, A. M. L., & Van Luijtelaar, G. (2005). Morphometric Golgi study of cortical locations in WAG/Rij rats: The cortical focus theory. *Neuroscience Research*, *51*(2), 119–128. https://doi.org/10.1016/j.neures.2004.10.004

Khoo, H. M., Hall, J. A., Dubeau, F., Tani, N., Oshino, S., Fujita, Y., Gotman, J., & Kishima, H. (2020). Technical aspects of seeg and its interpretation in the delineation of the epileptogenic zone. *Neurologia Medico-Chirurgica*, *60*(12), 565–580. https://doi.org/10.2176/nmc.st.2020-0176

Kim, T., Masamoto, K., Fukuda, M., Vazquez, A., & Kim, S. G. (2010). Frequency-dependent neural activity, CBF, and BOLD fMRI to somatosensory stimuli in isoflurane-anesthetized rats. *NeuroImage*, *52*(1), 224–233. https://doi.org/10.1016/j.neuroimage.2010.03.064

Klein, J. P., Khera, D. S., Nersesyan, H., Kimchi, E. Y., Waxman, S. G., & Blumenfeld, H. (2004). Dysregulation of sodium channel expression in cortical neurons in a rodent model of absence epilepsy. *Brain Research*, *1000*(1–2), 102–109. https://doi.org/10.1016/j.brainres.2003.11.051

Ko, K. R., Ngai, A. C., & Winn, H. R. (1990). Role of adenosine in regulation of regional cerebral blood flow in sensory cortex. *American Journal of Physiology - Heart and Circulatory Physiology*, *259*(6 28-6). https://doi.org/10.1152/ajpheart.1990.259.6.h1703

Köhling, R., Lücke, A., Nagao, T., Speckmann, E. J., & Avoli, M. (1995). Extracellular potassium elevations in the hippocampus of rats with long-term pilocarpine seizures.

Neuroscience Letters, *201*(1), 87–91. https://doi.org/10.1016/0304-3940(95)12136-R

Kohno, S., Sawamoto, N., Urayama, S. I., Aso, T., Aso, K., Seiyama, A., Fukuyama, H., & Le Bihan, D. (2009). Water-diffusion slowdown in the human visual cortex on visual stimulation precedes vascular responses. *Journal of Cerebral Blood Flow and Metabolism*, *29*(6), 1197–1207. https://doi.org/10.1038/jcbfm.2009.45

Komaki, Y., Debacker, C., Djemai, B., Ciobanu, L., Tsurugizawa, T., & Le Bihan, D. (2020). Differential effects of aquaporin-4 channel inhibition on BOLD fMRI and diffusion fMRI responses in mouse visual cortex. *PLoS ONE*, *15*(5), e02228759. http://journal.um-surabaya.ac.id/index.php/JKM/article/view/2203

Kombos, T., & Süss, O. (2009). Neurophysiological basis of direct cortical stimulation and applied neuroanatomy of the motor cortex: A review. *Neurosurgical Focus*, *27*(4), 1–7. https://doi.org/10.3171/2009.8.FOCUS09141

Kortelainen, J., Vipin, A., Yuan, T. X., Mir, H., Thakor, N., Al-Nashash, H., & All, A. (2014). Effect of isoflurane on somatosensory evoked potentials in a rat model. *2014 36th Annual International Conference of the IEEE Engineering in Medicine and Biology Society, EMBC 2014*, 4286–4289. https://doi.org/10.1109/EMBC.2014.6944572

Kozai, T. D.Y., Marzullo, T. C., Hooi, F., Langhals, N. B., Majewska, A. K., Brown, E. B., & Kipke, D. R. (2010). Reduction of neurovascular damage resulting from microelectrode insertion into the cerebral cortex using in vivo two-photon mapping. *Journal of Neural Engineering*, *7*(4). https://doi.org/10.1088/1741-2560/7/4/046011

Kozai, Takashi D.Y., Jaquins-Gerstl, A. S., Vazquez, A. L., Michael, A. C., & Cui, X. T. (2015). Brain tissue responses to neural implants impact signal sensitivity and intervention strategies. *ACS Chemical Neuroscience*, *6*(1), 48–67. https://doi.org/10.1021/cn500256e

Kozai, Takashi D.Yoshida, Vazquez, A. L., Weaver, C. L., Kim, S. G., & Cui, X. T. (2012). In vivo two-photon microscopy reveals immediate microglial reaction to implantation of microelectrode through extension of processes. *Journal of Neural Engineering*, *9*(6). https://doi.org/10.1088/1741-2560/9/6/066001

Krishnan, G. P., Filatov, G., Shilnikov, A., & Bazhenov, M. (2015). Electrogenic properties of the Na+/K+ ATPase control transitions between normal and pathological brain states. *Journal of Neurophysiology*, *113*(9), 3356–3374. https://doi.org/10.1152/jn.00460.2014

Krucoff, M. O., Chan, A. Y., Harward, S. C., Rahimpour, S., Rolston, J. D., Muh, C., & Englot, D. J. (2017). Rates and predictors of success and failure in repeat epilepsy surgery: A meta-analysis and systematic review. *Epilepsia*, *58*(12), 2133–2142. https://doi.org/10.1111/epi.13920

Kubánek, J., Miller, K. J., Ojemann, J. G., Wolpaw, J. R., & Schalk, G. (2009). Decoding flexion of individual fingers using electrocorticographic signals in humans. *Journal of Neural Engineering*, *6*(6). https://doi.org/10.1088/1741-2560/6/6/066001

Kudlacek, J., Chvojka, J., Kumpost, V., Hermanovska, B., Posusta, A., Jefferys, J. G. R., Maturana, M. I., Novak, O., Cook, M. J., Otahal, J., Hlinka, J., & Jiruska, P. (2021). Long-term seizure dynamics are determined by the nature of seizures and the mutual interactions between them. *Neurobiology of Disease*, *159*, 105347. https://doi.org/10.1016/j.nbd.2021.105484

Kudomi, N., Hirano, Y., Koshino, K., Hayashi, T., Watabe, H., Fukushima, K., Moriwaki, H., Teramoto, N., Iihara, K., & Iida, H. (2013). Rapid quantitative CBF and CMRO2 measurements from a single PET scan with sequential administration of dual 15O-labeled tracers. *Journal of Cerebral Blood Flow and Metabolism*, *33*(3), 440–448.

https://doi.org/10.1038/jcbfm.2012.188

Kuhlmann, L., Lehnertz, K., Richardson, M. P., Schelter, B., & Zaveri, H. P. (2018). Seizure prediction — ready for a new era. *Nature Reviews Neurology*, *14*(10), 618–630. https://doi.org/10.1038/s41582-018-0055-2

Kuncel, A. M., & Grill, W. M. (2004). Selection of stimulus parameters for deep brain stimulation. *Clinical Neurophysiology*, *115*(11), 2431–2441. https://doi.org/10.1016/j.clinph.2004.05.031

Kusske, J. A., & Rush, J. L. (1978). Corpus callosum and propagation of afterdischarge to contralateral cortex and thalamus. *Neurology*, *28*(9), 905–912. https://doi.org/10.1212/wnl.28.9.905

Kwan, P., & Sander, J. W. (2004). The natural history of epilepsy: An epidemioloqical view. *Journal of Neurology, Neurosurgery and Psychiatry*, *75*(10), 1376–1381. https://doi.org/10.1136/jnnp.2004.045690

Kyle, J. J., Sharma, S., Tiarks, G., Rodriguez, S., & Bassuk, A. G. (2023). Fast Detection and Quantification of Interictal Spikes and Seizures in a Rodent Model of Epilepsy Using an Automated Algorithm. *Bio-Protocol*, *13*(6), 1–12. https://doi.org/10.21769/BioProtoc.4632

Lacroix, A., Toussay, X., Anenberg, E., Lecrux, C., Ferreirós, N., Karagiannis, A., Plaisier, F., Chausson, P., Jarlier, F., Burgess, S. A., Hillman, E. M. C., Tegeder, I., Murphy, T. H., Hamel, E., & Cauli, B. (2015). COX-2-derived prostaglandin E2 produced by pyramidal neurons contributes to neurovascular coupling in the rodent cerebral cortex. *Journal of Neuroscience*, *35*(34), 11791–11810. https://doi.org/10.1523/JNEUROSCI.0651-15.2015

Lang, E., Kapila, A., Shlugman, D., Hoke, J. F., Sebel, P. S., & Glass, P. S. A. (1996). Reduction of Isoflurane Minimal Alveolar Concentration by Remifentanil. *Anesthesiology*, *85*, 721–728.

Lassen, N. A., Ingvar, D. H., & Skinh, E. (1978). Brain Function and Blood Flow are graphically revealed with the aid of a radioactive isotope. *Scientific American*, *239*(4), 62–71.

Latikka, J., Kuurne, T., & Eskola, H. (2001). Conductivity of living intracranial tissues. *Physics in Medicine and Biology*, *46*(6), 1611–1616. https://doi.org/10.1088/0031-9155/46/6/302

Laxer, K. D., Trinka, E., Hirsch, L. J., Cendes, F., Langfitt, J., Delanty, N., Resnick, T., & Benbadis, S. R. (2014). The consequences of refractory epilepsy and its treatment. *Epilepsy and Behavior*, *37*, 59–70. https://doi.org/10.1016/j.yebeh.2014.05.031

Le Bihan, D. (2014). Diffusion MRI: What water tells us about the brain. *EMBO Molecular Medicine*, *6*(5), 569–573. https://doi.org/10.1002/emmm.201404055

Le Bihan, D., Urayama, S. I., Aso, T., Hanakawa, T., & Fukuyama, H. (2006). Direct and fast detection of neuronal activation in the human brain with diffusion MRI. *Proceedings of the National Academy of Sciences of the United States of America*, *103*(21), 8263–8268. https://doi.org/10.1073/pnas.0600644103

Lee, C. W., Cooper, R. J., & Austin, T. (2017). Diffuse optical tomography to investigate the newborn brain. *Pediatric Research*, *82*(3), 376–386. https://doi.org/10.1038/pr.2017.107

Lee, J., & Kim, S. J. (2010). Spectrum measurement of fast optical signal of neural activity in brain tissue and its theoretical origin. *NeuroImage*, *51*(2), 713–722. https://doi.org/10.1016/j.neuroimage.2010.02.076

Leijten, F. S. S., Huiskamp, G. J. M., Hilgersom, I., & Van Huffelen, A. C. (2003). High-resolution source imaging in mesiotemporal lobe epilepsy: A comparison between MEG and simultaneous EEG. *Journal of Clinical Neurophysiology*, *20*(4), 227–238. https://doi.org/10.1097/00004691-200307000-00001

LeVan, P., Tyvaert, L., & Gotman, J. (2010). Modulation by EEG features of BOLD responses to interictal epileptiform discharges. *NeuroImage*, *50*(1), 15–26. https://doi.org/10.1016/j.neuroimage.2009.12.044

Li, J., & Iadecola, C. (1994). Nitric oxide and adenosine mediate vasodilation during functional activation in cerebellar cortex. *Neuropharmacology*, *33*(11), 1453–1461. https://doi.org/10.1016/0028-3908(94)90049-3

Lionheart, W. R., & Adler, A. (2021). The EIT inverse problem. In A. Adler & D. Holder (Eds.), *Electrical Impedance Tomography: Methods, History and Applications* (Second, pp. 109–136). CRC Press. https://doi.org/10.1201/9780429399886-6

Lipton, P. (1973). Effects of membrane depolarization on light scattering by cerebral cortical slices. *The Journal of Physiology*, *231*(2), 365–383. https://doi.org/10.1113/jphysiol.1973.sp010238

Liston, A., Bayford, R., & Holder, D. (2012). A cable theory based biophysical model of resistance change in crab peripheral nerve and human cerebral cortex during neuronal depolarisation: Implications for electrical impedance tomography of fast neural activity in the brain. In *Medical and Biological Engineering and Computing* (Vol. 50, Issue 5, pp. 425–437). https://doi.org/10.1007/s11517-012-0901-0

Liu, C., Yu, T., Ren, Z. W., Xu, C. P., Wang, X. Y., Qiao, L., Ni, D. Y., Zhang, G. J., & Li, Y. J. (2017). Properties of afterdischarges from electrical stimulation in patients with epilepsy. *Epilepsy Research*, *137*(August), 39–44. https://doi.org/10.1016/j.eplepsyres.2017.09.002

Liu, Z., Rios, C., Zhang, N., Yang, L., Chen, W., & He, B. (2010). Linear and nonlinear relationships between visual stimuli, EEG and BOLD fMRI signals. *NeuroImage*, *50*(3), 1054–1066. https://doi.org/10.1016/j.neuroimage.2010.01.017

Logothetis, N. K. (2008). What we can do and what we cannot do with fMRI. *Nature*, *453*(7197), 869–878. https://doi.org/10.1038/nature06976

Logothetis, N. K., Kayser, C., & Oeltermann, A. (2007). In Vivo Measurement of Cortical Impedance Spectrum in Monkeys: Implications for Signal Propagation. *Neuron*, *55*(5), 809–823. https://doi.org/10.1016/j.neuron.2007.07.027

Longden, T. A., Dabertrand, F., Koide, M., Gonzales, A. L., Tykocki, N. R., Brayden, J. E., Hill-Eubanks, D., & Nelson, M. T. (2017). Capillary K+-sensing initiates retrograde hyperpolarization to increase local cerebral blood flow. *Nature Neuroscience*, *20*(5), 717–726. https://doi.org/10.1038/nn.4533

Lu, C. Q., Zeng, C. H., Cui, Y., Meng, X. P., Luan, Y., Xu, X. M., & Ju, S. (2022). An Investigation of the Impacts of Three Anesthetic Regimens on Task-Functional Magnetic Resonance Imaging and Functional Connectivity Resting-State Functional Magnetic Resonance Imaging in Sprague Dawley and Wistar Rats. *Brain Connectivity*, *12*(1), 74–84. https://doi.org/10.1089/brain.2020.0875

Luccarelli, J., Mccoy, T. H., Seiner, S. J., & Henry, M. E. (2021). Total Charge Required to Induce a Seizure in a Retrospective Cohort of Patients Undergoing Dose Titration of Right Unilateral Ultrabrief Pulse Electroconvulsive Therapy. *Journal of ECT*, *37*(1), 40–45. https://doi.org/10.1097/YCT.0000000000000714

Ludwig, K. A., Miriani, R. M., Langhals, N. B., Joseph, M. D., Anderson, D. J., & Kipke, D. R. (2009). Using a common average reference to improve cortical neuron recordings from microelectrode arrays. *Journal of Neurophysiology*, *101*(3), 1679–1689. https://doi.org/10.1152/jn.90989.2008

Luo, C., Li, Q., Xia, Y., Lei, X., Xue, K., Yao, Z., Lai, Y., Martínez-Montes, E., Liao, W., Zhou, D., Valdes-Sosa, P. A., Gong, Q., & Yao, D. (2012). Resting state basal ganglia network in idiopathic generalized epilepsy. *Human Brain Mapping*, *33*(6), 1279–1294. https://doi.org/10.1002/hbm.21286

Luo, C., Xia, Y., Li, Q., Xue, K., Lai, Y., Gong, Q., Zhou, D., & Yao, D. (2011). Diffusion and volumetry abnormalities in subcortical nuclei of patients with absence seizures. *Epilepsia*, *52*(6), 1092–1099. https://doi.org/10.1111/j.1528-1167.2011.03045.x

Ma, Z., Cao, P., Sun, P., Lu, Z., Li, L., Chen, Y., & Chai, X. (2017). Negative hemodynamic response without neuronal inhibition investigated by combining optical imaging and electrophysiological recording. *Neuroscience Letters*, *637*, 161–167. https://doi.org/10.1016/j.neulet.2016.11.029

MacEachern, S. J., Santoro, J. D., Hahn, K. J., Medress, Z. A., Stecher, X., Li, M. D., Hahn, J. S., Yeom, K. W., & Forkert, N. D. (2020). Children with epilepsy demonstrate macro- and microstructural changes in the thalamus, putamen, and amygdala. *Neuroradiology*, *62*(3), 389–397. https://doi.org/10.1007/s00234-019-02332-8

Mălîia, M. D., Meritam, P., Scherg, M., Fabricius, M., Rubboli, G., Mîndruţă, I., & Beniczky, S. (2016). Epileptiform discharge propagation: Analyzing spikes from the onset to the peak. *Clinical Neurophysiology*, *127*(4), 2127–2133. https://doi.org/10.1016/j.clinph.2015.12.021

Malone, E., Jehl, M., Arridge, S., Betcke, T., & Holder, D. (2014). Stroke type differentiation using spectrally constrained multifrequency EIT: Evaluation of feasibility in a realistic head model. *Physiological Measurement*, *35*(6), 1051–1066. https://doi.org/10.1088/0967-3334/35/6/1051

Mandeville, J. B., Jenkins, B. G., Kosofsky, B. E., Moskowitz, M. A., Rosen, B. R., & Marota, J. J. A. (2001). Regional sensitivity and coupling of BOLD, and CBV changes during stimulation of rat brain. *Magnetic Resonance in Medicine*, *45*(3), 443–447. https://doi.org/10.1002/1522-2594(200103)45:3<443::AID-MRM1058>3.0.CO;2-3

Mapelli, L., Gagliano, G., Soda, T., Laforenza, U., Moccia, F., & D'Angelo, E. U. (2017). Granular layer neurons control cerebellar neurovascular coupling through an NMDA receptor/NO-dependent system. *Journal of Neuroscience*, *37*(5), 1340–1351. https://doi.org/10.1523/JNEUROSCI.2025-16.2016

Mareš, P., Haugvicová, R., & Kubová, H. (2002). Unequal development of thresholds for various phenomena induced by cortical stimulation in rats. *Epilepsy Research*, *49*(1), 35–43. https://doi.org/10.1016/S0920-1211(02)00009-8

Masamoto, K., Fukuda, M., Vazquez, A., & Kim, S. G. (2009). Dose-dependent effect of isoflurane on neurovascular coupling in rat cerebral cortex. *European Journal of Neuroscience, 30*, 242–250.

Masamoto, K., Kim, T., Fukuda, M., Wang, P., & Kim, S. G. (2007). Relationship between neural, vascular, and BOLD signals in isoflurane-anesthetized rat somatosensory cortex. *Cerebral Cortex*, *17*(4), 942–950. https://doi.org/10.1093/cercor/bhl005

Mason, K., Maurino-alperovich, F., Holder, D., & Aristovich, K. (2024). Noise-based correction for electrical impedance tomography. *Physiological Measurement*, *45*(6), 065002.

Matsuoka, Y., & Hossmann, K. A. (1982). Cortical impedance and extracellular volume changes following middle cerebral artery occlusion in cats. *Journal of Cerebral Blood Flow and Metabolism*, *2*(4), 466–474. https://doi.org/10.1038/jcbfm.1982.53

Matta, B. F., Heath, K. J., Tipping, K., & Summors, A. C. (1999). Direct cerebral vasodilatory effects of sevoflurane and isoflurane. *Anesthesiology*, *91*(3), 677–680. https://doi.org/10.1097/00000542-199909000-00019

Mayer, M. L. (2005). Glutamate receptor ion channels. *Current Opinion in Neurobiology*, *15*(3 SPEC. ISS.), 282–288. https://doi.org/10.1016/j.conb.2005.05.004

McBain, C. J., Traynelis, S. F., & Dingledine, R. (1990). Regional variation of extracellular space in the hippocampus. *Science*, *249*(4969), 674–677. https://doi.org/10.1126/science.2382142

McConnell, G. C., Rees, H. D., Levey, A. I., Gutekunst, C. A., Gross, R. E., & Bellamkonda, R. V. (2009). Implanted neural electrodes cause chronic, local inflammation that is correlated with local neurodegeneration. *Journal of Neural Engineering*, *6*(5). https://doi.org/10.1088/1741-2560/6/5/056003

McCormick, D. A., & Bal, T. (1997). Sleep and arousal: Thalamocortical mechanisms. *Annual Review of Neuroscience*, *20*(February 1997), 185–215. https://doi.org/10.1146/annurev.neuro.20.1.185

McCormick, D. A., & Contreras, D. (2001). On the cellular and network bases of epileptic seizures. *Annual Review of Physiology*, *63*(1), 815–846.

McCreery, D. B., Yuen, T. G. H., Agnew, W. F., & Bullara, L. A. (1992). Stimulation with chronically implanted microelectrodes in the cochlear nucleus of the cat: Histologic and physiologic effects. *Hearing Research*, *62*(1), 42–56. https://doi.org/10.1016/0378-5955(92)90201-W

McCreery, Douglas B., Agnew, W. F., Yuen, T. G. H., & Bullara, L. (1990). Charge density and charge per phase as cofactors in neural injury induced by electrical stimulation. *IEEE Transactions on Biomedical Engineering*, *37*(10), 996–1001. https://doi.org/10.1109/10.102812

McCreery, Douglas B., Yuen, T. G. H., Agnew, W. F., & Bullara, L. A. (1997). A characterization of the effects on neuronal excitability due to prolonged microstimulation with chronically implanted microelectrodes. *IEEE Transactions on Biomedical Engineering*, *44*(10), 931–939. https://doi.org/10.1109/10.634645

McEwan, A., Cusick, G., & Holder, D. S. (2007). A review of errors in multi-frequency EIT instrumentation. *Physiological Measurement*, *28*(7). https://doi.org/10.1088/0967-3334/28/7/S15

McEwan, A., Romsauerova, A., Yerworth, R., Horesh, L., Bayford, R., & Holder, D. (2006). Design and calibration of a compact multi-frequency EIT system for acute stroke imaging. *Physiological Measurement*, *27*(5). https://doi.org/10.1088/0967-3334/27/5/S17

Meeren, H. K. M., Pijn, J. P. M., Van Luijtelaar, E. L. J. M., Coenen, A. M. L., & Da Silva, F. H. L. (2002). Cortical focus drives widespread corticothalamic networks during spontaneous absence seizures in rats. *Journal of Neuroscience*, *22*(4), 1480–1495. https://doi.org/10.1523/jneurosci.22-04-01480.2002

Meeren, H. K. M., Veening, J. G., Möderscheim, T. A. E., Coenen, A. M. L., & van Luijtelaar, G. (2009). Thalamic lesions in a genetic rat model of absence epilepsy: Dissociation between spike-wave discharges and sleep spindles. *Experimental Neurology*, *217*(1), 25–37. https://doi.org/10.1016/j.expneurol.2009.01.009

Meeren, H., Van Luijtelaar, G., Lopes Da Silva, F., & Coenen, A. (2005). Evolving concepts on the pathophysiology of absence seizures: The cortical focus theory. *Archives of Neurology*, *62*(3), 371–376. https://doi.org/10.1001/archneur.62.3.371

Megill, K. C., Cummins, K. L., Dorfman, L. J., Berlizot, B. B., Luetkemeyer, K., Nishimura,

D. G., & Widrow, B. (1982). On the Nature and Elimination of Stimulus Artifact in Nerve Signals Evoked and Recorded Using Surface Electrodes. *IEEE Transactions on Biomedical Engineering*, *BME-29*(2), 129–137. https://doi.org/10.1109/TBME.1982.325019

Midzianovskaia, I. S., Kuznetsova, G. D., Coenen, A. M. L., Spiridonov, A. M., & Van Luijtelaar, E. L. J. M. (2001). Electrophysiological and pharmacological characteristics of two types of spike-wave discharges in WAG/Rij rats. *Brain Research*, *911*(1), 62–70. https://doi.org/10.1016/S0006-8993(01)02705-6

Miranda, P. C., Mekonnen, A., Salvador, R., & Ruffini, G. (2013). The electric field in the cortex during transcranial current stimulation. *NeuroImage*, *70*, 48–58. https://doi.org/10.1016/j.neuroimage.2012.12.034

Miyamoto, H., Tatsukawa, T., Shimohata, A., Yamagata, T., Suzuki, T., Amano, K., Mazaki, E., Raveau, M., Ogiwara, I., Oba-Asaka, A., Hensch, T. K., Itohara, S., Sakimura, K., Kobayashi, K., Kobayashi, K., & Yamakawa, K. (2019). Impaired cortico-striatal excitatory transmission triggers epilepsy. *Nature Communications*, *10*(1), 1–13. https://doi.org/10.1038/s41467-019-09954-9

Moeller, F., Siebner, H. R., Wolff, S., Muhle, H., Boor, R., Granert, O., Jansen, O., Stephani, U., & Siniatchkin, M. (2008). Changes in activity of striato-thalamo-cortical network precede generalized spike wave discharges. *NeuroImage*, *39*(4), 1839–1849. https://doi.org/10.1016/j.neuroimage.2007.10.058

Montes-Restrepo, V., Van Mierlo, P., Strobbe, G., Staelens, S., Vandenberghe, S., & Hallez, H. (2014). Influence of skull modeling approaches on EEG source localization. *Brain Topography*, *27*(1), 95–111. https://doi.org/10.1007/s10548-013-0313-y

Moshkforoush, A., Ashenagar, B., Harraz, O. F., Dabertrand, F., Longden, T. A., Nelson, M. T., & Tsoukias, N. M. (2020). The capillary Kir channel as sensor and amplifier of neuronal signals: Modeling insights on K+-mediated neurovascular communication. *Proceedings of the National Academy of Sciences of the United States of America*, *117*(28), 16626–16637. https://doi.org/10.1073/pnas.2000151117

Motamedi, G. K., Okunola, O., Kalhorn, C. G., Mostofi, N., Mizuno-Matsumoto, Y., Cho, Y. won, & Meador, K. J. (2007). Afterdischarges during cortical stimulation at different frequencies and intensities. *Epilepsy Research*, *77*(1), 65–69. https://doi.org/10.1016/j.eplepsyres.2007.08.001

Nasrallah, F. A., Lew, S. K., Low, A. S. M., & Chuang, K. H. (2014). Neural correlate of resting-state functional connectivity under α2 adrenergic receptor agonist, medetomidine. *NeuroImage*, *84*, 27–34. https://doi.org/10.1016/j.neuroimage.2013.08.004

Nathan, S. S., Sinha, S. R., Gordon, B., Lesser, R. P., & Thakor, N. V. (1993). Determination of current density distributions generated by electrical stimulation of the human cerebral cortex. *Electroencephalography and Clinical Neurophysiology*, *86*(3), 183–192. https://doi.org/10.1016/0013-4694(93)90006-H

National Instruments. (2014). NI 625 Specifications. In *National Instruments Product Guide*. https://docs-be.ni.com/

Neafsey, E. J., Chuman, C. M., & Ward, A. A. (1979). Propagation of focal cortical epileptiform discharge to the basal ganglia. *Experimental Neurology*, *66*(1), 97–108. https://doi.org/10.1016/0014-4886(79)90066-9

Neckelmann, D., Amzica, F., & Steriade, M. (2000). Changes in neuronal conductance during different components of cortically generated spike-wave seizures. *Neuroscience*, *96*(3), 475–485. https://doi.org/10.1016/S0306-4522(99)00571-0

Nelson, M. T., Cheng, H., Rubart, M., Santana, L. F., Bonev, A. D., Knot, H. J., & Lederer, W. J. (1995). Relaxation of arterial smooth muscle by calcium sparks. *Science*, *270*(5236), 633–637. https://doi.org/10.1126/science.270.5236.633

Nolan, M., Bergazar, M., Chu, B., Cortez, M. A., & Carter Snead, O. (2005). Clinical and neurophysiologic spectrum associated with atypical absence seizures in children with intractable epilepsy. *Journal of Child Neurology*, *20*(5), 404–410. https://doi.org/10.1177/08830738050200050201

Ogawa, S., Lee, T. M., Kay, A. R., & Tank, D. W. (1990). Brain magnetic resonance imaging with contrast dependent on blood oxygenation. *Proceedings of the National Academy of Sciences of the United States of America*, *87*(24), 9868–9872. https://doi.org/10.1073/pnas.87.24.9868

Ogawa, S., Tank, D. W., Menon, R., Ellermann, J. M., Kim, S. G., Merkle, H., & Ugurbil, K. (1992). Intrinsic signal changes accompanying sensory stimulation: Functional brain mapping with magnetic resonance imaging. *Proceedings of the National Academy of Sciences of the United States of America*, *89*(13), 5951–5955. https://doi.org/10.1073/pnas.89.13.5951

Ogawa, Seiji, Lee, T. -M, Nayak, A. S., & Glynn, P. (1990). Oxygenation-sensitive contrast in magnetic resonance image of rodent brain at high magnetic fields. In *Magnetic Resonance in Medicine* (Vol. 14, Issue 1, pp. 68–78). https://doi.org/10.1002/mrm.1910140108

Ogawa, Seiji, Lee, T. M., Stepnoski, R., Chen, W., Zhu, X. H., & Ugurbil, K. (2000). An approach to probe some neural systems interaction by functional MRI at neural time scale down to milliseconds. *Proceedings of the National Academy of Sciences of the United States of America*, *97*(20), 11026–11031. https://doi.org/10.1073/pnas.97.20.11026

Oh, T., Gilad, O., Ghosh, A., Schuettler, M., & Holder, D. S. (2011). A novel method for recording neuronal depolarization with recording at 125-825 Hz: Implications for imaging fast neural activity in the brain with electrical impedance tomography. *Medical and Biological Engineering and Computing*, *49*(5), 593–604. https://doi.org/10.1007/s11517-011-0761-z

Okada, Y. C., Lahteenmäki, A., & Xu, C. (1999). Experimental analysis of distortion of magnetoencephalography signals by the skull. *Clinical Neurophysiology*, *110*(2), 230–238. https://doi.org/10.1016/S0013-4694(98)00099-6

Oldendorf, W. H. (1977). The blood-brain barrier. *Experimental Eye Research*, *25*, 177–190. https://doi.org/10.1016/S0014-4835(77)80016-X

Olejniczak, P. (2006). Neurophysiologic basis of EEG. *Journal of Clinical Neurophysiology*, *23*(3), 186–189. https://doi.org/10.1097/01.wnp.0000220079.61973.6c

Olman, C. A., Inati, S., & Heeger, D. J. (2007). The effect of large veins on spatial localization with GE BOLD at 3 T: Displacement, not blurring. *NeuroImage*, *34*(3), 1126–1135. https://doi.org/10.1016/j.neuroimage.2006.08.045

Olsson, T., Broberg, M., Pope, K. J., Wallace, A., Mackenzie, L., Blomstrand, F., Nilsson, M., & Willoughby, J. O. (2006). Cell swelling, seizures and spreading depression: An impedance study. *Neuroscience*, *140*(2), 505–515. https://doi.org/10.1016/j.neuroscience.2006.02.034

Ono, K., Mori, K., Baba, H., & Wada, J. A. (1987). A role of the striatum in premotor cortical seizure development. *Brain Research*, *435*(1–2), 84–90. https://doi.org/10.1016/0006-8993(87)91589-7

Osol, G., Brekke, J. F., McElroy-Yaggy, K., & Gokina, N. I. (2002). Myogenic tone, reactivity, and forced dilatation: A three-phase model of in vitro arterial myogenic behavior. *American Journal of Physiology - Heart and Circulatory Physiology*, *283*(6 52-6), 2260–2267. https://doi.org/10.1152/ajpheart.00634.2002

Pan, W. J., Lee, S. Y., Billings, J., Nezafati, M., Majeed, W., Buckley, E., & Keilholz, S. (2018). Detection of neural light-scattering activity in vivo: optical transmittance studies in the rat brain. *NeuroImage*, *179*(May), 207–214. https://doi.org/10.1016/j.neuroimage.2018.06.039

Parkes, L. M., Schwarzbach, J. V., Bouts, A. A., Deckers, R. H. R., Pullens, P., Kerskens, C. M., & Norris, D. G. (2005). Quantifying the spatial resolution of the gradient echo and spin echo BOLD response at 3 Tesla. *Magnetic Resonance in Medicine*, *54*(6), 1465–1472. https://doi.org/10.1002/mrm.20712

Parvizi, J., & Kastner, S. (2017). Human Intracranial EEG: Promises and Limitations. *Physiology & Behavior*, *176*(5), 139–148. https://doi.org/10.1038/s41593-018-0108-2.Human

Paxinos, G., & Watson, C. (2013). *The Rat Brain in Stereotaxic Coordinates* (7th Editio). Academic Press.

Paz, J. T., Deniau, J. M., & Charpier, S. (2005). Rhythmic bursting in the cortico-subthalamo-pallidal network during spontaneous genetically determined spike and wave discharges. *Journal of Neuroscience*, *25*(8), 2092–2101. https://doi.org/10.1523/JNEUROSCI.4689-04.2005

Pechstein, U., Nadstawek, J., Zentner, J., & Schramm, J. (1998). Isoflurane plus nitrous oxide versus propofol for recording of motor evoked potentials after high frequency repetitive electrical stimulation. *Electroencephalography and Clinical Neurophysiology*, *108*(2), 175–181. https://doi.org/10.1016/s0168-5597(97)00086-5

Perucca, P., Dubeau, F., & Gotman, J. (2014). Intracranial electroencephalographic seizure-onset patterns: Effect of underlying pathology. *Brain*, *137*(1), 183–196. https://doi.org/10.1093/brain/awt299

Petrik, S., San Antonio-Arce, V., Steinhoff, B. J., Syrbe, S., Bast, T., Scheiwe, C., Brandt, A., Beck, J., & Schulze-Bonhage, A. (2021). Epilepsy surgery: Late seizure recurrence after initial complete seizure freedom. *Epilepsia*, *62*(5), 1092–1104. https://doi.org/10.1111/epi.16893

Petrova, G. I. (1999). Influence of electrode impedance changes on the common-mode rejection ratio in bioimpedance measurements. *Physiological Measurement*, *20*(4). https://doi.org/10.1088/0967-3334/20/4/401

Pfeuffer, J., McCullough, J. C., Van De Moortele, P. F., Ugurbil, K., & Hu, X. (2003). Spatial dependence of the nonlinear BOLD response at short stimulus duration. *NeuroImage*, *18*(4), 990–1000. https://doi.org/10.1016/S1053-8119(03)00035-1

Pfeuffer, J., Van De Moortele, P. F., Yacoub, E., Shmuel, A., Adriany, G., Andersen, P., Merkle, H., Garwood, M., Ugurbil, K., & Hu, X. (2002). Zoomed functional imaging in the human brain at 7 tesla with simultaneous high spatial and high temporal resolution. *NeuroImage*, *17*(1), 272–286. https://doi.org/10.1006/nimg.2002.1103

Piastra, M. C., Nüßing, A., Vorwerk, J., Clerc, M., Engwer, C., & Wolters, C. H. (2021). A comprehensive study on electroencephalography and magnetoencephalography sensitivity to cortical and subcortical sources. *Human Brain Mapping*, *42*(4), 978–992. https://doi.org/10.1002/hbm.25272

Pisani, A., Calabresi, P., & Bernardi, G. (1997). Hypoxia in striatal and cortical neurones: Membrane potential and Ca2+ measurements. *NeuroReport*, *8*(5), 1143–1147. https://doi.org/10.1097/00001756-199703240-00017

Pizzo, F., Roehri, N., Giusiano, B., Lagarde, S., Carron, R., Scavarda, D., McGonigal, A., Filipescu, C., Lambert, I., Bonini, F., Trebuchon, A., Bénar, C. G., & Bartolomei, F. (2021). The Ictal Signature of Thalamus and Basal Ganglia in Focal Epilepsy: A SEEG Study. *Neurology*, *96*(2), e280–e293. https://doi.org/10.1212/WNL.0000000000011003

Poggio, G. F., Earl Walker, A., & Andy, O. J. (1956). The Propagation of Cortical After-Discharge Through Subcortical Structure. *AMA Archives of Neurology & Psychiatry*, *75*(4), 350–361.

Pohl, U., & de Wit, C. (1999). A unique role of NO in the control of blood flow. *Physiology*, *14*(2), 74–80.

Popescu, D. P., Choo-Smith, L. P. in., Flueraru, C., Mao, Y., Chang, S., Disano, J., Sherif, S., & Sowa, M. G. (2011). Optical coherence tomography: Fundamental principles, instrumental designs and biomedical applications. *Biophysical Reviews*, *3*(3), 155–169. https://doi.org/10.1007/s12551-011-0054-7

Porkkala, T., Janit, V., Kaukinen, S., & Hakkinen, V. (1997). Nitrous oxide has different effects on the EEG and somatosensory evoked potentials during isoflurane anaesthesia in patients. *Acta Anaesthesiologica Scandinavica*, *41*(4), 497–501.

Porkkala, T., Jantti, V., Kaukinen, S., & Hakkinen, V. (1994). Somatosensory evoked potentials during isoflurane anaesthesia. *Acta Anaesthesiologica Scandinavica*, *38*(3), 206–210. https://doi.org/10.1111/j.1399-6576.1994.tb03874.x

Poulsen, P. H., Smith, D. F., Østergaard, L., Danielsen, E. H., Gee, A., Hansen, S. B., Astrup, J., & Gjedde, A. (1997). In vivo estimation of cerebral blood flow, oxygen consumption and glucose metabolism in the pig by [15O]water injection, [15O]oxygen inhalation and dual injections of [18F]fluorodeoxyglucose. *Journal of Neuroscience Methods*, *77*(2), 199–209. https://doi.org/10.1016/S0165-0270(97)00127-1

Proix, T., Truccolo, W., Leguia, M. G., Tcheng, T. K., King-Stephens, D., Rao, V. R., & Baud, M. O. (2021). Forecasting seizure risk in adults with focal epilepsy: a development and validation study. *The Lancet Neurology*, *20*(2), 127–135. https://doi.org/10.1016/S1474-4422(20)30396-3

Quiroga, R. Q., Nadasdy, Z., & Ben-Shaul, Y. (2004). Unsupervised spike detection and sorting with wavelets and superparamagnetic clustering. *Neural Computation*, *16*(8), 1661–1687. https://doi.org/10.1162/089976604774201631

Raichle, M. E. (1983). Positron EmissionTomography. *Annual Review Neuroscience*, *6*(67), 249–267.

Raimondo, J. V., Burman, R. J., Katz, A. A., & Akerman, C. J. (2015). Ion dynamics during seizures. *Frontiers in Cellular Neuroscience*, *9*(OCTOBER), 1–14. https://doi.org/10.3389/fncel.2015.00419

Rajkumar, R., Farrher, E., Mauler, J., Sripad, P., Régio Brambilla, C., Rota Kops, E., Scheins, J., Dammers, J., Lerche, C., Langen, K. J., Herzog, H., Biswal, B., Shah, N. J., & Neuner, I. (2021). Comparison of EEG microstates with resting state fMRI and FDG-PET measures in the default mode network via simultaneously recorded trimodal (PET/MR/EEG) data. *Human Brain Mapping*, *42*(13), 4122–4133. https://doi.org/10.1002/hbm.24429

Ralay Ranaivo, H., & Wainwright, M. S. (2010). Albumin activates astrocytes and microglia through mitogen-activated protein kinase pathways. *Brain Research*, *1313*(51), 222–231. https://doi.org/10.1016/j.brainres.2009.11.063

Ramakrishnan, S., Asuncion, R. M. D., & Rayi, A. (2024). Localization-Related Epilepsies on EEG. *StatPearls*, 1–17. http://www.ncbi.nlm.nih.gov/pubmed/28276062%0Ahttp://www.pubmedcentral.nih.go v/articlerender.fcgi?artid=PMC5386840

Rao, A. (2000). *Electrical Impedance Tomography of Brain Activity: Studies into its accuracy and physiological mechanisms*. 1–228.

Rattay, F. (1999). The basic mechanism for the electrical stimulation of the nervous system. *Neuroscience*, *89*(2), 335–346. https://doi.org/10.1016/S0306-4522(98)00330-3

Rattay, Frank. (1998). Analysis of the electrical excitation of CNS neurons. *IEEE Transactions on Biomedical Engineering*, *45*(6), 766–772. https://doi.org/10.1109/10.678611

Ravagli, E., Mastitskaya, S., Holder, D., & Aristovich, K. (2022). Simplifying the hardware requirements for fast neural EIT of peripheral nerves. *Physiological Measurement*, *43*(1). https://doi.org/10.1088/1361-6579/ac43c0

Rector, D. M., Rogers, R. F., Schwaber, J. S., Harper, R. M., & George, J. S. (2001). Scattered-light imaging in vivo tracks fast and slow processes of neurophysiological activation. *NeuroImage*, *14*(5), 977–994. https://doi.org/10.1006/nimg.2001.0897

Rojas, M. J., Navas, J. A., & Rector, D. M. (2006). Evoked response potential markers for anesthetic and behavioral states. *American Journal of Physiology - Regulatory Integrative and Comparative Physiology*, *291*(1), 189–196. https://doi.org/10.1152/ajpregu.00409.2005

Rosidi, N. L., Zhou, J., Pattanaik, S., Wang, P., Jin, W., Brophy, M., Olbricht, W. L., Nishimura, N., & Schaffer, C. B. (2011). Cortical microhemorrhages cause local inflammation but do not trigger widespread dendrite degeneration. *PLoS ONE*, *6*(10). https://doi.org/10.1371/journal.pone.0026612

Ryvlin, P., & Rheims, S. (2008). Epilepsy surgery: Eligibility criteria and presurgical evaluation. *Dialogues in Clinical Neuroscience*, *10*(1), 91–103. https://doi.org/10.31887/dcns.2008.10.1/pryvlin

Sacino, M. F., Huang, S. S., Schreiber, J., Gaillard, W. D., & Oluigbo, C. O. (2019). Is the use of Stereotactic Electroencephalography Safe and Effective in Children? A Meta-Analysis of the use of Stereotactic Electroencephalography in Comparison to Subdural Grids for Invasive Epilepsy Monitoring in Pediatric Subjects. *Clinical Neurosurgery*, *84*(6), 1190–1200. https://doi.org/10.1093/neuros/nyy466

Sakatani, K., Iizuka, H., & Young, W. (1990). Somatosensory evoked potentials in rat cerebral cortex before and after middle cerebral artery occlusion. *Stroke*, *21*(1), 124–132. https://doi.org/10.1161/01.STR.21.1.124

Sakurai, K., Takeda, Y., Tanaka, N., Kurita, T., Shiraishi, H., Takeuchi, F., Nakane, S., Sueda, K., & Koyama, T. (2010). Generalized spike-wave discharges involve a default mode network in patients with juvenile absence epilepsy: A MEG study. *Epilepsy Research*, *89*(2–3), 176–184. https://doi.org/10.1016/j.eplepsyres.2009.12.004

Salvador, R., Mekonnen, A., Ruffini, G., & Miranda, P. C. (2010). Modeling the electric field induced in a high resolution realistic head model during transcranial current stimulation. *2010 Annual International Conference of the IEEE Engineering in Medicine and Biology Society, EMBC’10*, 2073–2076. https://doi.org/10.1109/IEMBS.2010.5626315

Sancho, M., Klug, N. R., Mughal, A., Koide, M., de la Cruz, S. H., Heppner, T. J., Bonev, A. D., Hill-Eubanks, D., & Nelson, M. T. (2022). Adenosine signaling activates ATP-sensitive K+ channels in endothelial cells and pericytes in CNS capillaries. *Science Signaling*, *15*(727). https://doi.org/10.1126/scisignal.abl5405

Sarmast, S. T., Abdullahi, A. M., & Jahan, N. (2020). Current Classification of Seizures and Epilepsies: Scope, Limitations and Recommendations for Future Action. *Cureus*, *12*(9).

https://doi.org/10.7759/cureus.10549

Satzer, D., Esengul, Y. T., Warnke, P. C., Issa, N. P., & Nordli, D. R. (2022). SEEG in 3D: Interictal Source Localization From Intracerebral Recordings. *Frontiers in Neurology*, *13*(February), 1–11. https://doi.org/10.3389/fneur.2022.782880

Schander, A., Tesmann, T., Strokov, S., Stemmann, H., Kreiter, A. K., & Lang, W. (2016). In-vitro evaluation of the long-term stability of PEDOT:PSS coated microelectrodes for chronic recording and electrical stimulation of neurons. *Proceedings of the Annual International Conference of the IEEE Engineering in Medicine and Biology Society, EMBS*, *2016-Octob*, 6174–6177. https://doi.org/10.1109/EMBC.2016.7592138

Schindelin, J., Arganda-Carreras, I., Frise, E., Kaynig, V., Longair, M., Pietzsch, T., Preibisch, S., Rueden, C., Saalfeld, S., Schmid, B., Tinevez, J. Y., White, D. J., Hartenstein, V., Eliceiri, K., Tomancak, P., & Cardona, A. (2012). Fiji: An open-source platform for biological-image analysis. *Nature Methods*, *9*(7), 676–682. https://doi.org/10.1038/nmeth.2019

Schmidt, R. F., Wu, C., Lang, M. J., Soni, P., Williams, K. A., Boorman, D. W., Evans, J. J., Sperling, M. R., & Sharan, A. D. (2016). Complications of subdural and depth electrodes in 269 patients undergoing 317 procedures for invasive monitoring in epilepsy. *Epilepsia*, *57*(10), 1697–1708. https://doi.org/10.1111/epi.13503

Schofield, R., King, L., Tayal, U., Castellano, I., Stirrup, J., Pontana, F., Earls, J., & Nicol, E. (2020). Image reconstruction: Part 1 – understanding filtered back projection, noise and image acquisition. *Journal of Cardiovascular Computed Tomography*, *14*(3), 219–225. https://doi.org/10.1016/j.jcct.2019.04.008

Scott, B. B., Thiberge, S. Y., Guo, C., Tervo, D. G. R., Brody, C. D., Karpova, A. Y., & Tank, D. W. (2018). Imaging Cortical Dynamics in GCaMP Transgenic Rats with a Head-Mounted Widefield Macroscope. *Neuron*, *100*(5), 1045-1058.e5. https://doi.org/10.1016/j.neuron.2018.09.050

Scott, R. N., McLean, L., & Parker, P. A. (1997). Stimulus artefact in somatosensory evoked potential measurement. *Medical and Biological Engineering and Computing*, *35*(3), 211–215. https://doi.org/10.1007/BF02530040

Sears, S. M. S., & Hewett, S. J. (2021). Influence of glutamate and GABA transport on brain excitatory/inhibitory balance. *Experimental Biology and Medicine*, *246*(9), 1069–1083. https://doi.org/10.1177/1535370221989263

Senarathna, J., Rege, A., Li, N., & Thakor, N. V. (2013). Laser speckle contrast imaging: Theory, instrumentation and applications. *IEEE Reviews in Biomedical Engineering*, *6*, 99–110. https://doi.org/10.1109/RBME.2013.2243140

Shannon, R. V. (1992). A Model of Safe Levels for Electrical Stimulation. *IEEE Transactions on Biomedical Engineering*, *39*(4), 424–426. http://scioteca.caf.com/bitstream/handle/123456789/1091/RED2017-Eng-8ene.pdf?sequence=12&isAllowed=y%0Ahttp://dx.doi.org/10.1016/j.regsciurbeco.2008.06.005%0Ahttps://www.researchgate.net/publication/305320484_SISTEM_PEMBETUNGAN_TERPUSAT_STRATEGI_MELESTARI

Sharafkhani, N., Kouzani, A. Z., Adams, S. D., Long, J. M., Lissorgues, G., Rousseau, L., & Orwa, J. O. (2022). Neural tissue-microelectrode interaction: Brain micromotion, electrical impedance, and flexible microelectrode insertion. *Journal of Neuroscience Methods*, *365*(October 2021). https://doi.org/10.1016/j.jneumeth.2021.109388

Sharon, D., Hämäläinen, M. S., Tootell, R. B. H., Halgren, E., & Belliveau, J. W. (2007). The advantage of combining MEG and EEG: Comparison to fMRI in focally stimulated visual cortex. *NeuroImage*, *36*(4), 1225–1235. https://doi.org/10.1016/j.neuroimage.2007.03.066

Shigeto, H., Boongird, A., Baker, K., Kellinghaus, C., Najm, I., & Lüders, H. (2013). Systematic study of the effects of stimulus parameters and stimulus location on afterdischarges elicited by electrical stimulation in the rat. *Epilepsy Research*, *104*(1–2), 17–25. https://doi.org/10.1016/j.eplepsyres.2012.10.002

Shimizu, T., Aihara, M., Yamaguchi, R., Sato, K., Aishima, K., & Yoshimoto, Y. (2020). Large Craniotomy Increases the Risk of Minor Perioperative Complications in Revascularization Surgery for Moyamoya Disease. *World Neurosurgery*, *141*, e498–e507. https://doi.org/10.1016/j.wneu.2020.05.227

Shukla, A. K., & Kumar, U. (2006). Positron emission tomography in medicine: An overview. *Cancer Imaging*, *31*(1), 39–44. https://doi.org/10.1016/B978-012374212-4.50009-2

Sicard, K., Shen, Q., Brevard, M. E., Sullivan, R., Ferris, C. F., King, J. A., & Duong, T. Q. (2003). Regional cerebral blood flow and BOLD responses in conscious and anesthetized rats under basal and hypercapnic conditions: Implications for functional MRI studies. *Journal of Cerebral Blood Flow and Metabolism*, *23*(4), 472–481. https://doi.org/10.1097/01.WCB.0000054755.93668.20

Siegel, A. M., Culver, J. P., Mandeville, J. B., & Boas, D. A. (2003). Temporal comparison of functional brain imaging with diffuse optical tomography and fMRI during rat forepaw stimulation. *Physics in Medicine and Biology*, *48*(10), 1391–1403. https://doi.org/10.1088/0031-9155/48/10/311

Silva, A. C., & Koretsky, A. P. (2002). Laminar specificity of functional MRI onset times during somatosensory stimulation in rat. *Proceedings of the National Academy of Sciences of the United States of America*, *99*(23), 15182–15187. https://doi.org/10.1073/pnas.222561899

Silva, A. C., Koretsky, A. P., & Duyn, J. H. (2007). Functional MRI impulse response for BOLD and CBV contrast in rat somatosensory cortex. *Magnetic Resonance in Medicine*, *57*(6), 1110–1118. https://doi.org/10.1002/mrm.21246

Silva, A. C., Lee, S. P., Iadecola, C., & Kim, S. G. (2000). Early temporal characteristics of cerebral blood flow and deoxyhemoglobin changes during somatosensory stimulation. *Journal of Cerebral Blood Flow and Metabolism*, *20*(1), 201–206. https://doi.org/10.1097/00004647-200001000-00025

Simfukwe, K., Iakimov, I., Sufianov, R., Borba, L., Mastronardi, L., & Shumadalova, A. (2022). Application of Intraoperative Ultrasound Navigation in Neurosurgery. *Frontiers in Surgery*, *9*(May), 1–11. https://doi.org/10.3389/fsurg.2022.900986

Singh, S. P. (2014). Magnetoencephalography: Basic principles. *Annals of Indian Academy of Neurology*, *17*(SUPPL. 1). https://doi.org/10.4103/0972-2327.128676

Sitnikova, E., & Van Luijtelaar, G. (2007). Electroencephalographic characterization of spike-wave discharges in cortex and thalamus in WAG/Rij rats. *Epilepsia*, *48*(12), 2296–2311. https://doi.org/10.1111/j.1528-1167.2007.01250.x

Slaght, S. J., Paz, T., Chavez, M., Deniau, J. M., Mahon, S., & Charpier, S. (2004). On the activity of the corticostriatal networks during spike-and-wave discharges in a genetic model of absence epilepsy. *Journal of Neuroscience*, *24*(30), 6816–6825. https://doi.org/10.1523/JNEUROSCI.1449-04.2004

Sokoloff, L., Reivich, M., Kennedy, C., Rosiers, M. H. D., Patlak, C. S., Pettigrew, K. D., Sakurada, O., & Shinohara, M. (1977). the [14C]Deoxyglucose Method for the Measurement of Local Cerebral Glucose Utilization: Theory, Procedure, and Normal Values in the Conscious and Anesthetized Albino Rat. *Journal of Neurochemistry*, *28*(5), 897–916. https://doi.org/10.1111/j.1471-4159.1977.tb10649.x

Somjen, G. G. (1973). Electrogenesis of sustained potentials. *Progress in Neurobiology*, *1*(PART 3). https://doi.org/10.1016/0301-0082(73)90012-9

Somjen, G. G. (2001). Mechanisms of spreading depression and hypoxic spreading depression-like depolarization. *Physiological Reviews*, *81*(3), 1065–1096. https://doi.org/10.1152/physrev.2001.81.3.1065

Sommers, M. G., van Egmond, J., Booij, L. H. D. J., & Heerschap, A. (2009). Isoflurane anesthesia is a valuable alternative for α-chloralose anesthesia in the forepaw stimulation model in rats. *NMR in Biomedicine*, *22*(4), 414–418. https://doi.org/10.1002/nbm.1351

Spencer, S. S. (1994). The Relative Contributions of MRI, SPECT, and PET Imaging in Epilepsy. *Epilepsia*, *35*, S72–S89. https://doi.org/10.1111/j.1528-1157.1994.tb05990.x

Srinivasan, V. J., Sakadžić, S., Gorczynska, I., Ruvinskaya, S., Wu, W., Fujimoto, J. G., & Boas, D. A. (2010). Quantitative cerebral blood flow with Optical Coherence Tomography. *Optics Express*, *18*(3), 2477. https://doi.org/10.1364/oe.18.002477

Stankiewicz, J., Stankiewicz, M., Wiaderna-Stepien, D., Tomas, T., & Gralewicz, S. (1995). Effects of repeated systemic penicillin injections on nonconvulsive and convulsive epileptic seizures in the rat. *Acta Neurobiologiae Experimentalis*, *55*(4), 281–287. https://doi.org/10.55782/ane-1995-1087

Steinmetz, N. A., Aydin, C., Lebedeva, A., Okun, M., Pachitariu, M., Bauza, M., Beau, M., Bhagat, J., Böhm, C., Broux, M., Chen, S., Colonell, J., Gardner, R. J., Karsh, B., Kloosterman, F., Kostadinov, D., Mora-Lopez, C., O'Callaghan, J., Park, J., … Harris, T. D. (2021). Neuropixels 2.0: A miniaturized high-density probe for stable, long-term brain recordings. *Science*, *372*(6539). https://doi.org/10.1126/science.abf4588

Stence, N., Waite, M., & Dailey, M. E. (2001). Dynamics of microglial activation: A confocal time-lapse analysis in hippocampal slices. *Glia*, *33*, 256–266. https://onlinelibrary.wiley.com/doi/10.1002/1098-1136(200103)33:3%3C256::AID-GLIA1024%3E3.0.CO;2-J

Steriade, M., & Contreras, D. (1998). Spike-wave complexes and fast components of cortically generated seizures. I. Role of neocortex and thalamus. *Journal of Neurophysiology*, *80*(3), 1439–1455. https://doi.org/10.1152/jn.1998.80.3.1439

Stern, Y., Neufeld, M. Y., Kipervasser, S., Zilberstein, A., Fried, I., Teicher, M., & Adi-Japha, E. (2009). Source localization of temporal lobe epilepsy using PCA - LORETA analysis on ictal EEG recordings. *Journal of Clinical Neurophysiology*, *26*(2), 109–116. https://doi.org/10.1097/WNP.0b013e31819b3bf2

Sutherland, B. A., Rabie, T., & Buchan, A. M. (2014). Laser doppler flowmetry to measure changes in cerebral blood flow. In R. Milner (Ed.), *Cerebfal Angiogenesis* (Vol. 1135, pp. 237–248). Humana Press. https://doi.org/10.1007/978-1-4939-320-7_20

Swartz, B. E., Halgren, E., Fuster, J., & Mandelkern, M. (1994). An18FDG-PET study of cortical activation during a short-term visual memory task in humans. *NeuroReport*, *5*(8), 925–928. https://doi.org/10.1097/00001756-199404000-00018

Szarowski, D. H., Andersen, M. D., Retterer, S., Spence, A. J., Isaacson, M., Craighead, H. G., Turner, J. N., & Shain, W. (2003). Brain responses to micro-machined silicon devices. *Brain Research*, *983*(1–2), 23–35. https://doi.org/10.1016/S0006-8993(03)03023-3

Tantawi, M., Miao, J., Matias, C., Skidmore, C. T., Sperling, M. R., Sharan, A. D., & Wu, C. (2021). Gray Matter Sampling Differences Between Subdural Electrodes and Stereoelectroencephalography Electrodes. *Frontiers in Neurology*, *12*(April), 1–9. https://doi.org/10.3389/fneur.2021.669406

Tasaki, I., & Byrne, P. M. (1992). Rapid Structural Changes in Nerve Fibers. *Biochemical and Biophysical Research Communications*, *188*(2), 559–564.

Tatum, W. O., Dworetzky, B. A., & Schomer, D. L. (2011). Artifact and recording concepts in EEG. *Journal of Clinical Neurophysiology*, *28*(3), 252–263. https://doi.org/10.1097/WNP.0b013e31821c3c93

Téllez-Zenteno, J. F., Dhar, R., & Wiebe, S. (2005). Long-term seizure outcomes following epilepsy surgery: A systematic review and meta-analysis. *Brain*, *128*(5), 1188–1198. https://doi.org/10.1093/brain/awh449

Ter-Pogossian, M. M., Phelps, M. E., & Hoffman andMullani, E. J. N. A. (1975). A positron emission transaxial tomograph for nuclear imaging (PETT). *Radiology*, *114*(1), 89–98. https://doi.org/10.1148/114.1.89

Theodore, W. H., Newmark, M. E., Sato, S., Brooks, R., Patronas, N., de la Paz, R., Dichiro, G., Kessler, R. M., Margolin, R., Manning, R. G., Channing, M., & Porter, R. J. (1983). {18F}fluorodeoxyglucose positron emission tomography in refractory complex partial seizures. *Annals of Neurology*, *14*(4), 429–437. https://doi.org/10.1002/ana.410140406

Thompson, N., Ravagli, E., Mastitskaya, S., Challita, R., Hadaya, J., Iacoviello, F., Idil, A. S., Shearing, P. R., Ajijola, O. A., Ardell, J. L., Shivkumar, K., Holder, D., & Aristovich, K. (2024). Towards spatially selective efferent neuromodulation: anatomical and functional organization of cardiac fibres in the porcine cervical vagus nerve. *Journal of Physiology*, *7*, 1983–2004. https://doi.org/10.1113/JP286494

Tidswell, T., Gibson, A., Bayford, R. H., & Holder, D. S. (2001). Three-dimensional electrical impedance tomography of human brain activity. *NeuroImage*, *13*(2), 283–294. https://doi.org/10.1006/nimg.2000.0698

Tikhonov, A. N., Goncharsky, A., Stepanov, V. V., & A., Y. (1995). *Numerical Methods for the Solution of Ill-Posed Problems*. Springer.

Timofeev, I., Grenier, F., & Steriade, M. (2002). The role of chloride-dependent inhibition and the activity of fast-spiking neurons during cortical spike-wave electrographic seizures. *Neuroscience*, *114*(4), 1115–1132. https://doi.org/10.1016/S0306-4522(02)00300-7

Timofeev, I., & Steriade, M. (2004). Neocortical seizures: Initiation, development and cessation. *Neuroscience*, *123*(2), 299–336. https://doi.org/10.1016/j.neuroscience.2003.08.051

Tsurugizawa, T., Ciobanu, L., & Le Bihan, D. (2013). Water diffusion in brain cortex closely tracks underlying neuronal activity. *Proceedings of the National Academy of Sciences of the United States of America*, *110*(28), 11636–11641. https://doi.org/10.1073/pnas.1303178110

Tsurugizawa, T., Takahashi, Y., & Kato, F. (2016). Distinct effects of isoflurane on basal BOLD signals in tissue/vascular microstructures in rats. *Scientific Reports*, *6*, 1–7. https://doi.org/10.1038/srep38977

Turner, J. N., Shain, W., Szarowski, D. H., Andersen, M., Martins, S., Isaacson, M., & Craighead, H. (1999). Cerebral astrocyte response to micromachined silicon implants. *Experimental Neurology*, *156*(1), 33–49. https://doi.org/10.1006/exnr.1998.6983

Ullah, G., Wei, Y., Dahlem, M. A., Wechselberger, M., & Schiff, S. J. (2015). The Role of Cell Volume in the Dynamics of Seizure, Spreading Depression, and Anoxic Depolarization. *PLoS Computational Biology*, *11*(8), 1–25. https://doi.org/10.1371/journal.pcbi.1004414

Uludag, K., & Ugurbil, K. (2015). Physiology and physics of the fMRI signal. In K. Uludag, K. Ugurbil, & L. Berliner (Eds.), *fMRI: From Nuclear Spins to Brain Functions* (pp.

163–213). Springer US. https://doi.org/10.1007/978-1-4899-7591-1_8

Urban, A., Dussaux, C., Martel, G., Brunner, C., Mace, E., & Montaldo, G. (2015). Real-time imaging of brain activity in freely moving rats using functional ultrasound. *Nature Methods*, *12*(9), 873–878. https://doi.org/10.1038/nmeth.3482

Valenti, P., Cazamajou, E., Scarpettini, M., Aizemberg, A., Silva, W., & Kochen, S. (2006). Automatic detection of interictal spikes using data mining models. *Journal of Neuroscience Methods*, *150*(1), 105–110. https://doi.org/10.1016/j.jneumeth.2005.06.005

Van Harreveld, A., & Schadé, J. P. (1962). Changes in the electrical conductivity of cerebral cortex during seizure activity. *Experimental Neurology*, *5*(5), 383–400. https://doi.org/10.1016/0014-4886(62)90051-1

van Luijtelaar, E. L. J. M., & Coenen, A. M. L. (1986). Two types of electrocortical paroxysms in an inbred strain of rats. *Neuroscience Letters*, *70*(3), 393–397. https://doi.org/10.1016/0304-3940(86)90586-0

Vergnes, M., Marescaux, C., Depaulis, A., Micheletti, G., & Warter, J. M. (1987). Spontaneous spike and wave discharges in thalamus and cortex in a rat model of genetic petit mal-like seizures. *Experimental Neurology*, *96*(1), 127–136. https://doi.org/10.1016/0014-4886(87)90174-9

Villien, M., Wey, H. Y., Mandeville, J. B., Catana, C., Polimeni, J. R., Sander, C. Y., Zürcher, N. R., Chonde, D. B., Fowler, J. S., Rosen, B. R., & Hooker, J. M. (2014). Dynamic functional imaging of brain glucose utilization using fPET-FDG. *NeuroImage*, *100*, 192–199. https://doi.org/10.1016/j.neuroimage.2014.06.025

Vlassenko, A. G., Rundle, M. M., & Mintun, M. A. (2006). Human brain glucose metabolism may evolve during activation: Findings from a modified FDG PET paradigm. *NeuroImage*, *33*(4), 1036–1041. https://doi.org/10.1016/j.neuroimage.2006.06.065

von Ellenrieder, N., Beltrachini, L., & Muravchik, C. H. (2012). Electrode and brain modeling in stereo-EEG. *Clinical Neurophysiology*, *123*(9), 1745–1754. https://doi.org/10.1016/j.clinph.2012.01.019

Vongerichten, A. (2015). *Imaging Physiological and Pathological Activity in the Brain using Electric Impedance Tomography*. *November*, 213.

Vongerichten, A., Aristovich, K., Dos Santos, G. S., McEvoy, A. W., & Holder, D. S. (2014). Design for a three-dimensional printed laryngoscope blade for the intubation of rats. *Lab Animal*, *43*(4), 140–142. https://doi.org/10.1038/laban.463

Vongerichten, A. N., Santos, G. S. dos, Aristovich, K., Avery, J., McEvoy, A., Walker, M., & Holder, D. S. (2016). Characterisation and imaging of cortical impedance changes during interictal and ictal activity in the anaesthetised rat. *NeuroImage*, *124*, 813–823. https://doi.org/10.1016/j.neuroimage.2015.09.015

Vorwerk, J., Cho, J. H., Rampp, S., Hamer, H., Knösche, T. R., & Wolters, C. H. (2014). A guideline for head volume conductor modeling in EEG and MEG. *NeuroImage*, *100*, 590–607. https://doi.org/10.1016/j.neuroimage.2014.06.040

Vuong, J., & Devergnas, A. (2018). The role of the basal ganglia in the control of seizure. *Journal of Neural Transmission*, *125*(3), 531–545. https://doi.org/10.1007/s00702-017-1768-x

Wang, C., Yang, Y., Ding, Z., Meng, J., Wang, K., Yang, W., & Xu, Y. (2011). Monitoring of drug and stimulation induced cerebral blood flow velocity changes in rat sensory cortex using spectral domain Doppler optical coherence tomography. *Journal of Biomedical Optics*, *16*(4), 046001. https://doi.org/10.1117/1.3560286

Wang, X., Luo, Y., Chen, Y., Chen, C., Yin, L., Yu, T., He, W., & Ma, C. (2021). A Skull-Removed Chronic Cranial Window for Ultrasound and Photoacoustic Imaging of the Rodent Brain. *Frontiers in Neuroscience*, *15*(May), 1–11. https://doi.org/10.3389/fnins.2021.673740

Wang, Y., Liu, B., Fu, L., & Cui, Z. (2015). Use of interictal 18F-fluorodeoxyglucose (FDG)-PET and magnetoencephalography (MEG) to localize epileptogenic foci in non-lesional epilepsy in a cohort of 16 patients. *Journal of the Neurological Sciences*, *355*(1–2), 120–124. https://doi.org/10.1016/j.jns.2015.05.039

Watanabe, E., Maki, A., Kawaguchi, F., Yamashita, Y., Koizumi, H., & Mayanagi, Y. (2000). Noninvasive cerebral blood volume measurement during seizures using multichannel near infrared spectroscopic topography. *Journal of Biomedical Optics*, *5*(3), 287–290. https://doi.org/10.1016/S0896-6974(98)00037-1

Waters, R. S., Li, C. X., & McCandlish, C. A. (1995). Relationship between the organization of the forepaw barrel subfield and the representation of the forepaw in layer IV of rat somatosensory cortex. *Experimental Brain Research*, *103*(2), 183–197. https://doi.org/10.1097/00001756-199610020-00009

Weber, B. (2015). Neurovascular coupling. *FMRI: From Nuclear Spins to Brain Functions*, 67–104. https://doi.org/10.1007/978-1-4899-7591-1_5

Wei, H. S., Kang, H., Rasheed, I. Y. D., Zhou, S., Lou, N., Gershteyn, A., McConnell, E. D., Wang, Y., Richardson, K. E., Palmer, A. F., Xu, C., Wan, J., & Nedergaard, M. (2016). Erythrocytes Are Oxygen-Sensing Regulators of the Cerebral Microcirculation. *Neuron*, *91*(4), 851–862. https://doi.org/10.1016/j.neuron.2016.07.016

Wei, H., Xie, L., Dibb, R., Li, W., Decker, K., Zhang, Y., Johnson, G. A., & Liu, C. (2016). Imaging whole-brain cytoarchitecture of mouse with MRI-based quantitative susceptibility mapping. *NeuroImage*, *137*, 107–115. https://doi.org/10.1016/j.neuroimage.2016.05.033

Wei, Y., Wang, G., & Hsieh, J. (2005). Relation between the filtered backprojection algorithm and the backprojection algorithm in CT. *IEEE Signal Processing Letters*, *12*(9), 633–636. https://doi.org/10.1109/LSP.2005.851615

Weise, K., Wartman, W. A., Knösche, T. R., Nummenmaa, A. R., & Makarov, S. N. (2022). The effect of meninges on the electric fields in TES and TMS. Numerical modeling with adaptive mesh refinement. *Brain Stimulation*, *15*(3), 654–663. https://doi.org/10.1016/j.brs.2022.04.009

Welkenhuysen, M., Andrei, A., Ameye, L., Eberle, W., & Nuttin, B. (2011). Effect of insertion speed on tissue response and insertion mechanics of a chronically implanted silicon-based neural probe. *IEEE Transactions on Biomedical Engineering*, *58*(11), 3250–3259. https://doi.org/10.1109/TBME.2011.2166963

Wellmer, J., Von Der Groeben, F., Klarmann, U., Weber, C., Elger, C. E., Urbach, H., Clusmann, H., & Von Lehe, M. (2012). Risks and benefits of invasive epilepsy surgery workup with implanted subdural and depth electrodes. *Epilepsia*, *53*(8), 1322–1332. https://doi.org/10.1111/j.1528-1167.2012.03545.x

Wendel, K., Väisänen, O., Malmivuo, J., Gencer, N. G., Vanrumste, B., Durka, P., Magjarević, R., Supek, S., Pascu, M. L., Fontenelle, H., & Grave De Peralta Menendez, R. (2009). EEG/MEG source imaging: Methods, challenges, and open issues. *Computational Intelligence and Neuroscience*, *2009*. https://doi.org/10.1155/2009/656092

Weng, J. C., Chuang, K. H., Goloshevsky, A., Dodd, S. J., & Sharer, K. (2011). Mapping plasticity in the forepaw digit barrel subfield of rat brains using functional MRI. *NeuroImage*, *54*(2), 1122–1129. https://doi.org/10.1016/j.neuroimage.2010.08.046

Widjaja, E., Shammmas, A., Valie, R., Otsubo, H., Ochi, A., Snead, O. C., Go, C., & Charron, M. (2013). *FDG-PET and magnetoencephalography in presurgical workup of children with localization-related* (pp. 691–699). Epilepsia.

Wijdenes, P., Haider, K., Gavrilovici, C., Gunning, B., Wolff, M. D., Lijnse, T., Armstrong, R., Teskey, G. C., Rho, J. M., Dalton, C., & Syed, N. I. (2021). Three dimensional microelectrodes enable high signal and spatial resolution for neural seizure recordings in brain slices and freely behaving animals. *Scientific Reports*, *11*(1), 1–13. https://doi.org/10.1038/s41598-021-01528-4

Winslow, B. D., Christensen, M. B., Yang, W. K., Solzbacher, F., & Tresco, P. A. (2010). A comparison of the tissue response to chronically implanted Parylene-C-coated and uncoated planar silicon microelectrode arrays in rat cortex. *Biomaterials*, *31*(35), 9163–9172. https://doi.org/10.1016/j.biomaterials.2010.05.050

Witkowska-Wrobel, A. (2020). Imaging Physiological Brain Activity and Epilepsy with Electrical Impedance Tomography. In *Doctoral Thesis*. University College London.

Witkowska-Wrobel, A., Aristovich, K., Crawford, A., Perkins, J. D., & Holder, D. (2021). Imaging of focal seizures with Electrical Impedance Tomography and depth electrodes in real time. *NeuroImage*, *234*(June 2020), 117972. https://doi.org/10.1016/j.neuroimage.2021.117972

Wong, C. H., Birkett, J., Byth, K., Dexter, M., Somerville, E., Gill, D., Chaseling, R., Fearnside, M., & Bleasel, A. (2009). Risk factors for complications during intracranial electrode recording in presurgical evaluation of drug resistant partial epilepsy. *Acta Neurochirurgica*, *151*(1), 37–50. https://doi.org/10.1007/s00701-008-0171-7

Woolsey, T. A., Rovainen, C. M., Cox, S. B., Henegar, M. H., Liang, G. E., Liu, D., Moskalenko, Y. E., Sui, J., & Wei, L. (1996). Neuronal units linked to microvascular modules in cerebral cortex: Response elements for imaging the brain. *Cerebral Cortex*, *6*(5), 647–660. https://doi.org/10.1093/cercor/6.5.647

Wu, C., & Sun, D. (2015). GABA receptors in brain development, function, and injury. *Metabolic Brain Disease*, *30*(2), 367–379. https://doi.org/10.1007/s11011-014-9560-1

Wyler, A. R., & Ward, A. A. (1981). Neurons in human epileptic cortex. *Journal of Neurosurgery*, *55*(6), 904–908. https://doi.org/10.3171/jns.1981.55.6.0904

Wyrwicz, A. M., Conboy, C. B., Ryback, K. R., Nichols, B. G., & Eisele, P. (1987). In vivo 19F-NMR study of isoflurane elimination from brain. *BBA - Molecular Cell Research*, *927*(1), 86–91. https://doi.org/10.1016/0167-4889(87)90069-3

Xiao, Y., Cui, X., & Martin, D. C. (2004). Electrochemical polymerization and properties of PEDOT/S-EDOT on neural microelectrode arrays. *Journal of Electroanalytical Chemistry*, *573*(1), 43–48. https://doi.org/10.1016/j.jelechem.2004.06.024

Xu, H. T., Pan, F., Yang, G., & Gan, W. B. (2007). Choice of cranial window type for in vivo imaging affects dendritic spine turnover in the cortex. *Nature Neuroscience*, *10*(5), 549–551. https://doi.org/10.1038/nn1883

Yaari, Y., Konnerth, A., & Heinemann, U. (1986). Nonsynaptic epileptogenesis in the mammalian hippocampus in vitro. II. Role of extracellular potassium. *Journal of Neurophysiology*, *56*(2), 424–438. https://doi.org/10.1152/jn.1986.56.2.424

Yang, B., Shi, X., Dai, M., Xu, C., You, F., Fu, F., Liu, R., & Dong, X. (2014). Real-time imaging of cerebral infarction in rabbits using electrical impedance tomography. *Journal of International Medical Research*, *42*(1), 173–183. https://doi.org/10.1177/0300060513499100

Yang, L., Dai, M., Xu, C., Zhang, G., Li, W., Fu, F., Shi, X., & Dong, X. (2017). The frequency spectral properties of electrode-skin contact impedance on human head and its frequency-dependent effects on frequency-difference EIT in stroke detection from 10Hz to 1MHz. *PLoS ONE*, *12*(1), 1–21. https://doi.org/10.1371/journal.pone.0170563

Yang, X., Hyder, F., & Shulman, R. G. (1996). Activation of single whisker barrel in rat brain localized by functional magnetic resonance imaging. *Proceedings of the National Academy of Sciences of the United States of America*, *93*(1), 475–478. https://doi.org/10.1073/pnas.93.1.475

Yasuda, N., Lockhart, S. H., Eger, E. I., Weiskopf, R. B., Liu, J., Laster, M., Taheri, S., & Peterson, N. A. (1991). Comparison of kinetics of sevoflurane and isoflurane in humans. *Anesthesia and Analgesia*, *72*(3), 316–324. https://doi.org/10.1213/00000539-199103000-00007

Yi, D., Yao, Y., Wang, Y., & Chen, L. (2024). Design, fabrication, and implantation of invasive microelectrode arrays as in vivo brain machine interfaces: A comprehensive review. *Journal of Manufacturing Processes*, *126*(July 2024), 185–207. https://doi.org/10.1016/j.jmapro.2024.07.100

Yoo, P. E., John, S. E., Farquharson, S., Cleary, J. O., Wong, Y. T., Ng, A., Mulcahy, C. B., Grayden, D. B., Ordidge, R. J., Opie, N. L., O’Brien, T. J., Oxley, T. J., & Moffat, B. A. (2018). 7T-fMRI: Faster temporal resolution yields optimal BOLD sensitivity for functional network imaging specifically at high spatial resolution. *NeuroImage*, *164*(March 2017), 214–229. https://doi.org/10.1016/j.neuroimage.2017.03.002

Yoon, H. H., Kwon, H. L., Mattson, R. H., Spencer, D. D., & Spencer, S. S. (2003). Long-term seizure outcome in patients initially seizure-free after resective epilepsy surgery. *Neurology*, *61*(4), 445–450. https://doi.org/10.1212/01.WNL.0000081226.51886.5B

Yu, X., Glen, D., Wang, S., Dodd, S., Hirano, Y., Saad, Z., Reynolds, R., Silva, A. C., & Koretsky, A. P. (2012). Direct imaging of macrovascular and microvascular contributions to BOLD fMRI in layers IV-V of the rat whisker-barrel cortex. *NeuroImage*, *59*(2), 1451–1460. https://doi.org/10.1016/j.neuroimage.2011.08.001

Zhang, M., Ladas, T. P., Qiu, C., Shivacharan, R. S., Gonzalez-Reyes, L. E., & Durand, D. M. (2014). Propagation of epileptiform activity can be independent of synaptic transmission, gap junctions, or diffusion and is consistent with electrical field transmission. *Journal of Neuroscience*, *34*(4), 1409–1419. https://doi.org/10.1523/JNEUROSCI.3877-13.2014

Appendix A

Technical details and specifications of the ActiChamp EEG amplifier*

Specification	Value
Maximum sampling rate with 64 EEG channels in use	50 kHz
Maximum sampling rate with 128 EEG channels in use	25 kHz
Maximum bandwidth of the EEG channels	DC up to 7.5 kHz
Anti-aliasing filter	8 kHz
Internal Gain	5
Resolution	24-bit
Input noise (DC – 35 Hz)	2 µV peak-to-peak
Input voltage range (EEG)	+/- 400 mV
Warm-up signal drift[§]	~0.3 %
Common-mode rejection (CMR)	100 dB
Operation	Temperature: 10 °C to 40 °C Relative humidity: 25 % to 75 %, non-condensing Atmospheric pressure: 700 hPa to 1,050 hPa

*Technical details and specifications listed in the above table were obtained from the following sources: ActiCHamp User Manual (Brain Products GmbH, 2016), Faulkner (2019), Ravagli et al. (2022), Thompson et al. (2024).

[§] Attributable to the current source.

Appendix B

Technical details and specifications of the NeuroLog™ NL106 amplifier* and the National Instruments DAQ**

Specification	**Value**
NL106 AC-DC amplifier	
Input impedance	1 MΩ
Input voltage range	±3 V (working): ±15 V (overload)
Input noise (100 Hz bandwidth)	<0.1 µV rms
Output voltage range	±12 V
Output impedance	600 Ω
Common-mode rejection (CMR)	>2500:1 at 50Hz
Warm-up signal drift[§]	~0.3 %
NI 625 DAQ	
Maximum sampling rate	1.25 MHz single channel 1.00 MHz multi-channel
Gain	0 – 100
Resolution	16-bit
Input voltage range	+/- 5V
Sensitivity (at +/- 1V range used in the recordings)	12.8 µV
Common-mode rejection (CMR)	100 dB

*Technical details listed in the above table were obtained from the NeuroLog™ System User Manual (Digimeter Ltd, 2001) and the NI 625 Specifications (National Instruments, 2014).

§Attributable to the current source.